

Fall 11-6-2018

# ENGINEERING VISCOELASTIC BEHAVIOR OF CARBON FIBER REINFORCED POLYMER COMPOSITES WITH NANOPARTICLES FOR CONTROLLING DEPLOYMENT OF AEROSPACE STRUCTURES

Mark Scherbarth  
*University of New Mexico*

Follow this and additional works at: [https://digitalrepository.unm.edu/me\\_etds](https://digitalrepository.unm.edu/me_etds)

Part of the [Mechanical Engineering Commons](#)

---

## Recommended Citation

Scherbarth, Mark. "ENGINEERING VISCOELASTIC BEHAVIOR OF CARBON FIBER REINFORCED POLYMER COMPOSITES WITH NANOPARTICLES FOR CONTROLLING DEPLOYMENT OF AEROSPACE STRUCTURES." (2018). [https://digitalrepository.unm.edu/me\\_etds/157](https://digitalrepository.unm.edu/me_etds/157)

This Dissertation is brought to you for free and open access by the Engineering ETDs at UNM Digital Repository. It has been accepted for inclusion in Mechanical Engineering ETDs by an authorized administrator of UNM Digital Repository. For more information, please contact [disc@unm.edu](mailto:disc@unm.edu).

Mark R. Scherbarth

*Candidate*

---

Mechanical Engineering

*Department*

---

This dissertation is approved, and it is acceptable in quality and form for publication:

*Approved by the Dissertation Committee:*

Mahmoud M. Reda Taha, Ph.D., Chairperson

---

Yu-Lin Shen, Ph.D.

---

Mehran Tehrani, Ph.D.

---

Kawai Kwok, Ph.D.

---

**ENGINEERING VISCOELASTIC BEHAVIOR OF CARBON  
FIBER REINFORCED POLYMER COMPOSITES WITH  
NANOPARTICLES FOR CONTROLLING DEPLOYMENT OF  
AEROSPACE STRUCTURES**

**BY**

**MARK R. SCHERBARTH**

B.S., Mechanical Engineering, Marquette University, 1999  
M.S., Mechanical Engineering, California State University, Long  
Beach, 2003

DISSERTATION

Submitted in Partial Fulfillment of the  
Requirements for the Degree of

**Doctor of Philosophy**

**Engineering**

The University of New Mexico  
Albuquerque, New Mexico

**December, 2018**

## ACKNOWLEDGEMENTS

I would like to thank and acknowledge the numerous individuals, companies and organizations who helped me complete this research work enabling award of my doctorate. I could not have made it to the finish line without all of their support.

First off, I want to thank my advisor, Dr. Mahmoud Reda Taha, for his guidance, direction and advice over the course of three years from selection and refinement of this dissertation research topic to several clarifications in scope to keep me on track. I would like to thank my committee members, Dr. Yu-Lin Shen, Dr. Mehran Tehrani and Dr. Kawai Kwok, for serving on my committee and ensuring I had a complete and quality research product both I and the university could be proud of.

I would like to thank my first and second level supervisors at the Air Force Research Laboratory (AFRL) who supported me in this PhD program from beginning to end over the last seven years: Mr. James Winter, Dr. Joel Mozer, Dr. Rich DeJonckheere, Col Sam Johnson, Mr. Barry Bunn and Col Russ Teehan. These leaders allowed me to attend classes during the work week, complete dissertation work during the work week and take a sabbatical at the end to get me to the finish line.

I would like to thank the AFRL Technical Library, in particular Ms. Elizabeth Luebchow, for all the help in retrieving the hundreds of references from all over the country and even the world. This assistance was much appreciated so I could focus on the content of the research, not the logistics of getting the resources.

I would like to thank the AFRL, Space Vehicles Directorate, Spacecraft Technologies Division, Integrated Structural Systems Group and the Composites Laboratory. In particular, Mr. Mike Peterson who helped me with some of the experimental testing and composites fabrication; Mr. Jeff Brumfield, for all his help in fabricating the 51 tape springs; Mr. Marty Wyse, for constructing my test fixture from my crude drawings and always willing to help me solve a tool or fixture issue such as the slots on the test stand, the stuck screw on the hub and the connector interface; Mr. Neil Vaughn, for all the help in shipping and receiving materials and parts from Adherent Technologies and Patz Materials and Technologies; Mr. Cody Griffin, for his help in setting up the Instron MTS machine and TestWorks 4 software; Dr. Joe Footdale, for his advice on tape spring modeling in Abaqus; and Mr. Joe Regalado and Ms. Jasmin Regalado, for their help in taking tape spring measurements and swapping out tape springs during the experimental test campaign.

I would like to thank Patz Materials and Technologies and Mr. Nick Patz for the donated epoxy and working with me to produce a unique, tailored version of their epoxy with the addition of nanoparticles. I also would like to thank Adherent Technologies and Dr. Ron Allred for dispersing the alumina nanoparticles (ANPs) in the epoxy, twice. I want to thank TA Instruments and Dr. Greg Kamykowski for the many discussions on DMA testing and data manipulation. I want to thank the UNM-SNL Center for High Technology Materials and Dr. John Plumley for his assistance with the SEM/EDS work.

I want to thank Ms. Elisa Borowski and Ms. Amy Garner for many thoughtful discussions regarding Abaqus modeling, composite laminate properties determination,

UMAT subroutine logic and Prony series curve fitting. I want to thank Dr. Aaron Adler for many enlightening discussions on Abaqus modeling strategy, experimental testing techniques and bouncing ideas back and forth with me. I want to thank Lt Col Robert Decker for discussions regarding data analysis, Fortran coding and Abaqus troubleshooting.

I want to thank the Abaqus Technical Support team, particularly Mr. Jody Hart and Mr. Tom Wilt, for their help in troubleshooting peculiar Abaqus error messages and understanding in great detail how Abaqus modeling options work “under the hood.”

Finally, last but not least, I want to thank my family, my wife Angie and my sons, Nathan, a sophomore at La Cueva High School, and Ryan, a freshman at La Cueva High School. I owe them a debt of gratitude for the family time when I was absent or mentally distracted by this research work. Angie has been supportive since the start of this endeavor, seven years ago, and has never faltered along the way. I hope Nathan and Ryan will look back on this time and realize the value of hard work and education and to always strive to reach your highest potential. You can do more than you think, if you set your mind to it. Education does not end at any particular age or accomplishment. When you stop learning, you stop living. I love you all.

**ENGINEERING VISCOELASTIC BEHAVIOR OF CARBON FIBER  
REINFORCED POLYMER COMPOSITES WITH NANOPARTICLES FOR  
CONTROLLING DEPLOYMENT OF AEROSPACE STRUCTURES**

**by**

**Mark R. Scherbarth**

**B.S., Mechanical Engineering, Marquette University, 1999**

**M.S., Mechanical Engineering, California State University, Long Beach, 2003**

**Ph.D., Engineering, University of New Mexico, 2018**

**ABSTRACT**

The United States Air Force is focused on reducing mass and power consumption of spacecraft to increase their capabilities for space missions. Low mass and power consumption can be achieved by using composites with low density and high stiffness and utilizing few satellite components. One way to achieve reduced mass is by eliminating attendant deployment mechanisms consuming valuable power and mass allocations on spacecraft with deployable structures. Secondary systems are typically used to assist deployable space structures to ensure 100% success. A passively deployed space structure would be of great value to the Department of Defense and the commercial marketplace. Attaining a passively deployed space structure that is reliable, predictable and controllable to tailored design applications would serve this objective.

The research presented herein was experimentally focused and involved incorporation of alumina nanoparticles (ANPs) dispersed into a three-ply composite

laminated tape spring structure. The FlexLam composite was designed and fabricated for this class of tape spring deployable structures. A total of 51 tape springs were structurally tested on a unique, custom-designed test fixture with methodology to analyze their stress relaxation behavior in a coiled state for lengths of time varying from 1 hour to 6 months. A finite element model (FEM) with a Fortran subroutine was built and simulations were correlated with the structural deployment testing of 26 control tape springs and 25 ANP tape springs. The FEM simulation-predicted results correlated within 5% of the experimental testing structural results. A total of 5 epoxy samples (3 neat epoxy and 2 ANP epoxy) were fabricated and cut into 29 coupons for Dynamic Mechanical Analysis (DMA) tests and Scanning Electron Microscope with Energy Dispersive X-ray Spectroscopy (SEM/EDS) examinations were also performed on 4 test coupons (3 ANP and 1 control) to characterize the microstructure of the composites, including the ANP dispersion and agglomeration. It was shown the ANP tape spring structures were able to retain 55% more tip force and experience less stress relaxation compared to the control tape springs. Future work is recommended in optimization of the composite and further development of the FEM simulation for improving structural behavior prediction.

## Publications

During the course of preparing this dissertation, the following publications were produced:

### **Conference Papers**

- Scherbarth, M., Reda Taha, M., (2018). Stowage Testing and Modeling of Viscoelastic Tape Springs, AIAA Science & Technology Forum, Jan 2019, San Diego, CA

### **Journal Papers**

- Scherbarth, M., Reda Taha, M., (2018). Stress Relaxation and Creep Control of a Thin Composite Laminate using Alumina Nanoparticles, AIAA Journal, *in preparation*

### **Technical Reports**

- Peterson, M., Scherbarth, M., Banik, J., Characterizing, Modeling, and Tailoring Strain Energy Release Rates in Flexible Composites, FY16 Annual Task Report, LRIR #: 15RVCOR174

### **Patents**

- Scherbarth, M., Reda Taha, M., A New Composite Tape Spring with Engineered Deployment Energy using Nanoparticles and Methods of Making, U.S. Provisional Patent filed, 1 October 2018

# TABLE OF CONTENTS

LIST OF FIGURES .....	xi
LIST OF TABLES .....	xv
CHAPTER 1 INTRODUCTION .....	1
1.1 Motivation and Problem.....	1
1.2 Scientific and Engineering Importance .....	9
1.3 Contribution and New Understanding.....	14
CHAPTER 2 LITERATURE REVIEW .....	20
2.1 Relevant Prior Research.....	20
2.2 Viscoelastic Materials .....	61
2.3 Viscoelastic Material Behavior .....	68
2.4 Material Properties .....	75
2.5 Modeling Considerations .....	80
CHAPTER 3 EXPERIMENTAL METHODS .....	95
3.1 Neat Epoxy Preparation .....	95
3.2 DMA Testing of Neat Epoxy .....	101
3.3 TTSP Analysis of Neat Epoxy .....	105
3.4 Fabrication of Control Tape Springs.....	112
3.5 Structural Testing of Control Tape Springs .....	113
3.5.1 Structural Test Fixture Design and Setup.....	113
3.5.2 Structural Testing Procedure Steps.....	116
3.5.3 Torque Calculations.....	123
3.6 ANP Epoxy Preparation.....	124
3.7 DMA Testing of ANP Epoxy.....	126
3.8 TTSP Analysis of ANP Epoxy.....	127
3.9 Fabrication of ANP Tape Springs .....	128
3.10 Structural Testing of ANP Tape Springs.....	130
3.11 SEM and EDS of Control and ANP Tape Springs.....	132
CHAPTER 4 NUMERICAL METHODS .....	145

4.1 FlexLam Composite Laminate Design.....	147
4.2 Abaqus Analysis Steps for Model Simulation .....	153
4.3 Abaqus Finite Element Model Definition .....	156
4.3.1 Tape Springs' Material Properties .....	162
4.3.2 Abaqus VUMAT Subroutine.....	165
4.3.3 Viscoelastic Modeling with the Prony Series.....	171
4.3.4 Micromechanics and Classical Lamination Theory (CLT) .....	172
4.4 Abaqus Modeling .....	181
CHAPTER 5 RESULTS AND DISCUSSION.....	189
5.1 Neat Epoxy DMA Test Results .....	189
5.2 Control Tape Springs' Test Results .....	196
5.2.1 One Hour Tape Springs' Test Results .....	196
5.2.2 One Day Tape Springs' Test Results.....	197
5.2.3 One Week Tape Springs' Test Results .....	198
5.2.4 One Month Tape Springs' Test Results.....	200
5.2.5 Six Months Tape Springs' Test Results .....	201
5.3 ANP Epoxy DMA Test Results .....	203
5.4 ANP Tape Springs' Test Results.....	208
5.4.1 One Hour Tape Springs' Test Results .....	209
5.4.2 One Day Tape Springs' Test Results.....	210
5.4.3 One Week Tape Springs' Test Results .....	212
5.4.4 One Month Tape Springs' Test Results.....	214
5.4.5 Six Months Tape Springs' Test Results .....	215
5.5 Comparison of Structural Test Results.....	217
5.6 Abaqus Finite Element Model Simulation Results .....	228
5.6.1 Correlation of Abaqus FEM and Control Tape Springs' Test Results .....	229
5.6.2 Correlation of Abaqus FEM and ANP Tape Springs' Test Results .....	240
5.7 Summary .....	250
CHAPTER 6 CONCLUSION AND RECOMMENDATIONS .....	252

6.1 Conclusions .....	252
6.2 Limitations and Constraints .....	257
6.3 Future Work .....	260
APPENDIX A: Control Tape Springs' Measurements.....	265
APPENDIX B: ANP Tape Springs' Measurements .....	267
APPENDIX C: Abaqus VUMAT Fortran Code.....	269
REFERENCES .....	279

## LIST OF FIGURES

Figure 2.1 Voigt (Left) and Maxwell (Right) Rheological Models.....	65
Figure 2.2 Generalized Maxwell Rheological Model.....	66
Figure 2.3 General Stress and Strain Behavior of a Material Subject to Creep.....	69
Figure 2.4 General Stress and Strain Response of a Material Subject to Stress Relaxation .....	70
Figure 2.5 Generic Modulus of a Polymer Through its Tg Transition .....	74
Figure 3.1 FlexLam Composite Laminate Layup .....	96
Figure 3.2 Flowchart of Experimental Testing and Numerical Modeling Workflow .....	97
Figure 3.3 Neat Resin Part A and Part B .....	98
Figure 3.4 Preparation of Neat Epoxy .....	98
Figure 3.5 AFRL's De-Gassing Chamber .....	99
Figure 3.6 Mold for Neat Epoxy Sample.....	100
Figure 3.7 Chemical Release Film for DMA Sample.....	100
Figure 3.8 Neat Epoxy Sample #2 .....	101
Figure 3.9 Laser Cutter and Neat Epoxy Samples for DMA Testing.....	102
Figure 3.10 Waterjet Cutting Machine at Holloman Air Force Base .....	103
Figure 3.11 Neat Epoxy Coupons for DMA Testing.....	103
Figure 3.12 DMA Test on Neat Epoxy Coupon .....	104
Figure 3.13a TTSP Data for Neat Epoxy DMA Tests, Loss Modulus – Trial #1 in Log- Log Plot.....	108
Figure 3.13b TTSP Data for Neat Epoxy DMA Tests, Storage Modulus – Trial #1 in Log-Log Plot.....	109
Figure 3.14 Lab-Temp Thermal Chamber .....	111
Figure 3.15 Control Group Tape Springs for Structural Testing.....	112

Figure 3.16	Tape Spring Test Fixture and Initial Test Setup.....	114
Figure 3.17	Tape Spring Radius Definition.....	115
Figure 3.18	Dowel for Securing Tape Spring Tip During Structural Testing .....	115
Figure 3.19	Tape Spring Boundary Conditions in Experimental Testing .....	116
Figure 3.20	Counter Mass for Tape Springs' Structural Testing.....	117
Figure 3.21	Structural Test Setup with Dowel Extension and Riser Slots .....	119
Figure 3.22	Tape Spring Structural Testing Load Profile.....	120
Figure 3.23	Structural Test Configuration for One Hour and One Day Tape Springs ..	121
Figure 3.24	Structural Test Configuration for One Week, One Month and Six Month Tape Springs .....	121
Figure 3.25	Full Test Setup and 26 Control Tape Springs Post Structural Testing.....	122
Figure 3.26	ANP DMA Coupons .....	125
Figure 3.27	DMA Testing of ANP Coupons .....	126
Figure 3.28	PW Prepreg and UD Prepreg.....	129
Figure 3.29	Vacuum Bagging Process for Fabrication of Tape Springs .....	129
Figure 3.30	ANP Tape Springs After Fabrication Complete.....	130
Figure 3.31	ANP Tape Spring Structural Testing One Hour and One Day.....	131
Figure 3.32	Tuf-Line for Structural Testing .....	132
Figure 3.33	Failed Tuf-Line.....	132
Figure 3.34	JEOL-JSM-IT100 SEM/EDS for ANP Dispersion Examination.....	133
Figure 3.35	SEM Coating Machine .....	133
Figure 3.36	SEM Coupon .....	133
Figure 3.37	SEM Image of Control Tape Spring.....	134
Figure 3.38	SEM/EDS Analysis of Control Tape Spring.....	135
Figure 3.39	SEM Images of ANP Tape Spring NA-1H-3 .....	136
Figure 3.40	SEM Images of ANP Tape Spring NA-1M-2 .....	136
Figure 3.41	SEM Image of ANP Tape Spring NA 6M-1 .....	137
Figure 3.42	SEM/EDS Analysis of ANP Tape Spring .....	138
Figure 3.43	Gold-Sputtered ANP Epoxy Coupon .....	139
Figure 3.44	SEM/EDS of ANP Epoxy .....	141
Figure 3.45	SEM Image of Analysis Box on ANP Epoxy Coupon.....	142
Figure 3.46	ANP Epoxy Elemental Composition (Box Analysis) .....	143
Figure 3.47	SEM Image of Analysis Point on ANP Epoxy.....	143
Figure 3.48	ANP Epoxy Element Composition (Point Analysis).....	144
Figure 4.1	FlexLam Composite Laminate Layup .....	149
Figure 4.2	Tape Spring Simulation Steps in Abaqus.....	154
Figure 4.3	Through Thickness Shell Elements Bending in Abaqus .....	159
Figure 4.4	Abaqus Import Analysis Modeling Strategy .....	160

Figure 4.5 Abaqus Data Flow and Logic for VUMAT Subroutine .....	169
Figure 4.6 Geometry of N-Layered Composite Laminate .....	176
Figure 4.7 Tape Spring Load Geometry and Equal Sense Bending/Rolling .....	176
Figure 4.8 Pristine Tape Spring Shape and Global Coordinates .....	178
Figure 4.9 Bending Moments and Curvatures in Tape Spring .....	179
Figure 5.1 Neat Epoxy Storage and Loss Moduli as a Function of Frequency (Log Scale) .....	191
Figure 5.2 Neat Epoxy Complex Modulus Master Curve in Log-Log Plot.....	193
Figure 5.3 Prony Series Curve for Relaxation Modulus of Neat Epoxy in Log-Log Plot .....	194
Figure 5.4 Control Tape Springs One Hour Stowage Results Showing Loss in Tape Spring Deployment Force Over Time.....	197
Figure 5.5 Control Tape Springs One Day Stowage Results Showing Loss in Tape Spring Deployment Force Over Time.....	198
Figure 5.6 Control Tape Springs One Week Stowage (via TTSP) Results Showing Loss in Tape Spring Deployment Force Over Time .....	200
Figure 5.7 Control Tape Springs One Month Stowage (via TTSP) Results Showing Loss in Tape Spring Deployment Force Over Time .....	201
Figure 5.8 Control Tape Springs Six Months Stowage (via TTSP) Results Showing Loss in Deployment Force Over Time .....	203
Figure 5.9 ANP Epoxy Storage and Loss Moduli in Log-Log Plot.....	204
Figure 5.10 ANP Epoxy Complex Modulus Master Curve in Log-Log Plot .....	204
Figure 5.11 Neat Epoxy and ANP Epoxy Complex Moduli Comparison in Log-Log Plot .....	205
Figure 5.12 Neat Epoxy and ANP Epoxy Comparison of Loss Moduli in Log-Log Plot .....	206
Figure 5.13 Neat Epoxy and ANP Epoxy Comparison of Storage Moduli in Log-Log Plot .....	206
Figure 5.14 Prony Series Curve for Relaxation Modulus of ANP Epoxy in Log-Log Plot .....	207
Figure 5.15 ANP Tape Springs One Hour Stowage Results Showing Loss in Tape Spring Deployment Force Over Time .....	210
Figure 5.16 ANP Tape Springs One Day Stowage Results Showing Loss in Tape Spring Deployment Force Over Time .....	211
Figure 5.17 Median Control Group Tape Spring and Median ANP Group Tape Spring One Day Stowage Tests' Comparison .....	212
Figure 5.18 ANP Tape Springs One Week Stowage (via TTSP) Results Showing Loss in Tape Spring Deployment Force Over Time.....	213

Figure 5.19 ANP Tape Springs One Month Stowage (via TTSP) Results Showing Loss in Tape Spring Deployment Force Over Time .....	215
Figure 5.20 ANP Tape Springs Six Months Stowage (via TTSP) Results Showing Change in Load Over Time.....	216
Figure 5.21 Comparison Between Neat Epoxy and ANP Epoxy Relaxation Modulus..	223
Figure 5.22 Energy Analysis for Steps 1 and 2 of Abaqus Simulation of Control Tape Springs with One Hour Stowage.....	232
Figure 5.23 Energy Analysis for Step 3 of Abaqus Simulation of Control Tape Springs with One Hour Stowage.....	233
Figure 5.24 Abaqus Predicted Strain in Control Tape Spring at End of 1 Hour Stow Period .....	234
Figure 5.25 Comparison of Abaqus Predicted Results and Experimental Structural Test Results for Median Control Tape Spring (Tape 5) for One Hour Stowage .....	235
Figure 5.26 Comparison of Abaqus Predicted Results and Experimental Structural Test Results for Median Control Tape Spring (Tape 6) for One Week Stowage.....	236
Figure 5.27 Comparison of Abaqus Predicted Results and Experimental Structural Test Results for Median Control Tape Spring (Tape 4) for One Month Stowage.....	238
Figure 5.28 Comparison of Abaqus Predicted Results and Experimental Structural Test Results for Median Control Tape Spring (Tape 5) for Six Months Stowage .....	239
Figure 5.29 Energy Analysis for Steps 1 and 2 of Abaqus Simulation of ANP Tape Springs with One Hour Stowage.....	240
Figure 5.30 Energy Analysis for Step 3 of Abaqus Simulation of ANP Tape Springs with One Hour Stowage.....	241
Figure 5.31 Abaqus Predicted Strain in ANP Tape Spring at End of 1 Hour Stow Period .....	242
Figure 5.32 Comparison of Abaqus Predicted Results and Experimental Structural Test Results for Median ANP Tape Spring (Tape 2) for One Hour Stowage .....	243
Figure 5.33 Comparison of Abaqus Predicted Results and Experimental Structural Test Results for Median ANP Tape Spring (Tape 1) for One Week Stowage .....	244
Figure 5.34 Comparison of Abaqus Predicted Results and Experimental Structural Test Results for Median ANP Tape Spring (Tape 5) for One Month Stowage.....	245
Figure 5.35 Comparison of Abaqus Predicted Results and Experimental Structural Test Results for Median ANP Tape Spring (Tape 1) for Six Months Stowage.....	246
Figure 5.36 Abaqus vs Experimental Tape Spring Tip Deployment Force Loss for Control Tape Springs .....	248
Figure 5.37 Abaqus vs Experimental Tape Spring Tip Deployment Force Loss for ANP Tape Springs .....	249

## LIST OF TABLES

Table 3.1	TTSP Reduced Test Times for Control Tape Springs .....	110
Table 3.2	TTSP Reduced Test Times for ANP Tape Springs .....	128
Table 3.3	Control Tape Springs' Elemental Composition.....	135
Table 3.4	ANP Tape Springs' Elemental Composition.....	139
Table 3.5	ANP Epoxy Elemental Composition (Point Analysis) .....	144
Table 4.1	Analysis Steps in Abaqus FEM Simulation.....	154
Table 4.2	Material Properties for Abaqus Model .....	164
Table 4.3	Abaqus Material Property Values for VUMAT .....	166
Table 4.4	Abaqus Solution-Dependent State Variables for VUMAT .....	167
Table 5.1	Prony Series Coefficients for Neat Epoxy .....	195
Table 5.2	Prony Series Coefficients for ANP Epoxy .....	208
Table 5.3	Average Force Recordings at Beginning and End of Stowage Period at Tape Spring Tips.....	219
Table 5.4	Average Percentage Loss in Tape Springs' Tip Force During Stowage .....	227
Table 5.5	Abaqus Consistent Unit Options.....	231
Table 5.6	Abaqus vs Experimental Tape Spring Tip Deployment Force Loss .....	247
Table A.1	Control Tape Springs' Measurements .....	265
Table B.1	ANP Tape Springs' Measurements .....	267

# CHAPTER 1 INTRODUCTION

## 1.1 Motivation and Problem

The United States Air Force is investing in science and technology to reduce mass and power consumption of operational spacecraft to maintain an advantage in space. Low mass and power consumption can be achieved by using composites with low density and high stiffness and utilizing fewer satellite components. Small satellites and CubeSat-class satellite missions are also driving requirements for low mass, small volume, low power and mechanical simplicity. These requirements enable rockets to launch with more spacecraft, and spacecraft with smaller stowage volume and lower mass permitting more mission payloads (i.e., more capabilities) to orbit. However, composites also inherently have more risk due to their complexity, and previous on-orbit failures of deployable composite structures have only increased pressure on the engineer.

One of the main reasons for the focus on reduced mass and smaller stowed volume of spacecraft is the very high cost of space launch at approximately \$10,000 per pound. (Wilkins and Armendariz, 2002) Thus, a continuing challenge for engineers is to package spacecraft and their associated large deployable structures in the confined volume of standardized launch vehicle fairings serving the government and commercial marketplace. Nearly all spacecraft require their structures to be compactly packaged during launch and subsequently deployed on orbit to a much larger configuration, such as solar arrays, antennas, solar sails and booms for payloads and gravity gradient control. These structures have to work perfectly upon deployment since on-orbit repair or

modification is rarely possible. Moreover, deployable space structures made from traditional metallic materials have intrinsic disadvantages such as high mass and deployment shock, and they cannot in general be tailored for specific properties. Additionally, the design of a deployable space structure often involves complex assembly and control mechanisms with numerous parts to ensure a reliable and predictable deployment. If a structure's deployment occurs via strain energy, the strain energy must be controlled during stowage and also during deployment to prevent shock to the structure itself and for any payload it may be supporting. Furthermore, complications involving solar radiation, magnetic fields, micro-gravity and atmospheric drag forces can have substantial implications on the design of these structures.

Unique requirements for space deployable structures, not often found in terrestrial structures, are radiation resistance and functionality in the harsh space environment. Space systems and their associated structures must survive extreme acoustic, thermal and radiation impacts. Since spacecraft structures often deploy sensitive instruments, provide gravity gradient attitude control and serve as antennas, materials for spacecraft need to be radiation resistant to maintain structural integrity and performance. Earth's magnetosphere shields our planet from the most damaging galactic cosmic rays, protons, electrons and ions. However, beyond low earth orbit (LEO), the Van Allen radiation belts in medium earth orbit (MEO) and further into geosynchronous orbit (GEO), consist of damaging radiation which is a major concern. At the same time, during solar maximum the most common form of radiation is proton radiation, and protons in LEO (< 1,000 km altitude) can have widely varying energy spectra, from 10's of KeV to GeV energy range. These levels of radiation can have negative consequences and alter the mechanical

properties of the structure. The sources of ionizing radiation in LEO include galactic cosmic rays, trapped particles in the radiation belts and solar particle events. (Boul et al., 2009) Deployable space structures must also operate in the vacuum of space across a very broad temperature range from approximately  $-50^{\circ}\text{C}$  to  $+100^{\circ}\text{C}$  so most of these structures also have additional design constraints levied from the spacecraft, a subsystem or the launch vehicle, including: minimum first vibration mode frequency, damping to minimize settling times, high reliability, cost, minimum mass and minimum volume. (Voevodin and Zabinski, 2005) Despite all the constraining requirements, satellites and deployable space structures keep evolving and have been improving and advancing since the late 1950's.

Four deployable booms served as spacecraft antennas on Sputnik I--the first artificial earth-orbiting satellite successfully launched in October 1957 by the U.S.S.R. Since then the majority of the booms flown in space have been made of Beryllium Copper (BeCu). (Yee et al., 2004) Spacecraft booms are typically long and slender and consequently, susceptible to buckling. Therefore, design of a boom structure should be validated through a series of analytical and numerical models, component level tests, system level tests and reliability assessments. The dominant cause of boom distortions is often deformation caused from the thermal environment, and this is true for the space environment as well. However, most spacecraft booms cannot be adequately tested in earth's environment (in the deployed configuration); the synergistic effect of simultaneously testing a broad thermal range under vacuum, microgravity and radiation with a large deployed gossamer structure is cost prohibitive and is simply not feasible or

practical. Accordingly, analytical and numerical models and modeling and simulation play a tremendously important role in spacecraft structural development.

A myriad of problems can plague space deployable structures. On-orbit structural issues can include deployment system motor failure, power system failure, thermal shock and cycling, micrometeorite impingement, atmospheric drag and manufacturing issues: nonhomogeneous material properties, uneven heat treatment, dimensional/geometric variations, surface treatment and aging materials. (Pellegrino, 2005) Moreover, the interaction of a spacecraft structure with the space environment most often includes: thermally induced bending and twisting, heating due to earth albedo, thermally induced oscillations, gravity gradients, variation of center of gravity due to orbit eccentricity, solar pressure, erosion of surface finishes, electromagnetic effects and radiation degradation effects on mechanical (and electrical) performance. The space environment is indeed an extremely harsh environment to design and operate a structure therein.

Challenges and problems aside, deployable structures offer a viable method for achieving very large structures in space without requiring larger (and costlier) launch vehicles which are usually not an option or do not even exist. Utilizing composites for deployable structures helps to overcome the aforementioned issues. Composites with low density, high stiffness and large strain capacity can accommodate compact packaging/stowage and subsequent on-orbit structural deployment. Common ways to stow a deployable structure include bending, rolling or folding. All of these methods can involve substantial straining of the material to obtain a volume efficient stowage design. Composites can enable such unique structural designs. A composite, by definition, is an

engineered material system with tailored mechanical properties allowing the possibility to design for significant elastic deformation and high strain capacity. However, material failure from strain directly limits bending, rolling, foldability and thus, packageability of deployable space structures. Deformations occurring during stowage can lead to permanent (i.e., plastic) deformations such as micro-buckles, de-laminations, fiber breakage and fiber kinking which occur when the strain exceeds the elastic limits of the material. (Maddux and Murphey, 2005) Also, a critical issue for these composite deployable structures is the loss of deployment force (after long stowage times) due to the inherent viscoelastic behavior of the constituent materials. Due to load and stress relaxation during these structures' stowage period, the stored strain energy available for structural deployment is atrophied and may become too low to motivate deployment once on-orbit. Thus, viscoelastic effects must be considered when designing the structures, as stress relaxation in the stowed structure can cause deployment and mission failure. For example, the Mars Advanced Radar for Subsurface and Ionospheric Sounding (MARSIS) instrument had two 20-meter antenna booms and a third 7-meter boom constructed of glass fiber-reinforced Kevlar high strain composites. The structures' on-orbit deployment failure was attributed to thermal effects and stress relaxation in the composite, specifically the lenticular hinges. Ultimately, the spacecraft had to be maneuvered to resolve the anomalous boom deployment. The severe temperature swings, vacuum and radiation environment and long stowage time contributed significantly to the composite structures' aging and available strain energy for deployment. (Adams and Mobrem, 2009, Murphey et al., 2015, Gomez-Delrio and

Kwok, 2018) Several options may have helped avoid the MARSIS problems such as an alternative concept of operations and/or a different structural design.

Deployable space structures have typically been designed either as rigid members with mechanical joints or with a material systematically deforming. The most efficient structures have high stiffness, low mass, high strength and can take large deformations (i.e., high strain tolerable). Historically there have been two common deployment architectures for space structures: The mechanical approach (e.g., pin-clevis or ball-socket with a motor) and the material deformation approach. Both approaches are used to allow a structure to be compactly stowed and subsequently deployed on-orbit. The material deformation approach is often exploited to allow the packaging of a structure by distributing strains evenly to minimize the maximum strain required to fold the structure. (Sanford et al., 2009) Material deformation-based deployable structures employ tensile and compressive material strains to allow packaging and deployment of a structure. Efficient architectures capable of high compaction ratios exist; however, a limitation is caused by a lack of materials both stiff and capable of taking large strains. It is apparent a diverging requirement set exists because materials for deployable space structures typically only need to be stiff in the fully deployed configuration; the materials do not necessarily need to be stiff during deployment or stowage. (Murphey and Sanford, 2008) Stored strain energy deployable structures may provide a viable option meeting this requirement set.

Deployable space structures are necessary to realize large, mass-efficient space systems and their architecture can be implemented as articulated systems, elastically

deformed systems or inflatable-rigidizable systems. (Straubel, 2011) Composites offer excellent stiffness, strength, damping, low mass and tailorability (i.e., design control) and can be utilized for each structural design approach. Composites can be passively deployed in space to avoid the complexity, mass and cost limitations of the purely mechanical systems and metallic approaches. Deployable structures made of thin composite elements present a promising solution due to their high specific stiffness, tailorability and high thermal stability with low coefficient of thermal expansion (CTE). Furthermore, as composite laminates get thinner, the strain required for bending, folding or rolling these structures to a small radius for stowage is much reduced, but failure may become a more important concern.

Space deployable structures must not fail under any operating conditions, including pre-launch, ascent flight, launch vehicle separation and deployment of the structure. The key environmental factors affecting the structure include shock, vibration, large thermal swings and dynamic loads. Increasing structural stiffness helps to resist important bending and buckling loads. (NASA, 1971) Therefore, stiffness, strength (to a lesser extent) and dimensional stability are critical requirements for deployable space structures. (Jenkins, 2006) Due to the micro-gravity environment, space structures are lightly loaded and are more stiffness limited than strength limited. As such, there is a need for high stiffness, low density composite space structures as strength is not a major design factor for space structures. A high stiffness is required in spacecraft because the lowest natural frequency of its vibration must exceed a specified value to avoid resonant coupling with the launch vehicle during launch. One way to enhance a composite's mechanical properties, such as its stiffness, is to add a filler material. Fillers on the

nanometer scale, e.g., CNTs or nanoparticles, can improve the key mechanical performance parameters of polymer-based composites, such as stiffness, strength and damping. For example, several researchers have experimentally demonstrated that nanoparticles have the ability to effectively reinforce common aerospace thermosetting polymers such as epoxy. (Wetzel et al., 2003, Ng et al., 1999)

Understanding material behavior from the nanoscale all the way to structural response has long been a challenge in this field of research. The properties of polymers can be difficult to characterize or predict due to their complex structure and numerous factors influencing the material's mechanical behavior, including thermomechanical processing, time-dependent behavior and anisotropy, to name a few. (Simoes, 2006) Interest in improving the fiber/matrix bonding as well as developing new materials altogether with nanotechnology continues to increase. Also, nanoengineering of polymers and composites has made it even more difficult to trace, understand and model design changes made at the nanoscale to a reliable predicted response at the structural level (and the micro- and meso-levels in between). For example, incorporation of CNTs in polymeric composites has been researched and tested for over two decades but there is a high purchasing cost of CNTs, purity and processing are concerns and dispersion and agglomeration issues remain substantial obstacles of practicality. Unique nanocomposite effects can be quite effective if the nanofiller is well dispersed in the polymer matrix.

## 1.2 Scientific and Engineering Importance

Due to limited funding, launch vehicle constraints and other clandestine reasons, spacecraft structures must be stowed smaller, contain less mass, provide multiple purposes simultaneously and be able to be deployed and retracted numerous times while on orbit. These new structural requirements levied on the engineering community present great challenges to an already difficult task. Such deployable space structures will serve as the future government, civil and commercial space systems' architectures enabling massive structures for interplanetary travel, orbiting laboratories and lunar bases, etc.

Deployable structures made of thin carbon fiber reinforced polymer (CFRP) composites are attractive for space missions because of their high stiffness to mass ratio. Deployable space structures are often stowed for very long periods of time and subject to frequent wide-ranging thermal cycles during flight on orbit. A composite's structural behavior with respect to temperature, deformation and loading history can be attributed largely to the viscoelastic phenomenon of the matrix material. Matrix materials are often classified as either soft, such as elastomeric or rigidizable, or stiff, such as a thermoplastic or thermoset type. In terms of material strain capacity, a soft matrix can facilitate more diverse fiber and/or particle micro-deformation modes enabling achievement of larger strains than the constituent by itself. Viscoelastic effects are observed with nearly all matrices as well due to their inherent material properties. Designing these structures for controlled, predictable and reliable on-orbit deployment

requires a characterization of the viscoelastic behavior of the composite and how this behavior affects the shape recovery upon deployment. (Kwok and Pellegrino, 2010) The maximum elastic strain in a composite is a function of the material thickness and the bending radius achievable. The primary mechanism enabling large material deformations associated with very tight folding and bending ratios is thought to be micro-buckling of fibers in a soft matrix. (Murphey et al., 2001) Thus, a material's failure strain directly limits the minimum bending ratio of the structure, and ultimately its stowage volume. Bending, folding or rolling a structure for stowage has been done for decades; the earliest form of these structures was the Storable (originally "Storage") Tubular Extendable Member (STEM) boom.

STEM booms have been flown in space many times in the past and are well known and characterized. A variation of the STEM boom, a tape spring, can be used as the basic structural element for a lightweight, deployable spacecraft boom. (Murphey et al., 2010) Tape spring structural elements are very similar to the familiar metallic carpenter tape measures except they are made from a composite and can have variations of their geometric parameters to optimize the desired structural performance. In contrast to STEMs, they can be designed to be bi-stable, i.e., stable in the coiled state and stable in the fully deployed state, or neutrally stable. Tape springs belong to a class of structures called collapsible tube masts or lenticular structures (Murphey et al., 2015). These thin shell deployable structures can be folded (and therefore stowed) extremely efficiently. A deployable structure for space must be stowed on the launch vehicle and deployed on orbit so there is a crucial requirement for deployment reliability. Deployment failure very often results in loss of the mission—an unacceptable option due to the enormous

cost and resources required for each launch into space. The typical space structure to be deployed has historically consisted of a large number of interconnected rigid elements and consequently a large number of mechanical joints necessary to fold and twist the structure for launch configuration and to subsequently deploy it on orbit. Mechanical joints, hinges and mechanisms, in general, are typically sources of reliability risk due to the vast number of pieces and parts potentially failing. Spacecraft structures need a slow, smooth, reliable and controllable deployment process. (Zolesi et al., 2012) However, long term stowage of the structure can have the effect of slowing down the predicted deployment time and shape recovery in viscoelastic composite structures. (Kwok and Pellegrino, 2012) Nevertheless, by utilizing the inherent elastic and viscoelastic properties of CFRP composites, a controlled, predictable and passive deployment process may possibly be achieved with the addition of nanoparticles to the composite. (Peterson and Murphey, 2013) The nanoparticles may be able to hinder the creep and stress relaxation effects in the structure to ensure sufficient deployment force even after long stowage periods.

Mechanical properties of materials are often dictated by phenomena which take place at the micron or nanoscale. The number, size and spatial arrangement of particles has a strong effect on the mechanical response of the composite, but molecular level phenomena are far from sufficiently well understood. (Simoes, 2006) Adding to this complexity and uncertainty, all materials contain imperfections either by design or usually inadvertently produced during processing and they have a very strong role in determining the mechanical response of the material. (Meyers and Chawla, 2010) For example, metals have complex behavior with point, line and volumetric defects. With

epoxy matrix, translational movements of the molecular chain segments are highly constrained by the chemical cross-linked three dimensional networks and the ductility is impaired. (Ma et al., 2009) Researchers have shown remarkable material property enhancements can be achieved by controlling and re-arranging the atomic architectures, using ultra-pure materials and integrating nanoparticles into composites. (Lau et al., 2005)

It is well known creep is a time, temperature and stress-dependent deformation phenomenon of a metal or polymer under constant load. Creep can occur readily at ambient or moderate temperatures and cause permanent failure of a part—even at stress levels well below the material’s strength. However, creep may have some structural benefits if exploited wisely. The viscoelastic response of a composite is primarily dependent upon its polymer matrix properties. The fibers are typically an order of magnitude or more stiffer than the matrix. During a deployable composite structure’s stowage, the fibers generally stay fairly consistent but the polymer matrix creeps. Exploiting this inherent creep behavior in a nanoparticle composite may provide a well-engineered composite with the desired structural deployment behavior for space applications.

Engineers want to squeeze every bit of performance out of materials, particularly in the aerospace industry where small advantages in mass or performance yield tremendous performance benefits. Metals, which are generally well-known and characterized, pose intrinsic limitations due to their fixed density, strain capacity and CTE. With composites, the material’s design space offers many variables with the

opportunity to tailor or engineer materials for very specific properties for the desired structural application. At the microscopic scale, the engineer can tailor the local stiffness, strength, toughness and other properties by controlling the fiber type, loading fraction and fiber orientation, among other factors. (Thostenson and Chou, 2003) As noted previously, suitable materials for large strain composite deployable space structures must simultaneously satisfy two diverging requirements: 1. Large strain capacity for compact packaging and 2. Stiffness in the deployed configuration. The structure does not necessarily need to be stiff in the stowed configuration. Space structures typically employ slender elements and shell elements which can fail in buckling under compressive loads; the primary material property governing this loading-material behavior is Young's modulus for its stiffness. Similarly, when loaded in tension, the material property of interest is modulus as it determines deflections and structural modes of vibration. It is acceptable and desirable if the composite's modulus decreases during packaging so less strain energy is stored and it is easier to work with on the ground. In light of these challenging restrictions, there is renewed interest in passive large strain composites not requiring heating and cooling thermal restrictions for deployment (i.e., inflatable-rigidizable structures) or are not too complex with many mass-restrictive components. These large strain composites are often subject to prescribed loads or enforced displacements for long periods of time for space deployable structures' applications. Thus, the prediction and understanding of time-dependent properties of these composites is critical for confidence in their usage. One of the challenges in developing nanocomposites is the limited ability to predict the properties and failure mechanisms. The understanding of viscoelastic properties in large strain deployed

composite structures is not well understood. (Murphey et al., 2015) For example, in 2013 Brinkmeyer et al. researched deployment of stowed viscoelastic composite tape springs and concluded their analytical models were insufficient to provide deployment confidence and an actuator would be needed to ensure successful deployment.

### **1.3 Contribution and New Understanding**

A high degree of autonomy is emerging as a technological area of strategic importance for the aerospace industry. For this research area, one point of focus could be manifested as passive deployable structures. However, the passive/autonomous deployment of a structure in space is not trivial. Self-deployable structures are designed to exploit minimization of the mass, volume and power otherwise allocated to the attendant spacecraft deployment mechanisms. Shedding mass and reducing volume is an Air Force objective for future spacecraft. Structural architectures with the capacity to store strain energy to motivate structural reconfiguration between stowed and deployed operational states customarily exhibit deployment force profiles with lower minimums than active alternatives. However, stored strain energy could completely replace deployment motors and related hardware, greatly reducing mass and cost—two very important considerations for aerospace systems. Though calculating strain energy of composites and using it to deploy structures has been done since the mid-1960's, it is even more difficult today with increasingly complex composites and the criticality of

these missions. (Hashin, 1965, Rimrott, 1965, Rimrott, 1966) Thus, deployable space structures typically require an attendant system with authority over sequence and rate to reconfigure between stowed and operational deployed states. For space applications, active mechanisms expend significant mass and volume budgets relative to the packaged structure and an active deployment system consumes considerable power resources relative to the other spacecraft demands. Although passive deployment schemes are more desirable as they are more efficient, they are higher risk and limited concepts have demonstrated feasibility to exploit the stored strain energy to deploy the structure. (Pollard et al., 2007) Space structures need to achieve high functionality under severe environmental conditions. They need to be dimensionally very stable under drastic temperature gradients and dynamic micro-excitations; they need to be able to drastically change their shape. Structural enrichment with nanoparticles can be done to potentially improve their performance under those conditions. The modulus, CTE, and thermal conductivity can typically be improved by a factor of 2 - 4 by adding nanoparticles as compared to a neat polymer. (Baier et al., 2012) However, polymeric-based composites are still subject to viscoelastic effects, namely, creep and stress relaxation, due to the inherent properties of the matrix, even with a nanofiller added.

The goal of this research is to control and exploit the creep and stress relaxation behavior in a composite tape spring structure using nanoparticles to alter the viscoelastic behavior of the structure. As the size of a filler particle decreases to the nanoscale, the massive surface to-volume ratio of the nanoparticles results in an enormous interfacial area and a high surface energy of the nanoparticle fillers. This circumstance leads to a strong interfacial adhesion between the polymeric matrix and the fillers and hence affects

the properties of the overall composites. (Zhao et al., 2016) The objective is not necessarily to minimize creep, but to engineer/tailor it in CFRP composites to produce the desired structural behavior. However, first there is a need to understand the significance of nanoparticles on creep compliance and stress relaxation and then subsequently tailor the matrix-dominated properties which are responsible for it.

The engineer must simultaneously consider both strength and stiffness requirements in designing spacecraft deployable structures. Deployment architectures can take the form of a distributed deformation, flexible material, or articulated with hinges and joints. (Jenkins, 2006) The flexible material approach with embedded nanoparticles may provide a significant performance increase that is predictable, controllable and reliable. A thorough understanding of the relationships between microstructure and overall bulk properties of polymer nanocomposites is of great importance. Stress relaxation and creep of thin CFRP composite structures under large strain have little research history in the literature. Hence, there is a need to characterize state of the art CFRP nanocomposites and model and engineer their behavior. However, on-orbit deployment behavior is not well developed due to difficulties analyzing the complex and highly nonlinear structures in space. This is important because analysis is playing a larger role in pre-flight verification and to help anticipate potential anomalies. High fidelity deployment and structural modeling is essential to have confidence to use these structures in more than a research application as these structures are notoriously difficult to test on the ground due to their sheer size and the gravity effects experienced on earth but not in service on-orbit.

To reiterate, the goal of this research is to exploit the stored strain energy and elastic-viscoelastic properties of an engineered nanocomposite to stimulate self-deployment of a tape spring space deployable structure. The motivation is to eliminate the mechanisms controlling damping, deployment path and rate which are often numerous, complex and relatively heavy. The vision is modeling tools can then be developed enabling strain energy deployed CFRP structures with passive rate-controlled deployments that have the necessary robustness, predictability and reliability for space applications. Structural characterization tests need to be developed to characterize the viscoelastic effects in high strain nanocomposites so viscoelastic tailoring can be used for controlling strain energy release rates for reliable and predictable deployable space structures. To this end, a tape spring of a flexible thin composite laminate for deployable space structures was developed with high stiffness, dimensional stability and could be folded, bent or rolled to very small diameters. The experimental testing and modeling tools necessary to evaluate the structural response of these types of structures is also required. This work was experimentally-focused at the structural level as prior research at the material and coupon level set the stage for this area of research. The goal was to tailor and engineer passive strain energy actuated deployments for space structures. To do this, energy dissipation during storage and release of the structure needs to be controlled to ensure sufficient deployment force and prevent shock loading. The viscoelastic composite matrix needs to be tailored to exploit the viscoelastic matrix properties, which determine the stress-strain behavior during the laminate's folding deformation. The structural deployment process was tailored by controlling the rates and magnitudes of stress relaxation and creep recovery in thin CFRP laminate composite tape

spring structures. ANPs were used to achieve a desired deployment profile (i.e., time and force). ANPs have shown promise for this work through previous research. (Tavakoli et al., 2013, Dudkin et al., 2007, Ash et al., 2001, 2002, Moreira et al., 2012, Yu et al., 2012, Schadler et al., 2007, Kuo et al., 2004, Zhang and Singh, 2004, Akinyede et al., 2009, West and Malhotra, 2006, Naous et al., 2006, Davis and Gutierrez, 2011, Borowski et al., 2017 Garner et al., 2017).

There is a need to understand what the role of ANPs play as reinforcements to the matrix material in tailoring the viscoelastic response in structural-level composites. What is the significance of nanoscale particles on controlling viscoelastic behavior of deployable aerospace structures? The research plan of work was to develop a new composite material structure with unique properties to provide synergistic and tailorable performance to achieve desired viscoelastic properties for efficient deployable space structures. Structural level experimental testing and modeling methods were used to predict the structure's response. The objective was to create a large strain capable material-based solution for structural deployment and control and eliminate the deployment mechanisms for their excessive mass and contribution to reliability concerns. CFRP composites with elastic and viscoelastic laminae were used to provide deployment force and passive deployment rate control, respectively.

The challenge was to control/tailor the stress relaxation and creep phenomena during a space deployable structure's stowage. This control is necessary for sufficient deployment force within the structure for it to deploy and to maximize the energy viscously dissipated to slow deployment sufficiently hence, kinetic energy (i.e.,

deployment shock) is minimized. Incorporation of ANPs into CFRP composites was hypothesized as a way to achieve the goals of this research. The hypothesis was ANPs will hinder creep and stress relaxation of the tape spring deployable structures by altering the polymer crosslinks, inhibiting the full resin curing/reaction with the hardner and reducing the material's glass transition temperature,  $T_g$ . The embedded nanoparticles in a nanocomposite laminate can exploit the creep and stress relaxation phenomena to provide the desired deployment profile autonomously within the space environment and launch vehicle constraints.

**Chapter 2** provides a comprehensive review of relevant research work with respect to viscoelasticity, nanocomposites, composite laminate mechanics, space structures, the Prony series and the Time-Temperature-Superposition Principle (TTSP). **Chapter 3** covers all the experimental testing conducted during the course of this research. **Chapter 4** addresses numerical modeling, the finite element model (FEM) and simulation. **Chapter 5** provides all the experimental and finite element results and discussion regarding implications and significance and correlation between the experimental testing and FEM results. **Chapter 6** provides the conclusion to this work, the limitations and constraints encountered and recommendations for future work.

## CHAPTER 2 LITERATURE REVIEW

### 2.1 Relevant Prior Research

A systematic observation of the creep phenomenon was first reported and experiments conducted in 1834 by Vicat. (Meyers and Chawla, 2010, Findley et al., 1976) Forty years later, Boltzmann formulated the classical theory of viscoelasticity in 1874. (Coleman and Noll, 1961) Twelve years after, U.S. patent 405,480, “Manufacture of Carbon Filaments” was submitted on 30 July 1886 and approved 18 June 1889. It addressed new improvements for the manufacture of carbon filaments for electric lighting as manufactured by the destructive distillation of a gaseous carbon compound (40 - 45% H) yielding carbon strands when decomposed by heat. Hair-like carbon filaments with great strength and flexibility were manufactured; some researchers consider these elements the grandfather of CNTs. (Hughes and Chambers, 1886) These early investigations were the basis for the key principles at play in this research, namely, creep, stress relaxation, viscoelasticity and nanofiller elements.

A material’s modulus plays a critical role for aerospace structures. The problem of determining the effective elastic modulus of a polycrystalline aggregate in terms of the constituent crystals’ moduli was first studied by Voigt in 1910, using the assumption of a uniform strain state for all the crystals. A similar approach was used by Reuss in 1929, except he assumed a uniform stress state for all the crystals. Later in 1951, Hill showed the Voigt and Reuss modulus values were purportedly upper and lower bounds, respectively, for the elastic moduli of a polycrystalline material. Hashin and Shtrikman

furthered this work in 1962 as well. These are the earliest known research efforts on determining the elastic limits of multi-constituent (i.e., composite-like) materials. (Jia et al. 2011, Spanos et al., 2015, Lionetto et al., 2014)

The Time-Temperature Superposition Principle (TTSP) was first noticed experimentally in the late 1930's and Thurston seems to be the first researcher to propose three stages of creep and to study stress relaxation. (Findley et al., 1976, Li, 2000) His study of creep and stress relaxation was focused on metals as the first publication mentioning "shape-memory" effects in polymers wasn't until Vernon in a 1941 U.S. patent. (Liu et al., 2007) However, while TTSP was first noticed in the late 1930's, it wasn't proposed as a principle of polymer physics until 1943 by Lenderman, stating time is equivalent to temperature for thermorheologically simple viscoelastic materials. (Cheng and Yang 2005) In other words, creep and stress relaxation testing can be accelerated by testing at elevated temperatures per the TTSP. This is an important principle of polymer physics very useful for experimental testing and was used for this research work.

The scientific and engineering fields were jumpstarted in the mid-1940's as countries engaged in war and researched technologies to gain a military advantage. The first engineering of polymer matrix composites was invented for aerial fairing during WWII as glass-fiber composites, or, "fiberglass". (Aniskevish et al., 2012) The TTSP also started to gain recognition and acceptance during the 1940's and 1950's, albeit, for a less critical objective than supporting a war effort. (Seitz and Balazs, 1968) Understanding and modeling polymer behavior started to gain traction since at least the

1950's. For example, many formulas have been proposed to link the shift factors of a polymer's master creep curve to its reference temperature,  $T_0$ . One of the most recognized formulas today was established by the collaboration of Williams, Landel and Ferry in 1955, better known as the WLF equation:

$$\log a_T(T) = \frac{C_1(T - T_0)}{C_2 + T - T_0} \quad (2.1)$$

where  $a_T(T)$  is the temperature shift factor,  $T$  is the temperature of interest and  $C_1$  and  $C_2$  are material constants depending on the particular polymer. For a temperature range above a material's  $T_g$  (i.e., glass transition temperature), it is generally accepted the shift factor-temperature relationship is best described by the WLF equation. For a temperature range below the  $T_g$ , the Arrhenius equation is generally acknowledged as appropriate to describe the relationship between the shift factors of the master creep curve and a reference temperature:

$$\ln a_T(T) = \frac{E_a}{R} \left( \frac{1}{T} - \frac{1}{T_0} \right) \quad (2.2)$$

where  $E_a$  is the viscoelastic activation energy of the polymer. (Li, 2000) Williams, Landel and Ferry demonstrated the viscoelastic phenomenon is limited to non-crystalline materials above their  $T_g$ . (41) Temperatures above  $T_g$  increase the free volume in polymers, thereby allowing robust motion of the atoms which facilitates creep and stress relaxation in these amorphous materials.

Many researchers have studied composites and their mechanical properties since at least the 1940's and 1950's. For instance, the Findley equation has been used since the

1950's as one of the primary mathematical models for the time-dependent mechanical behavior of solid polymeric materials as well as non-polymeric composite materials, especially under tensile creep. Findley's power law has been used extensively to model creep behavior of fiber reinforced polymer (FRP) composite systems with good agreement. The general form of Findley's power law can be represented as:

$$\varepsilon(t) = \varepsilon'_0 + \varepsilon'_t t^n \quad (2.3)$$

where  $\varepsilon(t)$  is the total time-dependent creep strain,  $\varepsilon'_0$  is the stress-dependent and temperature-dependent initial elastic strain,  $\varepsilon'_t$  is the stress-dependent and temperature-dependent coefficient,  $n$  is the stress-independent material constant and  $t$  is the time after loading. (Scott et al., 1995)

In 1951, Bishop and Hill researched the plastic distortion and properties of a polycrystalline aggregate in a metal in a series of two papers. Their first paper focused on predicting the macroscopic modes of crystal distortion based on the microscopic mechanisms of distortion. While slip along microscopic planes and directions was already established, this work was one of the first to attempt to predict macroscopic properties from microscopic behavior of “constituents”. The principles of work and energy were used for the analysis along with a unit cube—one of the first uses of a representative volume element (RVE) to correlate microscopic properties to macroscopic properties. Their second paper in 1951 focused on a face-centered cubic (i.e., FCC) metal, but they incorporated two functions, “ $f$ ” and “ $h$ ”, into a relation between the ratios of stress and strain tensors for the aggregate crystal. The  $f$  function was a surface and the  $h$  function was a relation of the stress and strain history, much like the Hereditary integral

in accounting for the stress or strain history of a material in analyzing viscoelastic materials. (Bishop and Hill, 1951a, 1951b)

In 1957, Eshelby investigated the elastic field surrounding an ellipsoidal inclusion in a composite material. He stated the strain field was homogeneous within an ellipsoidal inclusion embedded in an infinite medium and sought to describe the state around a particle in the composite. (Eshelby, 1957, Benveniste, 1987) His work is often cited as the basis for composites' research, i.e., what is the elastic state of stress in the matrix material? He used thermodynamics to justify the analog representation of isothermal and non-isothermal linear viscoelastic constitutive equations by spring and dashpot models. (Schapery, 1966) Also, in 1957, Radok studied viscoelastic stress analysis with quasi-static equations governing linear viscoelasticity and put forward a method of functional equations for solving viscoelastic problems. This method applied to a broader range of problems than just Laplace transforms. (Cheng et al., 2005)

Bueche's paper in 1957 may have been the first to research aluminum oxide ( $\text{Al}_2\text{O}_3$ ) filler particles in a polymer (i.e., silicone rubber) for size, shape, orientation and polymer-filler attachments. The size of the alumina particles was not reported, but ostensibly they were microparticle-sized. He found a decrease in modulus as concentration of alumina particles increased and ascertained it was due to the addition of benzoyl peroxide during the composite processing which interfered with the critical bonding between the alumina particles and the polymer chain. (Bueche, 1957)

Just a couple of years later in 1959, physicist Richard Feynman delivered his famous lecture "There's plenty of room at the bottom". This lecture is often cited as

visionary in the field of nanotechnology as most nanomaterials were not discovered and researched for another three to four decades later. (Feynman, 1959)

In 1960 Lee proposed an approach for solving viscoelastic problems; the stress-strain relation could be expressed in the form of an integral, called the Hereditary integral. (Findley, 1976, Chen, 2000) Later in 1961 at NASA, Hedgepeth researched stress concentrations in filamentary structures; his analysis was based on elastic, small deflection theory of a two-dimensional medium. He was the first to develop a shear-lag model for non-hybrid fiber-reinforced composites by assuming the fibers carry all axial load and the matrix carries only shear load. (Hedgepeth, 1961)

Between 1951 and 1963 Hill researched the moduli of crystal aggregates, elastic composites and developed the self-consistent method (SCM) to study the overall linear viscoelastic behavior of composites. (Laws and McLaughlin, 1978, Hill, 1952) His research on the SCM for mechanics of composite materials centered on the prediction of macroscopic properties of two-phase solid composites (in particular, when one phase is a dispersion of ellipsoidal inclusions). However, the theory is unreliable under high volume content of filler except when the dispersed phase is sufficiently dilute. (Hill, 1965) He cited Eshelby's work in the late 1950's and researched the behavior of two solid phases firmly bonded together with one phase as the 'inclusions' and the other phase as the 'matrix'. He placed no restrictions on the shape of the inclusions and assumed the mixture was homogeneous on the macroscopic scale, but not necessarily isotropic. He pondered for arbitrary geometry and concentrations, the task of determining internal field of stress was "hopelessly complex". Thus, he considered a

more tractable problem by imposing limitations on the problem. (Hill, 1963) Simplifying a real-world problem and making assumptions is often a viable approach for solving it.

Hashin conducted research at the University of Pennsylvania since at least the late 1950's until the mid-1960's on composites' viscoelasticity, variational principles in the theory of elasticity for isotropic and anisotropic nonhomogeneous bodies and prediction of the effective elastic properties of polycrystalline and fiber and particulate composites. (Hashin, 1962, Hashin and Shtrikman, 1962, Hashin and Shtrikman, 1962a, Hashin and Shtrikman, 1962b, Hashin and Rosen, 1964, Hashin, 1965, Hashin, 1966, Hashin, 1970) Hashin and Hill wrote several dueling papers in the 1960's on composite properties. Hashin's 1972 results indicated the viscoelastic problem could be solved by simply considering the associated elastic problem, i.e., he developed a correspondence principle relating effective elastic moduli of composites to effective relaxation moduli and creep compliances of viscoelastic composites. However, he and other researchers found difficulties often occurred when inverting Carson or Laplace Transforms, so it should be used with caution. (Laws and McLaughlin, 1978)

In the early 1960's composite materials began emerging as promising materials of the future. In the decades following, great success was achieved in micromechanics' estimates of effective elastic properties, homogenization and laminate plate theory. (Talreja, 2014) FRP composites were first introduced to the military and aerospace community in the mid-1960s. The Department of Defense drove much of the early composites research at the Air Force research laboratory at Wright-Patterson Air Force Base, Ohio. Various deployable space structures' concepts were also developed during

the 1960's. These included coilable slit tubes, STEMs, self-locking hinges and wrap rib antennas. Early examples include an 18-meter gravity gradient boom on the 1961 TRAAC (Transit Research Attitude and Control) mission and the 1962 Alouette I mission (Canada's first spacecraft, the Topside Sounder Satellite S27) using slit tube booms 38 meters tip to tip. (MacNaughton, 1963, Murphey et al., 2015)

STEM booms have long been a workhorse of the deployable structures community and have flown in space since the early 1960's. They were invented and developed by the Mechanical Division of Canada's National Research Council and then further developed by the Canadian Army Development Establishment and then developed even more yet by engineers at De Havilland Aircraft of Canada Ltd., the Special Products and Applied Research Division. By 1963, De Havilland had conceived of over 50 different models and deployed a 1,000-foot STEM. (MacNaughton, 1963) The stated principles behind the STEM design, compactness, simplicity and reliability, are just as important today as they were in 1965! (Rimrott, 1965) STEMs have a very high compaction ratio but due to their metallic (Beryllium Copper, BeCu, or Stainless Steel, SS) make-up they also have a high CTE. STEMs are a flat strip of thin material assuming a tubular shape when extended in their natural, stress-free state. They are convenient because they can be flattened and rolled for compact packaging and thereby inherently store strain energy to be used to entirely supply the STEM's subsequent necessary deployment force (without any additional power sources) as the strain energy is released. Thus, the element, when retracted, is stored in a strained, flattened state by winding it onto a hub. However, one key drawback to a typical STEM structure is the member will typically deploy very rapidly as the strain energy is released and the end or

tip, which often carries a sensitive payload, will experience a substantial amount of shock. For this reason, brakes, lanyards, motors and other types of attendant systems have been added to control deployment. But all these additional attendant systems add mass, power, complexity and cost which are all things to be avoided for an efficient aerospace system.

When an overlap in the tube cross section is avoided and a more open section is used the resulting structure is known as a tape spring. Tape springs are thin shells with a curved cross section, typically of symmetric and uniform cross section with a subtending angle less than  $180^\circ$ . The STEM boom is essentially a specialized application of the tape spring. A basic STEM deployable structure consists of a single tape spring with the material forming a slit tube of circular cross-section. It is folded by opening out its cross section until it becomes flat and then unwinding it from being coiled on a hub or having been placed in a cassette. These structures are particularly suitable for deployable structures because their curved cross section, whether tape spring or slit tube STEM, can be flattened and then longitudinally rolled onto a hub or into a cassette.

Both the tape spring and STEM store elastic strain energy during folding, and in principle, would both freely deploy into the straight, unstrained configuration when all constraints are released. STEM booms typically have high strain energy and large relaxation phenomena existing in the stowed state. Normally a structure folded in this way has to be stowed with a deployment mechanism preventing it from releasing its stored energy in an uncontrolled way. (Liu et al., 2014) Thus, the boom's deployment requires a complex set of mechanisms (with associated mass) to control the deployment

rate and path. In many applications the size, mass and complexity of the deployment mechanism are much greater than those of the deployable structure itself. (Iqbal et al., 1998) Similarly, once a tape spring is in a constrained, high energy stowed (i.e., rolled up) configuration, the constraint mechanism can be released to initiate it toward the stable, lower energy configuration powered by the release of its strain energy. In a neutrally stable tape spring the two configurations (rolled and unrolled) have the same strain energy density and the tape spring is at equilibrium at every position in the transition. Rolling up STEMs and tape springs stores strain energy later used to power their deployment. STEM booms are typically fabricated with resilient isotropic metals and strains are minimized so all deformations are elastic. In composite tape springs, due to the symmetry of the laminate, thermal stresses can be neglected. This result can be seen by performing a strain energy density analysis based on classical lamination theory (CLT).

Between 1965 - 1980 Rimrott investigated the elastodynamic process of flattening and rolling a tape spring and the deployment velocities of STEM booms in four different configurations: a. Rotating drum with root-based deployment, b. Rotating drum with tip-based deployment, c. Helical (drum stays at root while tip deploys) and d. reverse helical (drum travels up with tip during deployment). He derived the STEM deployment velocities starting with a strain energy analysis of a thin shell in bending. Admittedly absent are experimental results correlating the analytical equations, yet, even today this early work is often cited in deployable structures' analysis due to its scholarly significance. (Rimrott, 1965, 1966a, 1966b, 1967, 1980, Walpole, 1966)

Finite element method (FEM) research with regard to element locking was studied as far back as the 1960's. At that time the problems arising with locking of four node quadrilaterals and other lower order elements were combated with the development of higher order elements such as eight node quadrilaterals. Techniques to prevent locking for lower order elements were developed from the 1970's onwards. (Van den Oord, 2005)

In 1966 Walpole investigated the elastic behavior of an inhomogeneous composite composed of various phases at arbitrary loadings. His goal was to determine to what extent the constituents' properties determined the overall elastic moduli of the composite, relative to the phase volumes. Building on earlier work from Eshelby, Hashin and Hill (Eshelby, 1957, Hill, 1965, Hashin and Shtrikman, 1962a, 1962b, Hashin and Rosen, 1964), he used the principles of minimum potential energy and complementary energy of an RVE to calculate Young's modulus, bulk and shear moduli and Poisson's ratio for multi-phase materials, proving conjectures from Hashin. He also developed upper and lower bounds for bulk modulus, improving on the Reuss and Voigt estimates. (Walpole, 1966) Also, in the mid-1960's, Halpin researched composite material factors affecting stiffness and strength, including viscoelasticity, at the Air Force Materials Laboratory in Dayton, Ohio. (Halpin, 1969)

In 1969, Roscoe expanded upon the work of Voigt, Reuss, Hill, Hashin and Walpole to improve the general bounds for overall effective moduli of a composite by

incorporating linearly viscoelastic phases that were isotropic and utilizing an RVE to analyze the macroscopic behavior. (Roscoe, 1969, Hill, 1964)

Between 1966 and 1969 at Purdue University, Schapery researched the extension of linear constitutive equations to nonlinear thermoviscoelastic materials based on irreversible thermodynamics where the transient material behavior is defined by a master creep function. Nonlinearities can be considered by including factors that are functions of stress and temperature. (Schapery, 1966, Gerngross et al., 2008) As with Eshelby, his work is often cited as the basis for composite materials' research. Eshelby considered a viscoelastic material to be a closed thermodynamic system defined by  $n$  state variables. (Schapery, 1966) Schapery's single integral method, which consists of four nonlinear parameters determined from constant stress creep, is used to describe creep behavior of FRP composites under time dependent loading. (Scott et al., 1995) Schapery proposed a nonlinear viscoelastic constitutive model where the transient material behavior was defined by a function known as the master curve. Also, the creep compliance,  $D$ , and the instantaneous compliance,  $D_0$ , were provided in terms of a time variable  $\psi$ , known as the reduced time. Nonlinearities were captured by including four functions of stress and temperature. The total uniaxial strain was obtained from:

$$\varepsilon(t) = g_0 D_0 \sigma(t) + g_1 \int_0^t \left( D(\psi(t) - \psi(\tau)) \right) \frac{d(g_2 \sigma(\tau))}{d\tau} \quad (2.4)$$

Note the nonlinearity factors:  $g_0$  is the change of instantaneous elastic compliance,  $g_1$  is the change of transient compliance, and  $g_2$  is the sensitivity to transient stress. They are all functions of stress and temperature. (Gerngross and Pellegrino, 2007)

In 1968 Tsai and Melo researched an invariant theory for composites agnostic to laminate ply orientation to aid in the design and understanding of composite laminate structures. Tsai updated his theory over 40 years later (2014) by proposing an “omni strain” failure envelope and the stiffness matrix trace as the most significant properties to testing, designing and understanding composites. (Tsai and Melo, 2014)

In 1983, Zhang and Matthews investigated the influence of curvature, fiber angles, stacking sequence and panel aspect ratio on the buckling capability of curved laminates. They drew the conclusion curving the panel is always of benefit to its stability no matter what kind of load it is subjected to: axial, compression, shear forces or combination thereof. The critical load increased as curvature decreased. (Zhang and Matthews, 1983)

In 1985 Smalley et al. at Rice University performed experiments aimed at understanding the mechanisms by which long-chain carbon molecules formed in interstellar space. They vaporized graphite by laser irradiation producing a remarkably stable cluster of 60 carbon atoms which they called Buckminsterfullerene, or “bucky balls”. (Kroto et al., 1985) Iijima discovered CNTs in 1991 fabricated from an arc discharge evaporation method and examined them via transmission electron microscope (TEM). The synthesis of C<sub>60</sub> and other fullerenes had stimulated interest in further carbon structures research. (Iijima, 1991) Ajayan et al. researched how to organize CNTs into well aligned arrays and were the first to incorporate CNTs into polymer composite materials for aligned phases. They discovered as the size of the phases shrunk to molecular level dimensions, new properties became apparent. (Ajayan et al., 1994)

Later in the mid-1980's, Smalley et al. at Rice University developed the chemistry of fullerenes which are geometric cage-like structures of carbon atoms composed of hexagonal and pentagonal faces. The first closed, convex structure formed was the C<sub>60</sub> molecule, the “bucky ball”. A few years later their discovery led to the synthesis of CNTs. (Thostenson et al., 2001) The discovery of CNTs by Iijima opened the door to enhance the mechanical properties of polymer composites as the first polymer nanocomposites using CNTs as filler were reported in 1994 by Ajayan et al. (Moniruzzaman and Winey, 2006) Thus, the last three important forms of carbon discovered were fullerenes (1985), CNTs (1991) and graphene (2004). (Monthieux and Kuznetsov, 2006, McNeil, 2015)

Pellegrino et al. has researched various aspects of composite tape springs and deployable structures from the mid-1980's to the present day. He collaborated with You and Guest between 1992 -1994 researching structural computations, inextensional wrapping of flat membranes, the folding of triangulated cylinders, membrane wrapping and folding schemes for a membrane antenna reflector with CuBe ribs. (Guest and Pellegrino, 1992, Pellegrino, 1993, You and Pellegrino, 1994, Guest and Pellegrino, 1994a, 1994b) This research work, along with his comprehensive study of large retractable spacecraft appendages in 1995 (Pellegrino, 1995), was key for understanding how to compactly package deployable structures.

In 1994 Cousin and Smith investigated modifying the mechanical properties of a polystyrene (PS) composite filled with micro-sized alumina particles through the incorporation of sulfonic acid groups, i.e., toluene and silane. They concluded there was

significant bonding between the surface of the alumina particles and the sulfonic acid groups on the PS, resulting in a decrease in chain mobility and free volume and a corresponding increase in  $T_g$ . The modification of the alumina rendered it more successful at restricting free volume and yielded a significant increase in composite storage modulus. (Cousin and Smith, 1994)

Pellegrino teamed with Seffen in 1997 while at the University of Cambridge to study the deployment dynamics of tape springs. They tested 0.50 – 0.54 meter-long annealed BeCu tape springs by folding them at a  $90^\circ$  angle and analyzing the upward or downward deployment sequence as the tape springs deployed via strain energy and using Lagrange's equations. They hypothesized it was possible to estimate the total energy in the tape spring system by considering the strain energy in the elastic fold, the kinetic energy of the moving part and the potential energy. They modeled the tape springs in Abaqus with a mesh of S4R5 (i.e., conventional shell element, quadrilateral, 4 nodes, reduced integration, 5 degrees of freedom per node) elements with five elements forming half of the tape spring cross section and 48 elements along the length (only half was modeled due to symmetry). They considered the tape spring deployment dynamics to belong to the class of propagating instability problems. They found their analytical predictions were not accurate but the numerical predictions did agree very well with their experiments showing the inclusion of air drag was essential (using  $C_D = 1.24$ ) but including gravitational effects was only important for tape springs with the local folds as opposed to the coiled tape springs. (Seffen and Pellegrino, 1997)

Pellegrino teamed with Iqbal and Daton-Lovett in 1998 to research bi-stable composite slit tubes as a new deployable structure able to be rolled up similar to the familiar metallic carpenter tape measures well known since the 1920's. By design, their structure was stable in both the unstrained, extended configuration and in the strained, rolled up configuration, thus, no containment mechanism was needed for storage. The bi-stability was achieved through design and fabrication of the composite laminate, as discovered and exploited by Daton-Lovett. They used a thermoplastic material consisting of 0.213 mm thick UD plies of E-glass fibers in a polypropylene (PP) matrix. The strain energy analysis of the slit tubes was quantified via closed form solutions for the bending and stretching energies. Errors in their models were attributed to poor manufacturing techniques and neglecting coupling terms in the  $ABD$  matrix. (Iqbal et al., 1998)

Also, in 1998 Vermeulen and Heppler researched using B-splines to combat shear locking in FEM. The displacement and rotation of a general Timoshenko beam were discretized using independent B-spline based discretizations. Thus, it seems the earliest and most popular method for remedying shear lock was to use reduced integration in finite element modeling. (Vermeulen and Heppler, 1998)

In 2000, Iqbal and Pellegrino extended their work from 1998 on bi-stable composite slit tubes and focused on bi-stable composite shells for the application of tape spring deployable space structures. Bi-stable composite shells were discovered by Daton-Lovett in 1996 and he collaborated with Pellegrino for several years afterward. Daton-Lovett used an anti-symmetric composite lay-up of five plies almost eliminating coupling between bending and twisting. However, in this work Iqbal and Pellegrino used

Abaqus S8R5 elements (i.e., conventional thin shell element, quadrilateral, 8 nodes, reduced integration, 5 degrees of freedom per node) with the composite option to create five layers of thickness for the thin shell element (many other researchers have recommended using at least four elements in the thickness direction). They later found S4R5 elements had more robust convergence in the heavily nonlinear simulations normally experienced by tape springs. They correlated the FEM with tension testing and bending testing of a flat composite plate 535 mm x 102 mm and 252 mm x 40 mm, both with the antisymmetric lay-up of the bi-stable shell. Overall, they found they could only get their model to converge using S4 and S8R elements and it did not converge using thin shell elements S4R5 and S8R5 elements. The main source of discrepancies between the FEM and experimental results was thought to be due to material nonlinearities. (Iqbal and Pellegrino, 2000)

During 2001 - 2002 Ash et al. studied the *in-situ* polymerization of PMMA-ANP nanocomposites and their resulting mechanical and thermal composite properties. They used a silanol solution to tailor the alumina nanoparticles' surface properties to reduce agglomeration tendencies and to enhance the affinity for bonding between the ANP and the PMMA thermoplastic epoxy. Their composites with 5 % weight ANPs resulted in an increase in strain-to-failure of over 800% compared to neat PMMA from uniaxial tension testing. However, they also found the composite's  $T_g$  dropped substantially, 20° C - 26° C, and the moduli also decreased. They theorized the decreases in moduli were entirely due to the decrease in  $T_g$ . (Ash et al., 2001, 2002)

In 2002 Zhang et al. examined the performance of polymer composites with polyacrylamide (PAAM) grafted SiO<sub>2</sub> nanoparticles incorporated into a typical epoxy. The average size of the SiO<sub>2</sub> nanoparticles was 9 nm. After conducting TGA, FTIR, SEM, DSC, and DMA, they concluded the PAAM chains grafted on the SiO<sub>2</sub> nanoparticles enhanced the critical filler-matrix adhesion, the  $T_g$  and stiffness increased and the tribological performance of the composite increased all due to the increase in chemical bonding between particles and matrix. (Zhang et al., 2002)

Pellegrino teamed up with Yee in 2003 and researched the folding of a deployable structure tube hinge constructed of CFRP tape spring elements. Their main contribution in this research was advancing the understanding of the mechanics of tightly folded tape springs (i.e., large strain). The tape springs were of two variations, one and two-ply PW T300/913 prepregs (913C-814-40%, Hexcel, with 60% fiber volume fraction). They constructed an Abaqus FEM to predict the peak strains induced by the folding process and compared it to experimental testing of the tube hinges (i.e., tape spring elements). The S4R5 elements were adopted in their finite element model because they performed well for large rotations with only small strains and used reduced integration with hourglass control to prevent shear locking. The S4R5 elements also possess high accuracy in modeling shell structures. Their study focused on tape springs under opposite sense bending, but they found satisfactory behavior also for equal-sense tape spring bending. The one ply survived bending strains up to 2.5% and the two-ply survived bending strains up to 2.0%. It is logical a thinner laminate would be able to take more strain and bend to a smaller radius than a thicker one. (Yee and Pellegrino, 2003)

Also, in 2003 Wetzel et al. studied the performance optimization of composites with ANPs and calcium silicate microparticles to understand what role the particles had on the mechanical and tribological performance of the composites. They found the addition of alumina nanoparticles (1-2% volume) to an epoxy matrix improved stiffness, impact energy and failure strain. (Wetzel et al., 2003)

In 2004 Yee and Pellegrino (along with Soykasap) continued their work from a composite tube hinge made of tape springs to discrete CFRP tape springs. The tape springs were one, two or three plies PW style with four different epoxy systems: 913, 914, M36 and LTM45 and one thermoplastic matrix, PEI. The T300 carbon fiber contents varied between 48% – 60%, with tow size either 1K or 3K. They carried out detailed simulations of the tape spring folding in Abaqus with thin shell elements used to model the tape spring. Four node quadrilateral full integration general purpose elements (S4) and four node reduced integration shell elements (S4R5) were used. The S4R5 elements performed well for large rotations with only small strains. They used reduced integration with hourglass control to prevent shear locking. The tape spring behaved in an approximately linear elastic way for rotations  $< 20.5^\circ$ . It is important to note they found the maximum bending strain decreased as the number of plies in the laminate increased. Later in 2004, Yee and Pellegrino extended their research on folding and CFRP tape springs by studying folding of woven composite structures. They found self-deployable CFRP composite booms with integral self-locking hinges could be developed as an inspiration from tape spring hinges to provide a lightweight, reliable, low cost deployment mechanism for deployable booms. Since elastic folding of isotropic

materials is well understood, they showed the radius of transverse curvature to the thickness ratio,  $R/t$ , of a tape spring has to be greater than:

$$\frac{E}{\sigma_y(1-\nu)} \quad (2.5)$$

to avoid yielding of the material (where  $E$  is Young's modulus,  $\sigma_y$  is the yield stress and  $\nu$  is Poisson's ratio).

Extending the results to anisotropic materials is straightforward, but it was found tape springs made from woven pre-pregs were able to survive larger surface bending strains than the ultimate failure strains measured from standard coupon tests in tension and compression. There is only limited published data on woven fabric laminates. Because of their thinness, one and two-ply laminates could be folded to very small radii, hence, three and four-point bending tests are unsuitable. An alternative test layout was devised which permitted very large displacements and applied a relatively uniform bending moment and hence curvature over the center region of the specimen. The max bending strain in the direction of the fibers was 2.7% for one ply and 2.1% for two plies. When the fibers are at  $45^\circ$  to directions of principal strain, the max average fiber strain was 2.5% for one ply and 1.8% for two plies. The dominant mechanism of compressive failure in polymer matrix composites is plastic micro-buckling (shear deformation of the matrix). Their work here applied to folding in only one direction whereas a tape spring undergoes biaxial changes of curvature so the interaction between strains on two sets of orthogonal fibers needs to be considered. (Yee et al., 2003, 2004)

Also, in 2004 Kuo et al. studied  $\text{Al}_2\text{O}_3$  nanoparticles (with average diameter 15 – 30 nm) incorporated into PEEK (poly(ether-ether-ketone)) polymer at 0 – 10% weight loading. The ANPs had no surface modification. Upon tensile, hardness, DSC, SEM and TEM testing, they found their ANP composites had increased moduli and strength for corresponding increases in nanoparticle content. Additionally, as might be expected, they showed the 30 nm sized particles provided slightly lower increases in modulus, strength and hardness than the 15 nm particles. (Kuo et al., 2004)

Moreover, Zhang and Singh researched the incorporation of ANPs into a thermosetting polymer, an unsaturated polyester resin (MR 17090), in 2004. Their ANP sizes ranged from 15 nm to 1  $\mu\text{m}$  to 35  $\mu\text{m}$  in average diameter. All the particles were added in 0.9 – 4.4 volume %. Their experiments compared virgin, untreated alumina nanoparticles and those treated with silane. They concluded the addition of silane led to significant enhancement of the composite's fracture toughness (nearly 100% over the uncoated particles) because the organofunctional acted as a chemical bridge, enhancing the particle-matrix bonding between the unsaturated polyester resin and the alumina nanoparticles. (Zhang and Singh, 2004)

In 2005, Kuo et al. studied incorporating nanosilica and ANPs into the common thermoplastic, PEEK. The  $\text{SiO}_2$  and  $\text{Al}_2\text{O}_3$  nanoparticles had average diameters of 30 nm and 15 nm for  $\text{SiO}_2$  and 30 nm for  $\text{Al}_2\text{O}_3$  and weight percentages for each in the PEEK ranged from 2.5% to 10%. After conducting room temperature tensile testing and hardness testing, SEM (with EDS), TEM, DSC were used to evaluate the composites. They found the modulus increased with the silica nanoparticles versus the ANPs but the

composite toughness was the opposite for the ANP composites versus the nanosilica composites. They hypothesized the differences between the nanocomposites was due to the spherical shape and more uniform distribution of the alumina nanoparticles. (Kuo et al., 2005)

Later in 2005, Yee and Pellegrino studied bending and folding of very thin woven composite laminates, as an extension of their work from 2003 and 2004. They used one and two-ply PW laminates made from T300 carbon fabric (3K fibers per tow) with 913 and 914 epoxy resins. The one-ply was 0.22 mm thick and the two-ply laminate was 0.43 mm thick. They performed tension testing, in-plane shear testing, compression testing and bending testing to characterize the composites. The maximum bending strain was found to be 2.5% for one ply and 1.8% for two plies. One notable conclusion was the bending behavior of the composites was most useful from the viewpoint of the application of thin composites to deployable structures. (Yee and Pellegrino, 2005)

In 2006, West and Malhotra fabricated polymer nanocomposites with Shell EPON 826 epoxy resin and 10% weight ANPs (untreated), averaging 27 – 56 nm diameter. Their results showed considerable improvement in modulus (+39%) and strength of the nanocomposites compared to the neat epoxy via three-point bending flexural measurements. The nanocomposites were also able to withstand 14% more stress at 5% strain than the neat epoxy. (West and Malhotra, 2006)

Also, in 2006 Naous et al. studied tensile properties and fracture toughness of nanocomposites made of DGEBA epoxy with 30 nm average size ANPs. The nanoparticle loading varied from 2.5 – 10 per hundred resin. SEM, TEM, DMA, tensile

and fracture toughness tests revealed significant improvement in storage modulus, an increase in  $T_g$ , an order of magnitude increase in fracture toughness and a near 9% increase in modulus with 2% volume ANPs over the neat epoxy. (Naous et al., 2006)

In 2007, Gerngross and Pellegrino studied anisotropic viscoelastic behavior by modeling super pressure balloons made of a low-density polyethylene (LLDPE) film. They used a UMAT (user-defined material) in Abaqus as an alternative approach to the creep and relaxation models available in Abaqus which can only model isotropic viscoelastic behavior, not orthotropic or anisotropic. They found the UMAT approach was much more accurate than the built-in Abaqus models. Comparison of their results between Abaqus and the analytical solution showed very good agreement and proved the implemented subroutine (i.e., UMAT) worked correctly. (Gerngross and Pellegrino, 2007)

Dudkin et al. investigated the characteristics of composites filled with alumina nanoparticles, prepared via the sol-gel method, and alumina nanofibers. The matrix was ED-20 epoxy oligomer and the weight fraction of the ANP fibers and particles was 1%. They found the composites reinforced with alumina nanoparticles had a 60% increase in Young's modulus. (Dudkin et al., 2007)

Zhu et al. studied in-plane shear deformations of woven fabric composites. Their experiments showed wrinkling of the woven fabric occurs when the critical shear angle, the "locking angle", between the warp and weft yarns is reached. This finding was important because it demonstrated wrinkles have the potential to induce numerous processing and strength problems detrimental to the composite. (Zhu et al., 2007)

There are numerous studies investigating the creep behavior of UD or multidirectional composites but few published studies have focused on off-axis creep of woven composites. Motivated by this knowledge gap, Gupta and Raghaven's study focused on the development of a creep model to predict the in-plane creep of PW composites under any load orientation using creep data for UD composites as input. They modeled experimental creep data using a modified Kohlraush-Williams-Watts (KWW) equation with parameters defined by Schapery's nonlinear viscoelastic model. (Gupta and Raghaven, 2010)

In 2008, Gerngross and Pellegrino used an Abaqus UMAT to study the time variation of the stress and strain distribution in a pumpkin balloon. They used a Schapery-Rand non-linear anisotropic viscoelastic model and found it to be much more accurate compared to experimental data than to the two viscoelastic (creep/relaxation models) options in Abaqus, the standard power-law creep (*\*creep*) and viscoelastic (*\*viscoelastic*) models. Both Abaqus options gave rather poor results; the power-law model based on the *\*creep* option predicted strains up to 10% lower. The *\*viscoelastic* option, which follows the linear Schapery viscoelastic constitutive equation but similarly neglects the stress dependent nonlinearities of the material, under predicted the creep strains by up to 40%. Thus, an iterative algorithm in the UMAT was implemented to model the viscoelastic behavior. Every time the UMAT was called it started with an estimation of a trial stress increment,  $\Delta\sigma^{trial}$ , based on the nonlinearity parameters at the end of the previous time increment. With this initial guess an iterative loop was entered to increment the strain. If required, the trial stresses and the nonlinearity parameters were corrected and the loop was repeated. The accuracy of the nonlinear viscoelastic model

implemented via the Abaqus UMAT was verified with experimental creep test data. Ultimately, they found the power-law creep and viscoelastic models built into Abaqus were less accurate than using the Rand-Schapery model implemented via a UMAT. (Gerngross et al., 2008)

In 2008, Putz et al. found as the cross-link density was increased, the  $T_g$  of nanocomposites was observed to remain constant or decrease. They surmised this  $T_g$  decrease was related to two mechanisms working in tandem: First, a reduction in the cooperativity of the system with increased cross-link density which translated into less communication of interfacial dynamics through the bulk of the polymer matrix. Second, CNTs may disrupt the cross-linking network of the system, reducing the effective cross-link density and leading to degradation in  $T_g$ . In highly cross-linked thermosets (e.g., epoxy and unsaturated polyesters), the ability of nanoparticles to significantly alter the physical and thermal properties of the polymer through creation of a percolated interphase of altered polymer matrix properties will be significantly decreased. (Putz et al., 2008)

Also, in 2008 ATK Space Systems designed and built a 40-meter deployable truss boom for the Air Force Research Laboratory's Demonstration and Science Experiment (DSX) satellite. The DSX boom is a deployable lattice truss of triangular cross section consisting of three continuous length longerons of pultruded graphite (carbon fiber) epoxy, graphite epoxy batten members and stainless-steel cable diagonal members. The truss structure is coiled in a helical fashion for stowage in a small canister with compaction ratio greater than 100:1. The structure deploys via stored strain energy and

deployment rate is controlled via a tensioned lanyard running through the center of the truss cross section. Launch and on-orbit deployment of this structure is planned for mid-2019.

In 2009, Akinyede et al. researched a nanocomposite comprised of woven S2 bi-directional fiberglass and epoxy matrix with ANPs. As Ash et al. and Zhang and Singh before them, they coated the ANPs with a silane functionalizing agent to enhance the coupling with the 9504 epoxy resin system. Their ANPs were 110 nm in average diameter and they used 2% weight in their nanocomposites. They performed tensile and fatigue tests on five different composites and their results showed no significant changes in ultimate tensile strength and modulus compared to the baseline (i.e., epoxy-fiberglass) system, but did see over 20% improvements in fracture toughness. (Akinyede et al., 2009)

In 2010, Kwok and Pellegrino researched the shape recovery of viscoelastic deployable space structures at the California Institute of Technology. They focused on the viscoelastic behavior and shape recovery of CFRP composite deployable structures (i.e., tape springs). The tape springs were made of a homogeneous low-density polyethylene (LDPE), an uncrosslinked polymer. The LDPE was characterized through a series of creep tests on an MTS Instron machine with an environmental chamber. The test coupons were 165 mm long, 40 mm wide and 1.56 mm in thickness. Longitudinal and transverse strains in the specimen were measured using two laser extensometers with a recording rate of 5 Hz. They fitted the experimental data with a three term Prony series using a nonlinear optimization algorithm. Using the Elastic-Viscoelastic Correspondence

Principle, they developed the viscoelastic equivalent to the deflection equation in the Laplace domain by replacing the appropriate variables by their Laplace Transform and then taking the inverse Laplace Transform. They compared their theoretical predictions with experiments carried out on a viscoelastic beam on a four-point bending fixture. These test coupons were 170 mm long and 13 mm wide. Their Abaqus FEM consisted of 688 S4 elements and they used the option *\*viscoelastic, time=prony* and a geometrically nonlinear quasi-static analysis (*\*visco* option). They found good agreement between the Abaqus/Standard FEM simulation, experimental results and analytical predictions. They also fabricated an LDPE tape spring 340 mm long by 75 mm wide and 0.7 mm thick and conducted both equal and opposite sense deployment tests and recorded them with a high-resolution camcorder. The tape spring was rolled onto a steel tube over the course of 60 seconds and held in place there for 1000 seconds. They found the viscoelastic model predicted the change in reaction force and shape over time with high accuracy. (Kwok and Pellegrino, 2010)

Kwok and Pellegrino continued their 2010 research in 2011 by studying viscoelastic effects in an LDPE tape spring to capture the entire folding (90°), stowage and deployment process as a continuous timed event. Their experiments were carried out on tape springs with an inner diameter of 38 mm, a nominal thickness of 0.73 mm and a subtended angle of 150°. The 272 mm long tape springs underwent quasi-static folding and stowage tests. They conducted their experiments on an MTS Instron machine inside an environmental chamber at 15° C and 22° C. The tape springs were deployed vertically downward (i.e., compressed) with a displacement of 80 mm and held in the folded configuration for 5,000 seconds. Displacement rates of 1 mm/s and 5 mm/s were used in

the testing and load profiles were obtained. They also performed additional dynamic deployment tests of a 398 mm long tape spring in a vertical configuration at ambient temperature, folded to 87° and held folded/stowed for 983 seconds. While stowed, the force on the end of the tape spring was measured using a string tied to a load cell and deployment was initiated by cutting the string. A laser displacement sensor was used to track the deformation of the tape spring by a dot on the end of the tape spring's free end. They modeled the tape spring structure in Abaqus with the option *\*viscoelastic, time=prony* and a user subroutine was written to define the temperature shift factor. Their numerical simulations were based on isotropic linear viscoelasticity. They conducted simulations of the quasi-static folding of the tape spring with a model consisting of 6,800 S4 elements. The accuracy of the integration during the quasi-static steps was controlled using the Abaqus command *\*cetol*, which put a maximum change in creep strain rate allowed over a time increment and used a value of  $1 \times 10^{-4}$ . Relaxation tests were also carried out to determine LDPE's material constants, i.e.,  $C_1$  and  $C_2$ , which were -8.74 and -40.41, respectively. Overall, they found the Abaqus/Standard simulations showed good agreement with their test results and the folding and stowage process was characterized by significant load relaxation. (Kwok and Pellegrino, 2011)

In 2012, Kwok and Pellegrino studied the micromechanical modeling of deployment and shape recovery of CFRP tape spring deployable structures for space. Here they focused on bridging the gap between existing micromechanical models for viscoelastic composites and the global analysis of deployable structures with viscoelastic properties. For their deployment and shape recovery experiments, they used composite tape springs made of a +/- 45° PW fabric with 1K tows of T300 carbon fibers

impregnated with Patz' PMT-F4 epoxy resin. The tape springs were 596 mm long, 38 mm in diameter, had a thickness of 0.125 mm and an areal density of 131.2 g/m<sup>2</sup>. Each of their tests consisted of stowing (i.e., 90° fold) the tape spring for an extended amount of time in a thermally controlled chamber at a specified temperature, deploying it and then measuring the shape change over time after deployment. The deployed angle was extracted from images taken from a high-resolution camcorder with a frame rate of 30 frames per second. Full field displacements were measured using a three-dimensional digital image correlation (DIC) system consisting of two CCD cameras with a resolution of 2,448 x 2,048 and a pixel size of 3.45  $\mu\text{m}$  x 3.45  $\mu\text{m}$ . The thermal chamber was heated to 60° C and the tape spring was stowed to an angle of 90° for 8 hours and then allowed to deploy and recover. The tape spring's displacement was then continuously measured over time. The same experiment was also conducted at 23° C. The tape springs' deployment sequence was complete in less than one second. The master curve for the PMT-F4 epoxy was generated via creep tests and the material constants,  $C_1$  and  $C_2$ , were 28.4 and 93.3, respectively. They also performed analytical modeling of the tape spring viscoelastic behavior using a Prony series and the WLF equation. The viscoelastic properties of the fiber tows were determined via FEA of a unit cell of the composite. The tows were modeled via a UMAT in Abaqus/Standard and each tow consisted of 960 brick elements. The matrix consisted of 1,920 brick elements and 640 triangular prism elements. The overall model of the tape spring consisted of 2,268 S4 elements and the viscoelastic properties of the shell elements were defined by assigning the  $ABD(t)$  matrix obtained analytically via a user defined shell section subroutine (UGENS). Overall their results showed good agreement with their observed test results.

They found the tape springs deployed quickly and overshoot the deployed configuration--a common problem with strain energy deployed systems. Finally, they found the extended stowage period of composite viscoelastic tape springs had the effect of extending the time required for their deployment and shape recovery. (Kwok and Pellegrino, 2012)

In 2012 Lyle and Horta researched the deployment of a CuBe tape spring hinge at NASA. They used LS-Dyna for the FEM simulation and Matlab scripts were written to control the simulation execution. Considerable variation was evident during both folding and deployment of the tape spring. The deployment time was between 0.25 – 0.28 seconds with the tape spring thickness the primary contributor to the variance. (Lyle and Horta, 2012)

In 2012 Da Veiga et al. researched the shear locking problem using isogeometric analysis (IGA). The key feature of IGA is to extend FEM representing the geometry by spline functions. Their research on IGA showed the high regularity properties of the employed functions led in many cases to a better accuracy to computational effort ratio than standard FEM. (da Veiga et al., 2012)

In 2012 Canal et al. found strain fields obtained from digital image correlation (DIC) were in good agreement with the solution provided by FEA in the matrix and fiber regions far away from the interface. The fuzzy nature of DIC made it impossible to capture the sharp strain gradients at the fiber-matrix interface though. (Canal et al., 2012) However, DIC provided a powerful tool for correlating shape comparisons between pristine and folded, post-deployed structures.

In 2012 Moreira et al. analyzed the effect of particle size and volume fraction on modulus of epoxy resins with alumina nanoparticles. They used the thermoset epoxy RR515 with alumina nanoparticles of average diameter 35 nm and 200 nm with loadings varying from 0% - 10% by volume. They found the modulus increased with volume fraction of alumina nanoparticles and particle size had no significant effect. (Moreira et al., 2012)

Also, in 2012 Yu et al. studied the effects of the interface structure of  $\text{Al}_2\text{O}_3$  nanoparticles on the properties of epoxy nanocomposites. They used a 6105 epoxy resin from DOW Chemicals, alumina nanoparticles with average diameter 30 nm and modified them with a silanization treatment to enhance the dispersion process due to surface functionalization of the particles. They stated the silane acted as a coupling agent promoting better dispersion and improved the miscibility between the organic and inorganic phases of the composite. Their nanocomposites contained weight fractions of alumina nanoparticles ranging from 5% to 20%. Like Ash et al. in 2001-2002, they found the  $T_g$  decreased monotonously with increasing filler load of ANP particles. One conclusion they reached was silane treatment of the alumina nanoparticles yielded good interfacial adhesion between the nanoparticles and the epoxy resin and resulted in good overall particle dispersion in the composite. (Yu et al., 2012)

In 2013 Peterson and Murphey researched large deformation bending in thin composite tape spring laminates. They tested a laminate constructed of two plies of IM7 UD prepreg sandwiched between two plies of PW 45° impregnated with Patz' PMT-F7 resin. The laminate was +/- 45° PW/ 0° UD/+/- 45° PW (i.e., AFRL's FlexLam). They

fabricated 70-inch tape springs and performed bending tests with a four-point bending fixture. Their micromechanics analyses overestimated both the axial and transverse bending stiffness by 10% compared to the test results. They attributed the differences to inaccuracies in the material property values. Also, in 2013 at AFRL the Very Low Frequency (VLF) Particle Mapper (VPM) dipole antenna creep tests were conducted. The one-meter long tape spring booms were made from a composite layup of AstroQuartz PW sandwiching a middle layer of S2 glass UD and a copper conducting strip. Six boom antennas were stored for one to six months each all at 30° C. One at a time (i.e., one per month) the antennas were brought out of storage and deployed. The tape spring antennas had reflective tape and dots applied to them to get a pre and post deployment shape using a high-speed camera imaging system. They found the end of the tape springs experienced substantial creep and the average deployment time was 6 minutes 25 seconds with the fastest deployment in 4 seconds and the slowest in 17 minutes. In some cases, it took the last three inches of tape spring three days to fully deploy. Oddly enough, the conclusion was these tests had no direct correlation between deployment time and stowage duration time. (Peterson and Murphey, 2013, Hock, 2013)

Also, in 2013 Brinkmeyer and Pellegrino et al. investigated the deployment kinematics of bi-stable thin CFRP composite tape springs, specifically how stress relaxation affected the stowed/coiled structure and the development of a model (based on Rimrott's 1967 work (Rimrott, 1967)) to predict deployment speeds. They fabricated two five-ply antisymmetric composite layups composed of ThinPly T800H UD carbon fiber prepreg. An MTS Instron machine with a thermal chamber was used to heat the composite tape springs for three hours at 60 °C and 100 °C while applying a quasi-

instantaneous strain of 0.1%; the tape springs were then deployed at room temperature. They concluded relaxation effects due to the stowage conditions caused significant changes in the deployment behavior. In the 60 °C case, the tape spring had a substantial delay in deployment and in the 100 °C case, the tape spring failed to deploy at all—it did not have sufficient stored strain energy for the autonomous deployment. Their material constants were determined to be  $C_1 = -1.35$  and  $C_2 = 42.9$ . Their analytical model for deployment time utilized a four-term Prony series fitted to the experimental data using a Matlab nonlinear optimization algorithm. This model produced errors that grew with stowage time and they surmised the errors were due to poor material characterization or refinement of their dynamic model. They concluded relaxation effects due to stowage of the tape spring caused significant changes in the deployment behavior of the tape spring structure. Longer stowage times decreased the stored strain energy available for deployment and an actuator would be needed to deploy the structure. (Brinkmeyer et al., 2013)

Kwok and Pellegrino expanded on their previous work on viscoelasticity, tape springs and folding mechanics by researching geometric nonlinearity and the viscoelastic effects on an isotropic homogeneous tape spring made of LDPE. They fabricated two single ply LDPE tape springs and conducted an 87° opposite sense folding stowage test (stowed for 5,000 seconds) along with uniaxial tension relaxation testing for 3 hours. The tape spring for the folding stowage test was 272 mm long, 19 mm wide and 0.73 mm thick; the deployment recovery test tape spring was 398 mm long, 19 mm wide and 0.73 mm thick. The deployment test consisted of folding the tape spring to an 87° angle in 9 seconds, holding it stowed for 983 seconds and then releasing the tape spring to deploy.

The tests were performed in a thermal chamber and Prony series coefficients were determined. As expected, their data showed load relaxation during the stowage, losing approximately 1/3 of the reaction force at the end of the stowage period. Coupons were also tested at 0° C, 10° C and 22° C to determine the material constants with  $C_1 = -8.74$  and  $C_2 = -40.41$ . Their constructed FEM was linear viscoelastic in Abaqus/Standard, using 6,800 quad shell elements (S4) with a maximum dimension of 2 mm and a quasi-static analysis. Their quasi-static FEM simulation in Abaqus/Standard had an experimentally determined relaxation modulus master curve and the material model consisted of a 6 term Prony series and a WLF-type temperature shift function. Despite stress relaxation occurring during the tape spring stowage, they reported good agreement between predicted and measured responses in the tape springs. However, their numerical simulation techniques were limited to homogeneous viscoelastic structures. (Kwok and Pellegrino, 2013)

In 2014, Sprenger researched epoxy resins with various hardeners and silica nanoparticle reinforcements 20 nm in diameter. (Sprenger, 2014) Since standard epoxy resin systems are inherently brittle, he found epoxy properties such as modulus of elasticity, toughness and fatigue performance could be improved by incorporating silica nanoparticles into the epoxy. Test results showed the addition of the nanosilica improved the longitudinal compressive strength by 61% – 81%; longitudinal tensile strength increased by 11%. In the transverse direction, the tensile strength increased 32% and the modulus increased 41%. It is important to note the modulus in the longitudinal direction was unchanged. The mechanisms for toughening were de-bonding of the epoxy polymer

from the silica nanoparticles, plastic void growth of the epoxy, fiber de-bonding and fiber pullout.

Also, in 2014 Liu et al. reviewed shape memory polymer (SMP) research. Thermoset SMPs with high material stiffness, high  $T_g$  and environmental durability are potential composites for design and fabrication of space structures. On the flip side, thermoplastic SMPs lose their shape memory effects after several cycles. Near  $T_g$ , the SMPs exhibit viscoelastic behavior. (Liu et al., 2014) Considering space structures experience several drastic temperature swings per day going in and out of sun and the severe cold of deep space, SMPs may not be a good choice for space structures.

In 2015 Roh et al. researched viscoelastic time dependent unfolding behavior of shape memory composites. They found the relaxation of strain energy reduced the restoration capability of SMP composite booms. They fabricated a polyurethane SMP boom composite made of PW T300 carbon fibers combined with the SMP resin and hardener. The boom had an inner radius of 17 mm, a thickness of 0.35 mm, a length of 220 mm and a subtended angle of 120°. They modeled the boom in Abaqus with 7,200 S4R elements. They used an Instron MTS machine with a thermal chamber and laser extensometer to measure strain in the boom stress relaxation testing brought about by folding the boom over a mandrel. The shape recovery configurations were recorded over time using a high-resolution camcorder. The full shape recovery took almost 15 seconds per a high-resolution camcorder. The viscoelastic time dependent deployment of the boom was investigated at a constant temperature of 55° C. The recovery behavior was dominantly governed by a strain energy not a shape memory effect of the boom. They

concluded if sufficient time was given, slow creep-dominated recovery should occur to reach the original configuration. (Roh et al., 2015)

Hoskin studied the blossoming phenomenon of isotropic BeCu tape spring booms at the University of Surrey. His test setup included a central hub with four compression rollers at approximately two, four, eight and ten o'clock on the in-plane test rig to prevent the coiled tape spring boom from blossoming (i.e., starting to uncoil). His goal was to determine how much force could be applied to the tape spring boom tip before the coil started to blossom. He measured the compression rollers' force and tried to correlate the two but hypothesized that friction between the tape spring layers, coil geometry and differing amounts of compression force caused correlation problems with his Abaqus model. (Hoskin, 2015)

In 2016 Hoskin and Viquerat continued Hoskin's blossoming of coiled deployable booms work. They aimed to study the amount of force a coiled tape spring boom could resist before blossoming. They calculated the minimum energy state radius of the coil and placed it in an MTS Instron machine with rollers to prevent the tape spring from unwinding. A load cell measured the force applied to the end of the tape spring as the MTS Instron machine's cross head moved up and down. Their tape spring only had two, three or four coils and they surmised friction between the coils caused discrepancies between their test data and analytical models. However, their models gave a good first order indication of the force a coiled tape spring will apply when stowed at a smaller or larger diameter than its natural curvature. (Hoskin and Viquerat, 2016)

Also, in 2016 Zhu et al. researched the combined effects of constituent materials, and the geometry and size of the microstructure on the effective elastic properties of interpenetrating composites. The structure of the composites they modeled included a generic nano-sized filler, a matrix and a uniform interphase between the filler and matrix. One of the conclusions they reached was the interphase could either stiffen or weaken a composite with nanometer-sized filler, depending on the size of the constituent materials and the fabrication process. The size-dependent effects vanished when the size of the filler/particle was much larger than the interphase thickness ( $>20$ ). While these composites included nanoparticles and looked at interphase effects, they did not include fibers which would add constituent complexity. (Zhu et al., 2016)

Tian and colleagues investigated the strain-rate effect on the TGDDM epoxy polymer with sol-gel-formed nanosilica particles. In their research, adding 10% weight nanosilica particles only produced a trivial change (i.e., slight reduction) in  $T_g$ , but significantly improved the compressive modulus, strength and strain energy at fracture. (Tian et al., 2016)

In 2017, Rouzegar and Gholami employed a Dynamic Relaxation (DR) method to conduct shear deformation analysis of creep and recovery of fiber-reinforced laminate composite plates. The DR method is an iterative technique transforming the static governing equations into artificial dynamic equations using fictitious masses and damping parameters. They researched the effects of lamina stacking sequence, side-to-thickness ratio and different types of boundary conditions. While they got accurate

results, they only looked at linear materials and only common laminates, i.e., no nanomaterials. (Rouzegar and Gholami, 2017)

Pathan and co-workers researched the effects of fiber shape and interphase on the anisotropic viscoelastic response of composites. While they addressed the interphase, their study did not include nanomaterials and focused on the interphase between fibers and matrix. Regarding the interphase, they concluded with a stiff interphase the modulus increased but the damping decreased and vice versa. (Pathan et al., 2017)

Tian and co-workers studied the interfacial properties between carbon fiber epoxy (i.e., DGEBA resin) composite with sol-gel-formed nanosilica particles. They found nanosilica particles exhibited a remarkable effect on increasing the interfacial adhesion between the fibers and polymer resulting in a 38% increase in the interfacial shear strength of the composite. They theorized the improvements may have been due to the toughened matrix from the nanosilica particles which reduced the stress concentrations and dissipated more deformation energy for a better load/stress transfer. (Tian et al., 2017)

Kwok and Pellegrino investigated a viscoelastic model for a single ply  $\pm 45^\circ$  PW composite tape spring 60 cm long, with a transverse radius of 19 mm, a thickness of 0.125 mm and with one fold of  $87^\circ$ . The PW lamina was comprised of T300 carbon fibers (1K tows) impregnated with Patz' PMT-F4 epoxy resin. The resin was modeled as isotropic and linearly viscoelastic, while the PW viscoelastic model was developed via a 6-step/analysis homogenization of a representative unit cell. Prony series coefficients were calculated and then the ABD matrix coefficients were obtained comparing the two

with the same relaxation times. The finite element model (2268 quad elements in Abaqus/Standard) of the tape spring and quasi-static simulation of the fold and deployment were compared with experimental results from a uniaxial tensile creep test and a four-point bending creep test, both with 8-hour stow times. The material constants were found to be  $C_1 = 28.4$  and  $C_2 = 93.3$ . Ultimately, they concluded the viscoelastic effects associated with long term storage extended the time needed to obtain a full deployment. Furthermore, an extrapolated conclusion based on the Time, Temperature, Superposition Principle (TTSP) revealed a tape spring stowed for a year would be unable to deploy at all in a gravity environment. (Kwok and Pellegrino, 2017)

Also, in 2017 Deployable Space Systems, Inc., teamed up with the Air Force Research Laboratory and NASA to design, fabricate and fly the Roll-Out Solar Array (ROSA) mission—the first on-orbit deployment of high strain composite STEM booms. ROSA was a tensioned membrane deployable space structure supporting a flexible photovoltaic blanket elastically deployed via stored strain energy (primarily) and motors (secondarily, and for retraction). ROSA consisted of a thin, three-ply CFRP high strain composite laminate in the form of two longitudinal STEMs, four inches in diameter and reversed rolled. ROSA was 5.4 meters long by 1.7 meters wide and deployment rate was controlled via eddy current dampers in the structure's tip mandrel. The ROSA structure was stowed for 10 months prior to on-orbit deployment from the International Space Station. (Banik et al., 2018, Chamberlain et al., 2018)

In 2017, Borowski et al. researched stowage and deployment of CFRP laminate tape springs in a three ply layup consisting of +/- 45° PW plies sandwiching a 0° UD ply.

The PW plies used a Patz Materials and Technology GP2-61-2 epoxy (now discontinued) as the matrix and the UD ply used the Patz PMT-F7 epoxy as the matrix. The tape springs were 305 mm long and 25 mm wide in flattened width. Tension tests, fiber volume fraction tests, DMA tests and density measurements were taken of the tape springs to provide good material values for the FEM simulation in Abaqus/Standard of the tape springs' deployment. The tape springs were folded over in a 180° fashion and secured at both ends for a stowed period of time of 34 days. A master curve of the PMT-F7 epoxy (reported by Patz to be comparable to the GP2-61-2 epoxy) was produced and the Prony parameters were implemented into the stress relaxation modeling via a Fortran subroutine program in Abaqus (i.e., a UMAT). The model was shown to predict the tape springs' deployment with good accuracy and both the model and experimental results showed long term stowage affects tape spring deployment. (Borowski et al., 2017)

In 2017 Garner et al. researched the material properties of CFRP by incorporating ANPs into the matrix of the plies. The goal was to show the possibility of controlling strain energy storage dissipation by controlling the composite's stiffness and stress relaxation. The composite layup used in their research was the FlexLam design created by the AFRL Space Vehicles Directorate with a diglycidly ether Bisphenol-A resin from U.S. Composites and a carbon fiber PW fabric with 3K tow size also from U.S. Composites. It was a +/- 45° PW / 0° UD / +/- 45° PW layup. They conducted tension stress relaxation tests on the ANP-epoxy coupons, DMA tests of ANP-epoxy coupons to determine the viscoelastic properties of the ANP-epoxy matrix and FTIR measurements of the epoxy to understand the significance of ANPs on the polymerization process of the epoxy. They concluded from the stress relaxation master curves the incorporation of 2

weight % ANPs into the epoxy decreased the modulus by 38% and increased stress relaxation by 10% during a 1,800 second time period. They also concluded the DMA and FTIR results suggested ANPs inhibited the curing of the epoxy which lowered the epoxy's crosslinking and thus reduced the epoxy modulus. Finally, the ROM and Halpin-Tsai model did not adequately capture the effects of ANPs on the material properties. The bottom line was ANPs affected epoxy polymerization at 2% weight and resulted in substantial reduction of epoxy crosslinking (e.g., -20.9%) thereby reducing composite stiffness and increasing stress relaxation. (Garner, et al., 2017)

In 2018, Gomez-Delrio and Kwok furthered previous work on composite tape springs Kwok had done with Pellegrino et al. from 2010 – 2017. They researched an analytical, closed form solution for the relaxation and recovery of an opposite sense folded viscoelastic composite tape spring made from Patz F4 epoxy and T300 carbon fibers, undergoing quasi-static deployment. They found good agreement between their analytical model and four step (fold, stow, deploy, recover) quasi-static finite element model (FEM). The FEM consisted of 6250 quad elements in Abaqus/Standard modeling a homogeneous isotropic tape spring (F4 epoxy with  $C_1 = 13.1$  and  $C_2 = 102.3$ ) with a single ply PW composite tape spring, 0.125 mm thick. The closed-form analytical model predicted the moment relaxation well, but not the deployment and recovery. (Gomez-Delrio and Kwok, 2018)

## 2.2 Viscoelastic Materials

A succinct review of viscoelasticity is briefly given first to set the foundation for this research. The time-dependent response of a material can be classified as elastic, viscous or somewhere in between the two, viscoelastic. Thus, a viscoelastic material can be considered an intermediate combination of an ideal elastic solid and an ideal viscous fluid. A viscoelastic material contains the response of an elastic material and viscous material together in one with Hooke's law and Newton's law of viscosity representing the extreme range of limits for viscoelastic material behavior. The viscous properties provide the material's time dependence. Only perfectly crystalline materials are completely elastic; the vast majority of all materials are viscoelastic if observed for sufficiently long periods of time and/or at sufficiently high temperatures. Therefore, most real materials, i.e., not theoretical or fabricated in a controlled laboratory environment, are viscoelastic. Polymers in particular are usually described as viscoelastic which emphasizes their intermediate position between purely elastic solids and purely viscous liquids.

In 1676 Robert Hooke proposed for small strains, any strain is proportional to the stress producing it, which became known as Hooke's Law. The classical theory of elasticity deals with the mechanical properties of elastic solids which in accordance with Hooke's Law, stress,  $\sigma$ , is directly proportional to strain,  $\epsilon$ , for small deformations, but independent of the rate of strain itself. The material's isotropic modulus,  $E$ , is directly

proportional to the stress and strain. A solid obeying Hooke's Law is often called a Hookean elastic solid, and Hooke's Law in its simplest form can be given as:

$$\sigma = E\varepsilon \quad (2.6)$$

Alternatively, Hooke's Law for a composite in tensor form can be given in its most general form as:

$$\sigma_{ij} = C_{ijkl}\varepsilon_{kl} \quad (2.7)$$

where  $C_{ijkl}$  is the composite's compliance matrix and in general has 81 elements, but due to symmetry has at most 36 independent elements, i.e.,  $\sigma_{ij} = \sigma_{ji}$ , and  $\varepsilon_{kl} = \varepsilon_{lk}$ . Note, the inverse of the compliance matrix is  $S_{ijkl}$ , the composite's stiffness matrix and gives an expression for the strain when written as:

$$\varepsilon_{ij} = S_{ijkl}\sigma_{kl} \quad (2.8)$$

The classical theory of hydrodynamics deals with the properties of viscous liquids for in accordance with Newton's Law the stress is always directly proportional to the rate of strain but independent of the strain itself. When finite strains are imposed on solids, the stress-strain relations are much more complicated with non-Hookean deformation (i.e., nonlinear). Similarly, with finite strain rates, many fluids, especially polymeric solutions, exhibit substantial deviations from Newton's law and have non-Newtonian flow. (Ferry, 1980) Polymers do not perfectly obey the assumptions of the classical theory of linear elasticity either, they most often behave as viscoelastic and nonlinear.

In general, a structure is usually designed to remain in the elastic or viscoelastic range of its performance to ensure safe, reliable and predictable behavior. The conditions should be avoided where there is plastic deformation,  $\varepsilon_p > 0$ , because any plastic deformation is irreversible damage to the structure. Thus, an engineer typically designs a space deployable structure to remain in the elastic or viscoelastic region. As aforementioned, most materials are viscoelastic in nature to some degree, and certainly in this research work with an epoxy as the design basis for the matrix material used in all of the tape springs' laminate plies.

While Hooke's Law is not time-dependent for elastic materials, the time-dependent characteristics of the dynamic moduli of viscoelastic materials are strongly related to their internal structure and environmental conditions. (Findley, 1976) Viscoelasticity is time-dependent elastic behavior, existent in amorphous polymers and glasses in a certain temperature range. The glass transition temperature,  $T_g$ , for a polymer composite is a temperature range (as opposed to a specific point) below which molecular motions are highly restricted and the material is frozen into a so-called glassy state; it is a direct measurement of molecular mobility in a composite. (Li, 2000) An assessment of a material's  $T_g$  with respect to its structural behavior and material make-up (constituents, lay-up, etc.) can help determine design implications. For example, rigidizable-inflatable composite structures are influenced heavily by the location of their  $T_g$  with respect to the structure's thermal profile for terrestrial fabrication and stowage to on-orbit deployment and service life. This criticality was especially prevalent in work done on a joint AFRL-DARPA (Defense Advanced Research Projects Agency) program called ISAT (Innovative Space-Based Antenna Radar Technology) from 2003 - 2005 intending to

implement two 25-meter truss structures made from rigidizable-inflatable composites. Ultimately the program was cancelled, in small part to the difficulties encountered with engineering the deployable structures which were to host the mission's prime payload.

The theory of linear viscoelasticity is well established to describe the time and temperature dependence of the mechanical properties of polymers. However, it is only an approximation of the real material performance. For example, the strain during creep of many polymer composites can be separated into a time-independent linear part and a time-dependent nonlinear part. The nonlinear part of tensile creep is assumed to be mainly brought about by the strain induced through facilitation of the material's free volume increase. (Lv et al., 2014) Research has shown the phenomenological theory of viscoelasticity demonstrates retardation (i.e., relaxation) times are controlled by the fractional free volume available for molecular motions in polymeric materials. (Dorigato et al., 2010) The free volume implications for polymeric viscoelasticity will be discussed in more detail later in this chapter.

The linear viscoelastic behavior of many materials can be approximated and represented with an arrangement of rheological models composed of numerous spring and dashpot elements which obey Hooke's law and Newton's law of viscosity, respectively. This rudimentary modeling with one or more networks of physical springs and dashpot elements can often provide a reasonable approximation for a structure's linear viscoelastic behavior. The spring model represents an ideal linear elastic spring and the dashpot model represents an ideal viscous fluid. Various combinations and numbers of networked elements can be mathematically combined to model a structure's

stress relaxation or creep. For example, a network of one spring and one dashpot in series is known as a Maxwell model and a network of one spring and one dashpot in parallel is known as a Voigt (or Kelvin-Voigt) model as shown in **Figure 2.1**:

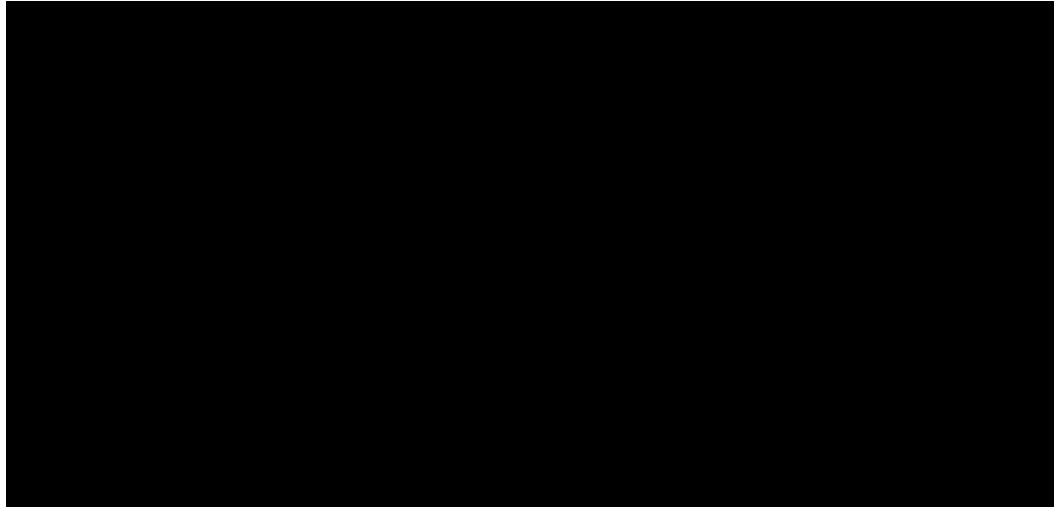


**Figure 2.1 Voigt (Left) and Maxwell (Right) Rheological Models**

These mechanical models do not represent the actual compositional structure of a material, they are merely models approximating the viscoelastic behavior. However, a representation of the real linear viscoelastic behavior of many viscoelastic materials can be obtained reasonably well by arranging an array of Maxwell elements in parallel, otherwise known as a generalized Maxwell model as shown in **Figure 2.2**:

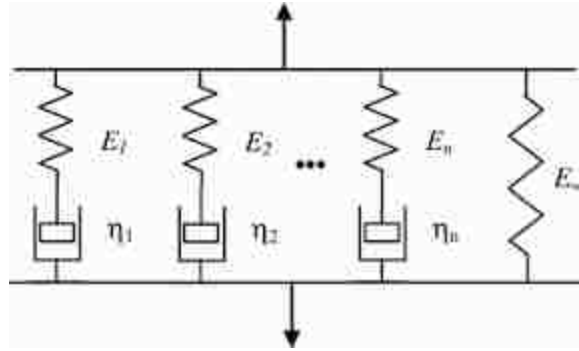


**Figure 2.2 Generalized Maxwell Rheological Model**

In the rheological models, the spring can be modeled mathematically as:

$$\sigma = k\varepsilon \quad (2.9)$$

and the damper as:

$$\sigma = \eta \frac{d\varepsilon}{dt} \quad (2.10)$$

where  $\eta$  is the viscosity and  $k$  is the stiffness. The Hookean spring models the instantaneous elastic deformation of the material with its magnitude related to the fraction of mechanical energy stored reversibly as strain energy. The Newtonian dashpot models the time-delayed deformation of the material with its magnitude related to the fraction directly proportional to viscosity and lost irreversibly due to heat.

While the linear theory of viscoelasticity is relatively straightforward, nonlinear viscoelasticity is decidedly more complex. This recognition is important because most real materials exhibit both linear and nonlinear behavior depending on strain rate,

temperature, boundary conditions, etc. Nonlinear behavior is most common in real materials under real load and boundary conditions. Case in point, the tape spring modeled in this research is viscoelastic and nonlinear due to its stress-strain response and the extreme bending it undergoes while in its stowed state. Therefore, understanding and using nonlinear viscoelastic models and theory provide a reasonable approach, or starting point, to describe the viscoelastic composite behavior. Nonlinear viscoelastic theory often includes stress terms of order higher than first order and is more complex than linear theory. (Findley et al., 1976) For example, a general nonlinear constitutive theory for multiaxial loading was developed from thermodynamics principles by Schapery. (Stolarski and Telytschko, 1983) Schapery's nonlinear viscoelastic theory, based on the fundamental principles of irreversible thermodynamics, has been used extensively by some researchers over the years. (Dutta and Hui, 2000) However, more than a decade before Schapery, Biot (1954) first used the thermodynamics of irreversible processes to derive constitutive laws for linear viscoelastic materials. The theory developed by Biot led to a linear system of differential equations, the solution of which leads to the constitutive law:

$$s_i(t) = \sum_{n=1}^N a_n(1 - e^{-t\tau_n}) \quad (2.11)$$

which is a form of the classic Prony series and where the functions,  $s_i$ , are Bernstein functions. (Levesque, 2007) The Prony series is a well-established method to model the relaxation modulus of viscoelastic materials and has been used in this research. It is discussed in more detail later in this chapter.

## 2.3 Viscoelastic Material Behavior

Viscoelastic behavior is concerned with materials exhibiting strain rate effects in response to applied stresses. These effects are manifested by the phenomena of creep under constant stress and stress relaxation under constant strain. While it is well known viscoelastic materials are significantly influenced by strain rate, creep and stress relaxation behavior are still not well understood. (Findley, 1976, Li et al., 2006) Creep behavior and stress relaxation are fundamental characteristics for describing the long-term mechanical performance of polymeric composites. Moreover, creep and stress relaxation in an anisotropic and multiphase material, such as a composite, are much more complex than creep and stress relaxation in a homogeneous metallic or pure polymeric material. In a CFRP composite, creep and stress relaxation can occur in both fiber-dominated and matrix-dominated directions. Furthermore, the complexity is increased even more when nanoparticles are added to the composite.

A material's viscoelastic response is very sensitive to its chemistry and microstructure. When subjected to an applied load (stress), polymers may deform by either changing the length and/or angle of their atomic bonds or achieving molecular rearrangements of their molecular chains which are often kinked, twisted and bent in an undulating fashion. The time-dependent response of a polymer is the result of these short and long-range rearrangements of its molecular chains associated with the global deformation of the material. The complexity of the polymer's microstructure and nanostructure will also play a role in the viscoelastic effect; the more disordered the

material is from an entropic point of view, the more magnitude and/or time it may take to creep or relax. Furthermore, the amount of imposed strain can also affect a polymer's microstructure as large strains can induce anisotropic molecular orientations. (Losi and Knauss, 1992)

With polymer composites being viscoelastic, their properties exhibit strong time and temperature dependencies. The main manifestations of viscoelasticity are the creep and stress relaxation phenomena, generally shown as depicted in **Figure 2.3**. Creep behavior results when a material is subject to a prescribed stress (force) and the material continues to strain over time to an asymptotic limit, which can be a combination of elastic, plastic, linear and nonlinear behavior. Viscoelasticity that is not linear (in stress) is nonlinear.

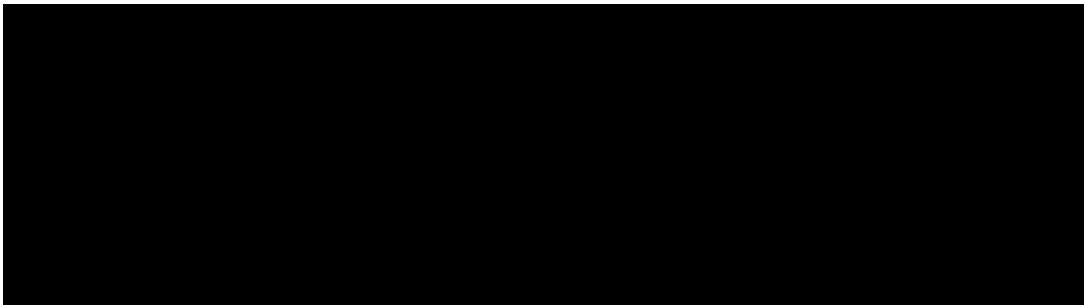


**Figure 2.3 General Stress and Strain Behavior of a Material Subject to Creep**

Stress relaxation behavior results when a material is subjected to a prescribed strain and over time the level of stress continues to be reduced until it asymptotically approaches a limit as generally shown in **Figure 2.4**.

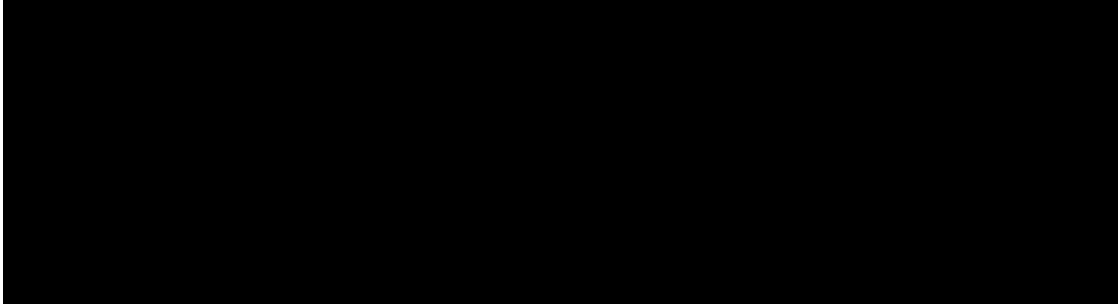


**Figure 2.4 General Stress and Strain Response of a Material Subject to Stress Relaxation**

For a stress relaxation test, the relaxation modulus,  $E(t)$ , can be expressed as:

$$E(t) = \frac{\sigma(t)}{\varepsilon_0} \quad (2.12)$$

Since the stress varies with respect to time the modulus also varies with respect to time, as the “relaxation modulus”.

If one uses a simplifying assumption that the material is a general Maxwell solid, i.e., a linear viscoelastic material approximated by a linear elastic spring and a viscous damper connected in series per **Figure 2.2**, the material’s relaxation modulus can be modeled as a Prony series:

$$E(t) = E_0 \left( 1 - \sum_{i=1}^N k_i \left( 1 - e^{-t/\tau_i} \right) \right) \quad (2.13)$$

Further decomposed as:

$$b_i = k_i \left( 1 - e^{-t/\tau_i} \right) \quad (2.14)$$

$$E(t) = E_0(1 - \sum_{i=1}^N b_i) \quad (2.15)$$

To this end, a Prony Series was used in this work to model the relaxation modulus of the composite laminate tape springs. Equations 2.13 – 2.15 were used in the VUMAT (Vector User Defined Material) to model the viscoelastic effects of the epoxy, both with and without nanoparticles. The VUMAT is discussed in Chapter 4.

Since a composite material's relaxation modulus is often dominated by the matrix material (as the fibers are usually linear elastic with much higher strength and stiffness compared to the matrix), only the matrix was modeled for the entire composite's relaxation modulus which drives the structural behavior. Moreover, the matrix is also typically nonlinear in its behavior and can be characterized by its bulk modulus and shear modulus. Another simplifying assumption is the epoxy used in this research experienced an insignificant change in volume, thus, the relaxation modulus of the PW plies and therefore the FlexLam composite laminate itself could be modeled sufficiently by the shear modulus of the epoxy matrix, with and without ANPs.

Viscoelastic behavior is exhibited by materials with history-dependent mechanical properties, therefore, the mechanical response of a polymer matrix is in general, not a simple, linear function of its strain history. To analyze a nonlinear viscoelastic material, a good starting point is to begin with a linear viscoelastic material. In linear viscoelastic materials, the material behavior is hereditary. In other words, the behavior at a particular instant in time depends on what happened to the material since the beginning of an applied force or strain, i.e., its history. Consequently, instead of Hooke's Law, the stress-

strain relation for linear viscoelastic materials can be expressed as an integral based on Boltzmann's Hereditary Theory:

$$\varepsilon(t) = \frac{\sigma(t)}{E} + \int_0^t k(t-s)\sigma(s)ds \quad (2.16)$$

Equation 2.16, specifically the integral, accounts for loading prehistory on the strain development. The kernel,  $k(t)$ , in the integral may be represented in the form of a series of decaying exponentials (i.e., a Prony series):

$$k(t) = \sum_{i=1}^n \frac{b_i}{\tau_i} e^{-\frac{t}{\tau_i}} \quad (2.17)$$

where  $\tau_i$  and  $b_i$  are the discrete retardation time spectrum. (Glaskova et al., 2015) In accordance with the Boltzmann Superposition Principle (also called the Hereditary Principle or Theory), the creep and stress relaxation of a material are functions of its total preloading history. (Aniskevich, 2012) For example, the representation of the creep of polymers,  $\varepsilon(t, \sigma, T)$ , consists of three components: 1. Elastic (instantaneous) deformation,  $\varepsilon_0(\sigma, T)$ , 2. Viscoelastic (reversible) deformation,  $\varepsilon_v(t, \sigma, T)$ , and 3. Plastic (irreversible) deformation,  $\varepsilon_p(t, \sigma, T)$ ; hence, the total viscoelastic creep response of a polymer is in general (Kolarik, 2007):

$$\varepsilon(t, \sigma, T) = \varepsilon_0(\sigma, T) + \varepsilon_v(t, \sigma, T) + \varepsilon_p(t, \sigma, T) \quad (2.18)$$

Since viscoelastic functions are phenomenological in nature, empirical functions are often used to describe polymeric behavior and the functions tend to fall into two classes:

1. Those based on power laws and 2. Those containing a kernel of the form:

$$e^{\left(\frac{t}{\tau}\right)^m} \quad (2.19)$$

to describe the creep of amorphous polymers over limited time scales, where  $t$  is time,  $\tau$  is the retardation time and  $m$  is a constant specific to the particular polymer. (Tomlins, 1996)

Hashin (1966) showed elastic moduli and viscoelastic relaxation moduli of heterogeneous materials of identical phase geometry are related by the analogy later known as the Correspondence Principle, or also known as the Elastic Viscoelastic Correspondence Principle (EVCP). (Hashin, 1966) This principle states if the solution to an elastic problem is known, then the corresponding solution to the viscoelastic problem can also be solved. In general, the strain of a viscoelastic material will be a function of stress, temperature and time and can be expressed as:

$$\varepsilon = f(\sigma, T, t) \quad (2.20)$$

A viscoelastic material can be further characterized as either linear or nonlinear with respect to stress and temperature:

$$\varepsilon = g(\sigma)h(T)k(t) \quad (2.21)$$

which is a separable equation. (Goertzen and Kessler, 2006)

To reiterate, the fundamental behavior of a viscoelastic material depends upon its relaxation modulus and prior loading history. At temperatures significantly below the material's  $T_g$ , the material is essentially linear elastic and follows Hooke's Law. The material's glassy behavior is predicated on the freezing of the mechanical relaxation plus

the locking of the residual free volume, both of which affect the compliance of the total volume to yield a CTE in the glassy regime. (Losi and Knauss, 1992) In the range near its  $T_g$ , the material is essentially midway between its glassy and viscous states. It's important to note a material's glass transition temperature is not a thermodynamic transition, it is a mechanical transition. As the material's temperature is increased beyond its  $T_g$  the stiffness drops dramatically and the modulus in this rubbery region is governed primarily by the crosslink density, or lack thereof. However, while neither the glassy or rubbery moduli depend heavily on time, in the vicinity of its  $T_g$ , the modulus is often greatly affected by time. Overall, a generic polymer's modulus could be affected as depicted in **Figure 2.5**:

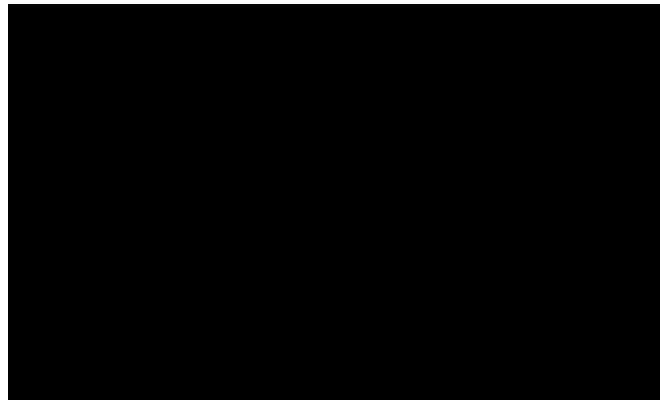


**Figure 2.5 Generic Modulus of a Polymer Through its  $T_g$  Transition**

Viscoelastic materials exhibit behavior somewhere between purely elastic and purely viscous materials. For an ideal elastic material, the stress and strain are in phase, on the flip side, for an ideal viscous material, the stress and strain are  $90^\circ$  out of phase. The viscoelastic region (which extends on both sides of the material's  $T_g$ ) occurs when the strain and stress are out of phase producing a storage modulus and loss modulus

characterizing the material. The storage modulus represents the immediate elastic response; the strain energy is stored and completely released upon removal of the applied strain. The loss modulus represents the out-of-phase contribution; the strain energy is completely dissipated and lost as heat.

The effects of viscoelasticity are often categorized via creep tests, stress relaxation tests or dynamic (sinusoidal) mechanical tests. Creep and stress relaxation tests are useful for studying a material's response for long periods of time (i.e., minutes to days and beyond) but not so accurate for short periods of time (i.e., ~ a second or less). Sinusoidal tests via DMA testing can provide the short-term material response. Both stress relaxation and DMA tests were done in this research to cover the full spectrum of the tape springs' structural behavior. DMA test results of the neat epoxy and the ANP epoxy are provided in sections 5.3 and 5.1, respectively. Structural stress relaxation test results of the tape springs with and without ANPs are provided in sections 5.4 and 5.2, respectively.

## **2.4 Material Properties**

Polymer-based composites consist of thermoplastics, thermosets and elastomers and are used frequently in the aerospace industry. Polymers consist of long, linear, branched or cross-linked molecules, the structure of which can substantially affect the mechanical behavior of a composite. (Aniskevish et al., 2012) In general, a polymeric

molecule is a very long and flexible chain and can change form easily because many independent vibrations and rotations of the atoms composing the molecular chain are possible. As a case in point, glassy-amorphous polymers show the phenomenon of time-dependent strain, i.e., viscoelasticity. Deformation of these polymers is not based on atomic displacements along crystallographic planes as is common in metals, but a continuous flow of the atoms and molecules with time. The absence of crystallinity usually means a lower modulus due to less efficient packing of the atoms. Polymers tend to be mostly amorphous but can be a combination of crystalline and amorphous in structure so they typically have a lower modulus than metals such as aluminum and titanium, two very common materials in the aerospace industry. Understanding the microstructure, constituent properties and their interactions is critical for determining the structural behavior and mechanical responses of polymeric-based composites.

Polymers have a much larger dependence on time and temperature than metals or ceramics and show creep and stress relaxation effects at much lower stresses and temperatures because of their weak van der Waals forces acting between the backbone polymer chains. More than 2/3 of polymer matrices used in aerospace applications are epoxy-based thermosets. Thermosets are commonly used because they are cross-linked polymers with a large number of three dimensional highly interconnected chains. The Patz PMT-F7 epoxy is an aerospace-grade thermoset epoxy. The main reasons epoxies are used in the aerospace industry are for high strength and low viscosity with flow rates allowing for good wetting of filling fibers and/or nanoreinforcements. (Aniskevish, 2012) Furthermore, epoxies are also widely used as a matrix for advanced composites because of their good stiffness, specific strength, dimensional stability and chemical resistance.

Most epoxies have relatively short molecular chains and they covalently crosslink into an intact three-dimensional network after curing. (Ma et al., 2009) This crosslinking provides the epoxy with superior stiffness and strength compared to uncrosslinked polymers. However, even with crosslinking, the creep and stress relaxation of epoxies under sustained loads can be significant and some researchers have suggested highly crosslinked epoxy matrices exhibit a reduced capability of forming interphases. (Taha et al., 2010, Weidt and Figiel, 2015) The interphase may be an important constituent in a nanocomposite, but its size, consistency, material properties and overall effect on the material's bulk behavior are not well known yet.

The subject of this research work consisted of a three-ply composite laminate with a relatively soft polymer matrix (compared to typical aerospace epoxies) containing silica fibers in the PW plies and carbon fibers in the UD ply. The laminate used the Patz Materials and Technology PMT-F7 epoxy as the matrix material which was several orders of magnitude lower stiffness than either of the fibers. Whereas a stiff matrix ( $> 6$  GPa modulus) composite would deform through fiber stretching, soft matrix composites typically deform through fiber bending. (Berg, 1998) Specifically, the fibers bend in microbuckling and kinking deformation modes to accommodate the large strains. To realize these deformations without plastic deformation, the matrix is subject to much larger strains. While glass/silica fibers tend to be linear, it has been observed carbon fibers can exhibit nonlinear behavior in both tension and compression, including flexural behavior. (Murphey et al., 2015) ANPs (i.e.,  $\text{Al}_2\text{O}_3$ , or also known as alumina nanoparticles) were added to the PW plies at 2% by weight to create a nanocomposite laminate for the tape springs' structural architecture.

Polymer nanocomposites can be defined as polymers containing at least one filler element with a dimension less than 100 nanometers (nm). In contrast to traditional micro-filler composites which can have high loadings, polymer nanocomposites are generally found to exhibit their greatest mechanical property increases at very low loadings, i.e., only a few volume or weight percentage of nanofiller. As such, the mechanical strength and stiffness of a composite with filler(s) depends on many factors, including shape of the particles, their dispersion (or lack thereof), physiochemical bonding between phases and the resin composition. Research has also shown the addition of nanoparticles can effectively suppress the formation and propagation of micro-cracks in the matrix. (Tian et al., 2017) The nanofillers of epoxy matrices are usually represented by materials with either hydrophobic properties or hydrophilic surface properties, of which aluminum oxides are a member of the latter group. However, experience using ANPs as a composite filler is rather limited as documented earlier in this chapter, but promising results portend an untapped potential for this research area.

The structural behavior of polymeric composites is affected largely by the microstructure including the size, shape, composition and weight fraction of the reinforcement filler(s), both micro-filler and nanofiller. Furthermore, the mechanical properties of nanoparticle composites depend strongly on nanoparticle size, nanoparticle shape, nanoparticle-matrix adhesion at the interfaces and nanoparticle weight/volume content within the composite. (Fu et al., 2008) A composite derives a considerable amount of its enhanced mechanical properties from the size of the filler, most especially a nanofiller. The large specific surface area of nanoparticles and strong interfacial

interaction between the polymer matrix and nanoparticles provide much improvement in mechanical properties of composites with a very small amount (mass or volume) of nanoparticles. This property is one of the biggest advantages of using nanoparticles. However, it's also a disadvantage as nanoparticles naturally tend to form clusters due to the strong van der Waals attraction between the nanoparticles. Moreover, there is often a poor compatibility between the polymer matrix and nanoparticles making processing and fabrication of nanostructures very difficult. Nanoparticle agglomeration and dispersion issues continue to be challenges and are an active area with considerable ongoing research efforts.

Another important material in a nanocomposite is the interphase. The interphase is a critical aspect of a nanocomposite due to the enormous surface area of the nanoparticles. The properties of the interphase must be understood and how they affect the bulk properties of the composite. The interphase can have dramatic effects on the structure, as an accumulation of nanoparticles as agglomerations can cause stress concentrations and reduce composite stiffness and strength, producing the exact opposite effect intended. (Zare, 2016) The interphase is defined as the region with altered chemistry, altered polymer chain mobility, altered degree of cure and altered crystallinity unique from those of the filler or matrix materials. (Ma et al., 2010) The dimensions of the interphase have only recently become known for the importance they portray for the composite properties. A poor modulus is observed when a thin interphase exists. Conversely, where there is a thick interphase with small nanoparticles there is often a high modulus. Thus, the strength and stiffness of a nanocomposite may depend strongly on the interphase properties. (Zare, 2016)

Composite stiffness can be easily improved with the addition of micro- or nanoparticles, however, composite strength depends heavily on the load and stress transfer between the constituents, i.e., matrix and particles (micro- or nano-) and/or fibers. For well-bonded constituent interfaces (including the interphase), the applied stress can be effectively transferred to the strongest constituents, namely, the fibers and/or particles. On the other hand, for poorly bonded constituent interfaces, the interface from the particles and/or fibers to the matrix may very well become stress concentrations and have the opposite intention and reduce composite strength. For dispersion and agglomeration, a continuing challenge for nanocomposites, this remains an important concern.

Nevertheless, the elastic mechanical constants of a composite are determined by the bonding between individual atoms, both within the polymer chain and to other composite elements such as the matrix, micro- and/or nanofillers and the interphase. Viscoelastic moduli in particular are also mainly governed by the volume fraction of particulate constituents and the strain rate has an important effect on the matrix-particle adhesion and overall structural behavior. (Fu et al., 2008)

## **2.5 Modeling Considerations**

The behavior of a composite must be known and predictable throughout a space structure's lifetime: from the extended stowage period on the ground to on-orbit

deployment and performance. There must be an adequate strain energy deployment margin of safety to ensure success on orbit. Structures cannot be easily, if at all, repaired or replaced in space. Thus, models are needed to analyze the strain energy, stresses and forces so there is high confidence in using the structure in a design and it will perform as intended. However, composites with large strains, heterogeneous multi-phase materials, viscoelastic behavior and nonlinearities cause significant difficulties in predicting accurate structural performance from a model.

It is therefore highly desirable to anticipate and select properties of composites because it is impractical to conduct long term viscoelastic testing for the entire design life of a material or perform every possible test scenario to determine all of a composite's properties. Predictive models can be alternative approaches to augment experimental testing, can save costly and time-consuming testing and can improve design efficiency immensely. For example, finite element methods are usually used for modeling and analyzing stresses of detailed microstructures for particle or fiber composites. It is common for models to treat multi-phase material properties as a smeared homogeneous material for simplifying reasons because it is quite difficult to accurately predict mechanical properties of complex nanocomposites. Most models also don't usually contain the important interphase, which can have dramatic effects on the structure, as an accumulation of nanoparticles can cause stress concentrations and reduce composite stiffness and strength. (Zare, 2016)

Historically, a micromechanics analysis has been often used to approximate composite properties. Micromechanics is the interaction of constituent materials and

their influence on the structural behavior of the macroscopic composite. Micromechanics can also be thought of as the analysis of composite or heterogeneous materials on the level of the individual constituents constituting these materials. Micromechanical analysis gives the relationship between fiber and matrix and allows for a detailed insight of the mechanical behavior of a composite by considering the influence of each constituent. If the proper constitutive model is developed for each constituent of a composite and special attention is given to the interface between constituents by using a combination of micromechanical analysis and homogenization techniques it is possible to study the mechanical behavior of a composite under most any load combination. Micromechanical analysis of heterogeneous materials provides their overall effective properties and behaviors; they depend primarily on the properties of the constituent materials. Micromechanics is used to predict properties of composite materials based on known (i.e., experimentally tested) properties of the constituents, and can be used to predict stiffness with great success and strength with much lesser success, at least for traditional fiber composites. Composites consist of clearly distinguishable constituents with different mechanical and physical material properties. Given the linear and nonlinear material properties of the constituents, one important goal of micromechanics consists of predicting the response of the heterogeneous material on the basis of the geometries, amounts and properties of the individual constituents (known as homogenization). The benefit of homogenization is the behavior of a heterogeneous material can be determined without resorting to testing it as such tests may be expensive and involve a large number of permutations. Attempting to model multiple discrete

constituents can be very difficult and homogenization may lose important constituent interactions affecting structural behavior.

While micromechanics analyses are often used for composites, they do not capture material behavior at the nanoscale. Thus, computational modeling approaches can be used for simulating the mechanical behavior of nanostructures and can be divided into atomistic methods, continuum mechanics-based methods and hybrid/multi-scale approaches. Atomistic methods are typically molecular dynamics-based and use very small length and time scales. Continuum mechanics uses models at the constitutive level to effectively model the mechanical behavior of nanostructures. Multi-scale modeling can then be used to bridge the gap between atomistic and continuum mechanics modeling and between other similar adjacent levels of modeling up to the structural level. One of the difficulties with modeling nanoparticles is determining whether to use a method such as the RVE, a homogenization technique or to use a statistical approach. All of these methods have limitations out of the scope of this research work, but in general, these methods neglect the precise locations and orientations of the nanoparticles so their applications are limited to the assumptions of uniform dispersion and no agglomerations. (Fu et al., 2008)

Another potentially important modeling consideration with respect to a viscoelastic material is in regard to the material's free volume. A polymer's total volume consists of occupied volume by atoms and molecules and free volume. The ratio of a polymer's free to occupied volume is not a constant. Molecular rearrangements can modify the chain topology, hence, trading between free and occupied volume occurs

while the composite is under loading. The free volume number of sites can change through a suddenly applied temperature or deformation with the average number of sites increasing but the average size decreasing. Therefore, upon application of a pressure or temperature change in a polymer, a free volume change will occur which immediately affects the material's relaxation behavior. The time scale of stress relaxation or creep is governed by the free volume induced time shift; the free volume change induces change in the relaxation time. (Coleman, 2006)

The time scale of the composite relaxation and the free volume content are connected by the Doolittle equation under the assumption of a maximum entropy state so it is valid only for equilibrium conditions in steady state. While there is a finite volume of vacancies, the free volume goes to zero as the composite temperature rises above its glass transition temperature. The microscopic free volume changes manifest themselves as dynamic phenomena at the molecular level. Chain segments undergo thermal motion and vibration which opens and closes vacancies. At equilibrium, the volume of vacancies generated balances the volume of vacancies closed, but at elevated temperatures, the free volume balance is perturbed and manifests itself as a viscoelastic volume change. The viscoelastic change can be considered the superposition of an average viscoelastic motion including a random Brownian motion disturbance incorporating the stochastic features of thermal vibration. The absence of the Brownian motion (i.e., the randomness of the thermal motion) would preclude the molecules "knowing" the open vacancies to fill. (Losi and Knauss, 1992) The time scale of the composite relaxation is affected by the instantaneous free volume through the time shift via the Doolittle equation:

$$\log(a_t) = \log\left(\frac{\eta}{\eta_0}\right) = B\left(\frac{1}{f} - \frac{1}{f_0}\right) \quad (2.22)$$

where  $f$  and  $f_0$  are two free volumes,  $a_t$  is the time-temperature shift factor and  $\eta$  and  $\eta_0$  are viscosities corresponding to the free volumes. As can be seen, an inverse linear dependence of the shift factor to free volumes occurs when  $B = 1$ :

$$f = f_0 + (\alpha_l - \alpha_g)(T - T_0) \quad (2.23)$$

where  $\alpha_l$  and  $\alpha_g$  are the coefficients of thermal expansion in the rubbery and glassy states, respectively. If the reference condition coincides with the material's glass transition temperature and with further algebra, the well-known Williams, Landel and Ferry (WLF) equation results. (Losi and Knauss, 1992)

Early simple composite models such as the Voigt (iso-strain, 1887) and Reuss (iso-stress, 1929) models provided estimates for composite modulus but only contained fibers and matrix, not particles as well. For many years it was assumed a composite's moduli were bounded by the Voigt and Reuss values. Improved models were later developed by Walpole in 1966. (Hill, 1952, Roscoe, 1969) Fu et al. stated these models were applicable to most particulate composites too, but the application to a composite containing all three constituents (i.e., matrix, fibers, nanoparticles) was uncertain and assumed not to be the case. (Fu et al., 2008) More recently (2012), Moreira et al. utilized three mathematical models to estimate the modulus of their epoxy-ANP composites: Einstein, Kerner and Nielsen. (Moreira et al., 2012) For example, the Einstein model for composite modulus is given as:

$$E_c^{Einstein} = E_m(1 + 2.5V_p) \quad (2.24)$$

where  $E_m$  is the matrix modulus and  $V_p$  is the particle volume fraction. This model does not account for fibers and cannot be used in this form for this research.

The simplest model providing a relatively close approximation to the real material behavior would be of great value. However, the myriad of design options with composite materials, while affording the engineer immense tailorable design space, also conversely provide a challenging modeling environment. As a case in point, the characterization and modeling of large strain composites present challenges not normally encountered with traditional composites due to their thinness, large strains, larger deformations and material nonlinearities. (Murphey et al., 2015) The tape spring structures in this work can be considered a large strain composite due to their thinness and extreme bending.

Aside from numerical modeling as discussed in depth in Chapter 4, analytical models have the advantage of rapid execution but have mostly been applied to materials with random composite microstructures of matrix and particles. Such models are often based on Eshelby's ellipsoidal inclusion problem to calculate homogenized properties of the whole material. (Levesque et al., 2007) In general, there is a need for reliable theoretical models from which generalizations about the long-term performance of a material can be made. There are a wide range of analytical models with varying degrees of accuracy: 1. Findley power law, 2. Rule of Mixtures (ROM) and inverse ROM, 3. Halpin-Tsai, 4. Schapery single integrated procedure, 5. Mori-Tanaka Method and 6. Boltzmann superposition principle are just some to name a few. (Coleman et al., 2006, Scott et al., 1995) The ROM and inverse ROM are likely the most well-known and used.

The work of Mori and Tanaka was concerned with calculating the average internal stress in the matrix of a material containing precipitates with eigen strains. Adding in Eshelby's equivalent inclusion idea dealt with many important micromechanics problems such as the calculation of effective properties of composites and the effects of cracks and void growth. (Benveniste, 1987) However, when the stress-strain relation of a given material is nonlinear, the Boltzmann Superposition principle is not applicable, therefore, a constitutive equation to describe the nonlinear behavior must be sought by other means. (Findley, 1976)

Nonlinear behavior increases the complexity of not only elastic materials but also viscoelastic materials' modeling. Prediction of the nonlinear mechanical response of polymer nanocomposites is a challenge arising from the hierarchical morphology of a nanocomposite and the use of a multi-scale modeling technique may be a good approach. Four distinct length scales are used: 1) Nanoscale, 2) Microscale, 3) Mesoscale (where the nanocomposite morphology is reconstructed using the RVE concept under assumptions of global periodicity and uniform deformation), and 4) Macroscale (where the nanocomposite stress-strain response is predicted using numerical homogenization of the RVE response). (Weidt and Figiel, 2015) The challenge lies in linking these models together to directly determine how design changes made at the nanoscale trace up to affect structural behavior. Linear behavior makes this process easier, but not substantially.

However, the analysis of viscoelastic nanocomposite materials is significantly more challenging than purely linear elastic analysis. A common simplification is to

assume in fiber-reinforced composites the viscoelastic effects are dominated by the matrix material. In viscoelastic analysis, the Boltzmann superposition principle causes the constitutive equation to be expressed as a time-dependent integral. This form requires substantially more computing time and resources and the accuracy depends on a time step. The solution to the problem loses fidelity as the time increases. Thus, approaches directly solving the time equations are not efficient or accurate for the prediction of long-term viscoelastic behavior such as creep and stress relaxation. (Nguyen, 2015) Stress-strain relations for creep and stress relaxation are primarily empirical; most equations were developed to fit experimental curves obtained under constant stress and constant temperature. The behavior of most real viscoelastic materials cannot be described very well by Maxwell or Kelvin mechanical models which only have two parameters. More complicated models with a larger number of parameters can be used to approximate more closely the behavior of real materials.

For stress analysis in viscoelastic materials, there is an associated elastic problem to which the viscoelastic problem reduces after removal of its time dependence by application of the Laplace Transform (LT) or Laplace Carson Transform (LCT). (Radok, 1956) If the solution is known for the elastic problem then solution of the viscoelastic problem can be obtained in the Laplace-Carson space by replacing the loadings by their corresponding LCTs. In order to obtain the time domain solution, the inverse LCT must be applied. The Elastic-Viscoelastic Correspondence Principle (EVCP) is the analogous systematic method for solving viscoelastic problems compared to elastic problems. The EVCP can also be used to calculate the relaxation modulus when the creep compliance is known and vice versa. (Levesque, 2007) It is evident any discussion of viscoelastic

composites must rely heavily on the corresponding analysis of elastic composites. (Hedgepeth, 1961) The use of the EVCP is, of course, dependent upon the ability to solve the associated elastic boundary value problem; if the elasticity solution is intractable, the viscoelastic solution will be even more so. (Halpin, 1969) The EVCP usually holds equally well for anisotropic heterogeneous materials as it does for isotropic materials. (Hashin, 1966)

Composite laminates made of carbon fibers and epoxy matrices in general exhibit anisotropic viscoelastic behavior. In reality, composite laminates are often composed of viscoelastic matrices filled with reinforcing elastic fibers and/or hard particles. Complex time-dependent viscoelastic behavior is typical for composite structures. Accurate prediction of this behavior is essential for confidence in their usage, especially for critical aerospace applications. As deployable space structures are routinely stowed for extended periods of time and subject to frequent, wildly varying thermal environments, realistic predictions on the loss of deployment force during stowage and the time required for a complete shape recovery on orbit are required for robust designs. Several issues are working against the aerospace engineer when designing a composite structure for a space application. Among them is an aversion to risk since the cost is so high for space applications, it must work perfectly the first time and the fact we do not yet completely understand the complex behavior of an engineered composite—especially nanocomposites. Thus, the superior properties of composites are typically severely penalized by the use of unusually large design safety margins. Also, in order to design less conservative composite structures, it is essential to account for the effects of damage/defects. This consideration is not easy since typical failure criteria are semi-

empirical phenomenological models attempting to describe experimental observations. However, to build composites with superior strength and flaw tolerance, nanoscale reinforcements have inherent natural advantages over their micro-sized counterparts because of their scarcity of structural defects and high aspect ratio. (Ma et al., 2009) Without nanoparticles, merely increasing the ply thickness of a laminate composite corresponds to an increasing amount of porosity and defects from a statistical point of view. It also makes the composite laminate harder to bend or fold compactly. But nanoparticles also inherently have an interphase, the influence of which cannot be ignored. The ideal objective in structural design is to use a material to its fullest potential and reduce wasteful conservatism in the design. The goal is to find the laminate structural configuration necessary to carry the required loads and achieve the optimal structural performance because the optimal microstructure for one physical property might not be the best microstructure of another physical property. Increasingly so, nanocomposites are seen as offering a substantial increase in composite performance which is extremely attractive to the hyper-cost and hyper-mass sensitive aerospace industry.

Despite the numerous advantages of thermosetting polymers (e.g., epoxy), they still generally have the drawbacks of brittleness, poor ductility, fracture toughness and low damping. However, they can be modified with filler materials to enhance their properties. Numerous researchers have demonstrated significant improvements in composite properties with the addition of nanofillers. (Tavakoli et al., 2013, Dudkin et al., 2007, Ash et al., 2001, 2002, Moreira et al., 2012, Yu et al., 2012, Kuo et al., 2004, Zhang and Singh, 2004, Akinyede et al., 2012, West et al., 2006, Naous et al., 2006,

Cousin and Smith, 1994, Kuo et al., 2005) Nanotechnology, broadly defined as systems with dimensions on the order of 0.1 – 100 nanometers, has immense potential to improve the performance of epoxy-based composites for space. (Wang and Liew, 2015)

Polymeric composites could prove vitally important for future space missions, in particular, for development of large deployable structures and gossamer spacecraft. Incorporation of very small weight fractions of nanoparticles (also called nanoreinforcements, nanoelements, or nanofillers) has the ability to significantly alter the bulk composite properties. The use of nanoparticles in polymer composites has already produced unprecedented improvements in the mechanical properties of composites and may be able to improve creep resistance and stress relaxation. Nanocomposite improvement levels are finally inching towards those levels predicted by theory. (Coleman et al., 2015) However, the study of nanocomposites for creep and stress recovery properties is still in its infancy and controlling nanometer-sized components offers countless possibilities for developing composites with unique, tailorable properties. For example, when embedded into a near surface layer, nanoparticles and nanostructures can form a barrier which prevents oxygen atoms from penetrating into underlying layers of a structural material, providing resistance to atomic oxygen (AO) which can be a significant concern for LEO space missions. (Novikov et al., 2009)

Classical elastic theories are still valid at the micro-scale, but this is not the case at the nanoscale where quantum mechanics govern the particle physics. The methods of quantum chemistry and molecular dynamics enable the determination of fundamental characteristics of nanostructures such as energy spectrum, electron state density, and even macroscopic bulk properties such as Young's modulus for its stiffness. (Novikov et al.,

2009) The stiffness of a composite is determined by the properties of its constituents, including the interphase. The structure and properties of this interphase region are not only different from the bulk composite, but they may be critical in dictating the overall nanocomposite mechanical properties. Not only are the properties and structure of the interphase region largely unknown, the geometry and dimensions are also not well quantified. Understanding and controlling the effects of nanoparticles on the bulk material properties of a composite to elicit desired structural behavior is not well known or researched.

Composite structures typically experience a reduction in mechanical performance due to the presence of defects from the manufacturing and fabrication processes but their structural performance is also complicated by material inhomogeneity and inherent anisotropy from multiple phases. (Zhang and Matthews, 1983, Francis and Hulse, 2015) Microstructural imperfections and nonlinearities inherent in composites also complicate their analysis and confidence in their usage. While a composite's modulus is very sensitive to defect concentration and type, radiation damage during space flight can alter the physical material by establishing crosslinks and causing strain in the material. (Coleman et al., 2006) This irradiation can also produce point defects, i.e., vacancies, interstitials, substitutions, electron displacements or material ionization. The point defects can have a pronounced effect on the mechanical properties of space composite materials. Furthermore, it has also been shown nanomaterials may be even more sensitive to ionizing radiation ubiquitous in space. (Chipara, 2005)

Polymer nanocomposites have been proven to be outstanding materials, characterized by a unique mix of physical and mechanical properties coming from the synergistic combination of constituent properties. (Salviato et al., 2013) Previous research has indicated creep and stress relaxation of CFRP composites are strongly governed by the matrix material, not the fibers. In particular, the shear modulus of a composite is usually dominated by the matrix modulus. (Murphey et al., 2010) Reinforcement fillers on the nanoscale level such as ANPs, nanosilica, nanoclay and CNTs can reduce/hinder creep and produce other desirable mechanical and electrical material properties. The interface behavior strongly affects the mechanical performance due to the large interface/volume ratio with nanocomposites. A fundamental understanding of the interface strength and de-bonding is of major importance for designing new materials. (Ben et al., 2015) The occurrence of nanoparticles in epoxy matrix can decelerate the relaxation processes underlying the creep. (Glaskova et al., 2013) Additionally, as expected, the creep strain of nanocomposites is typically lower than the neat matrix, or conversely, the creep behavior is improved with the addition of nanoparticles. (Jia et al., 2011) Also, high damping properties can be achieved in nanocomposites by taking advantage of the interfacial friction between the nanoparticles and the polymer matrix. (Ma et al., 2010) The interphase and the nanoparticle bonding may strongly affect the damping in the nanocomposite as a strong bond will have low damping and vice versa. Inherent damping of a structure is preferred for space applications to avoid excessive attendant systems utilizing power and consuming the mass budget of the spacecraft. A structure smartly designed meeting all the constraining requirements for space is needed.

Two main issues are widely recognized as being critical for development of mechanically strong and stiff nanocomposites: 1. Adequate dispersion of the nanoparticle filler within the matrix and 2. Strong interfacial bonding between the nanoparticles and matrix. (Hernandez-Perez et al., 2008) The most suitable matrices for multiscale nanocomposites for space applications seem to be thermosetting resins, notably epoxies. (Lionetto et al., 2014) However, epoxies are not ideal as-is as they are inherently brittle and have relatively high viscosity but the properties such as strength, modulus, toughness and fatigue performance can be improved by modification with nanoparticles. (Sprenger, 2014) Regarding selection of nanoreinforcements, one of the major obstacles to using CNTs, for example, is their high prohibitive cost in addition to the well-known problems of agglomeration and dispersion in a suitable matrix. The presence of agglomerations can negate the advantages of nanofillers and can initiate stress concentrations manifested as fractures and failure.

## CHAPTER 3 EXPERIMENTAL METHODS

### 3.1 Neat Epoxy Preparation

Experimental testing is essential to understanding complex composite behavior, validating models and verifying design principles. This research work was experimentally focused and used a thin composite laminate as the structural design architecture for a tape spring deployable space structure. DMA testing was conducted to determine the Prony series coefficients for characterizing the viscoelastic behavior of the composite. A Prony series is widely used for representation of viscoelastic material functions. For example, the creep compliance of a linear viscoelastic material can be expressed as:

$$D(t) = D_g + \sum_{i=1}^N D_i \left(1 - e^{-\frac{t}{\tau_i}}\right) \quad (3.1)$$

where  $t$  is time,  $D_g$  is the glassy compliance, representing the long-term behavior of the compliance,  $D_i$  is the retardation strength and  $\tau_i$  is the retardation time.

When testing viscoelastic materials, it is often desirable to accelerate the test time period via the Time-Temperature-Superposition Principle (TTSP). TTSP is applicable if the material is thermorheologically simple and it can be used to predict the creep and relaxation behavior of the composite. TTSP is often used to construct a material's master curve in conjunction with the WLF equation. (Cheng and Yang, 2005) Both the TTSP and the Prony series were used in this research work.

The composite laminate utilized for the tape spring structure in this research, called “FlexLam”, was a three ply layup consisting of a  $[+ 45^\circ / - 45^\circ$  plain weave (PW) /  $0^\circ$  unidirectional (UD) /  $+ 45^\circ / - 45^\circ$  PW] and was used for this work based on previous research by the AFRL, UNM and Pellegrino et al. (Yee and Pellegrino, 2005, Keil and Banik, 2011, Murphey et al., 2011, Murphey et al., 2013, Peterson and Murphey, 2013, Borowski et al., 2017, Garner et al., 2017) The laminate, shown in **Figure 3.1**, consisted of three plies with the following details: a middle UD ply of IM7 carbon fibers (12K per tow) impregnated with Patz Materials and Technology PMT-F7 epoxy and two outer plies of JPS AstroQuartz II Style 525 PW (99.99% pure silica filaments) also impregnated with PMT-F7 epoxy. It is a balanced, symmetric laminate. The fibers/filaments were  $9 \mu m$  in diameter with the warp and weft yarns consisting of 110 filaments each. This laminate was defined as the “control” for which 25 tape springs were fabricated and subdivided into five different test sets of five tape springs each based on the tape springs’ stowage time for structural testing: 1 hour, 1 day, 1 week, 1 month and 6 months.

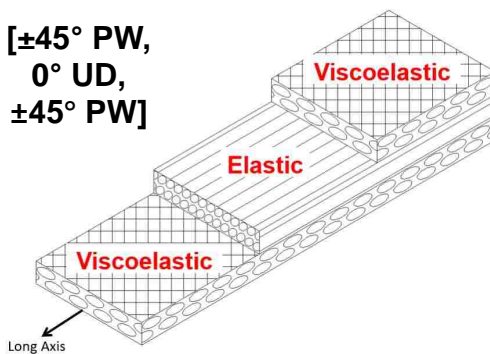


**Figure 3.1 FlexLam Composite Laminate Layup**

The experimental test strategy for this research work is graphically illustrated in **Figure 3.2**. The flowchart shows how the 25 control tape springs are first characterized and correlated with a finite element model and simulation in Abaqus, followed by repeating the same tests and process with 25 ANP-doped tape springs. All other aspects of the tape springs' design, fabrication and testing were identical between the control and ANP groups except for the addition of ANPs in the latter 25 tape springs. The number of tape springs chosen for this research work was based on practical resource constraints such as limited time and funding. As such, the results in **Chapter 5**, Results and Discussion, reflect a qualitative analysis of the hypothesis as opposed to a quantitative or statistical approach which would require many more test specimens.

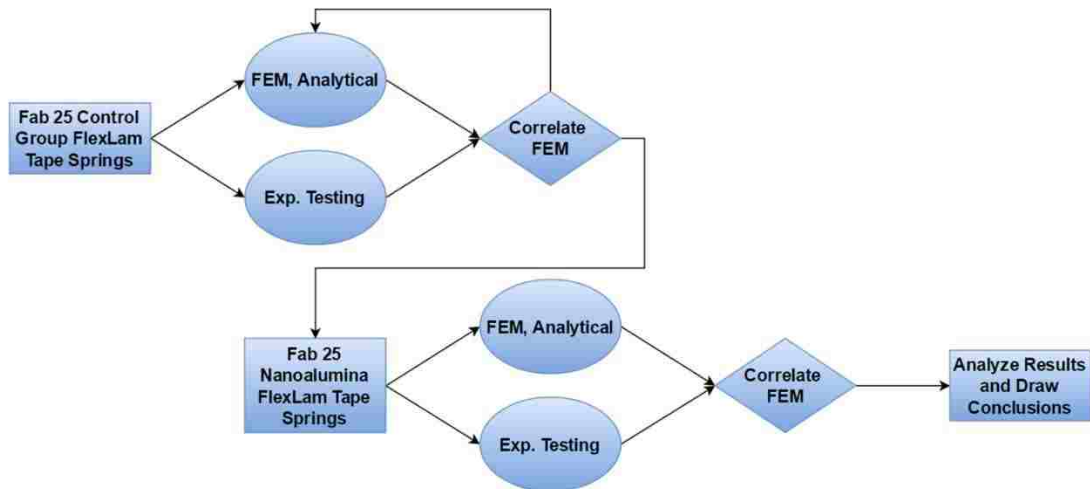


**Figure 3.2 Flowchart of Experimental Testing and Numerical Modeling Workflow**

To produce a master relaxation curve permitting accelerated experimental testing of the tape springs, DMA testing was conducted. A sample plate of neat epoxy was prepared at AFRL for the purpose of DMA testing. Patz Materials and Technologies provided the PMT-F7 resin part A and part B shown in **Figure 3.3**:



**Figure 3.3 Neat Resin Part A and Part B**

A Pyrex beaker in a bowl of vegetable oil was used to heat up the frozen part A between 160° – 180° F at which time the powdered part B was slowly added and mixed by hand until completely dispersed and then mixed via a hand drill with a spade bit per **Figure 3.4**. The epoxy was especially viscous and took considerable time and effort to ensure a thorough mixture.



**Figure 3.4 Preparation of Neat Epoxy**

The mix ratio was 100:32 for part A to part B. After mixing, the viscous epoxy was placed in a portable vacuum chamber shown in **Figure 3.5** to de-gas and remove trapped air bubbles from the vigorous mixing process.



**Figure 3.5 AFRL's De-Gassing Chamber**

Once the epoxy sample was de-gassed, after nearly an hour, it was poured onto the heated aluminum plate shown in **Figure 3.6** while on a vibration table at low power. This plate was used as a mold for the epoxy sample.



**Figure 3.6 Mold for Neat Epoxy Sample**

The plate was first cleaned with isopropyl alcohol, sprayed with a chemical release film (Loctite 700-NC Release, **Figure 3.7**) and squared off with layers of composite tape on the edges to create a “tray” or mold for the epoxy sample to cure in.



**Figure 3.7 Chemical Release Film for DMA Sample**

The neat epoxy sample was cured in AFRL's oven ramping up to 350° F, held there for two hours and then ramped back down to room temperature. A total of three samples were produced, with the first two deemed insufficient for DMA testing due to poor sample dispersion/quality and too much variation in the sample thickness, respectively. Sample #2 is shown in **Figure 3.8**. The third sample produced was deemed appropriate for cutting up into coupons for DMA testing.



**Figure 3.8 Neat Epoxy Sample #2**

### **3.2 DMA Testing of Neat Epoxy**

After a good sample for DMA testing was fabricated it was cut up into the requisite size for use in the TA Instruments Inc. Q800 DMA testing machine at the UNM (University of New Mexico) Composites Laboratory. The epoxy plate sample was first taken to the MakerHub® facility on Kirtland Air Force Base to utilize the laser cutter shown in **Figure 3.9**. Although two different power levels and various control speeds

were available, the laser cutter burned the coupons and caused notable charring on the surfaces.

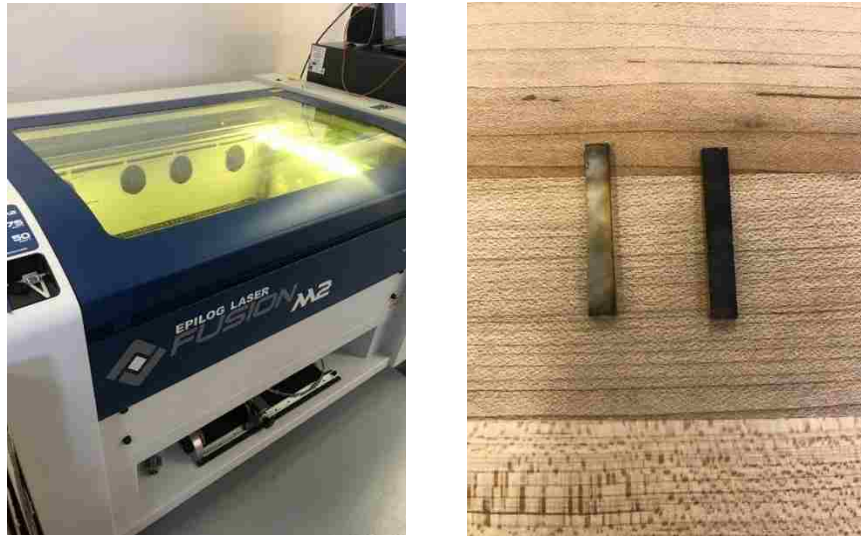


**Figure 3.9 Laser Cutter and Neat Epoxy Samples for DMA Testing**

It was uncertain if this charring would affect the mechanical properties of the samples, consequently, another solution to cut the samples was investigated. The neat epoxy sample plate was sent to Holloman Air Force Base and cut up on a water jet cutting machine as seen in **Figure 3.10**. The samples were cut to 5 mm wide x 30 mm long (they were notionally fabricated at 1 mm thick by Patz) per **Figure 3.11**.



**Figure 3.10 Waterjet Cutting Machine at Holloman Air Force Base**

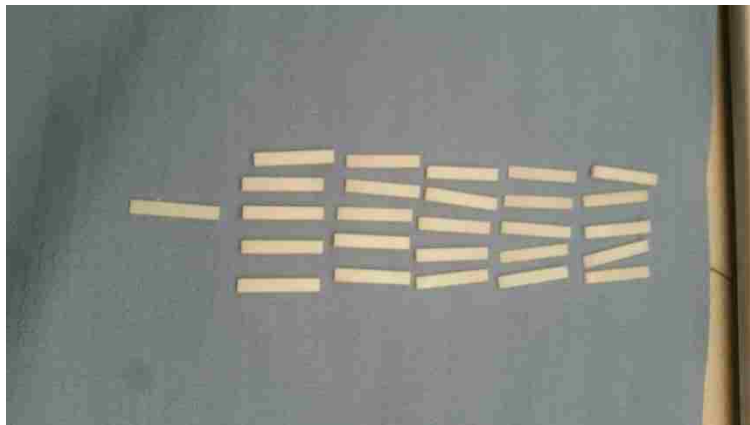


**Figure 3.11 Neat Epoxy Coupons for DMA Testing**

The neat epoxy coupons were subsequently taken to UNM to DMA test using the TA Instruments Q800 DMA machine shown in **Figure 3.12**. DMA analyzes both elastic and viscous material responses simultaneously and is useful for exploring the structure and its end use performance. The coupons were tested as a standard single cantilever clamp setup and tensile test per discussion with the Q800 manufacturer.

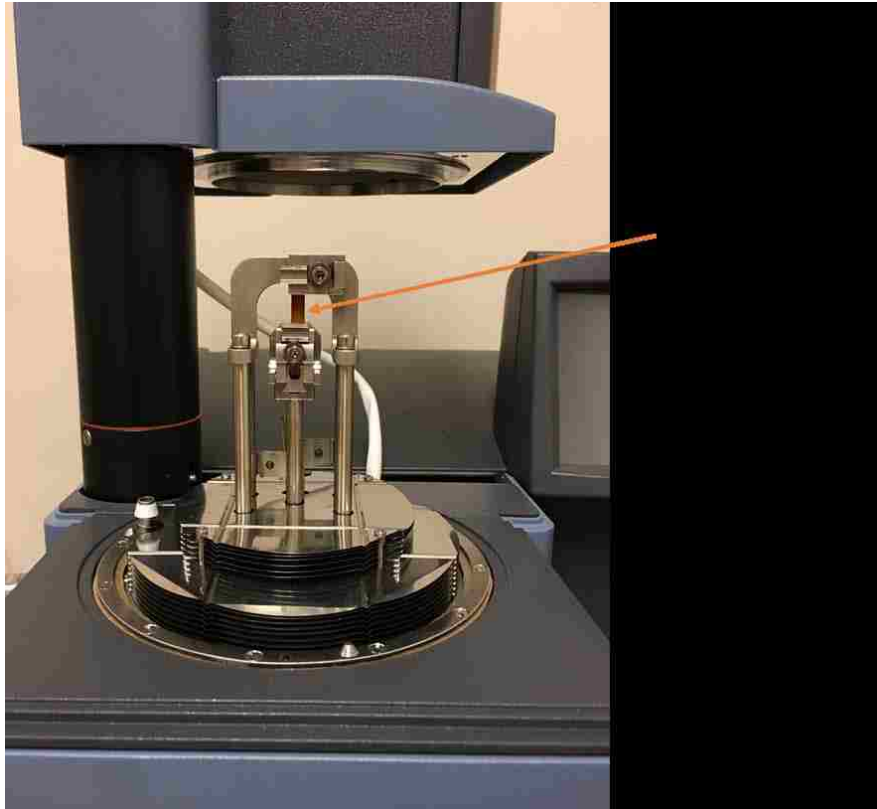


**Figure 3.12 DMA Test on Neat Epoxy Coupon**

In a DMA test three parameters are controlled in any given test: frequency of oscillation, amplitude of oscillation and test temperature. A typical DMA sweep test holds two of the three parameters constant while varying the third parameter. The first test conducted was a dynamic oscillation strain sweep at 30° C at a frequency of 1 Hz, amplitude range of 5 – 50  $\mu\text{m}$  and 10 data points each in linear mode. The results from this test revealed the strain amplitude in the linear viscoelastic region was 0.05%. With creep and stress relaxation testing it is common to test a pristine sample for each temperature, i.e., a temperature sweep test at a set frequency (usually 1 Hz). However, to do this type of DMA test to cover the desired temperature range from 30° C – 240° C would have required 22 different specimens and would have been extremely time and

resource consuming. As a viable alternative, multi-temperature frequency sweep tests from 10 to 0.1 Hz at 5 data points per logarithmic decade, 20° C temperature increments and the 0.05% strain amplitude from test #1 were conducted to acquire the necessary data for the TTSP analysis of the neat epoxy.

### **3.3 TTSP Analysis of Neat Epoxy**

Theoretical and experimental results indicate for a certain class of materials the effect due to time and temperature can be combined into a single parameter through the concept of the TTSP. (Findley et al., 1976) For FRP materials, the Time-Temperature-Equivalence (TTE) principle was experimentally verified by Schapery, Moelenpah, Kouriga and Urzhumstev. (Aniskevish et al., 2012) The determination of long term performance of FRP has often been hindered by expensive and time-consuming test experimentation necessary to obtain reliable results. Thus, much effort has been expended in the pursuit of accelerated procedures for the viscoelastic characterization of composite systems. In many cases, an increase in temperature is nearly equivalent to an increase in time or a decrease in frequency in its effect on modulus or compliance. This principle can be used to predict viscoelastic behavior in regions of time (or frequency) scale not experimentally accessible. (Ferry, 1980) TTSP, originally developed in the 1940's, has gained widespread use, is well grounded in theory and can be applied to the rheology data obtained from oscillation experiments such as DMA. (Kolarik et al., 2002)

TTSP relies on the fact elevated temperature accelerates the viscoelastic response, thus, short-term tests at higher temperatures can be used to predict long term results at room temperature. (Kolarik et al., 2002) TTSP allows an engineer to take data at one temperature and superimpose them on data taken at another temperature by a shift along the log-time axis. This principle is of great practical use in as much as obtaining data over a full range of creep compliance or stress relaxation behavior can involve years. TTSP involves the use of temperature dependent shift factors for the time or frequency scale (horizontal shift factor) on log-log plots of material properties such as storage and relaxation moduli. The data obtained at different temperatures is shifted to a reference temperature. If TTSP is obeyed, the use of shift factors will yield a master curve providing information about the viscoelastic behavior of the material over a range considerably broader than the experimental window. (Machado et al., 2016) For polymers in the viscoelastic range, time and temperature have similar effects, thus, TTSP is widely used in creep testing of polymeric composites to determine the effects of temperature on creep of CFRPs. (Goertzen, 2006) The effects of temperature on the material behavior can be treated in the same manner through the TTSP which states the modulus at temperature  $T$  and time  $t$  is the same as the modulus at a reference temperature  $T_0$  and at a reduced time  $t'$ :

$$E(t, T) = E(t', T_0) \quad (3.2)$$

$$t' = \frac{t}{a_T(T)} \quad (3.3)$$

where  $a_T(T)$  is the temperature shift factor. Based on this principle, a master curve can be constructed at any arbitrary reference temperature by shifting the relaxation moduli at

any other temperature to the reference temperature. On a log-log plot of relaxation modulus versus time, this is equivalent to a horizontal shift with a distance of  $\log a_T(T)$ .

Since the 1950's, dozens of formulas have been proposed to link the shift factors of a master curve to its reference temperature. One of the most recognized formulas was established by the collaboration of Williams, Landel and Ferry in 1955, better known as the WLF equation:

$$\log_{10} a_T(t) = \frac{-C_1(T - T_0)}{C_2 + (T - T_0)} \quad (3.4)$$

where  $C_1$  and  $C_2$  are material constants that depend on the particular polymer,  $T$  is the temperature of interest and  $T_0$  is the reference temperature. The WLF equation is used to describe the temperature effect on the relaxation behavior of many polymers with satisfactory results. The resultant smooth curve is obtained by horizontally shifting the stress relaxation curves at different temperature levels into a single, smooth curve called the master stress relaxation curve. (Findley et al., 1976) The TTSP states the modulus at temperature  $T$  and time  $t$  is the same as the modulus at a reference temperature  $T_0$  at a reduced time  $t'$ . Thus, one can relate the viscoelastic behavior at one temperature to another temperature by a shift in the time scale. The WLF equation is a consequence of TTSP which mathematically is an application of Boltzmann's superposition principle. It is TTSP, not WLF, allowing assembly of a compliance master curve spanning more time, or frequency, than afforded by the time available for the experimentation for the frequency range of the instrumentation such as a DMA. The WLF equation is an empirical equation associated with TTSP and shows the variation of modulus with temperature and frequency are remarkably similar.

The material constants can be determined via DMA testing. Hence, the DMA test data was analyzed using the manufacturer's Trios® version 4.3 software to determine the material's WLF constants,  $C_1$  and  $C_2$ . A master curve can be generated by shifting the individual isothermal curves (as observed in **Figure 3.13a** and **Figure 3.13b**) along the logarithmic frequency axis according to the TTSP.

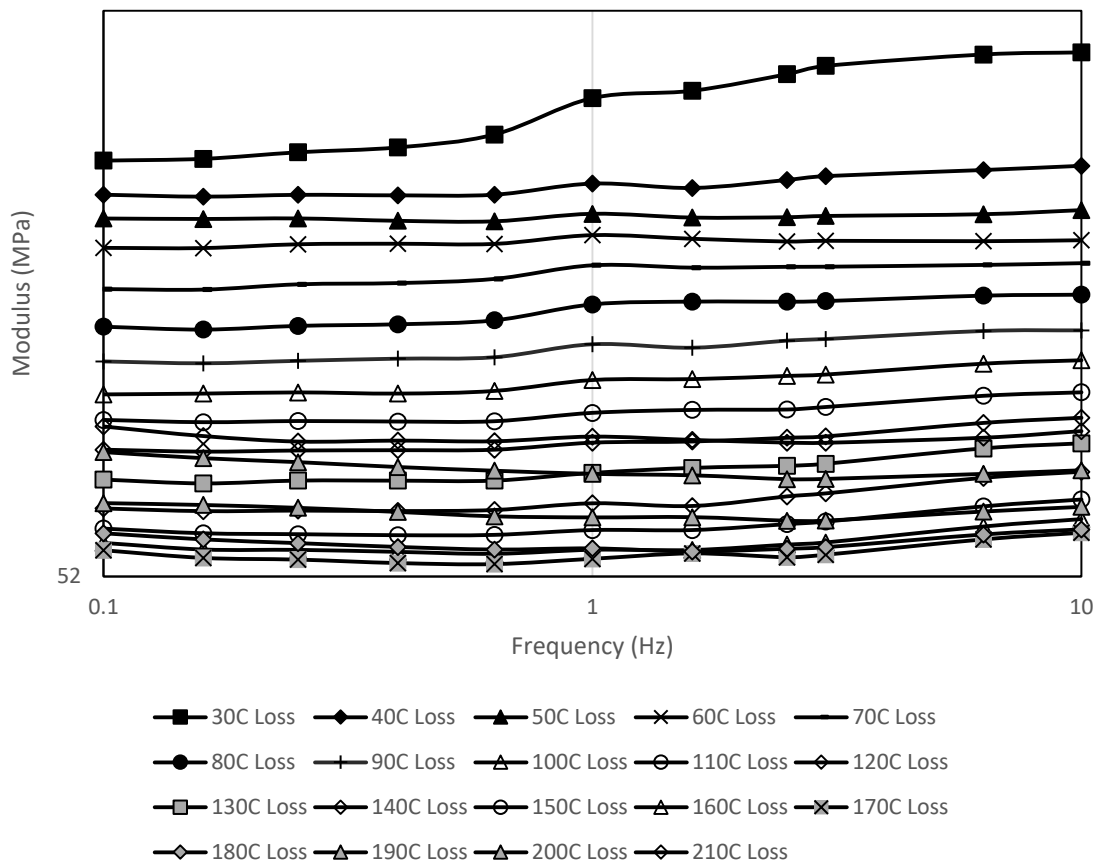


**Figure 3.13a TTSP Data for Neat Epoxy DMA Tests, Loss Modulus – Trial #1 in Log-Log Plot**

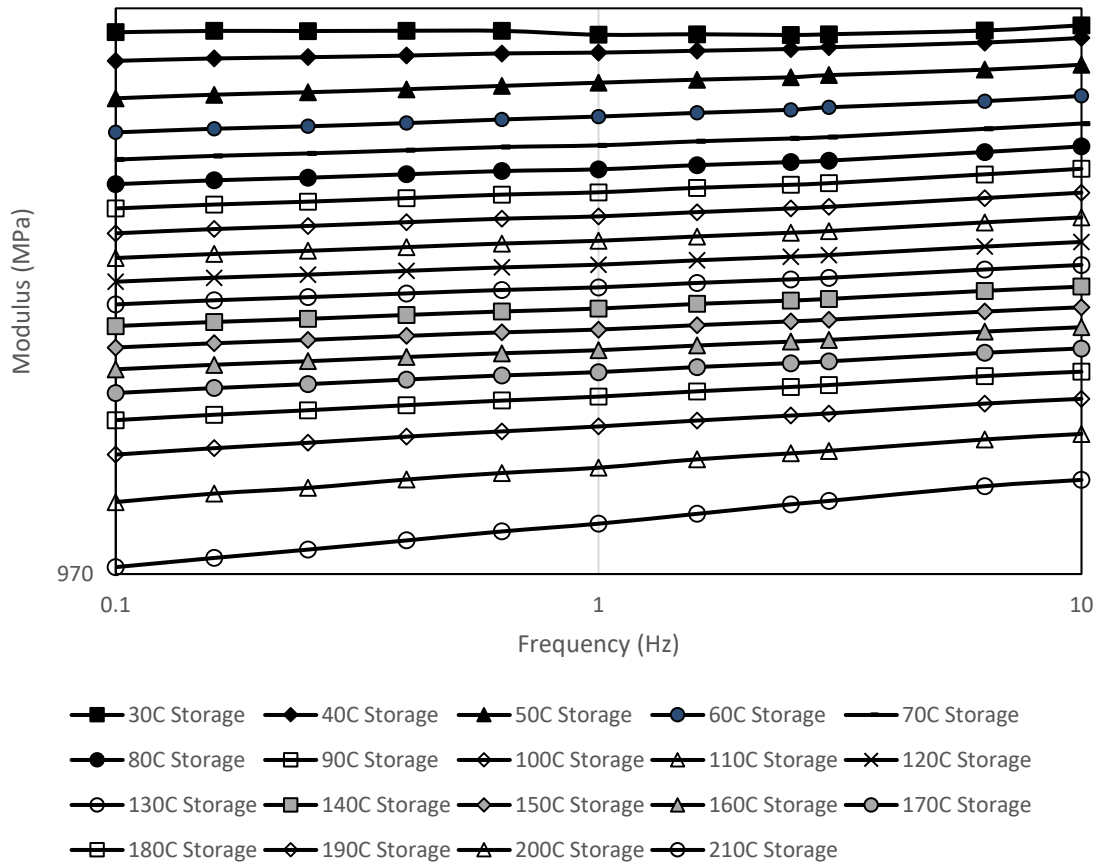


**Figure 3.13b TTSP Data for Neat Epoxy DMA Tests, Storage Modulus – Trial #1 in Log-Log Plot**

However, after shifting the isothermal data along the frequency axis, there were gaps in the data; ideally the data from each temperature isotherm would slightly overlap each other on each end resulting in a continuous, smooth master curve produced for confidence in the WLF constants. The  $C_1$  and  $C_2$  produced from this data were 62.13 and 539.3 K, respectively. Due to these gaps in the data, it was determined another set of multi-temperature frequency sweep tests should be done with all the same configuration parameters except using 10° C temperature increments instead of 20° C increments. These tests, trial #2, produced the requisite overlap in data for a good master curve. The

$C_1$  and  $C_2$  produced from DMA testing, trial #2, were 228.6 and 1820.1 K, respectively. These values were later used in the TTSP calculations to complete the tape springs' structural testing. The five tape springs stowed for 1 hour and the five tape springs stowed for 1 day were all tested in natural time. The five tape springs stowed for 1 week, five stowed for 1 month and five stowed for 6 months were artificially aged to complete the experimental testing in a reasonable amount of time, via the reduced times at elevated temperature as calculated from the TTSP analysis.

Using  $C_1 = 228.6$  and  $C_2 = 1820.1$  K from the DMA testing of the neat PMT-F7 epoxy, the WLF equation was used to calculate the time shift factor for reducing the test time for the 1-week, 1-month and 6-month stowed tape springs. Using a reference temperature of 393.2 K and a chamber temperature of 366.5 K, the shift factor was calculated from equation 3.3 to be 2527.9. Application of equation 3.2 provided the reduced testing times at 200° F as shown in **Table 3.1**:

Table 3.1 TTSP Reduced Test Times for Control Tape Springs

<b>Natural Time at ambient Temp</b>	<b>Reduced Time at 200° F</b>
<b>1 Week</b>	<b>4.0 Minutes</b>
<b>1 Month</b>	<b>15.9 Minutes</b>
<b>6 Months</b>	<b>95.7 Minutes</b>

The thermal chamber used was a Lab-Temp by Thermcraft, **Figure 3.14**, with a maximum operating temperature of 600° F.



**Figure 3.14 Lab-Temp Thermal Chamber**

The master curves, Prony series terms and the analyses are provided in **Chapter 5, Results and Discussion.**

### 3.4 Fabrication of Control Tape Springs

Twenty-five tape springs were fabricated at AFRL's composites laboratory in the FlexLam composite layup. The UD prepreg consisted of IM7/12K carbon fiber impregnated with Patz PMT-F7 epoxy and the PW prepreg consisted of JPS Astroquartz II style 525 impregnated with Patz PMT-F7 epoxy. All materials were taken from AFRL's freezer inventory to construct the tape springs. A 0.5-inch diameter mandrel was used for the layup with the 0° direction parallel to the long axis of the cylinder. Composite laminate strips 0.8-inch-wide and 1-meter long were cut and the edges sanded until the flattened width was 0.785 inches. The 1-meter tape springs were cut in half and labeled with date, type and serial numbers as seen in **Figure 3.15**.



**Figure 3.15 Control Group Tape Springs for Structural Testing**

## 3.5 Structural Testing of Control Tape Springs

### 3.5.1 Structural Test Fixture Design and Setup

The typical stowage method for tape spring structural elements is to flatten the cross section and then roll the tape spring onto a hub upon itself, much like a steel carpenter's tape measure. Several other researchers, notably Rimrott et al. and Pellegrino et al. (Rimrott, 1965, 1966, Kwok and Pellegrino, 2010, 2011, 2012, 2013, 2017, Yee et al., 2004, Yee and Pellegrino, 2003, 2005, Lyle and Horta, 2012) have done considerable research with foldable or rollable STEMs and tape springs. The viscoelastic composite tape springs were rolled onto a hub as part of the overall test fixture designed and fabricated for this research work. The test fixture frame was made from 80/20 aluminum framing and the shaft, risers, dowel (where the tape spring attaches to the load cell) and central roll hub were all made from 6061 aluminum. The ball bearing rings were ordered from McMaster and rated to a temperature of 240° F. The test fixture is shown in **Figure 3.16**.

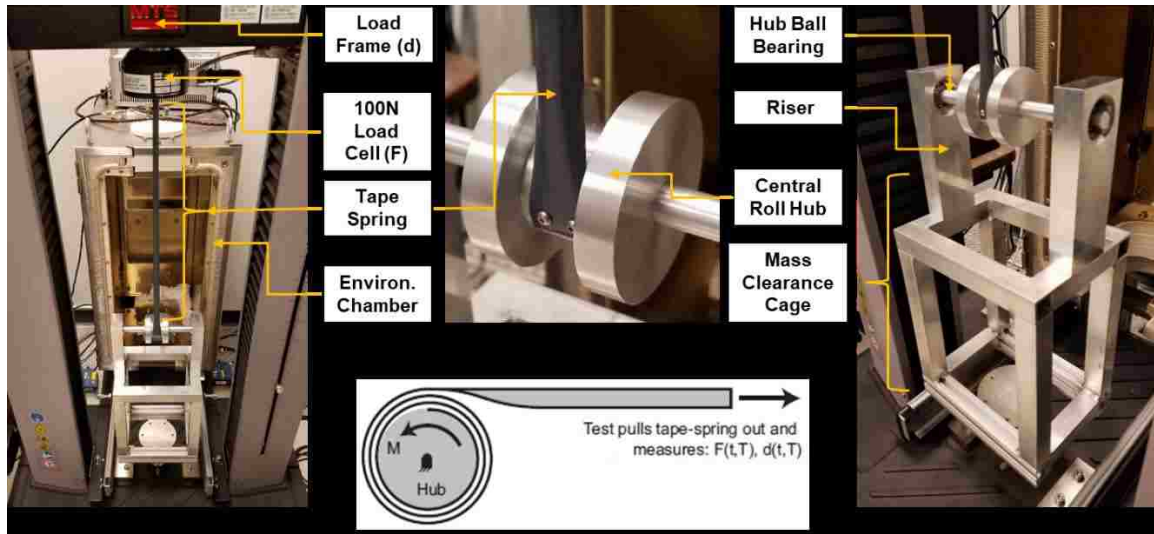


**Figure 3.16** Tape Spring Test Fixture and Initial Test Setup

The central rolling hub radius for rolling the tape spring onto during stowage was based on the laminate properties, as derived by Jeon and Murphey (Jeon and Murphey, 2011) and given as:

$$k_{xs} = \frac{1}{R} \frac{D_{12}}{D_{11}} = \frac{1}{r_{hub}} \quad (3.5)$$

where  $k_{xs}$  is the x-curvature at the secondary stable state, R is the tape spring radius shown in **Figure 3.17** and  $D_{11}$  and  $D_{12}$  are calculations from the well-known laminate *ABD* matrices. This hub roll radius, 0.75 inches, provided the minimum strain energy configuration for rolling and stowage of the tape spring.

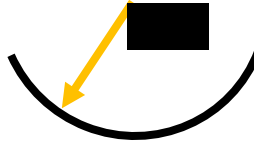


**Figure 3.17 Tape Spring Radius Definition**

The basic concept for the structural level testing of the viscoelastic composite tape springs consisted of attaching the tape spring at the root end (flattened) to the central roll hub with two countersunk 10-32 screws and attaching the tip end to the dowel in **Figure 3.18** which had a diameter matching the cross-sectional curvature of the tape spring, with a hose clamp tightened with two screws. The tape spring tip on the dowel end butted up against the dowel's larger diameter forward shaft which had a hole countersunk on the end to screw into the 100 N load cell.

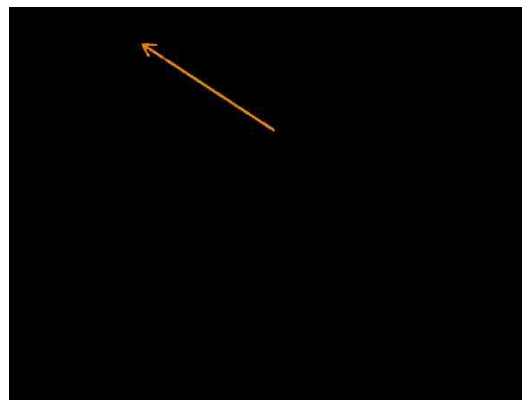


**Figure 3.18 Dowel for Securing Tape Spring Tip During Structural Testing**

A 100 N load cell was attached to the crosshead of a 10 kN MTS Instron machine. The load cell was calibrated by Load Path, LLC., prior to use in this experimental testing campaign. The key features of the test setup are shown in **Figure 3.19**.

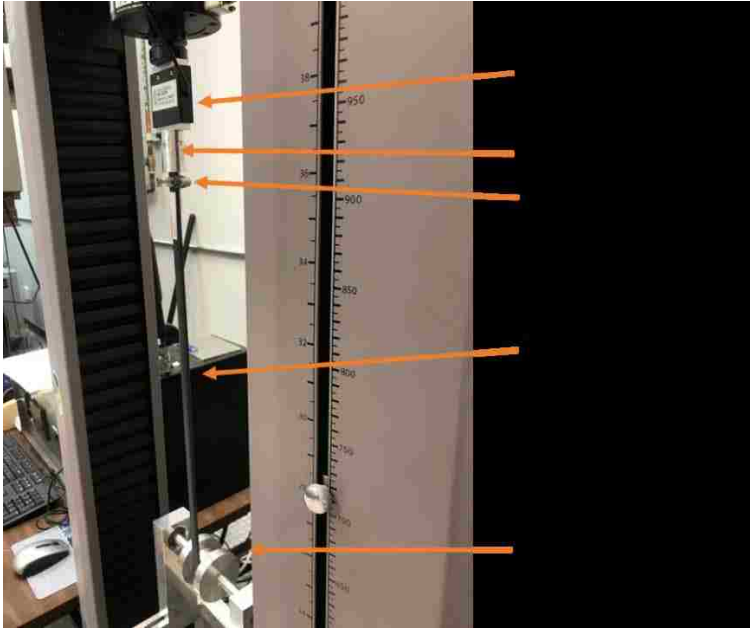


**Figure 3.19** Tape Spring Boundary Conditions in Experimental Testing

### 3.5.2 Structural Testing Procedure Steps

A test plan was written for the tape springs' structural testing; the following test steps detail how the tape springs were experimentally tested:

1. Each tape spring was measured for longitudinal length, flattened width and laminate thickness by taking the average of five measurements for each dimension of interest. These measurements are shown in Appendix A.
2. The root end of the tape spring was mounted to the central roll hub with two titanium 10-32 countersunk screws and the tip end of the tape spring was placed on the 0.5-inch diameter dowel, with the tip flush against the 1-inch diameter portion of the dowel and tightened in place with two screws via a standard hose clamp.
3. The 100 N load cell was calibrated with zero load applied through the “zero channel” option in the MTS *TestWorks 4* software.
4. A 14.36 N counter mass as shown in **Figure 3.20** was hung from the test fixture’s shaft in order to apply a torque opposite to the tape spring’s motivated deployment, therefore, the tape spring would not “bloom” in the stowed configuration. The load was manually zeroed in the TestWorks software.



**Figure 3.20 Counter Mass for Tape Springs’ Structural Testing**

5. All test configuration parameters were entered in TestWorks so the test would run autonomously. An excess tape spring was used to test the setup and configuration to ensure it performed the test as expected.
  - a. Two changes were made to the setup during initial checkout of the configuration:
    - i. The speed at which the tape spring rolled up and unrolled from the central roll hub was reduced from 16 inches per minute to 4 inches per minute. This change was to ensure smooth, quasi-static behavior.
    - ii. The test fixture's central roll hub did not initially line up at a 90° vertical angle to the MTS' machine crosshead interface. To correct this problem, the test fixture had slots machined into the top frame, per **Figure 3.21**, so the risers could float to the exact location for a completely vertical tape spring in the test configuration.

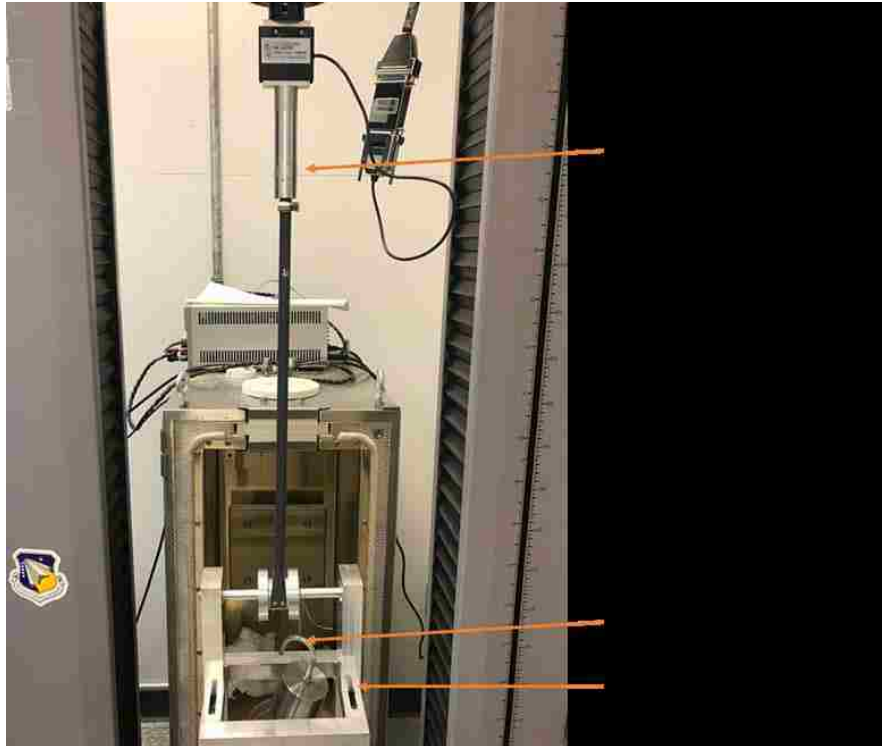


**Figure 3.21 Structural Test Setup with Dowel Extension and Riser Slots**

6. The MTS Instron machine's crosshead was tared and the tape spring took 4 minutes to roll up onto the central roll hub, remained stowed for the prescribed amount of time and took 4 minutes to unroll/deploy. The MTS Instron machine recorded time and load at the tape spring tip with the 100 N load cell.
  - a. Stowage times varied as follows:
    - i. 5 tape springs at 1 hour at room temperature
    - ii. 5 tape springs at 1 day at room temperature
    - iii. 5 tape springs at 1 week (4.0 min at 200° F)
    - iv. 5 tape springs at 1 month (15.9 min at 200° F)
    - v. 5 tape springs at 6 months (95.7 min at 200° F)

- b. Per section 3.3, the 15 tape springs targeted for stowage times between 1 week and 6 months were tested at elevated temperature to reduce the required stowage testing time per TTSP.

Figure 3.22 shows the loading profile and kinetics during the structural test process.

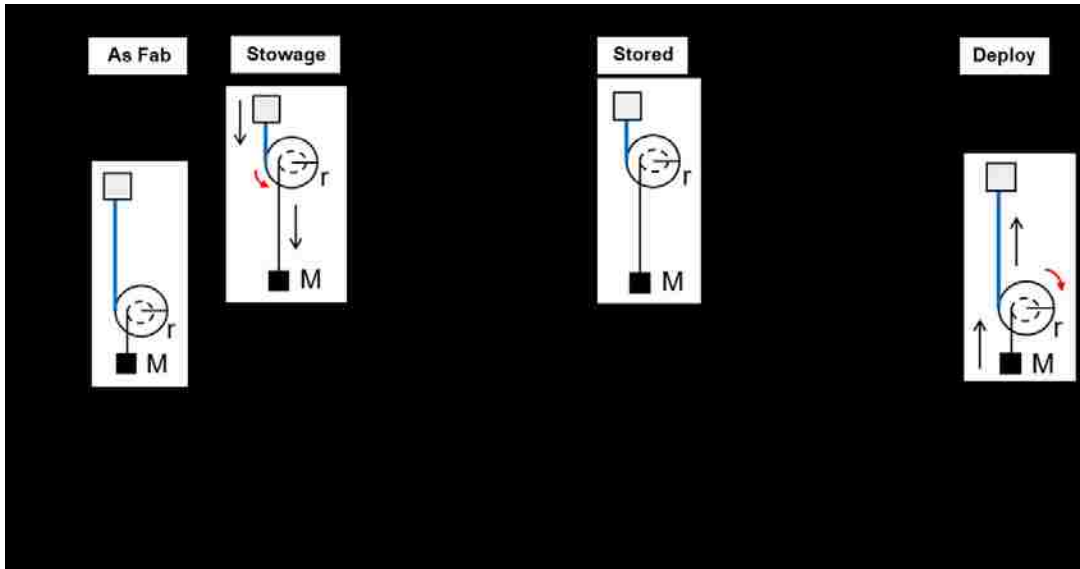
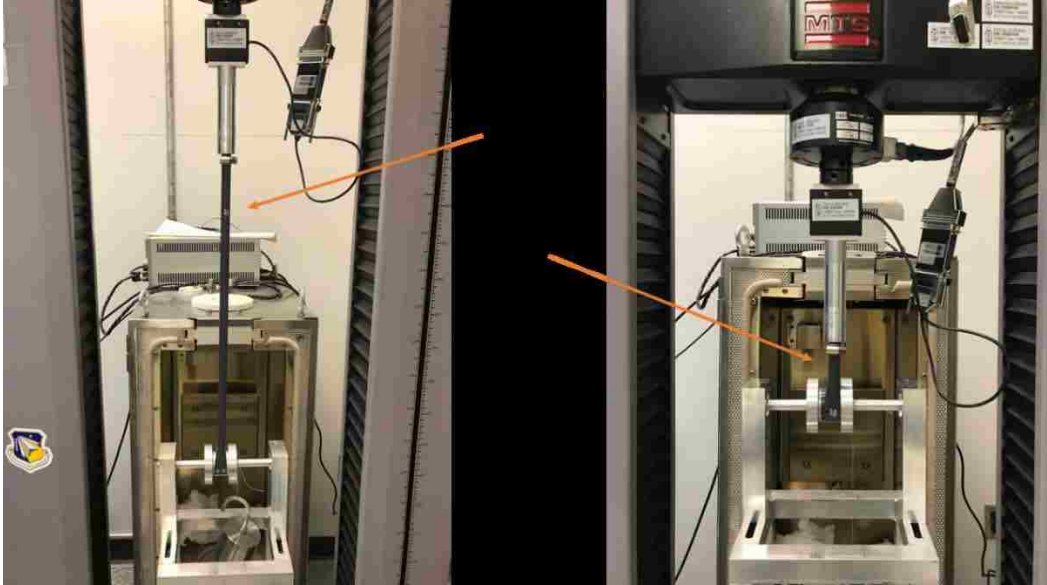
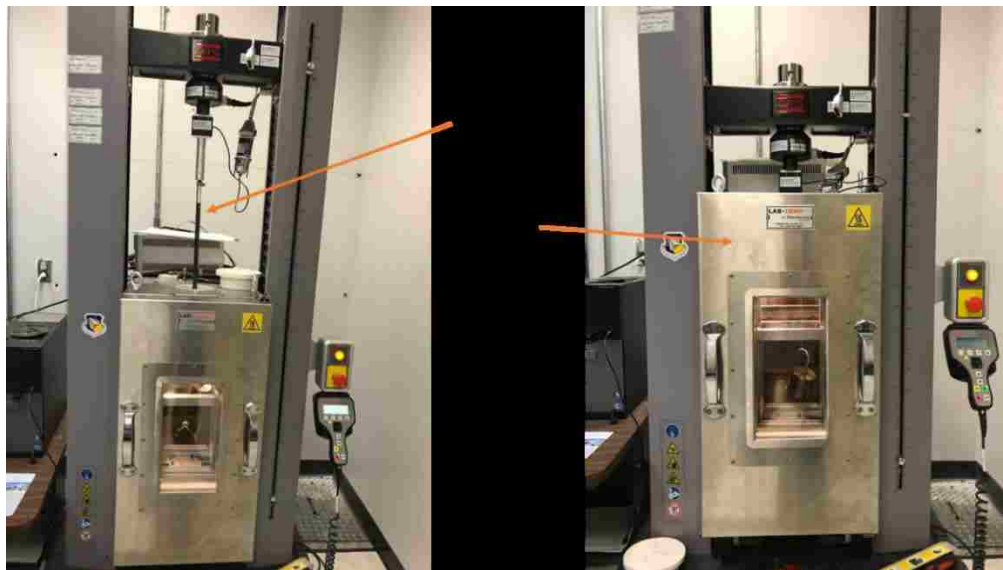


Figure 3.22 Tape Spring Structural Testing Load Profile

Figure 3.23 shows the first two sets of tape springs as they were being tested; Figure 3.24 shows the test setup for the last three sets of tape springs utilizing a thermal chamber. Figure 3.25 shows all 26 control tape springs after structural testing.



**Figure 3.23 Structural Test Configuration for One Hour and One Day Tape Springs**



**Figure 3.24 Structural Test Configuration for One Week, One Month and Six Month Tape Springs**



**Figure 3.25 Full Test Setup and 26 Control Tape Springs Post Structural Testing**

The TTSP-tested tape springs, i.e., 1 week, 1 month, 6 months, were heated while stowed but deployed out through the top of the thermal chamber. This technique was not seen as substantially impacting the results as previous research by Brinkmeyer et al. has shown there is no significant difference for deploying the structure at room temperature versus the elevated stowage temperature. The reason is the deployment time scale is substantially shorter than the relaxation time frame. Thus, viscoelastic effects during deployment can be neglected since it has very little to no effect on the deployment behavior. (Brinkmeyer et al., 2013).

### 3.5.3 Torque Calculations

It is of interest to determine the loss in torque (i.e., deployment authority) for the tape springs as they underwent progressively longer stowage periods of time. It is also of interest to evaluate how the addition of 2 weight % ANPs in the ANP tape springs altered this deployment profile. The test setup and test fixture were deliberately designed to make as many test parameters as possible consistent and/or automated without human interference. The geometry of the test setup and the automated nature of the MTS Instron machine and its associated TestWorks program permitted only minimal chance to introduce human error in the experimental test process. Based on the test setup, the following relation can be used to determine the loss in the tape springs' deployment torque due to the viscoelastic behavior of their composite structure:

$$\mathbf{T}_{t\text{ape spring}} = \mathbf{F}_{l\text{oad cell}}\mathbf{r}_{h\text{ub}} - (\mathbf{M}_{c\text{ounter mass}}\mathbf{g})\mathbf{r}_{s\text{haft}} \quad (3.7)$$

with:

$\mathbf{F}_{l\text{oad cell}} \rightarrow$  measured in experimental test campaign

$$\mathbf{r}_{h\text{ub}} = 0.75 \text{ in.} \times 25.4 \text{ mm/in.} = 19.05 \text{ mm}$$

$$\mathbf{M}_{c\text{ounter mass}} = 1,463.5 \text{ g} = 1.4635 \text{ kg} \times 9.81 \text{ m/s}^2 = 14.36 \text{ N}$$

$$\mathbf{r}_{s\text{haft}} = 0.25 \text{ in.} \times 25.4 \text{ mm/in.} = 6.35 \text{ mm}$$

The results and summary of the tape springs' structural testing are presented in **Chapter 5, Results and Discussion**.

### **3.6 ANP Epoxy Preparation**

A second group of 25 tape springs were fabricated from an altered FlexLam laminate with the addition of ANPs at 2% by weight to the two PW plies. Since commercially available nanoparticles are usually provided in an agglomerated state, measures must be taken to de-agglomerate and disperse them. The addition of nanoparticle agglomerations into a polymer using conventional processing techniques is insufficient to provide adequate de-agglomeration and a good homogeneous dispersion within the polymer. Patz stated adding the 2% weight of ANPs would not appreciably affect the A:B mixing ratio for the PMT-F7 resin parts, thus, the same mix ratio was used for both the control and ANP tape springs.

Adherent Technologies Inc. received the uncatalyzed PMT-F7 resin from Patz and dispersed the ANPs into the resin. Adherent initially mixed the ANPs with the liquid solvent MEK (Methyl Ethyl Ketone). MEK is a highly efficient and versatile solvent for surface coatings and, per Adherent, was used to provide a shell/encapsulation around the ANPs to match their surface energy and aid in de-agglomeration and dispersion. After mixing them with MEK, the ANPs were dried at room temperature overnight and then at 180° C for 1 hour. After they were thoroughly dry, the ANPs were slowly added to the

uncatalyzed PMT-F7 resin via mechanical stirring and mixing with a spade bit in a handheld drill.

Patz received the ANP-doped PMT-F7 resin part A from Adherent to produce a resin film with the JPS AstroQuartz PW silica fibers and a resin plate, 12 inches x 12 inches, to be cut up into coupons for DMA testing, per **Figure 3.26**.



**Figure 3.26 ANP DMA Coupons**

These test coupons provided the TTSP data for accelerated testing of the ANP tape springs. The resin film, at 44% fiber volume fraction and 2 weight % ANPs, provided the AFRL composites lab the necessary PW ply material to layup the ANP tape springs.

### 3.7 DMA Testing of ANP Epoxy

The first DMA test of the ANP-doped epoxy was a dynamic oscillation strain sweep at 30° C at a frequency of 1 Hz, amplitude range of 5 – 50  $\mu\text{m}$  and 10 data points each in linear mode as shown in **Figure 3.27**. The results from this test revealed the strain amplitude in the linear viscoelastic region was 0.07%. This strain amplitude was used in the remaining multi-temperature frequency sweep tests from 10 to 0.1 Hz at 5 data points per logarithmic decade, 10° C temperature increments with the 0.07% strain amplitude from the first test.



**Figure 3.27 DMA Testing of ANP Coupons**

### 3.8 TTSP Analysis of ANP Epoxy

TTSP was also used for the ANP epoxy to determine the time shift factor to artificially age the 1 week, 1 month and 6 month tape springs. The  $C_1$  and  $C_2$  produced from DMA testing of the ANP coupons, were  $6.08e16$  and  $5.0e17$  K, respectively. These values were later used in the TTSP calculations to complete the tape springs' structural testing. The five tape springs stowed for 1 hour and the five tape springs stowed for 1 day were all tested in natural time. The five tape springs stowed for 1 week, five stowed for 1 month and five stowed for 6 months were artificially aged to complete the experimental testing in a reasonable amount of time, via the reduced times as calculated from the TTSP analysis.

Using  $C_1 = 6.08e16$  and  $C_2 = 5.0e17$  K from the DMA testing of the ANP PMT-F7 epoxy, the WLF equation was used to calculate the time shift factor for reducing the test time for the 1 week, 1 month and 6 month stowed tape springs. With a chosen reference temperature of 393.2 K and a chamber temperature of 366.5 K, the shift factor was calculated from equation 3.4 to be 1742.3. Application of equation 3.3 provided the reduced testing times at 200° F as shown in **Table 3.2**:

Table 3.2 TTSP Reduced Test Times for ANP Tape Springs

Natural Time at ambient Temp	Shifted Time at 200° F
1 Week	5.8 Minutes
1 Month	23.1 Minutes
6 Months	138.9 Minutes

The same thermal chamber shown in **Figure 3.15** used for heating the control tape springs was also used for heating the ANP tape springs for their time-shifted stowage times in **Table 3.2**. Master curves, Prony series and analysis are provided in **Chapter 5, Results and Discussion**.

### 3.9 Fabrication of ANP Tape Springs

The ANP tape springs were fabricated in the same way as the control tape springs. The two PW plies and UD ply were laid up via hand on a 0.5-inch mandrel. The PW prepreg and UD prepreg are shown in **Figure 3.28**.

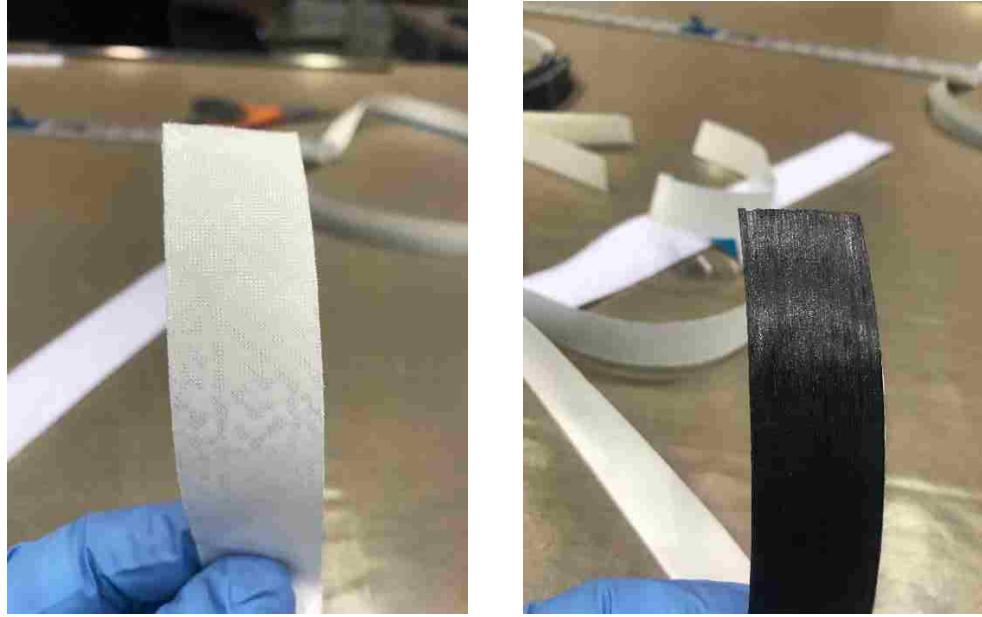


**Figure 3.28 PW Prepreg and UD Prepreg**

A Teflon-coated release film and bleeder fabric, shown in **Figure 3.29**, were placed on top of the layup to facilitate removal from the mandrel and to soak up excess resin during the curing process.



**Figure 3.29 Vacuum Bagging Process for Fabrication of Tape Springs**

A vacuum bagging process was used to clamp the tape springs with vacuum pressure at -24.5 mm Hg (at Albuquerque's altitude of ~ 5,000 feet elevation). The tape springs were cured in an autoclave for 1 hour at 220° F and then 2 hours at 350° F. After removal from the autoclave, the tape springs were cut to 20 inches in length, trimmed to a flattened width of 0.785 inches and individually labeled as shown in **Figure 3.30**.

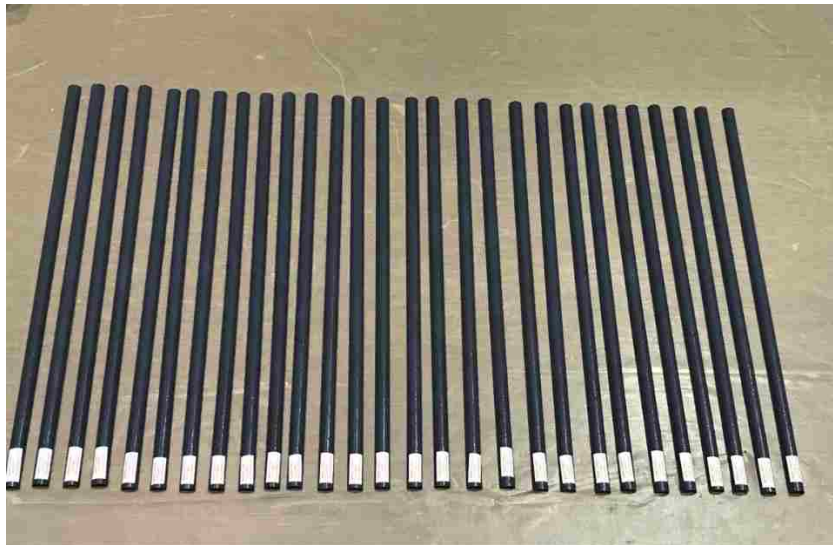


**Figure 3.30 ANP Tape Springs After Fabrication Complete**

### **3.10 Structural Testing of ANP Tape Springs**

The same test procedures and test setup used for the control tape springs in section 3.5.2 were used for the ANP tape springs as shown in **Figure 3.31**.



**Figure 3.31 ANP Tape Spring Structural Testing One Hour and One Day**

During the 6 month tests, for test specimen 3, the Tuf Line ® string (**Figure 3.32**) holding the counter-mass failed at approximately 7,700 seconds, as shown in **Figure 3.33**. This string was used for all the control tape spring tests and most of the ANP tape spring tests, lasting a total of 48 successful tests. However, since 89% of the stowage time had completed during this test, it was not re-accomplished. Additionally, it was discovered the test data from the 1 month test specimens was saved over the 1 week test specimens data so these five tests had to be repeated. Three extra tape springs were originally fabricated so those were used along with re-testing of specimens 1 and 2 which had already been tested as one hour specimens.

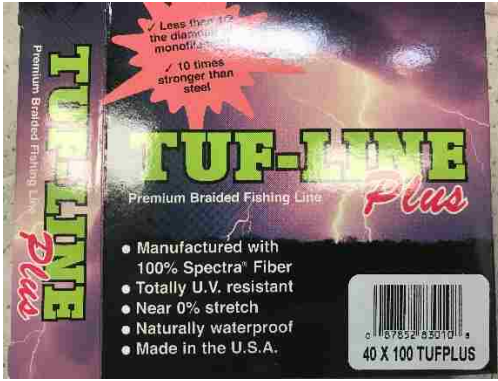


**Figure 3.32 Tuf-Line for Structural Testing**

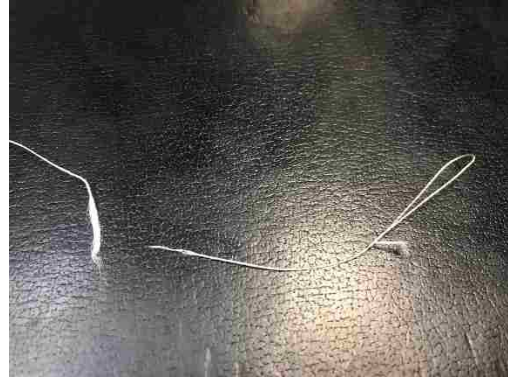


**Figure 3.33 Failed Tuf-Line**

### **3.11 SEM and EDS of Control and ANP Tape Springs**

The JEOL-JSM-IT100 Scanning Electron Microscope (SEM) equipped with Energy Dispersive X-ray Spectroscopy (EDS) at the UNM-Sandia National Laboratories Center for High Technology Materials (CHTM) was used to examine and analyze the effectiveness of the ANP dispersion in the PW plies of the ANP tape springs. The SEM setup is shown in **Figure 3.34**.



**Figure 3.34 JEOL-JSM-IT100 SEM/EDS for ANP Dispersion Examination**

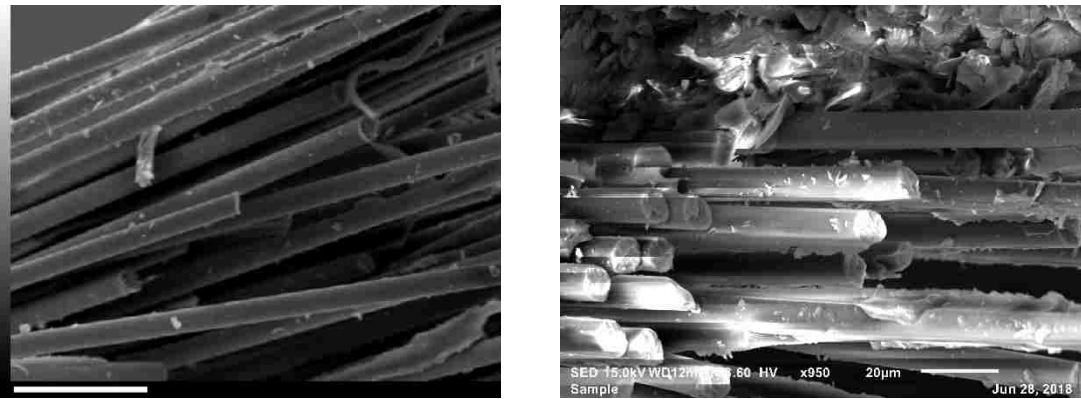
A control tape spring and three ANP tape springs were examined by first dipping the tape springs' tip ends into liquid Argon and then breaking off a small coupon suitable for the SEM. The coupons were first coated with a thin layer (150 – 200 Angstroms) of gold with the Polaron SEM Coating System machine in **Figure 3.35** to increase their conductivity in the SEM during examination.



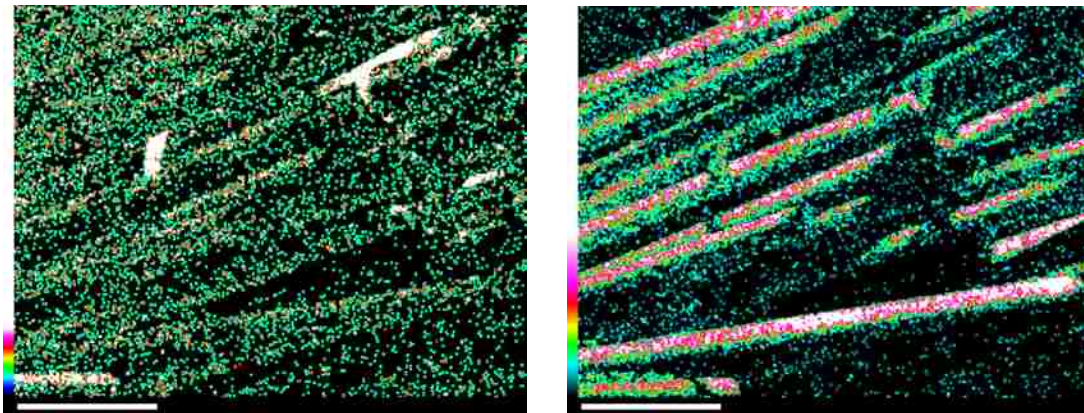
**Figure 3.35 SEM Coating Machine**

**Figure 3.36 SEM Coupon**

The fracture surfaces (e.g., **Figure 3.36**) of the tape springs were examined with the SEM and analyzed for elemental composition with EDS. SEM and EDS examination of a control tape spring were first done for comparison with three different ANP tape springs. **Figure 3.37** shows a SEM image from control tape spring NS-1H-3 (1 hour stow). **Figure 3.38** shows the EDS analysis of the control tape spring and various elements present, also displayed in **Table 3.3**.



**Figure 3.37 SEM Image of Control Tape Spring**



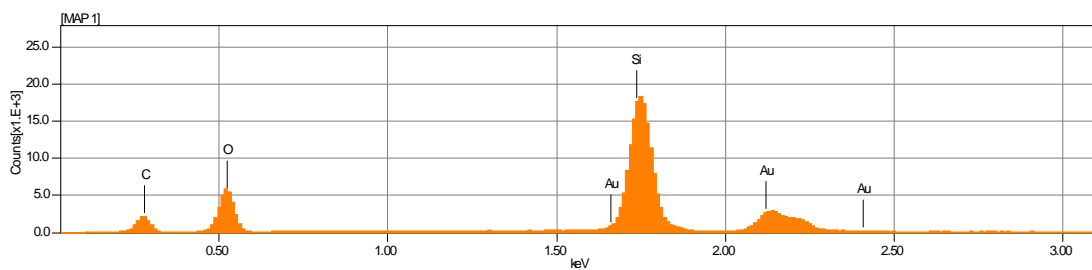
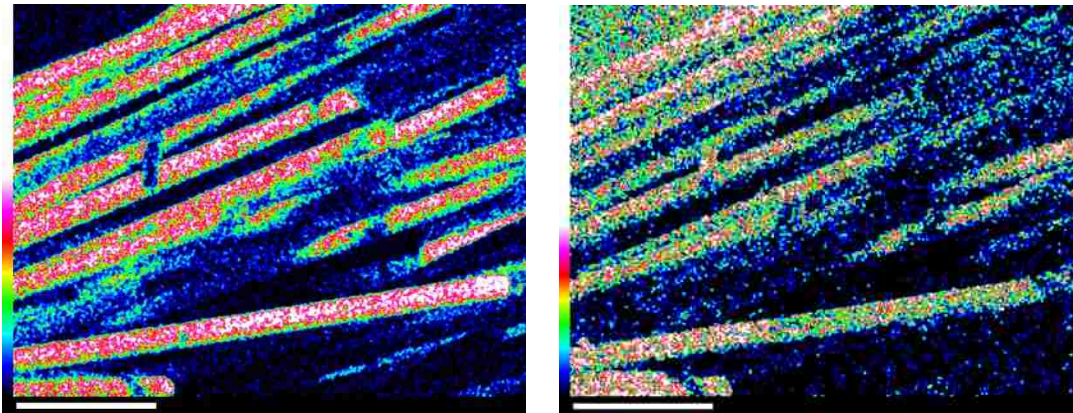


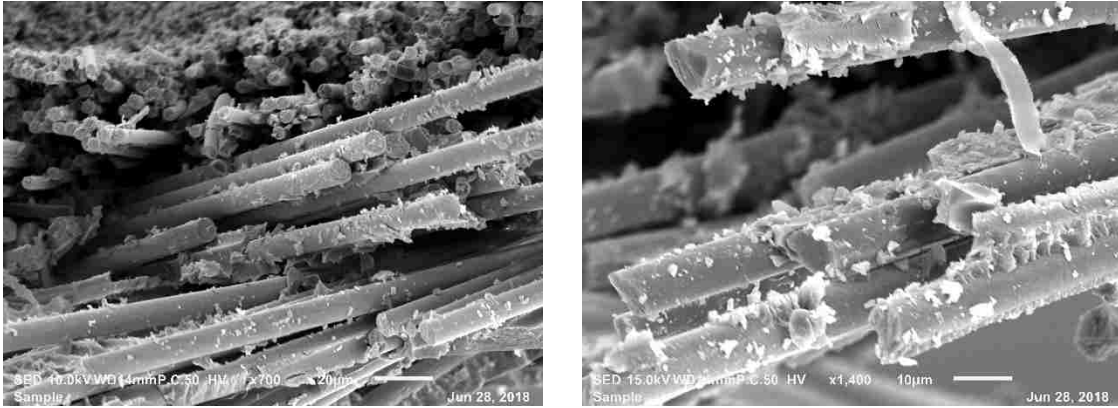
**Figure 3.38 SEM/EDS Analysis of Control Tape Spring**

**Table 3.3 Control Tape Springs' Elemental Composition**

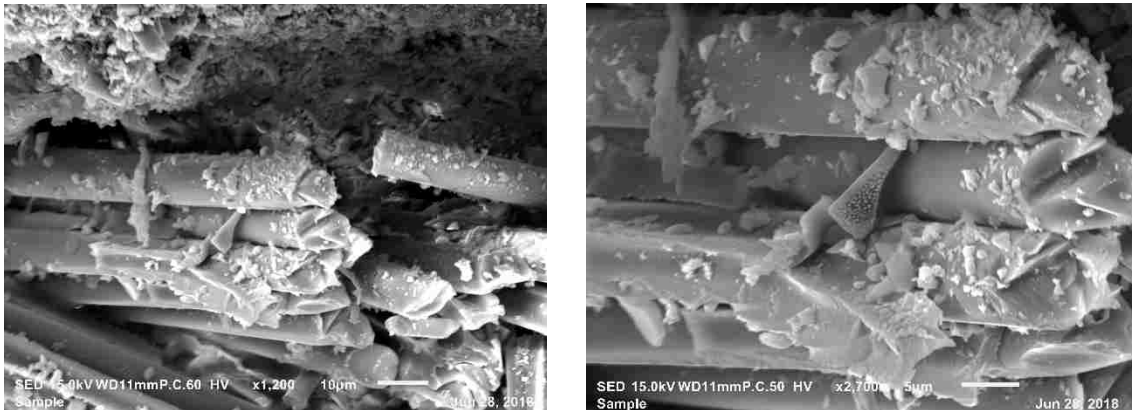
Element	Mass %	Atom %
C	26.64	40.89
O	31.33	39.03
Si	25.70	18.23
Au	18.32	1.85
Total	100.00	100.00

Similarly, three ANP tape springs were examined with the SEM/EDS. The three tape springs chosen for examination were: one structurally tested for 1 hour (specimen NA-1H-3), one tested for 1 month (specimen NA-1M-2) and one tested for 6 months

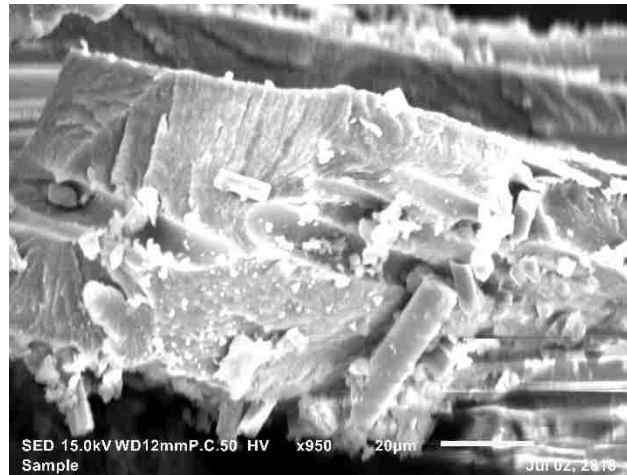
(specimen NA-6M-1). Specimens NA-1M-2 and NA-6M-1 were structurally tested in accordance with TTSP per sections 3.8 – 3.10. The SEM images of the ANP tape springs are shown in **Figures 3.39 – 3.41** below:



**Figure 3.39 SEM Images of ANP Tape Spring NA-1H-3**

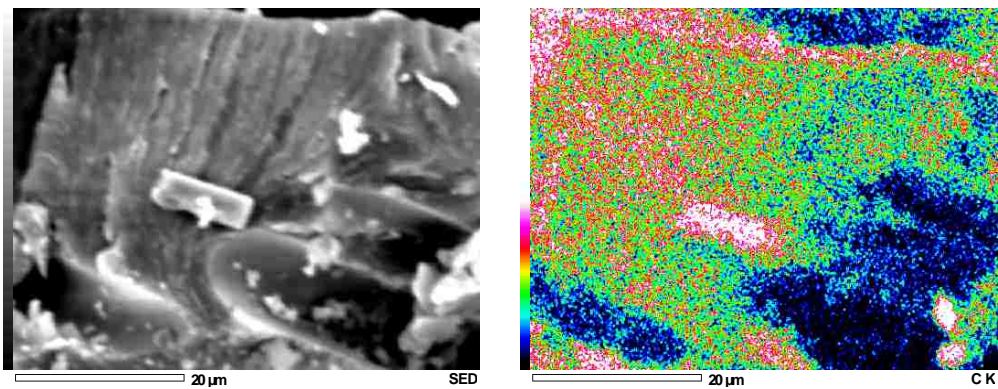


**Figure 3.40 SEM Images of ANP Tape Spring NA-1M-2**



**Figure 3.41 SEM Image of ANP Tape Spring NA 6M-1**

An EDS evaluation was performed on the ANP tape spring, NA-6M-1 with the elemental composition and results are shown in **Figure 3.42** and **Table 3.4**:



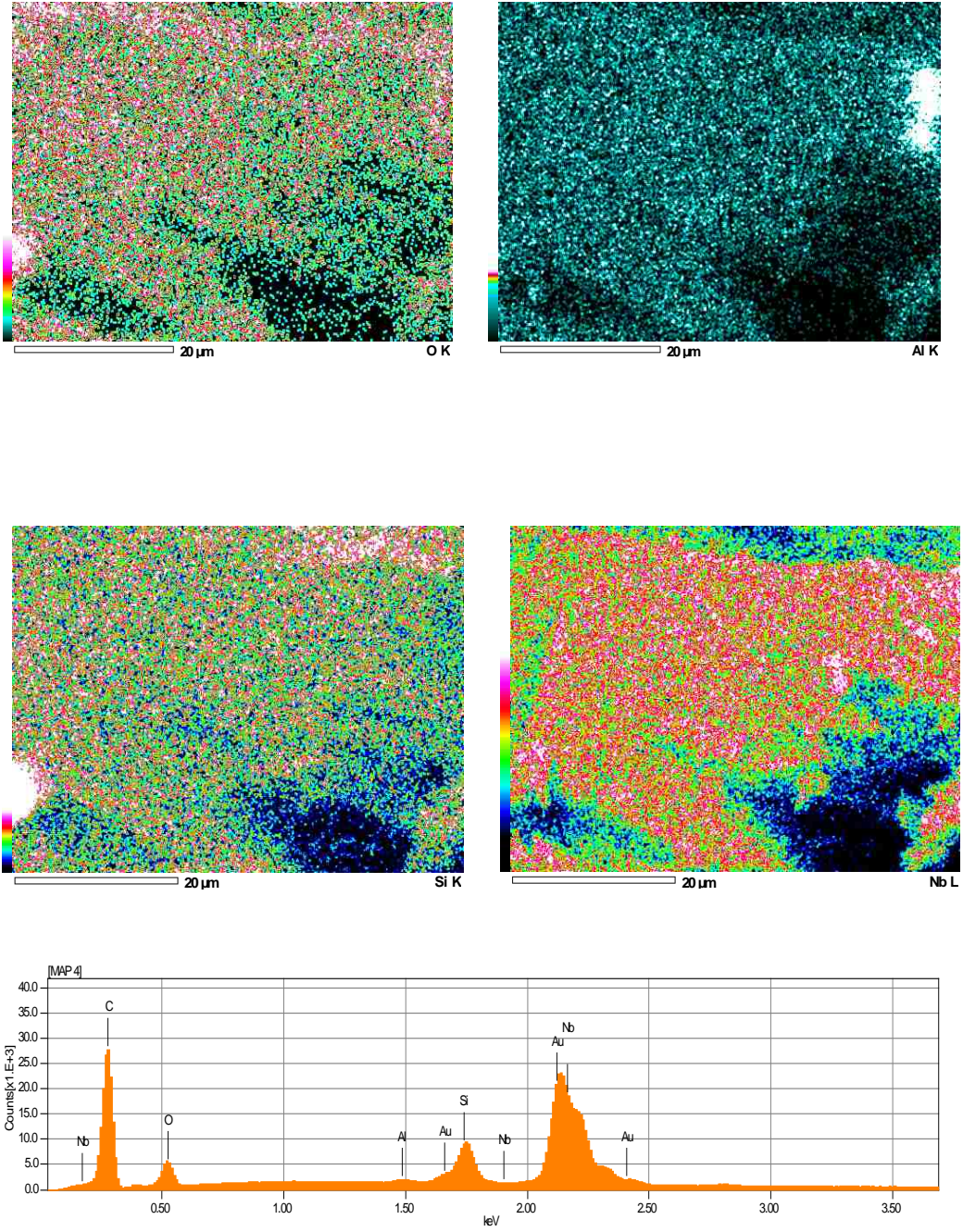


**Figure 3.42 SEM/EDS Analysis of ANP Tape Spring**

Table 3.4 ANP Tape Springs' Elemental Composition

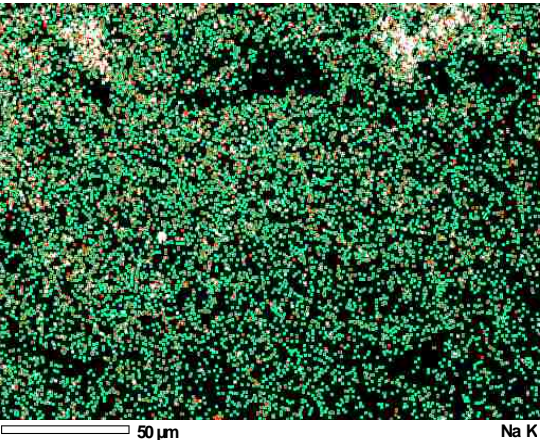
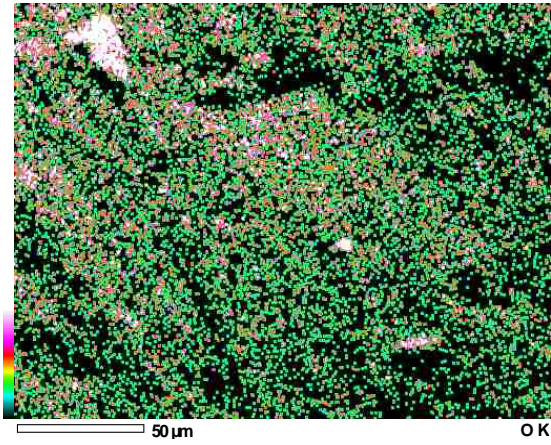
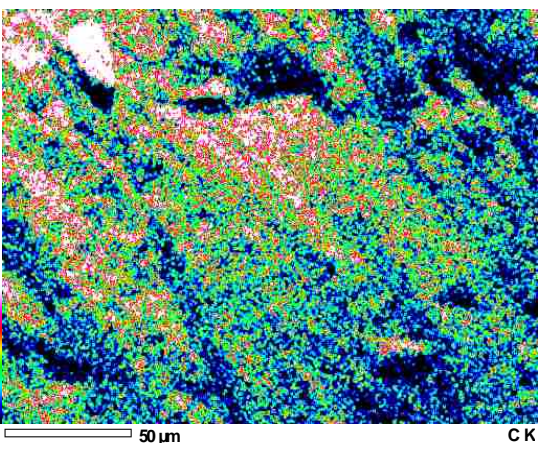
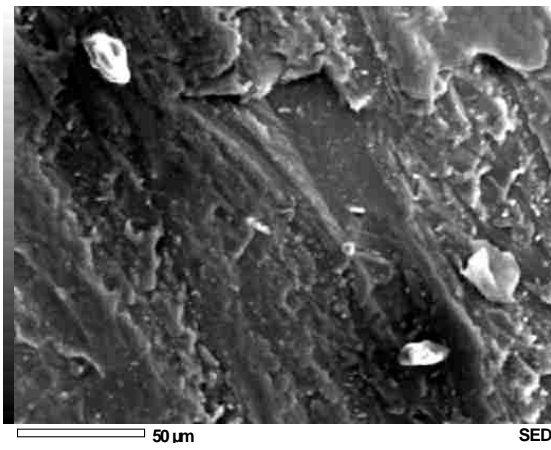
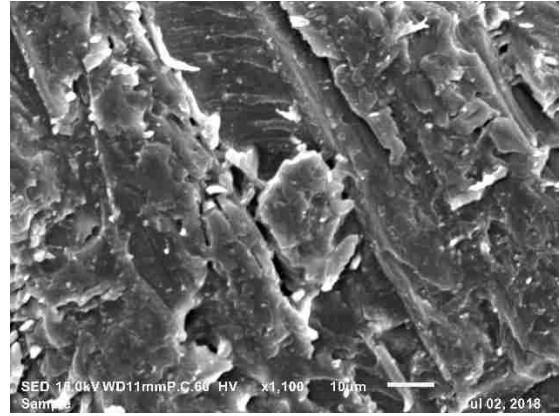
Element	Mass %	Atom %
C	44.88	77.63
O	11.34	14.72
Al	0.16	0.12
Si	3.07	2.27
Nb	8.23	1.84
Au	32.32	3.42
Total	100.00	100.00

The amount of aluminum (as part of  $\text{Al}_2\text{O}_3$ ) was observed as rather low per **Figure 3.42** and **Table 3.4**. To investigate this matter further, a DMA coupon of ANP-doped epoxy was also sputtered in gold (**Figure 3.43**) and examined with SEM and EDS.



**Figure 3.43 Gold-Sputtered ANP Epoxy Coupon**

SEM and EDS of the ANP-doped epoxy specimen were conducted as shown in **Figure 3.44** below:



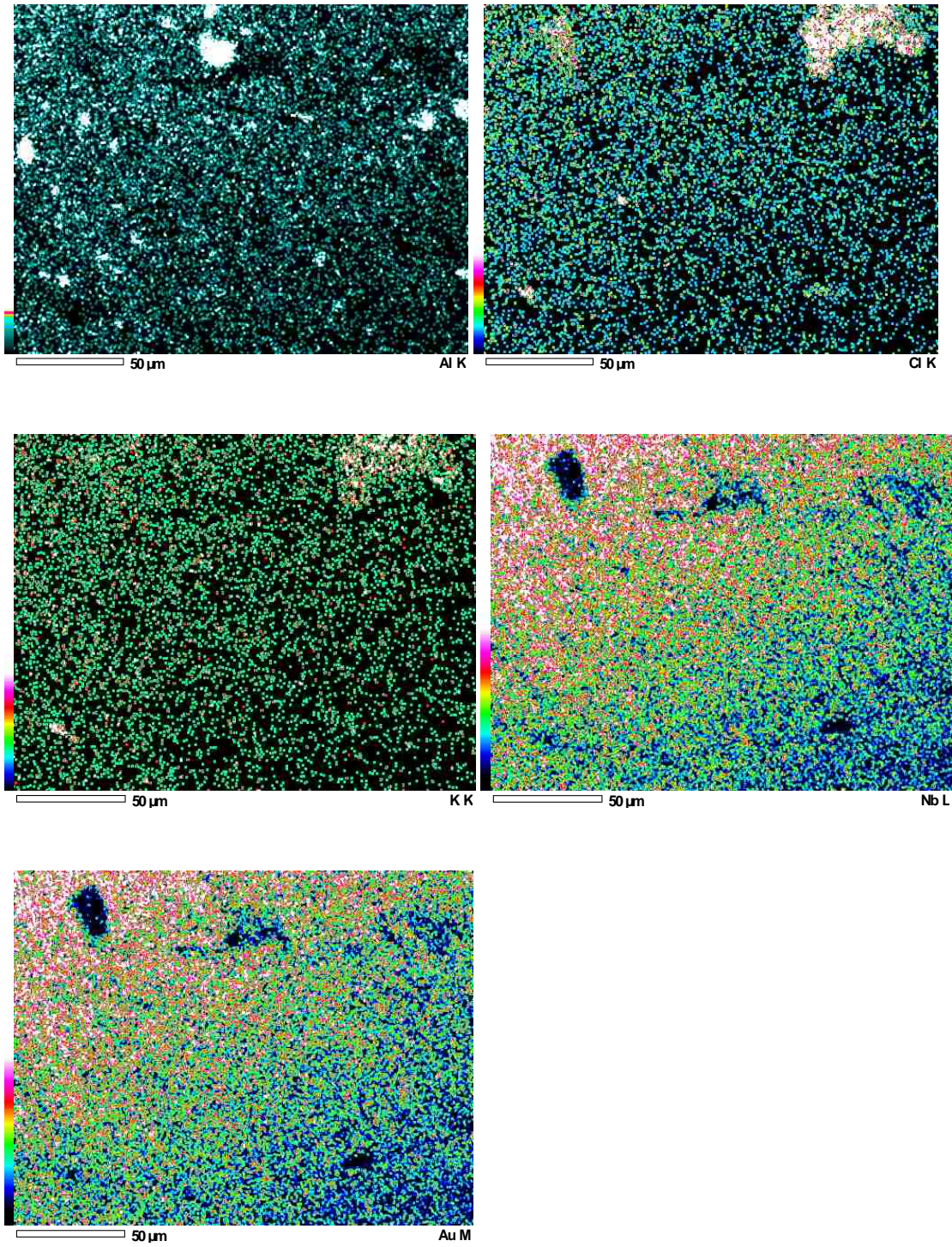


**Figure 3.44 SEM/EDS of ANP Epoxy**

The white spots and clumps in the aluminum SEM image of **Figure 3.44** warranted considerable interest and were examined further with the EDS by first analyzing a small boxed area around the large uppermost white agglomeration, i.e., orange box 004 in the image of **Figure 3.45**:

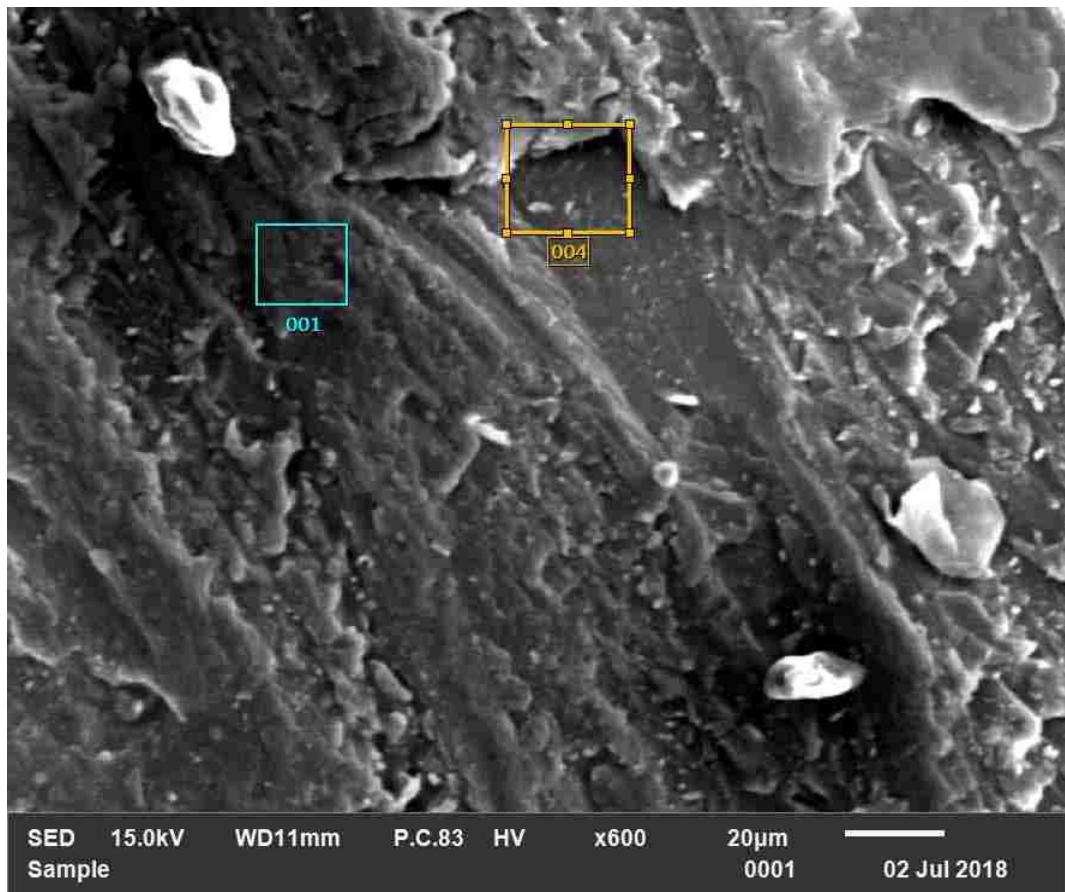


**Figure 3.45 SEM Image of Analysis Box on ANP Epoxy Coupon**

The corresponding elemental analysis of this orange boxed area was shown to be as follows per **Figure 3.46**:

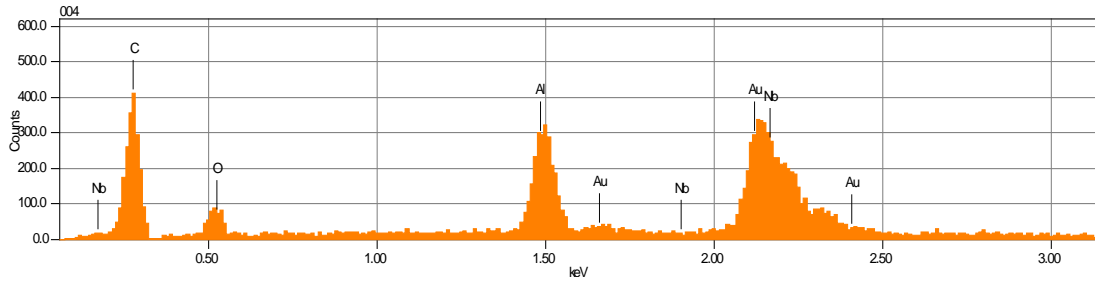


**Figure 3.46 ANP Epoxy Elemental Composition (Box Analysis)**

The significantly higher amount of aluminum in this box analysis was further examined with the EDS point analysis by placing the SEM pointer on the presumed  $\text{Al}_2\text{O}_3$  nanoparticle agglomeration in **Figure 3.47** with the following elemental results in **Figure 3.48** and **Table 3.5**:

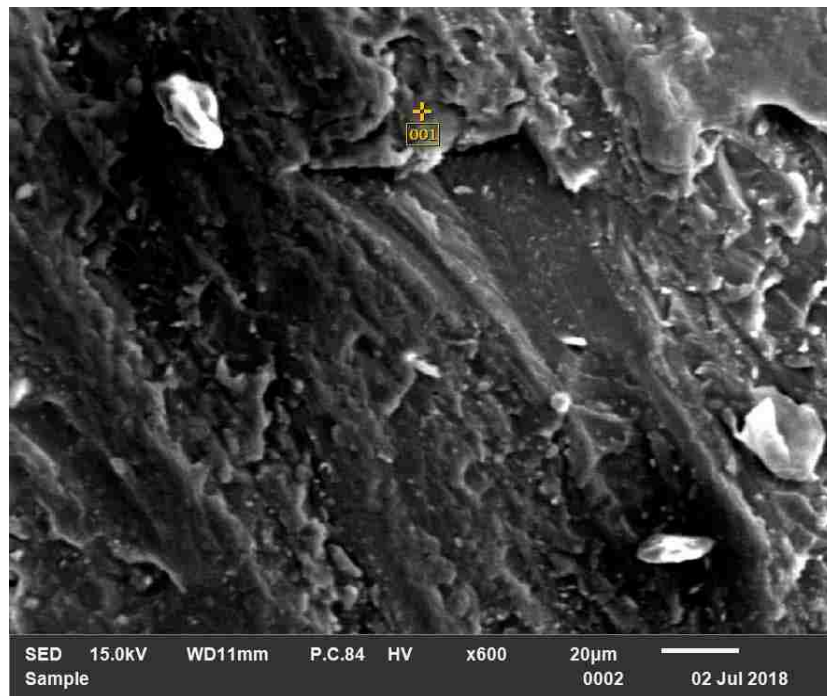


**Figure 3.47 SEM Image of Analysis Point on ANP Epoxy**

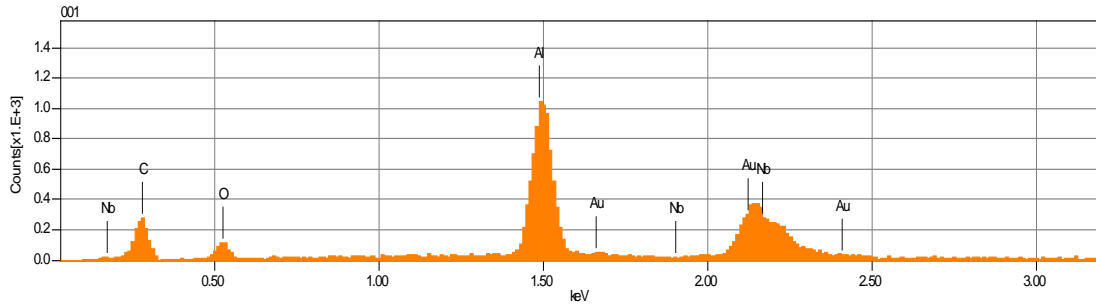


**Figure 3.48 ANP Epoxy Element Composition (Point Analysis)**

Table 3.5 ANP Epoxy Elemental Composition (Point Analysis)

Element	Mass %	Atom %
C	33.86	64.01
O	10.55	14.97
Al	18.72	15.75
Nb	7.87	1.92
Au	29.00	3.35
Total	100.00	100.00

## CHAPTER 4 NUMERICAL METHODS

Analytical closed-form solutions are usually restricted to systems with regular geometries, straightforward loading and well-defined boundary conditions. For this reason, the vast majority of complex systems today are modeled and simulated via numerical methods such as the finite element method (FEM). With this method, the system is subdivided (i.e., discretized) into a necessarily finite number of smaller elements, each with their own degrees of freedom (DOFs) for translation, rotation and even temperature and electrical potential if required. The key step in this numerical modeling process is the idealization of the highly complex physical system to a more simplified mathematical model and then reduction of the infinite number of DOFs to a finite number. Often the simplifications and assumptions implemented in the modeling process produce results out of sync with the behavior of the real system. Thus, the finite element model must be correlated to experimental data so it can be verified and validated and hence, stresses, strains and loads can be assessed with confidence in the structural design process.

Viscoelastic finite element analysis (FEA) was conducted to simulate the strain energy and deployment force dissipated during the tape springs' stowage times. Finite element modeling of viscoelastic composite laminate structures can be very challenging due to the complexity of the composite's design and the many mechanical variables to model. Thin composite laminates, such as the tape spring shell structure in this research, are typically modeled with orthotropic material properties in a plane stress condition. This modeling technique was the approach for the subject work. Furthermore, since

viscoelastic material models for constituents are usually isotropic, the models must be integrated with algorithms combining both composite laminate principles (e.g., micromechanics, classical lamination theory, etc.) with the principle of viscoelasticity and embedded nanoparticles.

At least two researchers (Kahn et al. and Pellegrino et al.) have previously implemented a subroutine within the Abaqus finite element software suite to effectively deal with the complex viscoelastic composite modeling challenge. Though Abaqus has viscoelastic modeling capability and a composites module in its CAE (Complete Abaqus Environment) preprocessor, Abaqus lacks the capability to define viscoelastic behavior in orthotropic or anisotropic materials for a structure at an instant of time during the finite element analysis processing. It also cannot model particulate composites explicitly with any of its current built-in features or tools. Thus, the use of an external subroutine enables Abaqus to conduct a viscoelastic finite element analysis with a step by step time approach as defined by the user and provides the necessary flexibility to tailor and completely define unique, new materials. The user is limited only in how skilled he/she is in being able to accurately model the material behavior within their authored subroutine, Abaqus FEM and simulation. A myriad of options abound to adjust and tune the model to correlate the FEM-produced results with the experimental test results. While this research was experimentally focused, a FEM was built and simulations run primarily to infer the composite mechanics were valid to correlate structural deployment forces and loss in deployment force during stowage.

## 4.1 FlexLam Composite Laminate Design

The challenges of molecular design and the inevitable inherent defects in a composite induce constraints on structural design. The design of structures must consider complex states of stress and strain, and the efficiency of load transfer in the composite depends on the interfacial bonds between the filler, matrix and nanoparticles. With traditional composites, mechanical properties are generally tailored by controlling the number and direction of the reinforcing fibers as with UD composites; carbon fiber and glass fiber are two of the most important reinforcement fibers. These conventional fillers in polymer composites are generally in the range of 10 – 70 wt. %. (Ma et al., 2010) Laminated composites take it one step further and behave in a more complex macro and micro-mechanical manner because many are essentially several to numerous composites (i.e., plies) joined together. (Zhang and Matthews, 1983)

Structure designers have employed thin composite laminates in tube or tape-spring cross sections for a number of years. Thinner laminates are desired because they reduce the strain required for bending and folding structures to a smaller radius within the elastic limit. The laminate must have bending stiffness to resist buckling, but the bulk material tensile or compressive strength is rarely a driving requirement for space structures. (Murphey and Sanford, 2008) A tape spring is an attractive structural element for space structures due to its simplicity and historical use and understanding. The most common application of tape springs is in tape measures (i.e., the familiar carpenter's steel tape measure) which were invented in the late 1920's. Metallic tape springs in space

(typically made of BeCu) have been used for decades as components of spacecraft structures. CFRP composite tape springs offer tailorable performance, low mass and low CTE. A tape spring can be folded in either the equal sense or in the opposite sense, and the bending behavior of a CFRP composite tape spring will depend on the laminate materials it is constructed from.

The tape springs' composite laminate requirements include axial stiffness and dimensional stability for deployed performance, large flexural strains for compact packaging and sufficient deployment torque. Due to limitations of polymers in many engineering applications, for example, low stiffness, low strength and poor toughness, additional constituents are added to enhance their properties. Common additions include carbon and glass fibers, micro-particulates of various shapes and sizes and more recently nanofillers such as CNTs and nanoparticles. These fillers can modify the mechanical (and in some cases electrical) properties of the composites substantially. Many researchers have shown dramatic increases in mechanical properties with only a minute (i.e., 0.5 – 2 weight %) addition of nanofillers. (Tavakoli et al., 2013, Dudkin et al., 2007, Ash et al., 2001, 2002, Moreira et al., 2012, Schadler et al., 2007, Yu et al., 2012, Kuo et al., 2004, Zhang and Singh, 2004, Akinyede et al., 2009, West and Malhotra, 2006, Naous et al., 2006, Davis and Gutierrez, 2011) For example, Young's modulus is greatly improved with the addition of micro- or nanoparticles to the composite matrix. In general, the smaller the size of the particle, the larger the stiffness increase—smaller particles provide better reinforcement. However, studies have shown composite modulus is insensitive to particle size above and below a critical value depending on the matrix properties. There is also a large improvement in tensile strength with decreasing particle

size. (Fu et al., 2008) The bottom line is, particle size has a substantial effect on composite properties which generally increase with diminishing particle size.

The composite laminate layup selected for this research work was three plies consisting of two +/- 45° PW plies sandwiching a UD, 0° ply as shown in **Figure 4.1**. The matrix material for all three plies was Patz Materials and Technologies PMT-F7 epoxy.

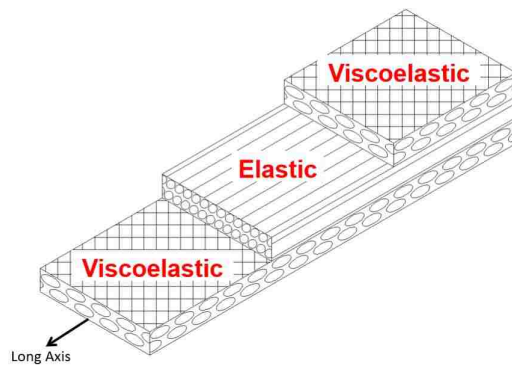


**Figure 4.1 FlexLam Composite Laminate Layup**

This layup and material system were selected based on prior research at AFRL and UNM. (Peterson and Murphey, 2013, Hock, 2013, Borowski et al., 2017, Garner et al., 2017) The PW fabric provides symmetrical and balanced properties coupled with good stability and reasonable porosity making it very suitable for tape spring manufacture. PW laminates are able to survive larger bending strains than the ultimate failure strains measured from standard coupon tests in pure tension or compression. The standard model for laminates, CLT, assumes fibers and matrix are uniformly distributed in each lamina. The maximum bending strain in PW laminates decreases as the number of plies increases. (Yee et al., 2004) During folding in the tape spring, the strain state

induced by this bending is pure shear with respect to the 45° PW plies. The axial bending of the UD ply also produces a strain state of pure shear; however, the orientation significantly strains the fibers. The central UD ply provides the deployment force and energy for deployment. In the next step, the stowed phase, strain energy stored in the viscoelastic laminae dissipates while that in the elastic lamina remains essentially unchanged. In the final step, the deployment phase, the strain energy stored in the elastic lamina works against external forces resisting deployment and the deployment is damped by the viscoelastic laminae.

Using this combination of PW and UD plies provided a thin composite laminate both rollable/very bendable and more resistant to creep and stress relaxation. The elastic UD middle lamina stores primary strain energy upon storage later driving the structure's deployment. The FlexLam laminate is balanced and symmetric so there is no coupling between bending, stretching and shearing. The UD ply also provides structural performance with high axial and bending stiffness, small CTE, and creep resistance but low buckling strength because it has extremely low transverse bending stiffness and transverse shear stiffness. The UD ply provides the deployment force and axial stiffness and ensures the PW plies' creep does not prevent successful structural deployment. The outer PW plies add shear stiffness and local bending stiffness to the laminate, but they are also sensitive to creep and add very little axial stiffness. They are subjected primarily to shear strains and they increase the twisting and torsional stiffness of the structure. (Peterson and Murphey, 2013) The viscoelastic behavior of the FlexLam tape spring is overwhelmingly controlled by the PW plies.

Since deployable space structures are often highly strained due to packaging and stowage limitations on the launch vehicle, they may experience creep strain and stress relaxation. Traditional CFRP laminates tend to gradually lose strain energy and change dimensions while packaged and stored for a long time due to stress relaxation. Therefore, the utility of composites is diminished when the stiffness is reduced sufficiently to cause structural instability. (Halpin, 1969) Nanoparticles have been researched as a method to achieve greater material performance and control/hinder creep effects. One of the most popular nanofillers is CNTs, but all known preparations of CNTs give mixtures of chiralities, diameters and lengths with different amounts of impurities and structural defects. (Moniruzzaman and Winey, 2006) This major issue makes structural modeling and prediction very difficult and CNT initial results have yet to achieve the magnitude of property enhancement believed possible. Several fabrication and modeling issues have been identified and need to be addressed to optimize the properties of such materials, including dispersion and agglomeration of the CNTs within the polymer, CNT-polymer bonding and interaction, and CNT orientation and alignment. The different forms (single-walled, multiwalled, and bundles) and various methods used to fabricate the CNTs also greatly influence the effectiveness of CNTs as structural reinforcement. Moreover, the high cost of CNTs, especially SWCNTs, compared with other fillers like graphite, carbon black, and carbon fibers limits the widespread applications of CNT-based nanocomposites. (Ma et al., 2010) SWCNTs are more expensive than MWCNTs and more difficult to exfoliate individually; MWCNTs are usually less agglomerated though. (Spitalsky et al., 2009) The time-dependent behavior of polymer nanocomposites is rarely examined and few studies have been undertaken to improve the shear creep

behavior. (Soliman et al., 2012) With these considerations in mind, other nanofillers such as graphene, nanosilica, ANPs and nanoclay were initially researched for enhancing the tape springs' mechanical properties.

The selection of ANPs as a filler was based on prior published research (Tavakoli et al., 2013, Dudkin et al., 2007, Ash et al., 2001, 2002, Moreira et al., 2012, Schadler et al., 2007, Yu et al., 2012, Kuo et al., 2004, Zhang and Singh, 2004, Akinyede et al., 2009, West and Malhotra, 2006, Naous et al., 2006, Davis and Gutierrez, 2011, Borowski et al., 2017, Garner et al., 2017). The ANP weight percentage chosen was 2% based on work by Garner et al. (Garner et al., 2017) The addition of the nanoparticles was hypothesized to help control/hinder the tape springs' stress relaxation to enable retention of more deployment torque after long stowage periods, as compared to non-ANP tape springs. To be clear, the main hypothesis of this research is ANPs embedded in CFRP composite laminate tape spring deployable structures can engineer them to produce desired structural behavior for controlled, passive deployment. While creep and stress relaxation are not new research areas in CFRP composites, the incorporation of nanoparticles to tailor composite properties for space applications is an area very little work has been published in the literature.

Nanocomposites are dependent upon many factors, including strain rate, fill fraction of the nanoparticles, fill morphology, fill orientation, dispersion quality and filler-matrix adhesion interface quality. (Tian et al., 2016) To take full advantage of the exceptional stiffness, strength and resilience of nanoparticles, strong interfacial bonding is critical for interfacial stress transfer. (Thostenson, 2001) The quality of the adhesion at

the particle to matrix interface is crucially important in effectively transferring loads and stresses. The strength of these bonds between the polymer's molecular chains and the particles is critical. Smaller particles such as nanoparticles offer immensely more particle surface area for this bonding to occur. To put it simply, more surface area and better bonding yield a much-improved composite in terms of both strength and stiffness, among other properties.

## 4.2 Abaqus Analysis Steps for Model Simulation

In the Abaqus modeling environment, an analysis is defined by dividing the problem of interest into steps with a procedure for each step. Loads, boundary conditions, constraints, interactions and output requests, etc. are specified for each analysis step. Furthermore, each step in the analysis is divided into multiple increments. A flowchart of the analysis process is shown in **Figure 4.5**.

The tape spring structural simulation in Abaqus was modeled with the following analysis steps and corresponding natural time periods as shown in **Table 4.1**:

Table 4.1 Analysis Steps in Abaqus FEM Simulation

	Analysis Step	Step Time Period
1	Flatten Tape Spring Root	1 Second
2	Roll Tape Spring onto Hub	240 Seconds (16 inches)
3	Stow / Hold Rolled Tape Spring	1 Hour, 1 Day, 1 Week, 1 Month, 6 Months
4	Deploy Tape Spring from Hub	240 Seconds (16 inches)
5	Tape Spring Settle	1 Second

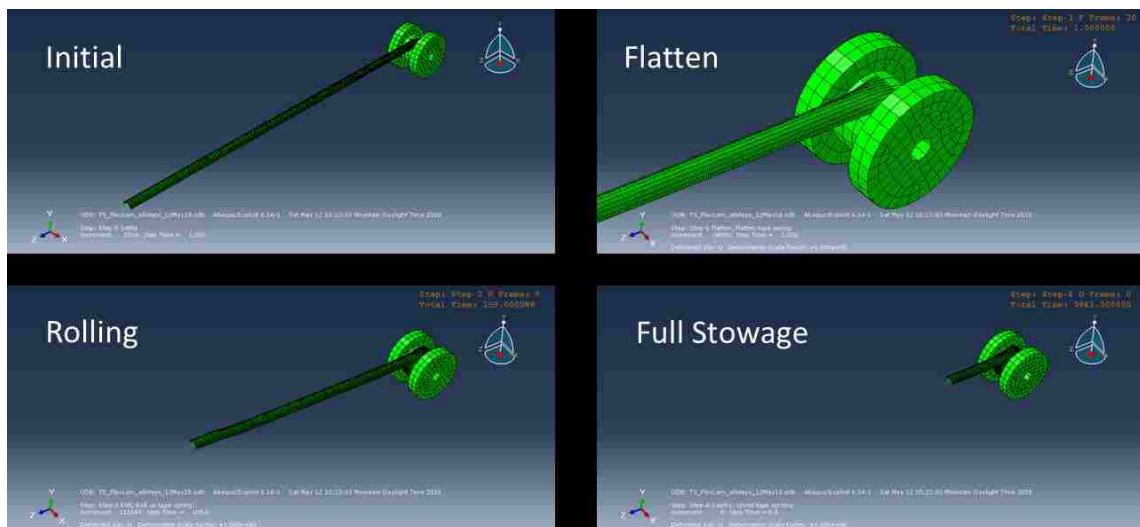


Figure 4.2 Tape Spring Simulation Steps in Abaqus

The analysis steps mimicked the actual steps during the experimental test campaign detailed in Chapter 3. Abaqus creates a special initial step at the beginning of the model's step sequence and names it *Initial* (see **Figure 4.2**) to begin the first step in the user-defined state per construction of the FEM. The initial step allows the user to define boundary conditions, predefined fields, and interactions applicable at the very

beginning of the analysis. For example, if a boundary condition or interaction is applied throughout the analysis, it is usually convenient to apply such conditions in the initial step. Likewise, when the first analysis step is a linear perturbation step, conditions applied in the initial step form part of the base state for the perturbation.

The initial step is followed by all the analysis steps. Each analysis step is associated with a specific procedure defining the type of analysis to be performed during the step, such as dynamic analysis or quasi-static analysis steps used in this research work. Steps 1 and 2 (flatten and roll) were run as dynamic analyses, step 3 (stowage) was run as a quasi-static step, and steps 4 and 5 (unroll and settle) were run as dynamic analyses. All steps were analyzed in Abaqus/Explicit. Since the state of the model (stresses, strains, etc.) is updated throughout all general analysis steps, the effects of previous history are always included in the structural response for each new analysis step. While an analysis is running, Abaqus provides increments, step time, total time, stable time increment and the kinetic energy and total energy of the model. The stable time increment and energies of the model provide the most insight into how well the model is performing during the analysis. The stowage step is the main focus of this research work, modeling the stress relaxation (manifested as loss in deployment force at the tape springs' tips) of the coiled stowed tape springs for lengthy periods of time.

### 4.3 Abaqus Finite Element Model Definition

The commercial FEA software Abaqus version 6.14-1 was used to model and simulate the tape springs in this research work. An Abaqus implicit model of the FlexLam composite laminate tape spring was built as an assembly of shell elements to analyze the stowage and subsequent deployment behavior. The hub part for the tape spring stowage was modeled with rigid body elements.

The composite layup feature in the composite module of Abaqus/CAE was used to model the three plies of the FlexLam composite laminate. The modeling assumptions implemented for the FlexLam composite were:

1. The UD middle ply does not contribute to the viscoelastic structural response because it is dominated by isotropic, high modulus carbon fibers in an epoxy matrix.
2. The PW outer plies contribute fully to the viscoelastic structural response and were modeled as orthotropic in a plane stress condition. They consisted of silica fibers in the same epoxy matrix.
3. There is elastic behavior only, no plastic fiber or plastic matrix behavior exists.
4. Standard CLT assumptions apply, e.g., perfect bonding between plies, plane sections remain plane after bending, etc.
5. The tape spring structure behaves in both a linear and nonlinear way depending on time, temperature, loading and stress levels.

6. The alumina nanoparticles in the nanocomposite tape springs were homogeneously dispersed and fully deagglomerated.
7. Friction in the test stand, MTS Instron machine and ball bearings was negligible.
8. The tape springs all had consistent geometric features and were all exactly the same in form, fit and function.

The structural parts used to build the FEM and their mesh statistics are as follows:

- Tape Spring
  - 5000 elements, type S4R (general-purpose conventional shell element, quadrilateral, 4 nodes/element, reduced integration, hourglass control, large strain)
  - 5511 nodes
  
- Hub
  - 533 elements
    - 499 elements, type R3D4 (rigid, linear three-dimensional quadrilateral element, 4 nodes/element)
    - 34 elements, type R3D3 (rigid, linear three-dimensional triangular element, 3 nodes/element)
  - 516 nodes

For conventional shell elements in Abaqus, only the shell reference surface is discretized; in this model, the middles of the plies were chosen as the reference surface. Additionally, shell faces can also experience contact on both top and bottom of their

faces such as this case with the tape spring rolling upon itself. Per the Abaqus reference manual, all elements are suitable for geometrically nonlinear analysis, which includes large displacements, rotations and large strain. Moreover, the change in shell thickness is also accounted for with these elements in a geometric nonlinear analysis and with the section Poisson's ratio. Nonlinear geometry/materials in the FEM correspond to large deflections or rotations or issues with the materials or boundary conditions. Since the stress is zero in the thickness direction (per typical plane stress conditions of thin materials), the thickness strain results only from Poisson's effect. In Abaqus the algebraic equations for the elements' stiffness matrices and force vectors must be solved repeatedly for nonlinear geometry/materials which significantly adds to the model's computational time even though S4R elements are cheap, effective elements minimizing computational expense. Also, it is important to note nonlinear geometry/materials in Abaqus are not defined the same as the standard mathematical definition. Many first order reduced integration elements (when used in Abaqus/Explicit) can result in mesh instability, i.e., hourglassing. In this research, the hourglassing problem was addressed in two ways, by using first order S4R elements with the election of enhanced hourglass control for the element type in the mesh module and by having at least four elements through the tape spring thickness as depicted in **Figure 4.3**. When both of these approaches are used, hourglassing is almost never a problem.

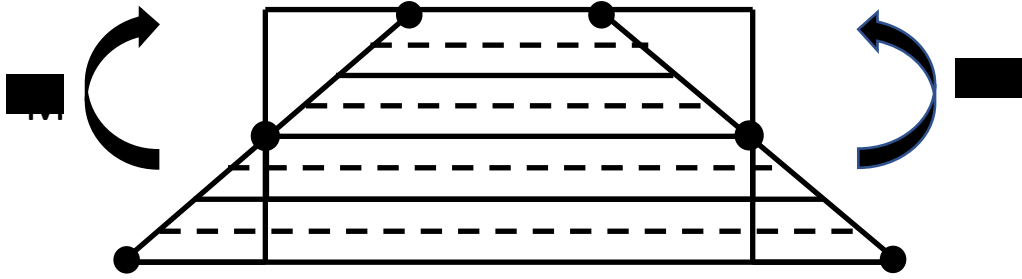


**Figure 4.3 Through Thickness Shell Elements Bending in Abaqus**

The hub part in the Abaqus model was modeled as a homogeneous rigid body of aluminum and as such, was computationally efficient. The motion during the FEM simulation was described by six DOFs and no element calculations were required for it.

The tape spring part in the Abaqus model was modeled as a deformable body with conventional S4R shell elements. Its structural behavior is viscoelastic, nonlinear and during the stowage step of particular interest, it is quasi-static. Challenging nonlinear quasi-static problems often involve very complex contact conditions as this case does with a composite laminate tape spring rolling upon itself for stowage on the hub member. Abaqus provides two solvers, Abaqus/Standard for true static equilibrium and Abaqus/Explicit for true dynamic equilibrium. Abaqus/Explicit is appropriate and more efficient for high speed dynamic events and highly nonlinear static problems, especially for three dimensional problems involving contact and/or very large deformations. The time increments are generally much smaller in the Explicit solver compared to the Standard solver. For these reasons, Abaqus/Explicit was used for the FEA of this research. However, another option considered was an Abaqus import and transfer analysis whereby an Abaqus model and its associated deformed mesh and material/element properties are transferred from Abaqus/Explicit to Abaqus/Standard, or

vice versa. This method is useful if performing the quasi-static analysis step in Standard instead of Explicit. Standard has some advantages over Explicit in its stable time increment convergence algorithm.

Because the tape spring is very flexible, it took very long simulation times to obtain a quasi-static solution of the stow step in Abaqus/Explicit. Thus, the FEA of the quasi-static stow step was first attempted with Abaqus/Standard using an import analysis / transfer results approach as graphically shown in **Figure 4.4**. The import capability is used to transfer model data (i.e., deformed mesh and the associated material properties and state) and results from one Abaqus analysis to another. This capability was useful for dividing the tape spring problem into three phases and importing the analysis and transferring the results between three different FEMs.

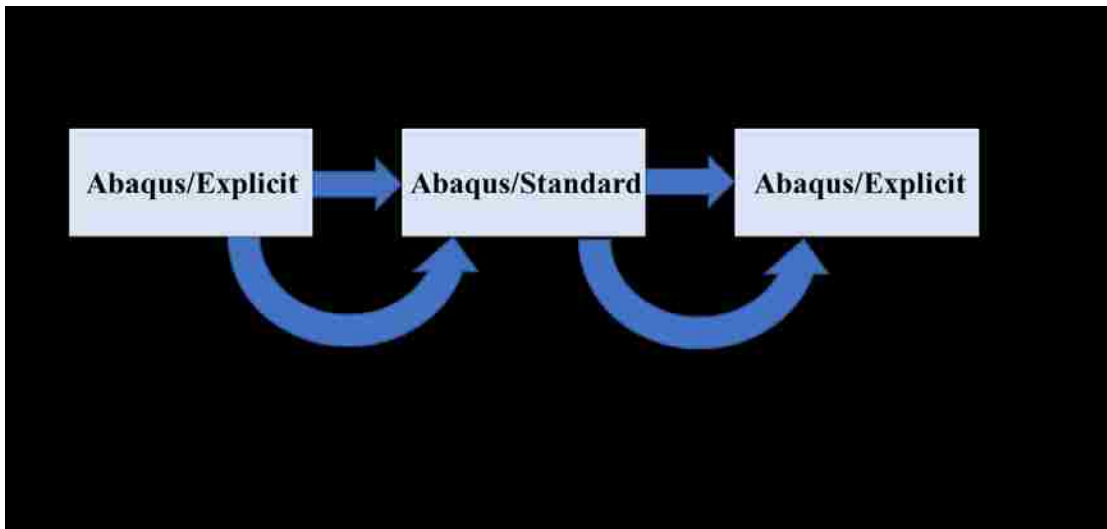


**Figure 4.4** Abaqus Import Analysis Modeling Strategy

In both Abaqus solvers, application of the tape spring FEM during the dynamic rolling and unrolling and quasi-static stowage requires special considerations because it is computationally impractical to model the entire stowage process in its natural time period; there would literally be many millions of time increments required resulting in a simulation time of many days to weeks or more depending on the particular model. Thus, there was a need to artificially increase the speed of the FEA process to obtain an economical solution during the quasi-static stow step. Abaqus has two ways to obtain economical solutions for dynamic and quasi-static events: Increased Loading Rates and Mass Scaling. While both methods achieve the same effect (i.e., fewer increments needed to complete the analysis job), because increasing the loading rates affect the material's strain rate sensitivity, it was not a good option for this work. On the other hand, mass scaling allows an increase in the material's density by a factor  $f^2$  which then in turn increases the stable time increment during processing by a factor of  $f$ . However, failure to use a small enough time increment will result in an unstable solution and it will cause the analysis job to abort. Quantitatively, the stable time increment during the model's solver step is computed as:

$$\Delta t = \left( \frac{L^e}{(E/\rho)^{1/2}} \right) \quad (4.1)$$

where  $L^e$  is the smallest characteristic element length, E is the material modulus and  $\rho$  is the material density. The figure of merit in the denominator of equation 4.1 is known as the dilatational wave speed. Qualitatively, the stable time increment is a measure of the shortest amount of time that it takes a pressure wave to transit any element within the model. Abaqus will issue a warning to the user if the ratio of the deformation speed to

the dilatational wave speed exceeds 1.0, meaning the element is deforming so quickly it is in danger of collapsing. As can be seen, the stable time increment depends directly on the mesh size and is inversely proportional to the square root of the stiffness divided by the density of the material or composite. Expounded details on this modeling technique for the stow step are given in section 4.4. Great care must be taken when using mass scaling so erroneous results are not used blindly without validation. Suffice to say, there are numerous mass scaling options available such as fixed mass scaling, variable mass scaling, mass scaling all elements, mass scaling only certain elements below a specified stable time increment, mass scaling uniformly, specifying a mass scaling factor or stable time increment, etc. The implications of the mass scaling used in this model are discussed in **Chapter 5**, Results and Discussion.

Numerous attempts consuming hundreds of hours of time with the three-phase modeling approach importing results between Explicit and Standard were tried but the simulation proved extraordinarily challenging within the time constraints of this work. Therefore, the FEM simulation was conducted entirely in Abaqus/Explicit.

### **4.3.1 Tape Springs' Material Properties**

The laminae material properties of the FlexLam composite laminate were determined solely or in combination with the following methods:

1. CompositePro® (Firehole Technologies Inc.) Commercial Software
2. TheLaminator.net online composite tool
3. CADEC-online.com online composite tool
4. Manufacturer's Data Sheets
5. Hand Calculations
6. Experimental Testing

Entering accurate material properties into the FEM is one of the most important aspects for a successful analysis of composite materials. The material properties strongly dictate how the structure is predicted to behave and what the stress-strain response will be. In this research, the fiber volume fraction required for a PW ply of thickness 68.87  $\mu\text{m}$  was 43.64% based on the AstroQuartz PW fabric areal density of 68  $\text{g}/\text{m}^2$  and the Patz PMT-F7 resin area weight of 41.7  $\text{g}/\text{m}^2$ . Using the constituent properties in the CompositePro micromechanics tool, the effective lamina properties were calculated for the PW plies and the UD ply. This method for determining lamina properties was verified and validated for the FlexLam composite, albeit with a different, but similar, UD ply resin (i.e., Hexply 8552) by Peterson and Murphey. (Peterson and Murphey, 2013)

The matrix material used in the FlexLam composite, for both the PW plies and the UD ply, was also Patz PMT-F7 with 10% by weight of 3M nanosilica spheres. It is a toughened aerospace-grade epoxy space qualified and cured at 350° F with a  $T_g > 440^\circ \text{F}$ .

The fiber volume fraction required for a UD ply of thickness 90.18  $\mu\text{m}$  was 68.53% based on the Patz F7-IM7/12K tow fiber area weight of 110  $\text{g}/\text{m}^2$  and the Patz

PMT-F7 resin area weight of 41.7 g/m<sup>2</sup>. Again, using the constituent properties in the CompositePro micromechanics tool with this fiber volume fraction, the effective lamina properties were calculated per **Table 4.2**:

Table 4.2 Material Properties for Abaqus Model

Lamina	Constituent	Constituent Property	Method	Lamina Property	Method
Plain Weave (PW)					
Patz PW Prepreg	Patz PMT-F7 Resin (with 10% weight 3M Nanosilica)			E <sub>1</sub> = E <sub>2</sub> = 8.69 GPa G <sub>12</sub> = 9.52 GPa Avg Thickness = 68.87 μm ρ = 1694 Kg/m <sup>3</sup> Fiber Vol. Fraction = 43.64%	Average of Micromechanics Calculations from CompositePro <sup>(R)</sup> and/or Hand Calculations
		E <sub>m</sub> = 3.529 GPa	Test		
		G <sub>m</sub> = 1.119 GPa	Test		
		ρ = 1301 Kg/m <sup>3</sup>	Test		
		ν = 0.377	Test		
	JPS Astroquartz II Style 525 PW (Silica Fibers)				
		Type of Yarn - Warp = QC9 16.5	Data Sheet		
		Type of Yarn - Fill = QC9 16.5	Data Sheet		
		Areal Density = 68 g/m <sup>2</sup>	Data Sheet		
		Warp Count = 19.7 strands/cm	Data Sheet		
		Fill Count = 19.7 strands/cm	Data Sheet		
	Fabric Thickness = 0.08 mm	Data Sheet			
	Warp Breaking Strength = 57 daN/5 cm	Data Sheet			
	Fill Breaking Strength = 57 daN/5 cm	Data Sheet			
Unidirectional (Uni)					
Patz Uni Prepreg	Patz PMT-F7 Resin (with 10% weight 3M Nanosilica)			E <sub>1</sub> = 163.3 GPa E <sub>2</sub> = 8.0 GPa G <sub>12</sub> = 5.4 GPa Avg Thickness = 90.18 μm ρ = 1628 Kg/m <sup>3</sup> Fiber Vol. Fraction = 68.53%	Average of Micromechanics Calculations from CompositePro®, TheLaminator, CADEC and/or Hand Calculations
		E <sub>m</sub> = 3.529 GPa	Test		
		G <sub>m</sub> = 1.119 GPa	Test		
		ρ = 1301 Kg/m <sup>3</sup>	Test		
		ν = 0.377	Test		
	IM7 12K Carbon Fibers				
		E <sub>1</sub> = 248.6 GPa	Data Sheet		
		E <sub>2</sub> = E <sub>3</sub> = 13.8 GPa	Data Sheet		
		G <sub>12</sub> = G <sub>13</sub> = 95.0 GPa	Data Sheet		
		G <sub>23</sub> = 5.52 GPa	Data Sheet		
		ν <sub>12</sub> = ν <sub>13</sub> = 0.22	Data Sheet		
	ν <sub>23</sub> = 0.25	Data Sheet			
	ρ = 1780 Kg/m <sup>3</sup>	Data Sheet			

Several of the composite tools mentioned above were not able to converge on a solution for determining lamina properties for the PW ply. For this reason, there is less confidence in the mechanical properties of the PW ply than the simpler UD ply. However, as will be seen in the next section, the PW lamina properties were determined via a VUMAT in Abaqus per a subroutine call, thus, the PW properties in **Table 4.1** were not used in the FEA for this work. The mechanical properties were calculated in the

Fortran subroutine and output as Solution Dependent Variables (SDV's) per the Field Outputs in Abaqus. This process is discussed in more detail in section 4.3.2.

### **4.3.2 Abaqus VUMAT Subroutine**

Abaqus has the capability to model viscoelastic properties of an isotropic material, but it cannot model orthotropic materials such as complex composite laminates or perform time-dependent calculations. Thus, the composite layup module in Abaqus was used to define the three plies of the FlexLam composite with the outer two plies modeled as viscoelastic via a VUMAT in Abaqus/Explicit. In this way it was possible to accurately represent the FlexLam composite laminate behavior for the tape springs. The middle UD ply was modeled as elastic and was assumed not to contribute to the viscoelastic behavior of the composite tape spring because it is heavily dominated by UD carbon fibers typically linear elastic and thus do not usually exhibit stress relaxation behavior. Therefore, the tape springs' viscoelastic behavior was modeled only in the two outer PW plies through implementation of the VUMAT subroutine. The VUMAT subroutine was used to define the mechanical constitutive behavior of the orthotropic viscoelastic plies so Abaqus could utilize time-dependent properties. The VUMAT allowed Abaqus to conduct the viscoelastic finite-element analysis using a step-by-step loop process in conjunction with a Prony series modeling the matrix stress relaxation over time.

To this end, the two outer plies of the FlexLam composite laminate were assigned the PW user-defined material for explicit dynamics during the flatten and roll steps and as quasi-static during the stowage step. An Abaqus/Explicit dynamics analysis uses displacements and velocities from the beginning of an integration increment to perform the necessary calculations of the equations of motion. Since the tape springs' behavior is nonlinear, a set of nonlinear equations must be iteratively solved for each analysis increment. (Abaqus, 2014)

Given the tape springs were inherently nonlinear, a direct solution procedure had to be used for the dynamic analyses. Therefore, the PW plies' material model was created as a VUMAT and coded via a Fortran subroutine to run in Abaqus/Explicit. The code of this subroutines is provided in Appendix C. The VUMAT subroutine logic was based on the previously verified and validated UMAT by Khan et al. (Khan et al., 2017). The VUMAT material property constants entered into Abaqus are shown in **Table 4.3**:

Table 4.3 Abaqus Material Property Values for VUMAT

Property	Value
	72,000 GPa
	72,000 GPa
	3,529 GPa
	0.28
	0.16
	44%

where FVF is the fiber volume fraction. The 22 Solution-Dependent state Variables (SDV's) in the VUMAT subroutine are shown in **Table 4.4**:

Table 4.4 Abaqus Solution-Dependent State Variables for VUMAT

<b>Number</b>	<b>Name</b>
STATEV(1)	Strain-1
STATEV(2)	Strain-2
STATEV(3)	Strain-3 (i.e., Strain-6)
STATEV(4)	Stress-1
STATEV(5)	Stress-2
STATEV(6)	Stress-3 (i.e., Stress-6)
STATEV(7)	Updated Strain-1
STATEV(8)	Updated Strain-2
STATEV(9)	Updated Strain-3
STATEV(10)	Matrix Modulus (Time-Dependent)
STATEV(11)	Shear Modulus (Time-Dependent)
STATEV(12)	Lamina Modulus, Longitudinal
STATEV(13)	Lamina Modulus, Transverse
STATEV(14)	Lamina Modulus, Shear
STATEV(15)	Lamina's Poisson's Ratio
STATEV(16)	Stress-X
STATEV(17)	Stress-Y
STATEV(18)	Shear Stress (XY)
STATEV(19)	Strain-X
STATEV(20)	Strain-Y
STATEV(21)	Shear Strain (XY)
STATEV(22)	Strain Energy

The subroutines allowed the state variables to be calculated for each incremental time step of the analysis and thus provide the structure's strain incrementation and stress relaxation. A flowchart of the UMAT/VUMAT basic flow of data and logic actions is shown in **Figure 4.5**:

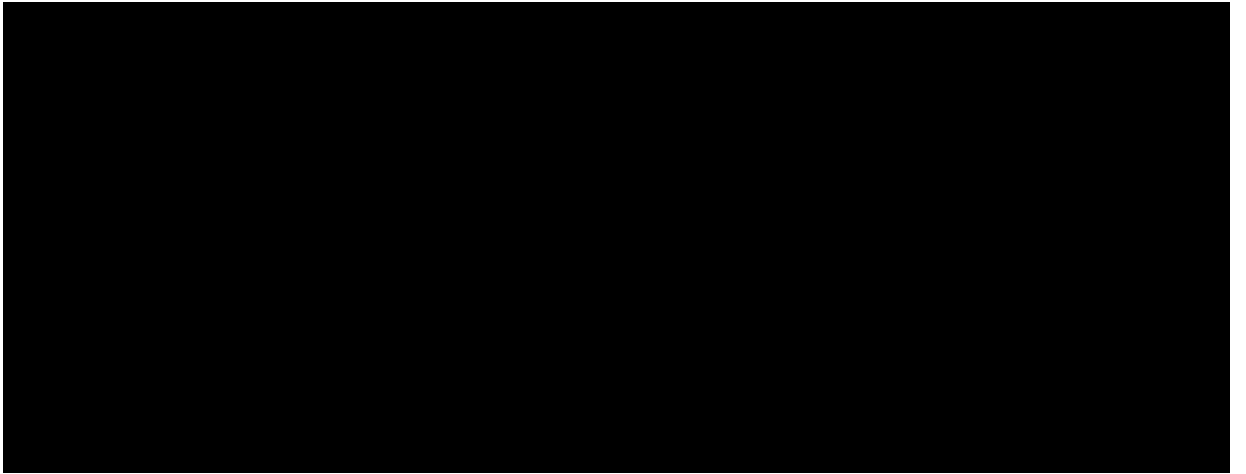


**Figure 4.5 Abaqus Data Flow and Logic for VUMAT Subroutine**

Abaqus/Standard uses a UMAT and it is important to note in the UMAT subroutine the Jacobian matrix, also known as the tangent stiffness matrix, is given as:

$$J_{ab} = \frac{\partial \Delta \sigma}{\partial \Delta \varepsilon} = \begin{bmatrix} \frac{E_1}{1 - \nu_{12}\nu_{21}} & \frac{\nu_{12}E_2}{1 - \nu_{12}\nu_{21}} & 0 \\ \frac{\nu_{12}E_2}{1 - \nu_{12}\nu_{21}} & \frac{E_2}{1 - \nu_{12}\nu_{21}} & 0 \\ 0 & 0 & G_{12} \end{bmatrix} \quad (4.2)$$

In a UMAT, the Jacobian is required to update the local stress state through the iterative numerical analysis process per **Figure 4.5**. The Abaqus interface for a UMAT passes the current time increment  $\Delta t$  and the corresponding strain increment  $\Delta \varepsilon$ , determined using the Jacobian matrix at the end of the previous time increment. In turn, it requires at the end of the current time increment an update of the stresses  $\sigma_j^t$  and the Jacobian matrix. The incremental method requires the transient strain function to be expressed in terms of a sum of exponentials, i.e., a Prony series, and the strain/stress history needs to be stored at the end of each increment for each strain/stress component and each set of Prony terms. (Khan et al., 2017)

To reiterate, the VUMAT is a vectorized version of the UMAT run in Abaqus/Explicit. A VUMAT has several distinct differences from a UMAT in that only strain increments are passed and only stresses are passed back in the iteration loop, consequently, no Jacobian is needed. Moreover, a VUMAT passes a block of elements (a vector of length *nblock*) per time increment unlike a UMAT which goes through one element at a time. Blocks of data are passed to the Fortran subroutine in a VUMAT. Extreme care must be taken with setting up the do loops from *1* to *nblock* to ensure the calculations and array dimensioning are accurate.

### 4.3.3 Viscoelastic Modeling with the Prony Series

The FlexLam composite laminate was modeled with viscoelastic plies for the two outer PW laminae and with an elastic ply for the middle UD lamina. Classical linear viscoelasticity (i.e., “small” strains) can be modeled in Abaqus using the viscoelastic option for stress relaxation or creep behavior, or a Prony series representation of the time-dependent shear and bulk moduli can be calculated from a curve fit using experimental stress relaxation (or creep) data. However, it is important to note the Prony series only represents behavior over the fitted time data from which the experimental testing occurred, extrapolated data is invalid. Also, because the stress relaxation behavior is dominated by shear relaxation, it is not necessary to specify the bulk moduli and subsequent volumetric relaxation.

Incorporating a Prony series representation of the PW plies’ viscoelasticity into a classical laminate analysis can yield a qualitative prediction for the tape spring’s deployment in the global frame of reference. However, in general, CLT is not suitable for thin, woven-fiber composite laminates because CLT assumes material homogeneity through the thickness and that is not the case with the FlexLam plies. Nevertheless, CLT is a good starting point as a way to evaluate aspects of an idealized composite laminate and is discussed in detail in the following section.

#### 4.3.4 Micromechanics and Classical Lamination Theory (CLT)

According to research by Karakaya and Soykasap in 2012, bending stiffness and strain values as calculated from CLT showed great differences as compared to the experiments they conducted on PW CFRP composites. (Karakaya and Soykasap, 2012) Thus, CLT should not be directly used to determine these values, but it is worthwhile to use as a starting point. The main assumptions used in CLT are given later in this chapter. However, micromechanics can often be used to predict the stiffness of a laminate with relatively good success. It uses known (tested) constituent properties and the laminate geometry to predict the macroscopic behavior of the composite material. The mechanics of materials approach is generally the most useful method and will be used here.

To approximate the composite bulk behavior by a Prony series representation of the stress relaxation behavior, CLT principles can be used as a point of departure. The FlexLam three-ply composite laminate tape spring is subject to bending as it wraps around the hub during rolling up for storage. Additionally, because the bending moment,  $M_z$ , is not constant along the longitudinal length of the tape spring, shear stress,  $\tau_{sx}$ , exists. In order to analyze the bending moment and shear stress in the tape spring during storage it is necessary to start with the laminae material properties, boundary conditions and loading.

The FlexLam composite's laminae are orthotropic in a plane stress state and as such, the following expression relates their stress,  $\sigma_{ij}$ , and strain,  $\varepsilon_{ij}$ , in principle coordinates:

$$\begin{bmatrix} \sigma_1 \\ \sigma_2 \\ \tau_{12} \end{bmatrix} = \begin{bmatrix} Q_{11} & Q_{12} & 0 \\ Q_{21} & Q_{22} & 0 \\ 0 & 0 & Q_{66} \end{bmatrix} \begin{bmatrix} \varepsilon_1 \\ \varepsilon_2 \\ \gamma_{12} \end{bmatrix} \quad (4.3)$$

where the reduced stiffness matrix,  $[Q]$ , terms are defined as:

$$Q_{11} = \frac{E_1}{1 - \nu_{12}\nu_{21}} \quad (4.4)$$

$$Q_{12} = Q_{21} = \frac{\nu_{12}E_2}{1 - \nu_{12}\nu_{21}} \quad (4.5)$$

$$Q_{22} = \frac{E_2}{1 - \nu_{12}\nu_{21}} \quad (4.6)$$

$$Q_{66} = G_{12} \quad (4.7)$$

where  $E$ ,  $G$  and  $\nu$  are the tensile modulus, shear modulus and Poisson's ratio, respectively, and the "1" and "2" are the principle coordinate directions under plane stress conditions. Note, the reduced stiffness matrix,  $[Q]$ , in equation 4.3 is the same as the Jacobian,  $J$ , equation 4.2, with:

$$\sigma_1 = \varepsilon_1 J_{11} + \varepsilon_2 J_{12} \quad (4.8)$$

$$\sigma_2 = \varepsilon_1 J_{12} + \varepsilon_2 J_{22} \quad (4.9)$$

$$\tau_{12} = \gamma_{12} J_{33} \quad (4.10)$$

In addition to these relations, the reciprocity relation exists and must be true for an orthotropic material:

$$\frac{\nu_{12}}{E_1} = \frac{\nu_{21}}{E_2} \quad (4.11)$$

To analyze the global/structural response of the tape spring in the geometric Cartesian natural “x” and “y” directions, the global stress and strain values in the principle material directions are calculated using the common transformation matrix, for the +/- 45° PW plies:

$$\begin{bmatrix} \sigma_x \\ \sigma_y \\ \tau_{xy} \end{bmatrix} = \begin{bmatrix} m^2 & n^2 & -2mn \\ n^2 & m^2 & 2mn \\ mn & -mn & m^2 - n^2 \end{bmatrix} \begin{bmatrix} \sigma_1 \\ \sigma_2 \\ \tau_{12} \end{bmatrix} \quad (4.12)$$

where  $m = \cos(\theta) = \cos(45^\circ)$  and  $n = \sin(\theta) = \sin(45^\circ)$ , but could be of any angular value for a different laminate design. In this way with sine 45° and cosine 45° both equal to  $1/2^{1/2}$ , the global stress values can then be determined as:

$$\sigma_x = \frac{\sigma_1}{2} + \frac{\sigma_2}{2} - \tau_{12} \quad (4.13)$$

$$\sigma_y = \frac{\sigma_1}{2} + \frac{\sigma_2}{2} + \tau_{12} \quad (4.14)$$

$$\tau_{xy} = \frac{\sigma_1}{2} - \frac{\sigma_2}{2} \quad (4.15)$$

To relate the global stress and strain in the laminate, the constitutive equation is as follows:

$$\begin{bmatrix} \sigma_x \\ \sigma_y \\ \tau_{xy} \end{bmatrix} = \begin{bmatrix} \overline{Q}_{11} & \overline{Q}_{12} & \overline{Q}_{16} \\ \overline{Q}_{12} & \overline{Q}_{22} & \overline{Q}_{26} \\ \overline{Q}_{16} & \overline{Q}_{26} & \overline{Q}_{66} \end{bmatrix} \begin{bmatrix} \varepsilon_x \\ \varepsilon_y \\ \gamma_{xy} \end{bmatrix} \quad (4.16)$$

where  $[\overline{Q}_{ij}]$  is the transformed reduced stiffness matrix with the terms as follows:

$$\overline{Q}_{11} = Q_{11} \cos^4 \theta + 2(Q_{12} + 2Q_{66}) \sin^2 \theta \cos^2 \theta + Q_{22} \sin^4 \theta \quad (4.17)$$

$$\overline{Q}_{12} = (Q_{11} + Q_{22} - 4Q_{66}) \sin^2 \theta \cos^2 \theta + Q_{12}(\sin^4 \theta + \cos^4 \theta) \quad (4.18)$$

$$\overline{Q}_{22} = Q_{11} \sin^4 \theta + 2(Q_{12} + 2Q_{66}) \sin^2 \theta \cos^2 \theta + Q_{22} \cos^4 \theta \quad (4.19)$$

$$\overline{Q}_{16} = (Q_{11} - Q_{12} - 2Q_{66}) \sin \theta \cos^3 \theta + (Q_{12} - Q_{22} + 2Q_{66}) \sin^3 \theta \cos \theta \quad (4.20)$$

$$\overline{Q}_{26} = (Q_{11} - Q_{12} - 2Q_{66}) \sin^3 \theta \cos \theta + (Q_{12} - Q_{22} + 2Q_{66}) \sin \theta \cos^3 \theta \quad (4.21)$$

$$\overline{Q}_{66} = (Q_{11} + Q_{22} - 2Q_{12} - 2Q_{66}) \sin^2 \theta \cos^2 \theta + Q_{66}(\sin^4 \theta + \cos^4 \theta) \quad (4.22)$$

Furthermore, the stress in the  $k^{th}$  layer of a composite laminate can be given as:

$$[\sigma]_k = [\overline{Q}]_k [\varepsilon]_k \quad (4.23)$$

which clearly indicates each ply has its own reduced stiffness matrix. Note, strengths do not necessarily transform like stresses. Fortunately, stiffness and stress are of primary concern for this space structural application and not so much strength.

The constitutive equations for an N-layered laminate are obtained by integrating equations 4.16 through the laminate thickness. The geometric details of a generic

laminate cross section can be depicted as shown in **Figure 4.6** and the tape spring rolling geometry can be seen in **Figure 4.7**:

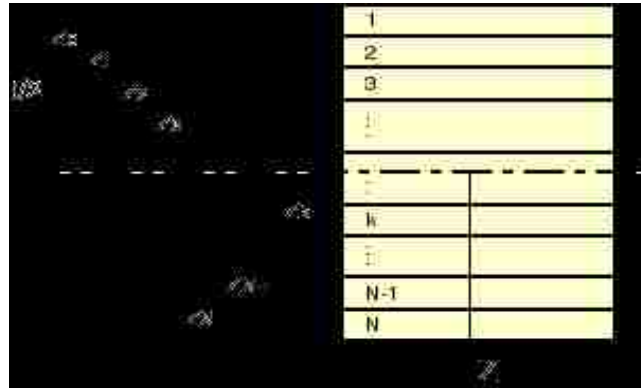


**Figure 4.6** Geometry of N-Layered Composite Laminate

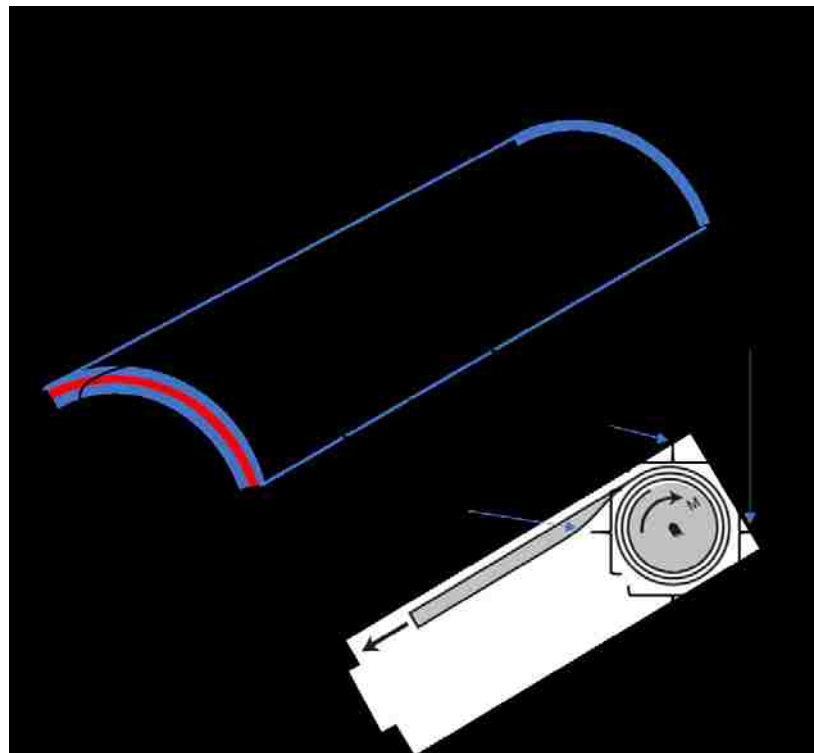


**Figure 4.7** Tape Spring Load Geometry and Equal Sense Bending/Rolling

Note the plane stress coordinates in this research work are the X-Z plane but the generalized equations are given in the usual X-Y plane as is typically the case.

In order to relate a laminate's applied loads and moments to the resulting strains, curvatures and ultimately stresses, the strain variation through the laminate is first given as:

$$\begin{bmatrix} \varepsilon_x \\ \varepsilon_y \\ \gamma_{xy} \end{bmatrix} = \begin{bmatrix} \varepsilon_x^0 \\ \varepsilon_y^0 \\ \varepsilon_{xy}^0 \end{bmatrix} + z \begin{bmatrix} \kappa_x \\ \kappa_y \\ \kappa_{xy} \end{bmatrix} \quad (4.24)$$

where  $\varepsilon_k^0$  are the mid-ply extensional strains and  $\kappa_x$ ,  $\kappa_y$ , and  $\kappa_{xy}$  are the out of plane mid-surface curvatures (i.e., bending strains when multiplied by the thickness,  $z$ ) in the global directions. The global stresses are then given as:

$$\begin{bmatrix} \sigma_x \\ \sigma_y \\ \tau_{xy} \end{bmatrix} = [\bar{Q}] \begin{bmatrix} \varepsilon_x^0 \\ \varepsilon_y^0 \\ \varepsilon_{xy}^0 \end{bmatrix} + z \begin{bmatrix} \kappa_x \\ \kappa_y \\ \kappa_{xy} \end{bmatrix} \quad (4.25)$$

Because the reduced stiffness matrix can be different for each ply, the stress variation through the laminate is not necessarily linear, even though the strain variation is linear.

Using CLT as a simplifying assumption, the following principles are utilized:

1. Laminae are perfectly bonded
2. Bonds are infinitesimal and non-shear deformable
3. Laminate cross-section remains plane after bending
4. Planes remain plane after bending (i.e., transverse shear strains = 0)

- Fibers and matrix are uniformly distributed in each lamina (i.e., material homogeneity)

The pristine tape springs are depicted as shown in **Figure 4.8**:

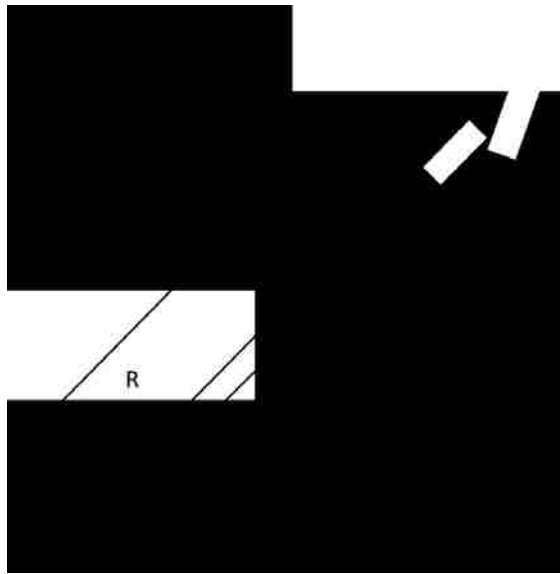


**Figure 4.8 Pristine Tape Spring Shape and Global Coordinates**

The tape spring is subject to two simultaneous bending moments as it first flattens across its transverse axis and then rolls flat as it wraps (i.e., bends) around the diameter of the central rolling hub along its longitudinal axis, per **Figure 4.9**.

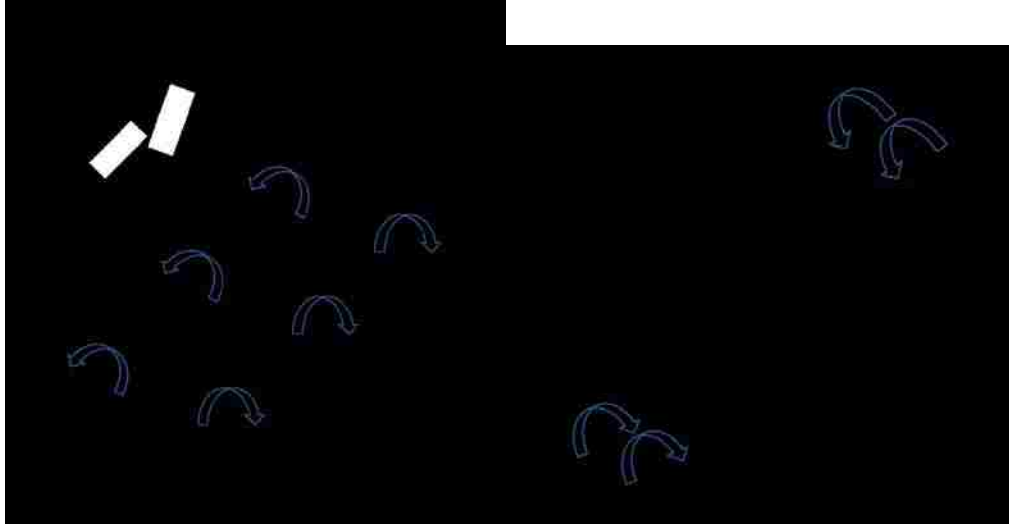


**Figure 4.9 Bending Moments and Curvatures in Tape Spring**

The tape spring curvatures  $\kappa_x$  and  $\kappa_z$  are defined as:

$$\kappa_x = \frac{1}{R} = \frac{1}{r_x} \quad (4.26)$$

$$\kappa_z = \frac{1}{r_z} \quad (4.27)$$

The general constitutive relations for forces and moments on a thin laminate are given as:

$$\begin{bmatrix} N_x \\ N_y \\ N_{xy} \end{bmatrix} = \begin{bmatrix} A_{11} & A_{12} & A_{16} \\ A_{12} & A_{22} & A_{26} \\ A_{16} & A_{26} & A_{66} \end{bmatrix} \begin{bmatrix} \varepsilon_x^0 \\ \varepsilon_y^0 \\ \varepsilon_{xy}^0 \end{bmatrix} + \begin{bmatrix} B_{11} & B_{12} & B_{16} \\ B_{12} & B_{22} & B_{26} \\ B_{16} & B_{26} & B_{66} \end{bmatrix} \begin{bmatrix} \kappa_x \\ \kappa_y \\ \kappa_{xy} \end{bmatrix} \quad (4.28)$$

$$\begin{bmatrix} M_x \\ M_y \\ M_{xy} \end{bmatrix} = \begin{bmatrix} B_{11} & B_{12} & B_{16} \\ B_{12} & B_{22} & B_{26} \\ B_{16} & B_{26} & B_{66} \end{bmatrix} \begin{bmatrix} \varepsilon_x^0 \\ \varepsilon_y^0 \\ \varepsilon_{xy}^0 \end{bmatrix} + \begin{bmatrix} D_{11} & D_{12} & D_{16} \\ D_{12} & D_{22} & D_{26} \\ D_{16} & D_{26} & D_{66} \end{bmatrix} \begin{bmatrix} \kappa_x \\ \kappa_y \\ \kappa_{xy} \end{bmatrix} \quad (4.29)$$

where the [A], extensional in-plane stiffness matrix, the [B], bending-extension coupling stiffness matrix and the [D], bending stiffness matrix terms are given as:

$$A_{ij} = \sum_{k=1}^N (\overline{Q}_{ij})_k (z_k - z_{k-1}) \quad (4.30)$$

$$A_{ij} = \sum_{k=1}^N (\overline{Q}_{ij})_k t_k$$

$$B_{ij} = \frac{1}{2} \sum_{k=1}^N (\overline{Q}_{ij})_k (z_k^2 - z_{k-1}^2) \quad (4.31)$$

$$D_{ij} = \frac{1}{3} \sum_{k=1}^N (\overline{Q}_{ij})_k (z_k^3 - z_{k-1}^3) \quad (4.32)$$

The  $ABD$  matrices provide a connection between the applied loads and the associated strains in the laminate, but are time independent (i.e., not viscoelastic). Due to their complex structure, various coupling effects exist in composite laminates. For example, the presence of the  $[B]$  matrix implies coupling of bending and extension of the laminate and is generally undesirable structural behavior. Often times, as in this research, the laminate is constructed in a symmetric fashion so  $[B] = 0$  and no such laminate coupling exists. However, it is not possible to eliminate all of the “16” and “26” stiffness terms for a laminate including angle plies, but the laminate can be tailored to reduce those terms (i.e.,  $A_{16}$  and  $A_{26}$  for in-plane shear-extension coupling and  $D_{16}$ , and  $D_{26}$  for bending-twisting coupling), therefore, their effect is minimal. The use of equations 4.30 to 4.32 allow determination of the effective two-dimensional engineering material properties of the homogeneous orthotropic laminate with the following expressions (Mikulas, 2000):

$$E_x = \frac{1}{t} \left( A_{11} - \frac{A_{12}^2}{A_{22}} \right) \quad (4.33)$$

$$E_y = \frac{1}{t} \left( A_{22} - \frac{A_{12}^2}{A_{11}} \right) \quad (4.34)$$

$$G_{xy} = \frac{1}{t}A_{66} \quad (4.35)$$

$$v_{xy} = \frac{A_{12}}{A_{22}} \quad (4.36)$$

where  $t$  is the total laminate thickness. The reciprocity relation,  $v_{xy}E_y = v_{yx}E_x$ , is also true. The engineering constants determined here enable a proper physical determination of the stiffness performance of the laminate.

Referencing **Figure 4.9** and equations 4.26 - 4.29 and using the X-Z plane as the plane stress plane, the bending moments applied to the tape spring per unit length for the curvature changes  $\kappa_x$ ,  $\kappa_z$  and  $\kappa_{xz} = 0$  are given as:

$$M_x = D_{12}\kappa_z + D_{22}\kappa_x \quad (4.37)$$

$$M_z = D_{11}\kappa_z + D_{12}\kappa_x \quad (4.38)$$

In this way the bending moments applied to the tape spring can be calculated in closed-form.

## 4.4 Abaqus Modeling

A time-dependent implicit finite element model was developed to model and simulate the stress relaxation and strain energy dissipation of an orthotropic CFRP composite laminate tape spring during stowage on a hub and subsequent deployment. In

all analysis steps, the applied loads and boundary conditions were ramped from zero with a smooth step amplitude curve to promote a quasi-static response in concert with how the experimental structural testing was conducted per Chapter 3.

Due to the complexity of the microstructure, homogenization techniques are often used in FEMs to simplify the analysis of loads and stresses. For example, a thin laminate consisting of a woven ply usually does not receive accurate results from CLT, for which UD composites work well. While in-plane properties can be achieved reasonably well, flexural/bending properties produce significant differences from real structural behavior. Previous research has shown CLT calculations can result in errors up to 200% in the maximum bending strain or stress and up to 400% in the bending stiffness. This deviation is because CLT assumes the laminate mid-plane as a reference plane and fibers are distributed homogeneously across the lamina thickness. Homogenized properties are then obtained by integrating through the lamina thickness. (Soykasap, 2006, 2011) It is clear CLT is not appropriate to use, directly, for thin composite laminate properties. However, there is value in using CLT as a point of departure. For example, Soykasap found predictions based on a CLT-hybrid for a three-ply composite laminate did approach FEM-produced values. (Soykasap, 2011)

The tape springs were modeled with conventional shell elements and with a laminated composite shell the transverse shear stress is zero at the free (i.e., outer) surfaces and may vary rapidly throughout the laminate thickness. While a continuous strain is reasonable to assume (unless there is delamination, debonding, etc.) through the plies, the stress is not continuous due to the inherently different lamina properties,

including modulus. Another key modeling consideration in the FEM is the Poisson's ratio in a viscoelastic material can be time-dependent for stress relaxation behavior. This aspect is addressed via the Prony Series implementation in the VUMAT.

Although FEMs can provide very good approximations of solutions to problems which cannot be solved analytically, there are some situations for which problems arise in using a FEM. Shear locking and hourglassing are two common major numerical problems because they may cause spurious solutions in certain situations. These problems involve interpolation failure in the elements and can lead to unexpected and unwanted behavior. Under some circumstances the displacements calculated by the FEM are orders of magnitude smaller than they should be and the elements are said to be locking. This behavior of excessive element stiffness in a FEM is characteristic of locking. Locking occurs in first order (i.e., linear) elements because an element's kinematics are not rich enough to represent the correct solution. Locking can occur for a number of reasons and, for some element types, can even depend on the shape of an element. Locking happens when an element cannot interpolate a field property correctly with the nodal values and element's shape functions. Increasing the number of elements can delay the effects of locking to values of Poisson's ratio closer to 0.5. However, this option is not a very desirable solution because it merely takes more computational power and still does not solve the problem completely; it only delays it. The two most common types of FEM locking are shear locking and pressure locking. Shear locking occurs when elements are subjected to bending and arises when the shear component is calculated by means of a wrongly interpolated displacement field that is prescribed to describe in plane bending using a plane stress formulation. The size of the error caused by this type of

locking depends on the aspect ratio of the element and grows larger with increasing aspect ratios. (Van den Oord, 2005) The overall effect is the linear fully integrated element becomes locked or overly stiff under the bending moment. Wrong displacements, false stresses and spurious natural frequencies may be reported because of shear locking. (Vermeulen and Hepler, 1998, Sun, 2010)

Using reduced integration with first order elements in Abaqus can alleviate locking, but it can also cause unwanted behavior of the element because reduced integration reduces the rank of the total stiffness tensor and the tensor can then become singular or ill-conditioned. (Van den Oord, 2005, Stolarski and Telytschko, 1983) Better results (i.e., no shear locking) can be achieved with fully integrated second order elements as an alternative to using reduced integration first order elements. However, this solution is not perfect either as reduced integration second order elements suffer from their own numerical difficulty called hourglassing (especially with a coarse mesh). In order to make the second order reduced integration elements useful, Abaqus provides default hourglassing control internally. With hourglassing control the fully integrated second order elements behave differently since their edges are able to bend to curves and no shear locking is associated with this type of element either. While a second order element with reduced integration can suffer from hourglassing, it rarely causes numerical problems because it virtually vanishes with two or more layers of elements. No special technique is needed to control it, but at least four layers of elements is recommended in a bending problem. (Sun, 2010)

It is computationally impractical to model the tape spring simulation process in its natural time period as millions of time increments would be required in the FEA. Abaqus provides two methods for obtaining a computationally efficient solution in an Abaqus/Explicit simulation: mass scaling and increased load rates. Thus, artificially increasing the speed of the process in the simulation was necessary to obtain an economical solution. In this way, the material can be modeled in its natural time period with mass scaling. Mass scaling artificially increases the material density by a factor of  $f^2$ , which then increases the stable time increment by a factor of  $f$ . (Abaqus, 2014) Mass scaling increases the size of the stable time increment during the element calculations, hence, fewer increments are needed to complete the job. As the speed of the process is increased, a state of static equilibrium evolves into a state of dynamic equilibrium. Since viscoelastic materials are sensitive to strain rate, the increased load rate option was not used in this work.

However, excessive mass scaling can lead to erroneous solutions. A plethora of mass scaling options may produce FEM simulation results, but they must be checked for validity. For this reason, many different mass scaling factors were modeled and analyzed to achieve reasonable results. The overall goal was to model the process in the shortest time period. In the Abaqus/Explicit model used for steps 1 and 2 (flatten and rolling of the tape spring) a fixed mass scaling factor was used at the beginning of step 1 with a stable target time increment of  $1 \times 10^{-5}$ . A variable mass scaling factor was used throughout step 2 with a target time increment of  $1 \times 10^{-4}$  at a frequency of every 500 increments with mass scaling applied to only elements below the minimum target value specified or uniformly to all elements. Both options produced results. Several

conclusions can be drawn from the mass scaling sensitivity analysis. The stable time increment is incredibly sensitive for convergence of the model. Increasing the stable time increment up or down just one order of magnitude caused the analysis to abort with excessive rotations and displacements of tape spring elements and inappropriate ratios of deformation speed to wave speed in the material. However, the frequency of the mass scaling update per step time incrementation permitted a wider latitude of hundreds to thousands of increments wherein the model would still converge. Finally, Abaqus offers mass scaling to be performed as either fixed or variable. Fixed mass scaling worked well for the flatten tape spring step and variable mass scaling worked well for the rolling and unrolling steps. One of the major differences in these approaches lies in *when* during the analysis step the mass scaling occurs. Fixed mass scaling occurs at the beginning of the step and variable mass scaling occurs throughout the analysis step. Note Abaqus also offers the option to perform both fixed and variable mass scaling during an analysis step but the fixed mass scaling occurs first followed by the variable mass scaling. However, this option did not work in this research.

A viscous pressure load was applied to the tape spring as an effective way to damp out the dynamic effects quickly and reach quasi-static equilibrium after the tape spring deployment in the minimum number of increments. A viscous pressure load is commonly used in FEMs to damp out kinetic energy associated with structural motion, usually on the surface of a body. Without the viscous pressure load applied, the tape spring experienced wave-like structural motion as dynamic perturbations. The viscous pressure was applied to the surface of the tape spring only as structural damping itself is distinctly different and implemented in the FEM within the material properties. The

value used for viscous damping,  $C_v$ , in the model is typically set equal to 1% – 2% of the product of the tape spring’s laminate density,  $\rho$ , and dilatational wave speed,  $C_d$ :

$$\rho C_d = \rho \sqrt{\frac{E(1-\nu)}{\rho(1+\nu)(1-2\nu)}} \quad (4.39)$$

where  $E$  is the laminate’s longitudinal modulus and  $\nu$  is the laminate’s major Poisson’s ratio.

Abaqus/Explicit has an interface allowing the user to implement general constitutive equations with the user-defined material model in the user subroutine VUMAT. This subroutine interface makes it possible to define any (including proprietary) constitutive material model of arbitrary complexity. One advantage is a user-defined material model can be used with any Abaqus structural element type as well.

Transformation of the constitutive rate equation into an incremental equation using a suitable integration procedure is done in Abaqus via the Backward Euler operator for Implicit integration (and via the Forward Euler operator for Explicit integration). Thus, for the quasi-static tape spring stowage application, the operator matrix is inverted and a set of simultaneous nonlinear dynamic equilibrium equations are solved for each time increment of the stow analysis step in the model. (Abaqus, 2014) The solution is then calculated iteratively using Newton’s method, though Abaqus has the option of “Full Newton” versus “Quasi-Newton” solution techniques for this analysis. The analysis can also be done in single precision model (i.e., to 8 decimal points) or done per double precision (i.e., to 16 decimal points). In some Abaqus model runs the model would abort

in single precision model, which runs faster, but converge in double precision model. In general, double precision mode took approximately twice as long computationally.

In summary, the key techniques implemented in the tape spring FEM included the Prony series via the VUMAT, both fixed and variable mass scaling, common CLT assumptions, reduced integration elements for shear locking and hourglass control, a viscous pressure load and a classical modeling simulation to address the different types of analysis required for this problem, namely, rolling and contact dynamics with the tape spring rolling onto the hub, a quasi-static tape spring stowage period of time and the subsequent tape spring deployment (unrolling and contact) and settling dynamics.

## CHAPTER 5 RESULTS AND DISCUSSION

### 5.1 Neat Epoxy DMA Test Results

DMA tests were conducted on coupons of both the neat epoxy and ANP-doped epoxy. The DMA test results of the ANP coupons are presented and discussed in section 5.3. DMA testing was conducted to characterize the viscoelastic performance of the matrix material of the tape springs. Analysis of the DMA test results produced a master relaxation curve of the epoxy from which the two Williams, Landel and Ferry (WLF) constants, i.e.,  $C_1$  and  $C_2$ , could be ascertained through a nonlinear curve fitting method, the Levenberg Marquardt Method. The  $C_1$  and  $C_2$  were used in the WLF equation:

$$\log a_T(T) = \frac{C_1(T - T_0)}{C_2 + T - T_0} \quad (5.1)$$

Evaluation of the WLF equation per the TTSP permitted the determination of the shift factor,  $a_T(T)$ , to efficiently perform long duration viscoelastic tests at higher temperature and shorter duration. This procedure permitted viscoelastic structural testing at equivalent times up to 6 months of natural time at a mere fraction of test time.

The DMA test data consisted of a uniformly sampled series of nonlinear exponentials, and as such, a Prony analysis has been shown to be a viable technique for modeling these kinds of complex exponentials. The Prony method was developed in 1795 by Gaspard Riche, Baron de Prony. It is a numerically intensive algorithm involving solution of an over-determined set of linear equations and rooting of a high

order polynomial and fits a curve to a sum of damped complex exponentials. A least-squares fit of a Prony series was fit to the experimental data/curve from the DMA testing. A form of a general Prony series for the constitutive equation of the material's relaxation modulus is given as:

$$\sum_{i=1}^N \kappa_i e^{-t/\tau_i} \quad (5.2)$$

where  $\kappa_i$  are the relaxation coefficients and  $\tau_i$  are the time constants and both together constitute a Prony set. Each Prony set is associated with the material's internal state at a specific time and each set in the series adds a considerable number of global variables, and thus, finite element computation time. Therefore, it is desirable to have as short a Prony series as possible which can accurately represent the material's behavior.

In this research work the epoxy matrix was modeled as an isotropic viscoelastic solid and thus its modulus (i.e., relaxation modulus,  $E_r(t)$ ) can also be modeled via a Prony series of the form:

$$E_r(t) = E_\infty + \sum_{i=1}^N E_i e^{-t/\tau_i} \quad (5.3)$$

where  $E_\infty$  is the long term (or glassy) modulus,  $E_i$  are the relaxation coefficients and  $\tau_i$  are the retardation time constants. The  $\tau_i$  are also known as relaxation times of the material and can be further defined as:

$$\tau = \eta/k \quad (5.4)$$

where  $\eta$  is the viscosity and  $k$  is the stiffness.

Experimental data for the time-dependent behavior (i.e., stress relaxation) of polymers can be represented not only in the time domain but also in the frequency domain as a complex modulus, as a function of frequency,  $\omega$ , and temperature,  $T$ :

$$E^*(\omega, T) = E'(\omega, T) + iE''(\omega, T) \quad (5.5)$$

where  $E'(\omega, T)$  is the storage modulus describing the elastic properties of the material and  $E''(\omega, T)$  is the loss modulus describing the viscous properties of the material corresponding to energy loss. The storage and loss moduli of the neat epoxy are shown below in **Figure 5.1**:

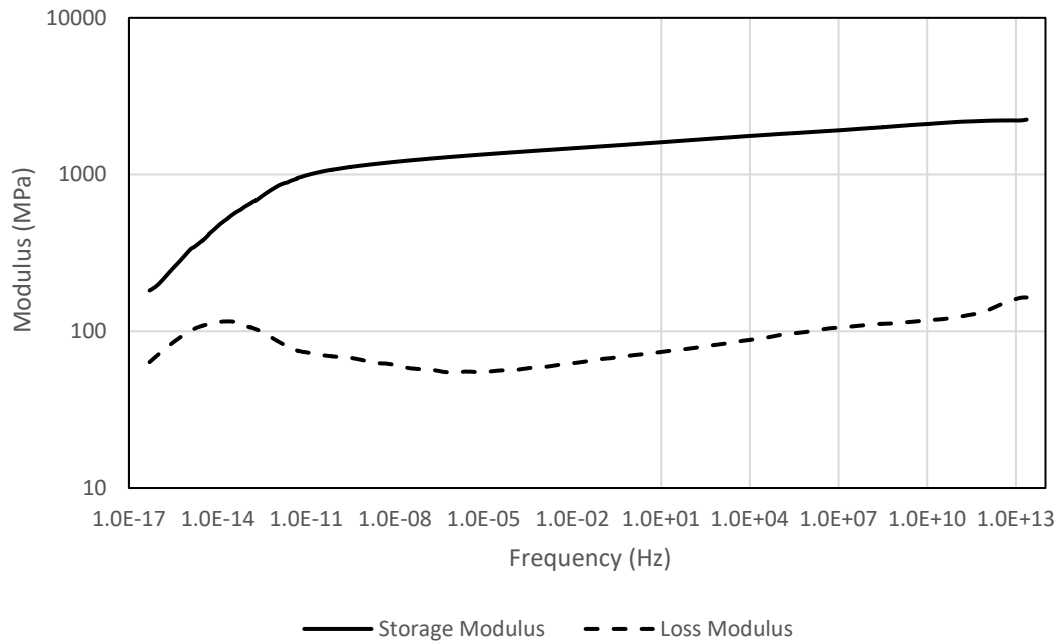


**Figure 5.1 Neat Epoxy Storage and Loss Moduli as a Function of Frequency (Log Scale)**

The storage modulus,  $E'$ , describes the elastic properties of the material and the loss modulus,  $E''$ , describes the viscous properties. The loss modulus corresponds to the amount of energy loss dissipating in the material and is related to the material's ability to dissipate stress through irreversible heat loss.

The storage modulus and the loss modulus can be expressed using Prony series parameters as a function of frequency and time:

$$E'(\omega) = E_{\infty} + \sum_{j=1}^N E_j \frac{\omega^2 \tau_j^2}{1 + \omega^2 \tau_j^2} \quad (5.6)$$

$$E''(\omega) = E_{\infty} + \sum_{j=1}^N E_j \frac{\omega \tau_j}{1 + \omega^2 \tau_j^2} \quad (5.7)$$

where  $E_j$  are the relaxation coefficients and  $\tau_j$  are the relaxation times. (Ng et al., 2008, Liebich et al., 2012) Both terms together constitute a set of Prony series coefficients which represent one Maxwell element. The Prony series relaxation coefficients and relaxation time constants can be determined with a regression analysis of the complex modulus in the frequency domain, which is equivalent to the relaxation modulus in the time domain. This approach is based on time-temperature-equivalence and frequency-temperature-equivalence and implies the viscoelastic behavior at one temperature can be related to that at another temperature by a change in the time or frequency scale. Using the frequency-temperature-equivalence principle with the DMA test data at 22 different isotherms, a smooth master curve was formed of the complex modulus versus frequency. Instead of a time-shifted curve it is a frequency-shifted curve as shown in **Figure 5.2**.

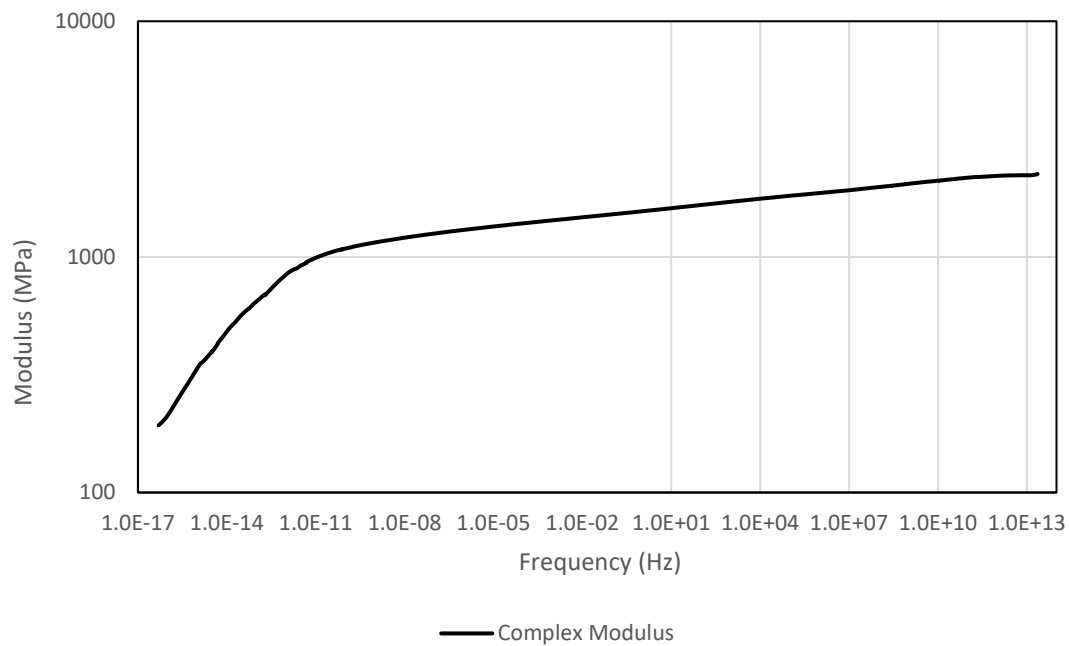


**Figure 5.2 Neat Epoxy Complex Modulus Master Curve in Log-Log Plot**

The data comprising the master curve in **Figure 5.2** was analyzed via a discrete relaxation spectrum curve fit. The parameters were set to calculate the long-term modulus with 10 Prony series coefficients. The curve fitting technique implemented in the TA Instruments' Trios software is the Levenberg-Marquardt algorithm, also known as the damped least squares method, and is used to solve nonlinear least squares problems such as the present one. Graphically, the Prony series is displayed as shown in **Figure 5.3**:

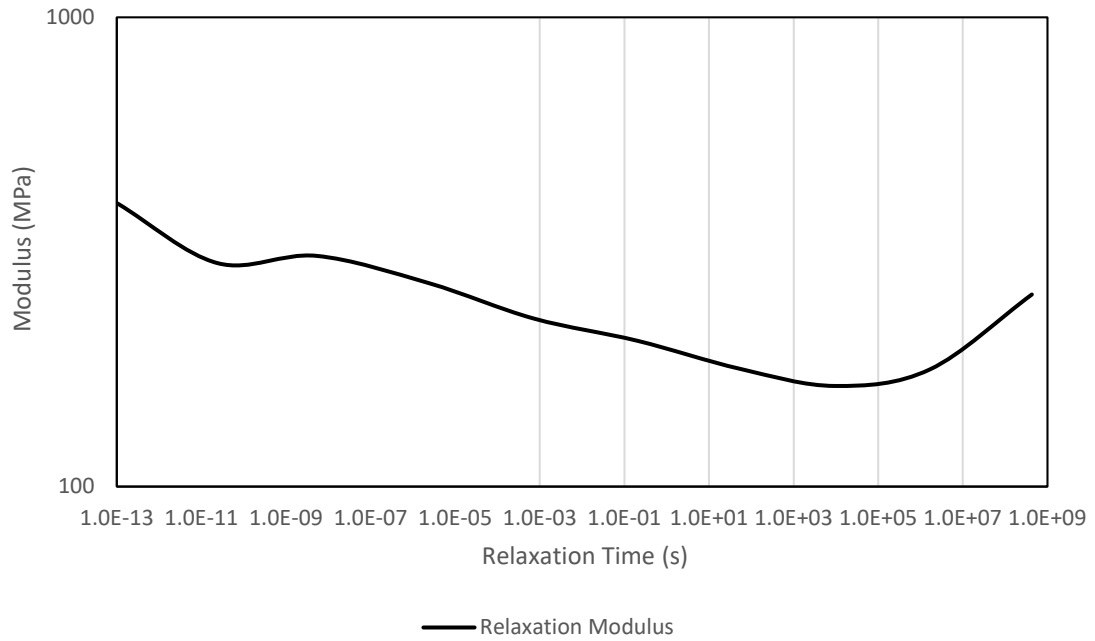
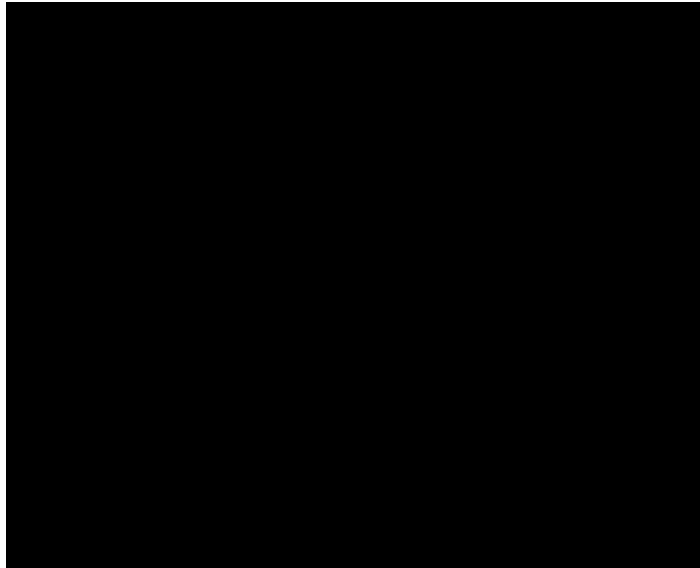


**Figure 5.3 Prony Series Curve for Relaxation Modulus of Neat Epoxy in Log-Log Plot**

The elements of the Prony series are given in **Table 5.1** as:

Table 5.1 Prony Series Coefficients for Neat Epoxy



The Prony series coefficients were coded directly into the VUMAT subroutine material models in Abaqus to govern the viscoelastic behavior of the tape springs during the roll up onto the hub, stowage and subsequent deployment. The Prony series parameters in the VUMAT can be seen in Appendix C.

## 5.2 Control Tape Springs' Test Results

Twenty-six control tape springs were structurally tested on a 10 kN MTS Instron machine. Per the process, procedures and setup detailed in **Chapter 3**, five tape springs each were tested at stowage times of 1 hour and 1 day, and at the time-temperature-equivalence (per TTSP) of 1 week, 1 month and 6 months. One extra tape spring was tested in the 1 week group. Detailed measurements for each tape spring are provided in Appendix A.

### 5.2.1 One Hour Tape Springs' Test Results

The structural test results for the five 1 hour control tape springs are shown in **Figure 5.4** below. The change in tape spring tip deployment force manifests itself as a decrease in deployment force. The average decrease in the control tape springs' deployment force after 1 hour of stowage was 0.086%. These results will be compared to the other structural tests results in section 5.5. One hour of stowage had negligible effects upon the control tape springs' deployment force.

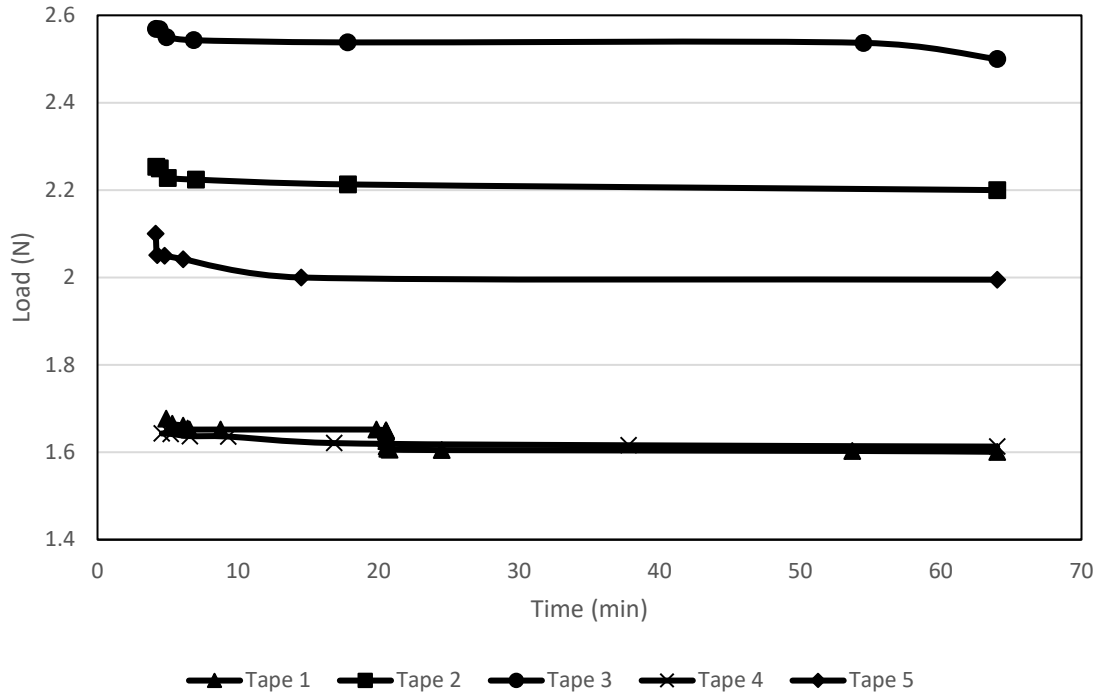


**Figure 5.4 Control Tape Springs One Hour Stowage Results Showing Loss in Tape Spring Deployment Force Over Time**

### 5.2.2 One Day Tape Springs' Test Results

The structural test results for the five control tape springs with 1 day of stowage are shown in **Figure 5.5** below. The average loss of deployment force at the tape springs' tips was 0.004% over the course of 24 hours. This deployment force loss is very small and insignificant in the realm of design margin for sufficient deployment force on-orbit, but it will be put into perspective when compared to all the tape springs' test data in

section 5.5. One day of stowage had negligible effect on the control tape springs' deployment force.

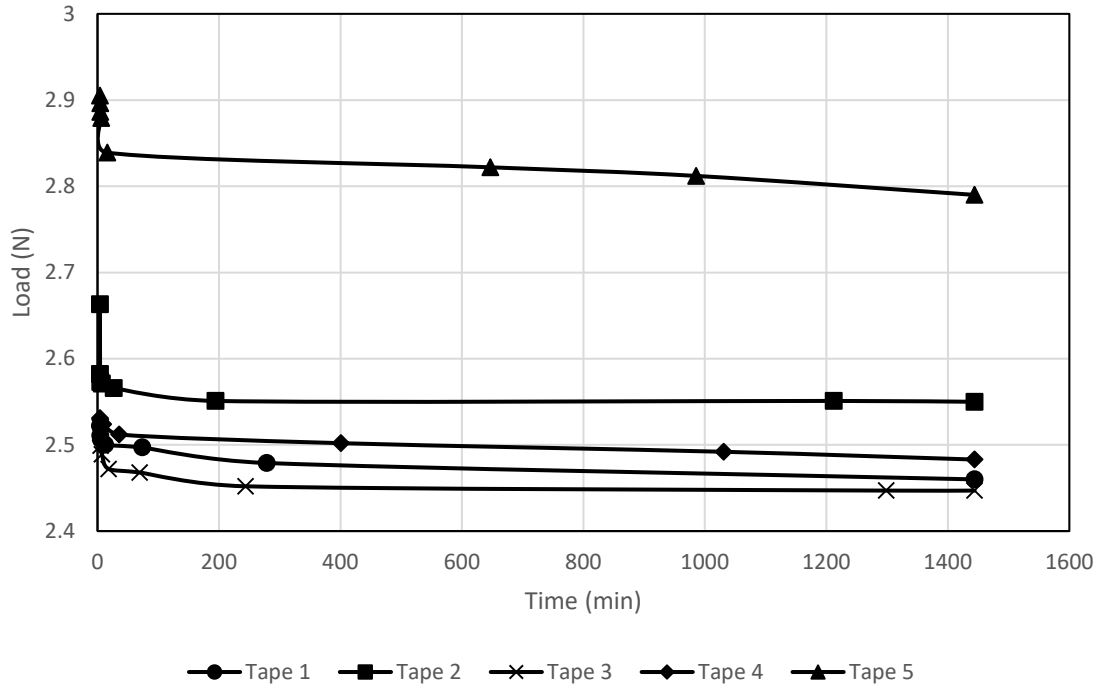


**Figure 5.5 Control Tape Springs One Day Stowage Results Showing Loss in Tape Spring Deployment Force Over Time**

### 5.2.3 One Week Tape Springs' Test Results

The structural test results for the 6 control tape springs stowed for an equivalent 1 week of natural time are shown in **Figure 5.6** below. Per the neat epoxy DMA testing and subsequent TTSP analysis, 1 week of structural test time at ambient temperature was

reduced to 4.0 minutes at 200° F, per section 3.3 and equation 3.3. It is evident from **Figure 5.6** there was a non-trivial difference in how tape spring 1 behaved with respect to the remaining four tape springs which were bunched relatively close together. The cause for this difference can't be known for certain, but could be due to slight laminate fabrication differences, test setup deltas in geometry, or lamina material irregularities.

The average loss of deployment force at the tape springs' tips was 4.4% over the course of 1 week of equivalent natural time. This loss of deployment loss force is substantially more than the amount observed for the 1 hour and 1 day stowage tests. However, the tape springs' composite laminate behavior is clearly nonlinear for the tape springs and, in general, a substantial amount of relaxation occurs within the first quarter to third of the structure's service life.

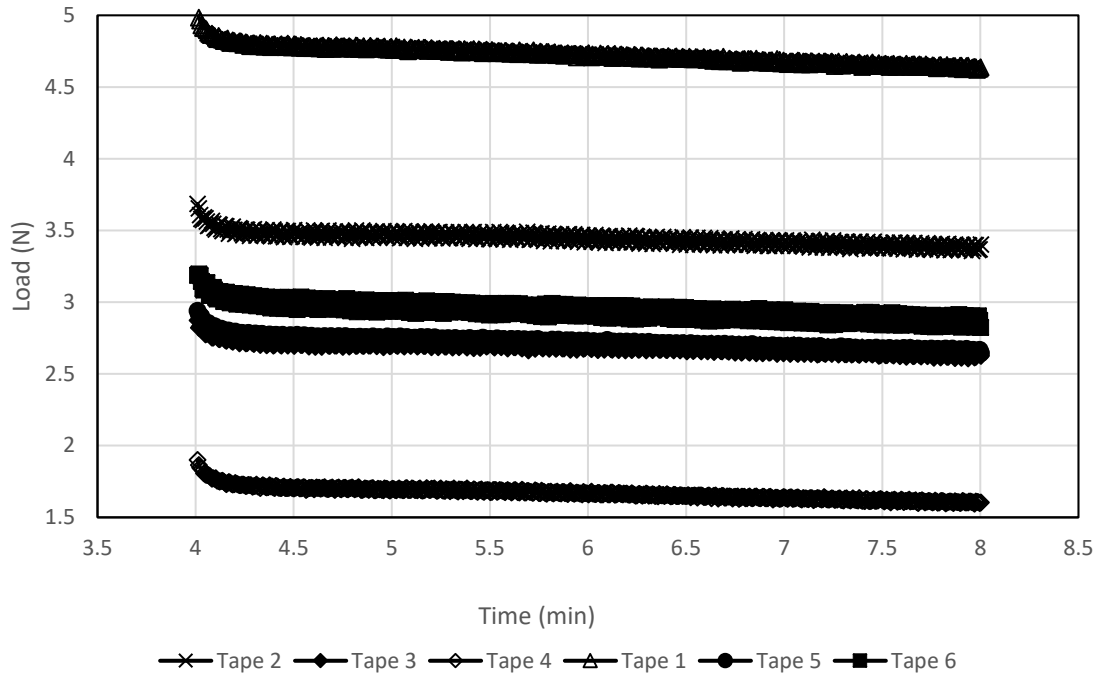


**Figure 5.6 Control Tape Springs One Week Stowage (via TTSP) Results Showing Loss in Tape Spring Deployment Force Over Time**

### 5.2.4 One Month Tape Springs' Test Results

The structural test results for the five control tape springs stowed for an equivalent of 1 month of natural time are shown in **Figure 5.7** below. Per the neat epoxy DMA testing and subsequent TTSP analysis, 1 month of structural test time at ambient temperature was reduced to 15.9 minutes at 200° F, per section 3.3 and equation 3.3. The average loss of deployment force at the tape springs' tips was 1.8% over the course of 1 month of equivalent natural time. This is an important amount of loss of deployment

force over only a month of time considering the typical stowage time for space deployable structures is usually on the order of months.

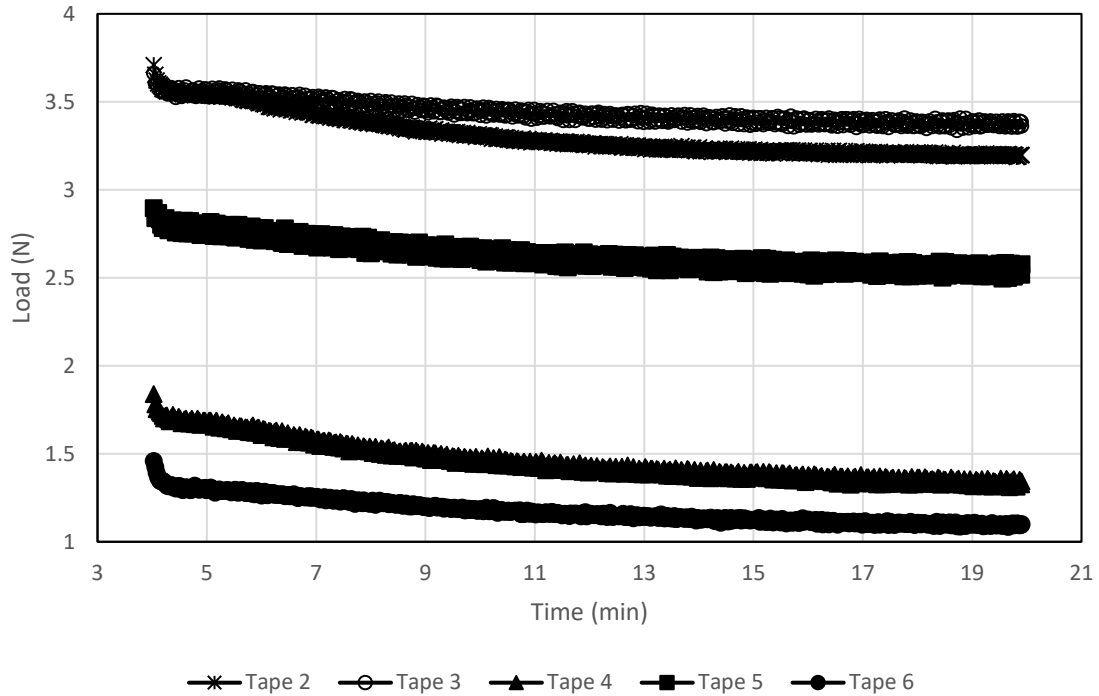


**Figure 5.7 Control Tape Springs One Month Stowage (via TTSP) Results Showing Loss in Tape Spring Deployment Force Over Time**

### 5.2.5 Six Months Tape Springs' Test Results

The structural test results for the five control tape springs stowed for an equivalent of 6 months of natural time are shown in **Figure 5.8** below. Per the neat epoxy DMA testing and subsequent TTSP analysis, 6 months of structural test time at

ambient temperature was reduced to 95.7 minutes at 200° F, per section 3.3 and equation 3.3. The average loss of deployment force at the tape springs' tips was 0.15% over the course of 6 months of equivalent natural time. It is also worth observing from **Figure 5.8**, tape springs 3, 4 and 5 are relatively close together in structural behavior and tape springs 1 and 2 are also relatively close together but there is a considerable gap ( $\sim 2$  N) in their deployment force performance. This may be due to variations in the tape springs' fabrication because of their extremely thin cross-sectional dimension. Even slight imperfections in geometry, loading, layup construction and constituents' irregularities in purity can all perturb the tape springs' structural behavior from an ideal one. However, the deployment force loss observed with this group of tape springs was very small.

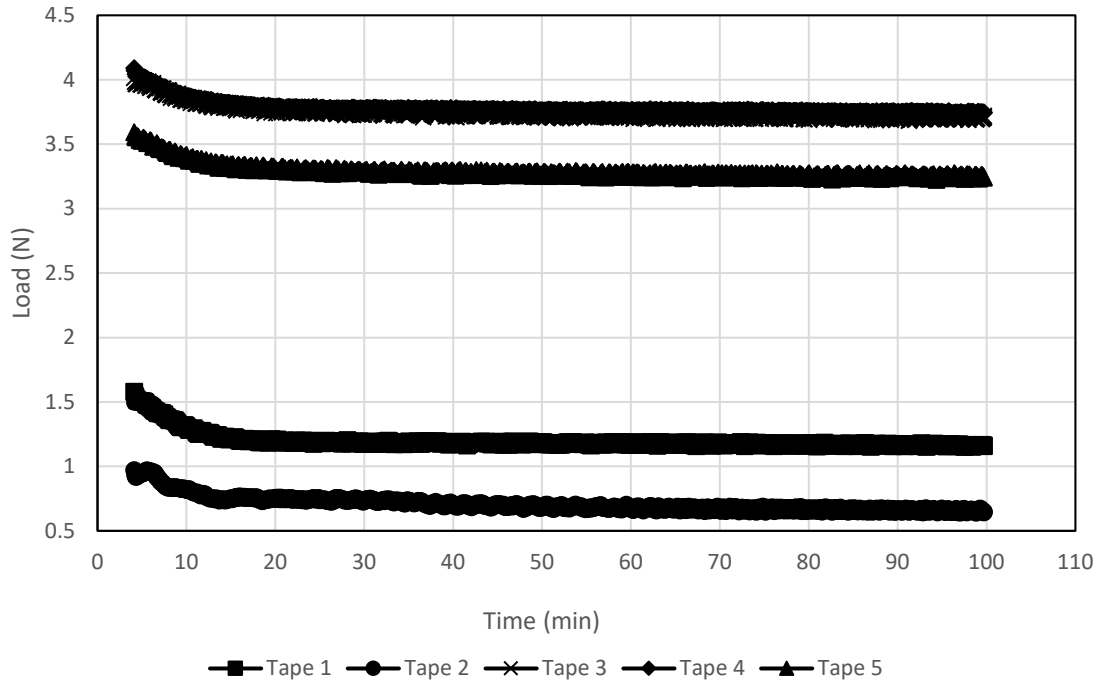


**Figure 5.8 Control Tape Springs Six Months Stowage (via TTSP) Results Showing Loss in Deployment Force Over Time**

### 5.3 ANP Epoxy DMA Test Results

DMA testing of the ANP-doped epoxy was conducted analogously to how the neat epoxy DMA testing was done. Coupons were tested at UNM’s Composites Laboratory using the TA Instruments Q800 DMA machine. Per section 5.1 above, the DMA experimental test data can be represented as storage modulus and loss modulus versus frequency per **Figure 5.9**, or combining them as a complex modulus versus

frequency per **Figure 5.10**. A comparison of the neat and ANP complex moduli is shown in **Figure 5.11**.

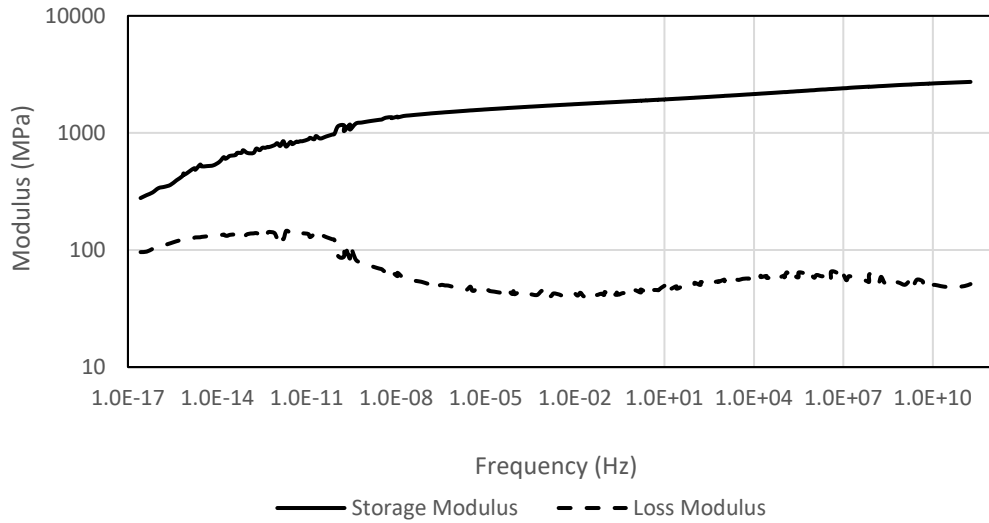


**Figure 5.9 ANP Epoxy Storage and Loss Moduli in Log-Log Plot**

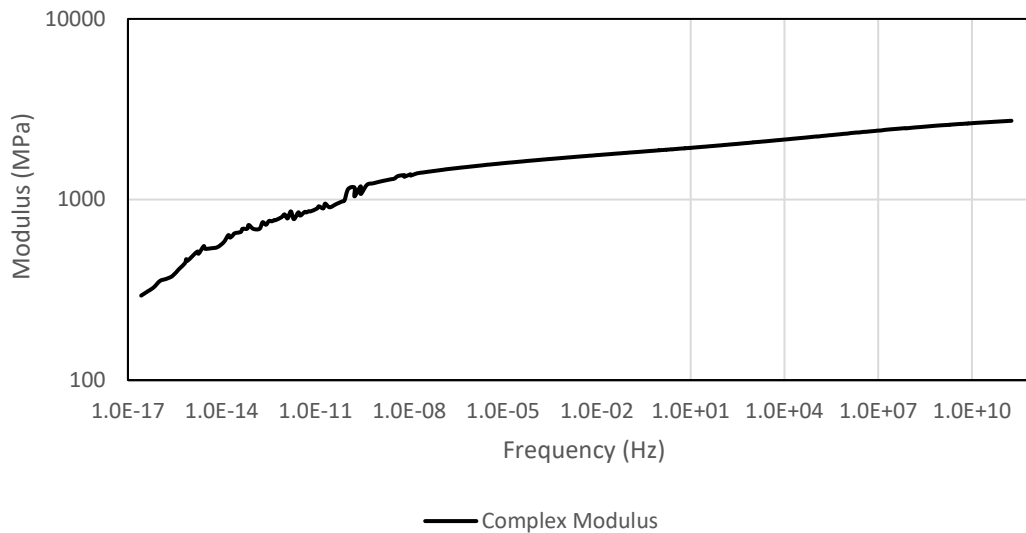


**Figure 5.10 ANP Epoxy Complex Modulus Master Curve in Log-Log Plot**

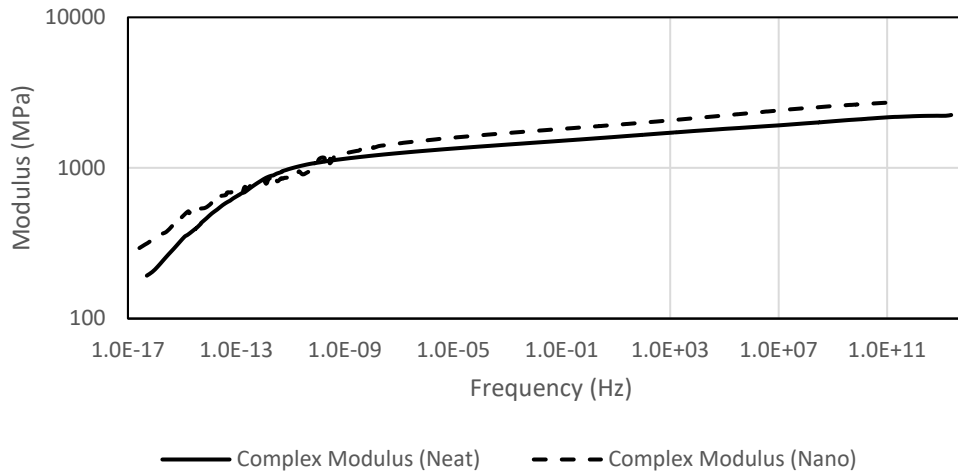


**Figure 5.11 Neat Epoxy and ANP Epoxy Complex Moduli Comparison in Log-Log Plot**

A further comparison between the loss and storage moduli of the neat epoxy and the ANP epoxy is show in **Figures 5.12 and 5.13** below.

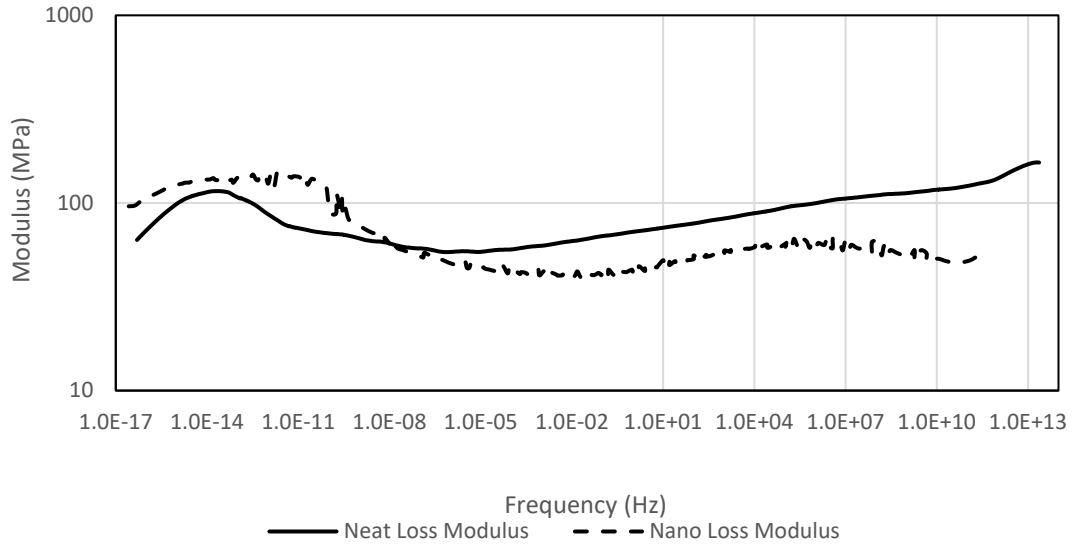


**Figure 5.12 Neat Epoxy and ANP Epoxy Comparison of Loss Moduli in Log-Log Plot**

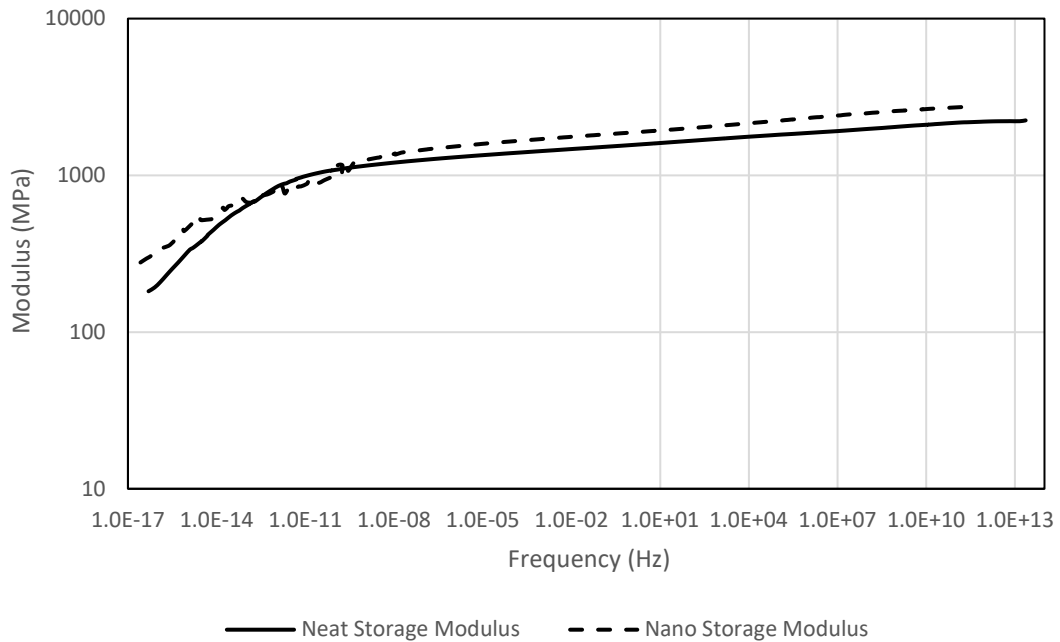


**Figure 5.13 Neat Epoxy and ANP Epoxy Comparison of Storage Moduli in Log-Log Plot**

As with the neat epoxy, the Prony series curve fit of the experimental ANP epoxy DMA test data was done via TA Instruments' Trios version 4.3 software as downloaded

from the manufacturer. The Prony series analysis of the DMA data resulted in a graph of relaxation mode versus relaxation time, as shown in **Figure 5.14**, and the Prony series coefficients were extracted as documented in **Table 5.2** below.

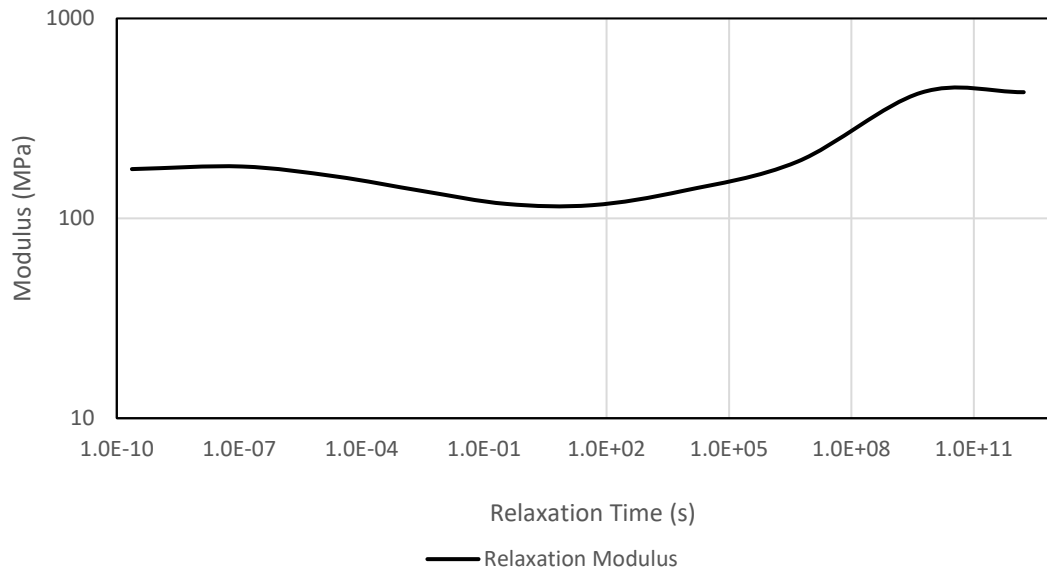


**Figure 5.14 Prony Series Curve for Relaxation Modulus of ANP Epoxy in Log-Log Plot**

Table 5.2 Prony Series Coefficients for ANP Epoxy

	$\kappa_i$	$\tau_i$
1	0.176	2.35E-10
2	0.182	1.18E-07
3	0.162	2.31E-05
4	0.137	2.99E-03
5	0.118	3.50E-01
6	0.116	4.43E+01
7	0.137	7.80E+03
8	0.192	4.84E+06
9	0.425	5.05E+09
10	0.428	1.67E+12

#### 5.4 ANP Tape Springs' Test Results

The 25 ANP tape springs were tested in exactly the same manner as the 26 control tape springs. The identical test setup, process and procedures were used. Detailed measurements for each of the ANP tape springs are found in Appendix B. It is important to note the length and width of the 51 tested tape springs were quite consistent; the average measured thickness for the control tape springs was 0.216 mm while the average

measured thickness for the ANP tape springs was 0.256 mm. It was not possible to measure the individual ply thicknesses during the composite laminate fabrication process. However, from prior research work on the FlexLam composite by Peterson (Peterson and Murphey, 2013), in which his composite was the same composite used as the control tape springs in this research, his plies were found to be 0.069 mm for the PW plies and 0.090 mm for the UD ply. The fact the ANP tape springs were on average 19% thicker in the cross section may play a role in their structural performance.

#### **5.4.1 One Hour Tape Springs' Test Results**

The structural test results for the five ANP tape springs with 1 hour of stowage time are shown in **Figure 5.15** below. The average loss of deployment force at the tape springs' tips was 0.28% over the course of 1 hour. In comparison, all five tape springs were within approximately 0.8 N of structural deployment force performance.

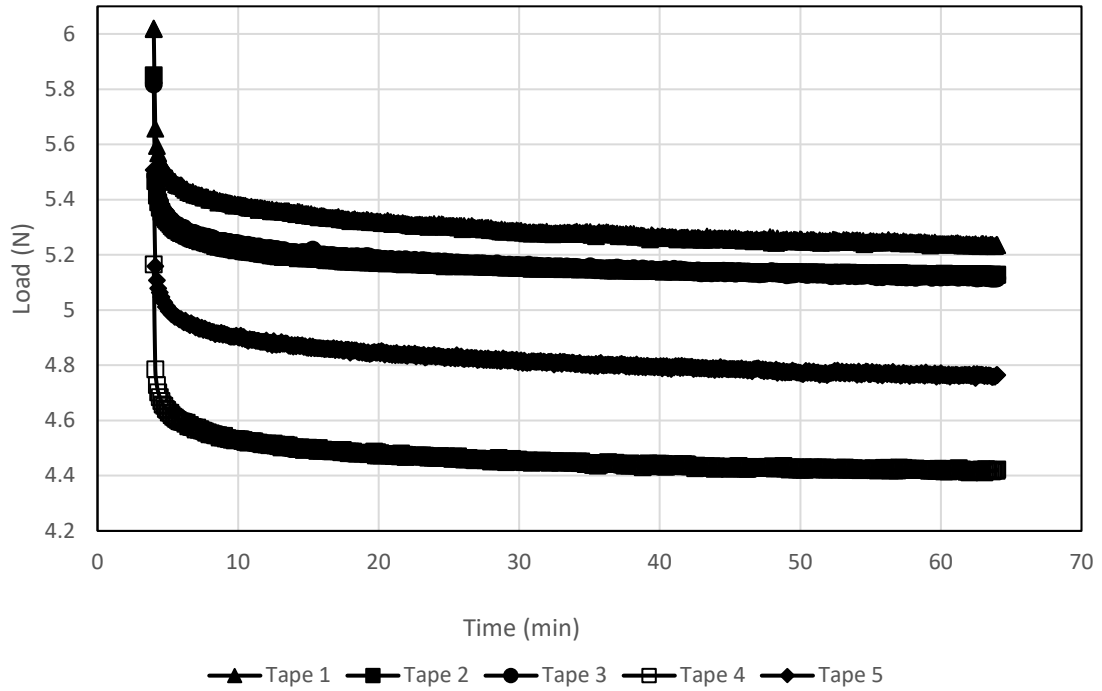


**Figure 5.15 ANP Tape Springs One Hour Stowage Results Showing Loss in Tape Spring Deployment Force Over Time**

#### 5.4.2 One Day Tape Springs' Test Results

The structural test results for the five ANP tape springs with 1 day of stowage time are shown in **Figure 5.16** below. It is readily apparent from viewing **Figure 5.16** these tape springs did not perform as any of the other test tape springs, control or ANP.

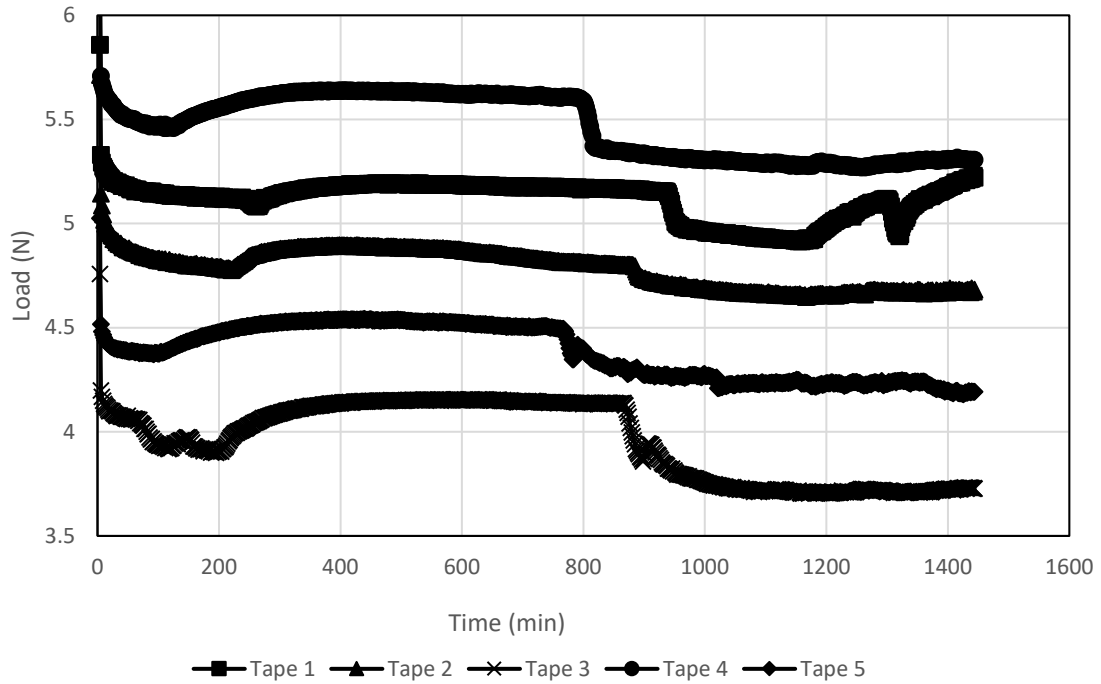


**Figure 5.16 ANP Tape Springs One Day Stowage Results Showing Loss in Tape Spring Deployment Force Over Time**

All the tape springs had similar behavior but much different than all the other tape spring testing results. The tape springs do appear to behave similar to the other tape springs for the first 150 – 250 minutes and then all gradually have increasing deployment force. This behavior persists until 790 – 900 minutes when four of the five tape springs show more characteristic behavior compared to the other structural tests. It is useful to investigate why the tape springs relaxed for 3 – 4 hours, then unleashed additional strain energy for approximately 9 hours and finally returned to relaxation behavior. For this reason, it is worthwhile to compare the results in **Figure 5.16** with the corresponding results from the control tape springs tested for 1 day. **Figure 5.17** shows this comparison.

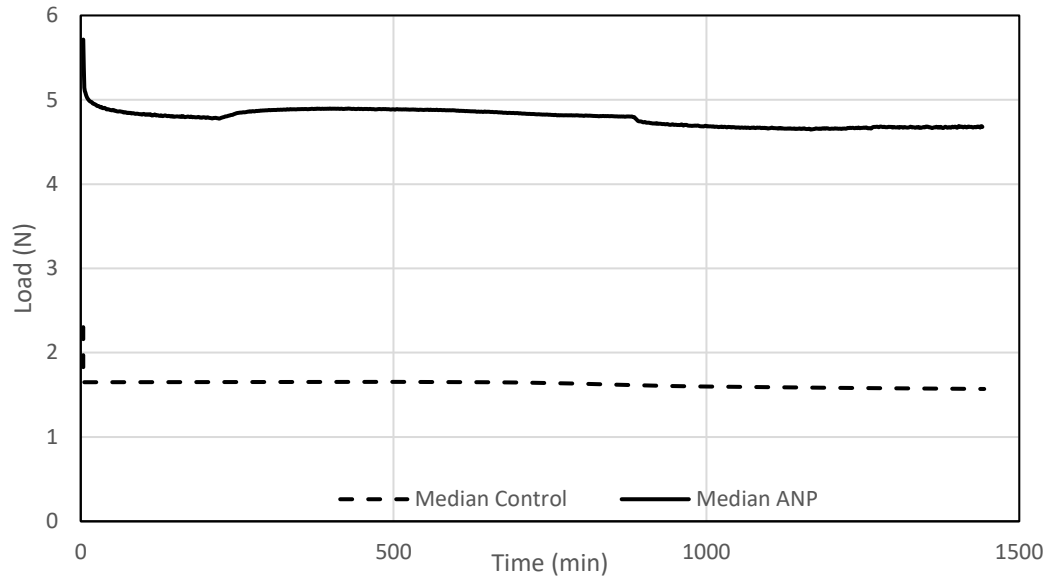


**Figure 5.17 Median Control Group Tape Spring and Median ANP Group Tape Spring One Day Stowage Tests' Comparison**

Comparing the 1 day median control tape spring and the 1 day median ANP tape spring reveals a more normalized behavior per **Figure 5.17**. The ANP tape spring shows approximately 3 N more deployment force at the tip compared to the control tape spring. However, the control tape spring experiences more deployment force loss at the tape spring tip at 0.03% over the course of 1 day compared to 0.02% for the ANP tape spring.

### 5.4.3 One Week Tape Springs' Test Results

The structural test results for the five ANP tape springs with 1 week of stowage time are shown in **Figure 5.18** below. Per the ANP epoxy DMA testing and subsequent

TTSP analysis, 1 week of structural test time at ambient temperature was reduced to 5.8 minutes at 200° F, per section 3.3 and equation 3.3. The average loss of deployment force at the tape springs' tips was 5.9% over the course of 1 week equivalent natural time. In comparison, all five tape springs were within 1 N for their structural deployment performance behavior.

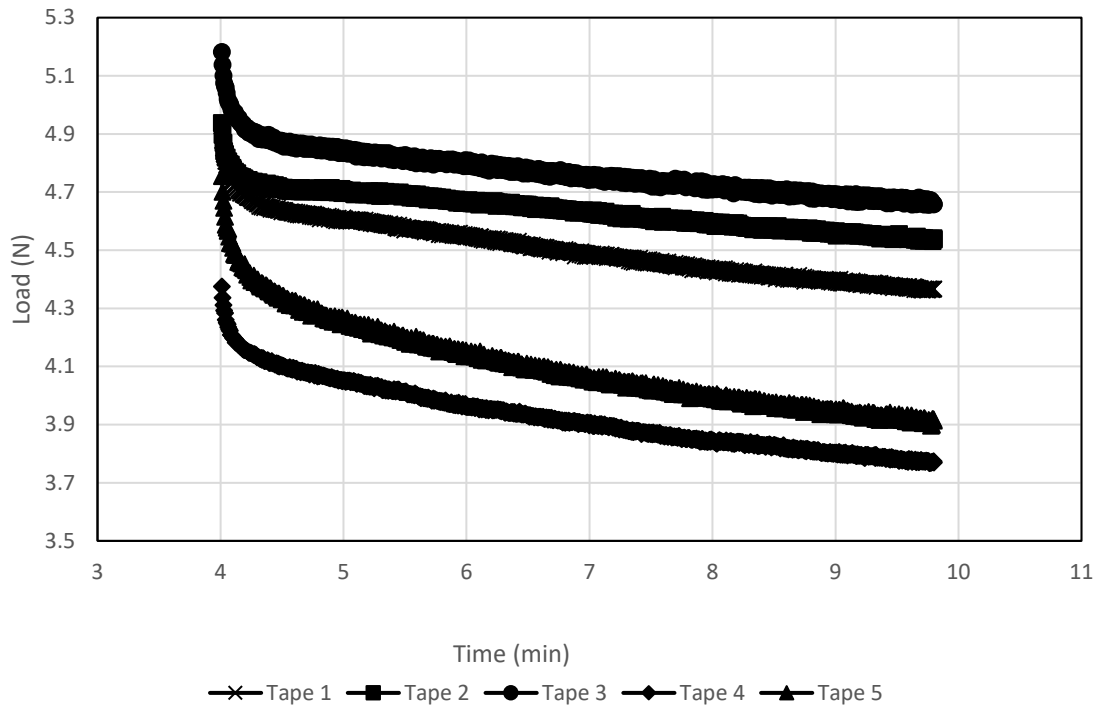


**Figure 5.18 ANP Tape Springs One Week Stowage (via TTSP) Results Showing Loss in Tape Spring Deployment Force Over Time**

#### 5.4.4 One Month Tape Springs' Test Results

The structural test results for the five ANP tape springs with 1 month of stowage time are shown in **Figure 5.19** below. Per the ANP epoxy DMA testing and subsequent TTSP analysis, 1 month of structural test time at ambient temperature was reduced to 23.1 minutes at 200° F, per section 3.3 and equation 3.3. The average loss of deployment force at the tape springs' tips was 1.2% over the course of 1 month equivalent natural time. Four of the tape springs were within approximately 1 N for their structural deployment performance. Tape spring 4 was a bit of an outlier and had approximately 0.75 – 1 N less deployment force than the other tape springs. The reason for this difference may be due to fabrication variances or layup and geometry irregularities.

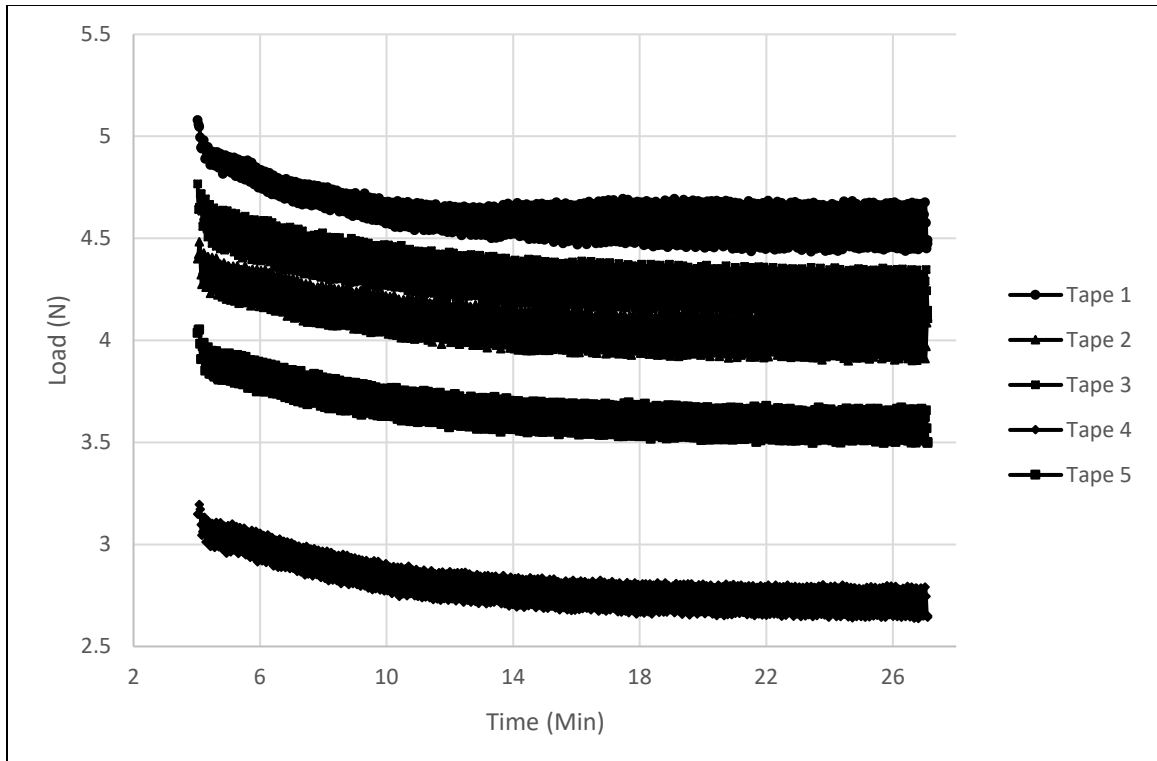


**Figure 5.19 ANP Tape Springs One Month Stowage (via TTSP) Results Showing Loss in Tape Spring Deployment Force Over Time**

#### 5.4.5 Six Months Tape Springs' Test Results

The structural test results for the five ANP tape springs with 6 months of stowage time are shown in **Figure 5.20** below. Per the ANP epoxy DMA testing and subsequent TTSP analysis, 6 months of structural test time at ambient temperature was reduced to 138.9 minutes at 200° F, per section 3.3 and equation 3.3. The average loss of deployment force at the tape springs' tips was 0.13% over the course of 6 months

equivalent natural time. However, this calculation does not include tape spring 4 which experienced a failed string on the counter mass, but it did include 90% of the data for tape spring 3 before its string failed on the counter mass. Both of these string failures are readily observed from **Figure 5.20**.

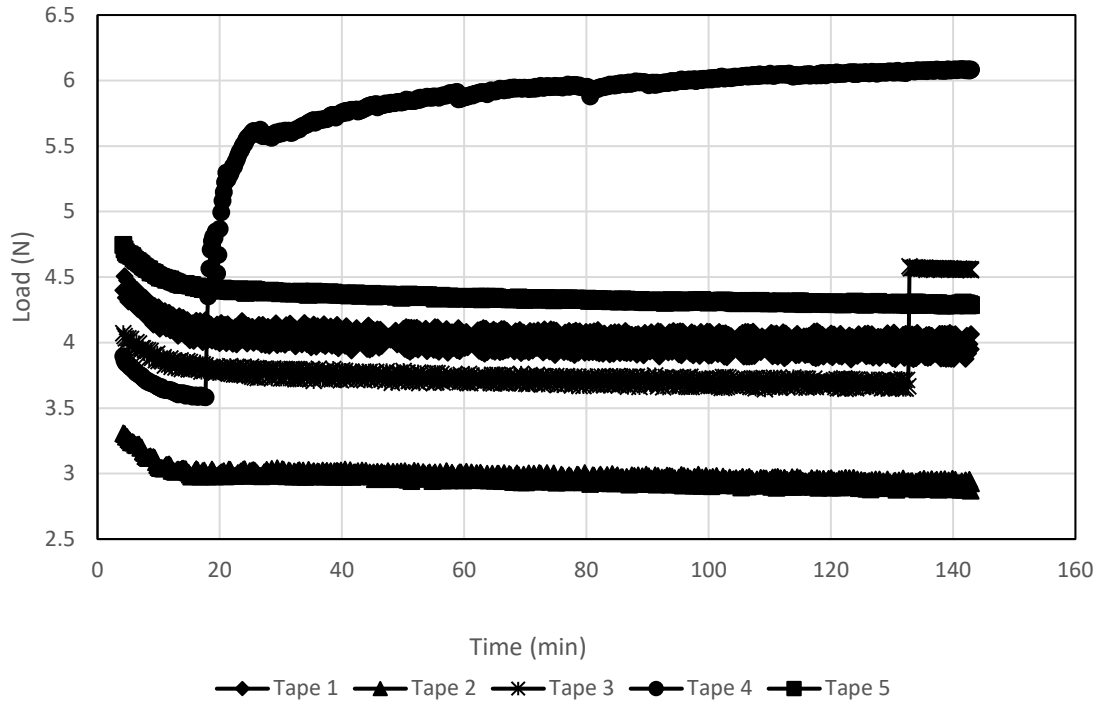


**Figure 5.20 ANP Tape Springs Six Months Stowage (via TTSP) Results Showing Change in Load Over Time**

It is evident from **Figure 5.20** two tape springs, numbers 3 and 4, experienced aberrations in their test performance. Tape spring 3 had nominal performance for 90% of its stow time at which time the string supporting the counter mass stretched and the mass contacted the bottom of the test fixture. This incident resulted in the tape spring being

relieved of its proper stowage constraints and losing approximately 0.5 N of deployment force. Tape spring 4 was given a new string, from the same stock used for the previous 49 tests. The exact same piece of string was used for all previous 49 structural tests. The new piece of string used for tape spring number 4, test number 50, broke after only 17 minutes. The failed string is seen in **Figure 3.33**.

## **5.5 Comparison of Structural Test Results**

The main objective of this research was to investigate the ability to engineer composite laminate tape springs with embedded ANPs to achieve tailorable structural performance behavior with respect to maintaining sufficient passive and controllable deployment force.

The tape springs were cured in the straight/deployed configuration and this was their stress-free state, but it is important to note the behavior of tape springs is highly nonlinear. (Seffen and Pellegrino, 1997) Another complicating factor is epoxy materials exhibit reduced shear stiffness at high strains and bending of the tape spring results in large shear strains in the PW outer plies which happen to primarily govern the tape springs' viscoelastic behavior.

The process of flattening and rolling the tape springs for stowage purposes introduced strain in two mutually perpendicular axes of the laminate, i.e., its transverse

and longitudinal curvatures, respectively. These strains are additive and represent stored strain energy in the material. Controlled release of this energy can provide the required force for autonomous deployment of the tape springs.

Recall from **Chapter 3**, the relation for determining the deployment torque from the tape spring is given as:

$$\mathbf{T}_{tape\ spring} = \mathbf{F}_{load\ cell}\mathbf{r}_{hub} - (\mathbf{M}_{counter\ mass}\mathbf{g})\mathbf{r}_{shaft} \quad (5.8)$$

with:

$\mathbf{F}_{load\ cell} \rightarrow$  measured in experimental test campaign

$$\mathbf{r}_{hub} = 0.75\ \text{inch} \times 25.4\ \text{mm/inch} = 19.05\ \text{mm}$$

$$\mathbf{M}_{counter\ mass} = 1,463.5\ \text{g} = 1.4635\ \text{kg} \times 9.81\ \text{m/s}^2 = 14.36\ \text{N}$$

$$\mathbf{r}_{shaft} = 0.25\ \text{inch} \times 25.4\ \text{mm/inch} = 6.35\ \text{mm}$$

The force recorded from the load cell during the experimental testing is summarized in **Table 5.3** below.

Table 5.3 Average Force Recordings at Beginning and End of Stowage Period at Tape Spring Tips

Stowage Time	Control Group		ANP Group	
	Beginning	End	Beginning	End
1 Hour	2.36	1.49	5.31	4.93
1 Day	2.07	1.71	4.98	4.63
1 Week	3.27	2.49	4.83	4.25
1 Month	2.71	2.32	4.29	3.78
6 Months	2.85	2.50	4.15	3.76
Average Loss in Force at Tape Spring Tip (%)	17.3		9.4	

**Table 5.3** shows the ANP tape springs experienced 9.4% less force loss at their tips after stowage versus the 17.3% loss in force experienced by the control tape springs. However, the tape springs were not allowed to freely deploy after stowage, their deployment path and constant velocity were controlled by the MTS Instron machine as part of the experimental test procedures. Therefore, the force recorded in **Table 5.3** is not necessarily representative of what the actual tape spring deployment force would have been. To investigate this matter further we must first address prior research with ANPs at the material level and how those results correlate to the structural results herein.

The viscoelastic effects in the tape springs are most significant at the beginning of the relaxation period. The typical nonlinear relaxation modulus experiences the vast majority of its relaxation in the first quarter to third of its stowage time and as the stowage time increased the overall effect was much less pronounced. This result can be seen in all the structural test results data earlier in this chapter and in **Table 5.3**.

However, the comparison of these structural results with the material level results as reported by Garner (Garner et al., 2017) should be addressed. Garner's results showed higher stress relaxation and lower stiffness with embedded ANPs in the laminate but those results were for a 3 ply plain weave layup (vice the FlexLam layup in this research); they used a different epoxy (diglycidyl ether Bisphenol-A versus PMT-F7); and they reported off-axis values versus on-axis/longitudinal values in this research. To analyze the results further, closed form analytical math models can provide additional insight.

Using a modified ROM equation for the ANP matrix composite modulus,  $E_c$ , with a discontinuous reinforcement under elastic deformation gives:

$$E_c = \eta E_p v_p + E_m v_m \quad (5.9)$$

where  $\eta$  is the strengthening coefficient (assumed to be 0.1 for nanoparticles with aspect ratio  $\sim 1$ ),  $E_p$  and  $E_m$  are the particulate (i.e., ANP) and neat matrix moduli, respectively, and  $v_p$  and  $v_m$  are the volume fractions of the particulate and matrix, respectively.

(Borowski et al., 2017, Kuo et al., 2005) Using 393 GPa for the ANP modulus, 3.529 GPa for the neat epoxy modulus, and the following equation to calculate the volume

fraction,  $v_p$ , of ANPs based on the mass fraction of 2 wt. % that was used in this research:

$$v_p = \frac{\phi_m}{\phi_m + (1 - \phi_m) \frac{\rho_p}{\rho_m}} \quad (5.10)$$

where  $\phi_m$  is the ANP mass fraction,  $\rho_p$  is the ANP density and  $\rho_m$  is the matrix density. Using 0.02 ANP mass fraction, ANP density of 3.98 g/cm<sup>3</sup>, and a matrix density of 1301 kg/m<sup>3</sup>, gives  $v_p = 0.66\%$ . (Moreira et al., 2012) This calculation is in line with Kuo's reported comparison of weight and volume percentages of ANPs in PEEK composites with 2.5 wt. % equivalent to 0.8 vol. %. (Kuo et al., 2005).

The ANP epoxy modulus is then calculated per equation 5.9 as 3.77 GPa, which is a 6.7% higher modulus than the neat epoxy modulus of 3.53 GPa. To look at the composite as a whole, we must calculate the lamina level moduli to then calculate the laminate level modulus. The modulus of the UD middle ply (used for both the control and ANP tape spring layups) is found simply from the ROM equation with IM7 carbon fibers and PMT-F7 neat epoxy constituent properties per **Table 4.2**. The ROM equation for the on-axis modulus is given as:

$$E_1 = E_m v_m + E_f v_f \quad (5.11)$$

where  $E_m$  is the neat matrix modulus (3.53 GPa),  $v_m$  is the volume fraction of matrix (32%),  $E_f$  is the modulus of the IM7 carbon fibers (248.6 GPa) and  $v_f$  is the volume fraction of unidirectional fibers (68%). This gives  $E_1 = 171$  GPa. The modulus of the PW plies can be calculated as:

$$E_{pw} = \frac{E_{1,pw} + E_{2,pw}}{2} \quad (5.12)$$

where  $E_{1,pw}$  and  $E_{2,pw}$  are the moduli in the on axis and transverse axis, respectively.

(Khan et al., 2017) They are given as:

$$E_{1,pw} = E_{1f}V_f + \dot{E}_m(1 - V_f) \quad (5.13)$$

$$E_{2,pw} = \frac{\dot{E}_m E_{2f}}{(1 - V_f)E_{2f} + V_f \dot{E}_m} \quad (5.14)$$

where  $E_{1f}$  and  $E_{2f}$  are the on axis and transverse moduli of the silica fibers (72 GPa for both, transversely isotropic),  $V_f$  is the fiber volume fraction (44%), and  $\dot{E}_m$  is the time-dependent modulus of the matrix (with the ANP epoxy per equation 5.9 and calculated as 3.77 GPa above, or 3.53 GPa for the next epoxy). The modulus of the PW plies was then calculated to be 19.9 GPa for the neat epoxy and 20.1 GPa for the ANP epoxy.

There is only a 1.3% increase in stiffness in the ANP plain weave plies compared to the neat plain weave plies and the UD ply stiffness is the same for both control and ANP tape springs. Therefore, we'll turn our attention to the experimental test process and dynamics as another potential source of difference in tape spring tip forces after stowage, first the difference in relaxation moduli and then how the tape spring tip force is related to the tape spring's strain energy with a Lagrangian dynamic analysis.

The difference in stiffness and stress relaxation between the control and ANP tape springs can be further understood by evaluating the difference in the Prony series models for the modulus decay of both the neat epoxy and ANP epoxy since all other parameters remain constant. A plot comparing the Prony series is given in **Figure 5.21** below:

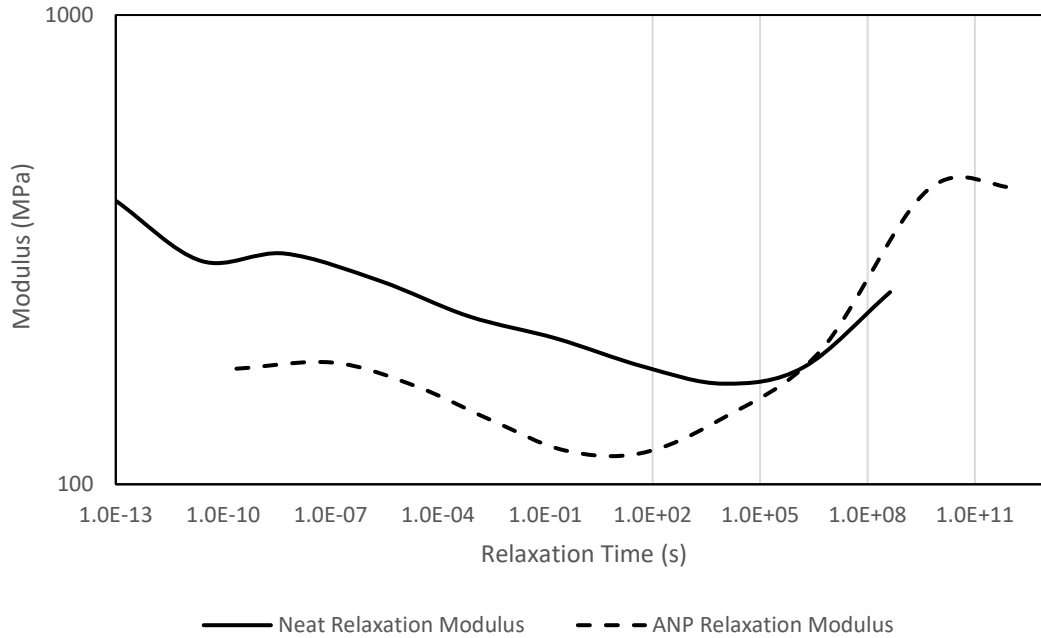


**Figure 5.21 Comparison Between Neat Epoxy and ANP Epoxy Relaxation Modulus**

It is clear from **Figure 5.21** the ANP tape springs were modeled with higher relaxation and correspondingly lower stiffness at periods of relaxation time greater than 1E6 seconds (~ 12 days) compared to the control tape springs. These relaxation models for the neat and ANP epoxies, as used in the FEM, were based on the respective DMA test results in sections 5.1 and 5.3.

An alternative way to represent the results is to look at the loss in force per groups of stowage times. **Table 5.4** shows the averaged percentage loss of force at the tape springs' tips (i.e., the load cell end) after stowage, by stowage group and overall. The test results showed the ANP tape springs had 55% more force at the tip as compared to the control tape springs, i.e., 9.5% loss of tip force versus 20.9% loss of tip force. However, it is important to note the deployment velocity was constant and controlled by the MTS Instron machine, by design; typically a strain energy deployed structure deploys with significant velocity when allowed to deploy freely, i.e., no path or rate control. As such, the force measured at the load cell was the force to pull the tape spring and unroll it, not the actual tape spring deployment force. This is an important distinction.

It is hypothesized the tape springs' controlled and constant quasi-static deployment rate in this research's experimental campaign enabled the stress relaxation to increase and the modulus to decrease for the ANP tape springs as compared to the control tape springs during the post stowage deployment. This hypothesis is based on examination of the analytical dynamic equations for a tape spring developed by Seffen and Pellegrino in their 1997 "Deployment Dynamics of Tape Springs" research. The total kinetic energy of the coiled tape spring on the hub includes contributions from the hub, coiled tape spring and a portion of the tape spring that is straight. The total potential energy of the coiled tape spring on the hub includes contributions from the strain energy stored within the tape spring and the gravitational potential energy. The tape spring will have potential energy as a function of its position, and kinetic energy as a function of its velocity. It is the difference in the energies that is relevant, not the actual values. A

simplified energy balance for the tape spring energies related to the forces required to pull them from the coiled state to deployed state can be given as:

$$E_{deployment} = E_{stored} + E_{lost} \quad (5.15)$$

where  $E_{deployment}$  is the energy available to deploy the tape spring at the beginning of stowage,  $E_{stored}$  is the energy available to deploy the tape spring at the end of the stowage period and  $E_{lost}$  is the energy lost during the stowage period due to the viscoelastic phenomena. The deployment energy and stored energy decline during the stowage period and per conservation of energy, the energy lost correspondingly increases during the stowage period. The force required to pull the deploying spring is significantly higher for the ANP tape springs as compared to the control tape springs (per table 5.4) because there is substantial relaxation in the ANP tape springs and they lose considerable force during stowage. The force required to pull the deploying tape spring is inversely proportional to the deployment energy. This force is not the tape spring's deployment force, it is the force required by the MTS Instron machine to pull the tape spring in a controlled path with a controlled quasi-static rate.

Additional insight can be gained by performing a dynamic analysis, applying Lagrange's equations and studying the resulting equations of motion for a coiled tape spring system. This analysis indicates the tape springs' motions and associated forces are directly related through the following equations of motion:

$$\frac{1}{3}\rho(L - r\theta)^3(\ddot{\zeta} + \ddot{\theta}) + \frac{1}{2}\rho r(L - r\theta)^2(\dot{\zeta}^2 - \dot{\theta}^2) + D(1 + \nu)\alpha - \frac{1}{2}\rho g(L - r\theta)^2 \sin(\theta + \zeta) = Q_1 \quad (5.16)$$

$$\rho \left[ r^2 L \ddot{\zeta} + \frac{1}{3}(L - r\theta)^3(\ddot{\zeta} + \ddot{\theta}) - r(L - r\theta)^2 \dot{\theta}(\dot{\zeta} + \dot{\theta}) \right] + I \ddot{\zeta} + 2\rho g r^2 \sin \frac{1}{2} \theta \cos \left( \zeta + \frac{1}{2} \theta \right) + \rho g r(L - r\theta) \cos(\theta + \zeta) - \frac{1}{2}\rho g(L - r\theta)^2 \sin(\theta + \zeta) = Q_2 \quad (5.17)$$

where  $\rho$  is the mass per unit length of the tape spring,  $r$  is the radius of the hub,  $L$  is the tape spring length,  $\theta$  is the total coiled rotation of the tape spring,  $\zeta$  is the angle of skew from the gravity normal direction,  $g$  is gravity,  $I$  is the polar moment of inertia and  $D$  is:

$$D = \frac{Et^3}{12(1-\nu^2)} \quad (5.18)$$

where  $E$  is Young's Modulus,  $t$  is the tape spring thickness and  $\nu$  is Poisson's ratio.

Per equations 5.16 and 5.17, the magnitude of the tape spring deployment force may be directly proportional to the length of coiled tape spring, the geometry of the hub, and most importantly, to the velocity of the uncoiling/deploying tape spring. However, because the forces in equations 5.16 and 5.17 are generalized forces, they do not necessarily represent the tape spring tip forces. At best it can be concluded the Lagrange method for analyzing this problem involving the tape spring deployment displacement and constant deployment velocity via its strain energy reveals the tape spring deployment force is *likely* proportional to the deployment velocity. This assessment may be why the constant velocity deployed tape springs had less tip force because the quasi-static velocity was only 1 inch per minute. A tape spring allowed to freely deploy will ostensibly have greater deployment velocity and greater tip force. On the other hand, a tape spring with

controlled deployment path and controlled deployment velocity will have tip forces directly related to the magnitude of the velocity and it will be the pulling force, not the deploying force.

Table 5.4 Average Percentage Loss in Tape Springs' Tip Force During Stowage

<b>Stowage Time</b>	<b>Control Group (%)</b>	<b>ANP Group (%)</b>	<b>% ANP &lt; Control</b>
<b>1 Hour</b>	<b>36.6</b>	<b>7.1</b>	<b>80.6</b>
<b>1 Day</b>	<b>17.3</b>	<b>7.1</b>	<b>59.0</b>
<b>1 Week</b>	<b>23.9</b>	<b>12.1</b>	<b>49.4</b>
<b>1 Month</b>	<b>14.6</b>	<b>11.9</b>	<b>18.7</b>
<b>6 Months</b>	<b>12.2</b>	<b>9.4</b>	<b>22.5</b>
<b>Average Loss in Force at Tape Spring Tip (%)</b>	<b>20.9</b>	<b>9.5</b>	

It is important to reiterate here the analysis of the experimental results above are qualitatively-based and not based on a quantitative or statistical approach. Testing more tape springs was not feasible from a cost, resources, facilities and schedule perspective.

## 5.6 Abaqus Finite Element Model Simulation Results

Viscoelastic behavior of composites is often difficult to characterize because it involves linking the different behaviors of the fiber, matrix and nanofiller constituent properties, which also vary with time, temperature and stress. Homogenization techniques at the macro-scale or unit cells (e.g., representative volume elements) at the micro-scale are often implemented to try and model the effective engineering properties of the composite, but these techniques are limited in their ability to capture important material interactions, and thus, structural behavior, due to the complexity of these composites. A FEM was created to model the tape springs and simulate the structural behavior in this research work. Previous researchers have found one of the greatest simulation challenges for deployable structures was the presence of contact between flexible bodies as one finds with a coiled tape spring boom on a hub. (Mobrem et al., 2017) Contact between flexible and rigid bodies is only one of the many challenges in modeling thin, flexible, viscoelastic composite structures.

As discussed in **Chapter 4**, conventional shell elements were used to model the tape springs in this research. However, the behavior of thin shells is known to be sensitive to geometric imperfections from sources such as fabrication and loading misalignment. (Kwok and Pellegrino, 2011) If these effects are not considered, the response of the structure usually will appear much stiffer than observed in experiments. Thermal variations in the experimental environment can also be a cause of discrepancies between experimental results and simulation results. The Hexcel IM7 carbon fibers used

in this research are assumed to be linear elastic and transversely isotropic. However, it is worth noting previous research by Murphey et al. found carbon fibers in thin flexures under high strain to exhibit nonlinear elastic behavior (in the axial direction). (Murphey et al., 2011) This nonlinearity can affect changes in both  $E$  and  $I$ , as bending stiffness is  $EI$ .

The Abaqus finite element software can also produce problems if great care is not taken in the modeling process. For example, excessive mass scaling can lead to erroneous solutions. The items affected by mass scaling include the system's mass, rotary inertia, rigid elements, bulk viscosity and mass proportional damping. Numerous mass scaling options were investigated for the FEM to seek both convergence of the model and an appropriate result regarding engineering principles. Also, in laminated shells, transverse shear effects can be significant. Abaqus assumes transverse shear strains are constant through the shell thickness, transverse shear stresses are zero at the shell surfaces, but continuous through the layers. Consequently, as long as an elastic response occurs, the formulations for shear stiffness and stress calculations properly account for all these issues.

### **5.6.1 Correlation of Abaqus FEM and Control Tape Springs' Test Results**

Before correlating the results from the structural testing experimental campaign with the results predicted from the FEM simulation, it is necessary to first check the

validity of the FEM-produced simulation results. One way to do this check is via an energy analysis of the model simulation results. Examination of the energy content during a simulation provides a measure to evaluate whether the Abaqus results reflect a quasi-static solution. As a general rule of thumb, the kinetic energy of the deforming tape spring should be a small fraction, i.e., 5% - 10%, of the work done during the majority of the quasi-static analysis. In this research, the rolling tape spring is a dynamic event and the stowage period is a quasi-static event. Thus, the FEM analysis steps were evaluated as such, respectively.

The energy balance can help evaluate whether an Abaqus simulation yielded an appropriate response and results. Reviewing the energy balance and plots can identify and reveal problems to watch out for:

1. Existence of excessive artificial strain energy (i.e., ALLAE) for a dynamic simulation event. ALLAE acts to suppress hourglass modes of the tape spring's shell elements during bending. ALLAE should only be a few percent of the model's internal energy (i.e., ALLIE).
2. Existence of excessive kinetic energy (i.e., ALLKE) for a quasi-static simulation event. ALLKE should be a small fraction (e.g., < 10%) of the work (i.e., ALLWK) done during the tape spring's stowage simulation.

The kinetic energy, KE, of the tape spring in Joules (J) can be represented as:

$$KE = \frac{1}{2}I\omega^2 \quad (5.19)$$

where  $I$  is the moment of inertia and  $\omega$  is the angular speed of the tape spring hub. Also, the work done,  $W$ , in Newtons (N) in rolling up and unrolling the tape spring is given as:

$$W = \tau\theta \quad (5.20)$$

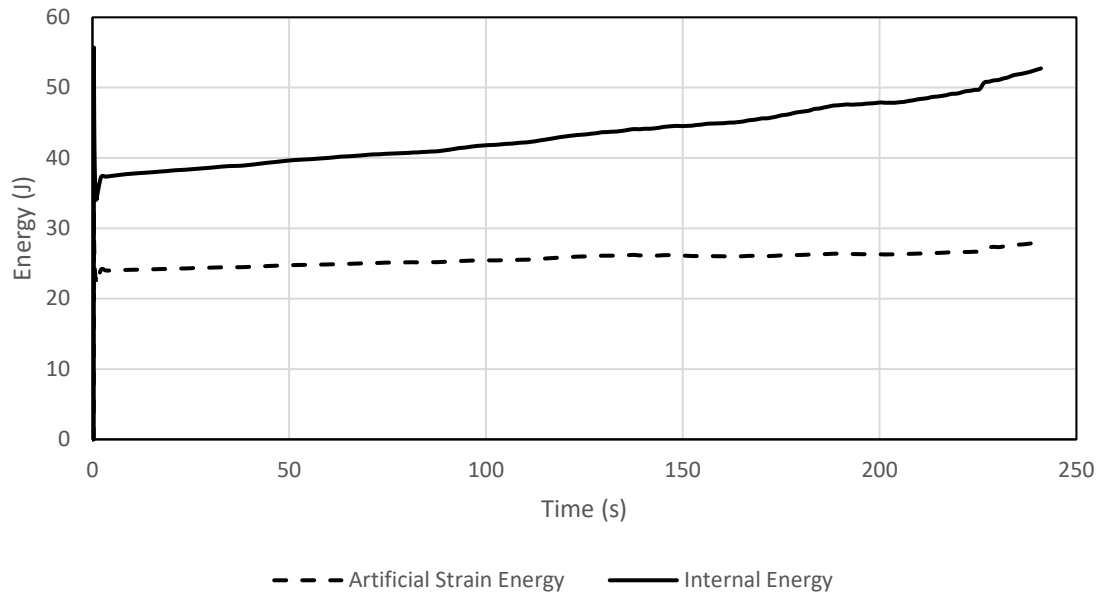
where  $\tau$  is the applied torque in N-mm and  $\theta$  is the angle of rotation of the tape spring hub in radians, where  $1 \text{ J} = 1,000 \text{ N-mm}$ . The consistent SI units used in Abaqus for this research were Newtons and millimeters as given in **Table 5.5** below.

Table 5.5 Abaqus Consistent Unit Options

**Table 2-1** Consistent units.

Quantity	SI	SI (mm)	US Unit (ft)	US Unit (inch)
Length	m	mm	ft	in
Force	N	N	lbf	lbf
Mass	kg	tonne ( $10^3 \text{ kg}$ )	slug	$\text{lbf s}^2/\text{in}$
Time	s	s	s	s
Stress	Pa ( $\text{N/m}^2$ )	MPa ( $\text{N/mm}^2$ )	$\text{lbf/ft}^2$	psi ( $\text{lbf/in}^2$ )
Energy	J	mJ ( $10^{-3} \text{ J}$ )	ft lbf	in lbf
Density	$\text{kg/m}^3$	$\text{tonne/mm}^3$	$\text{slug/ft}^3$	$\text{lbf s}^2/\text{in}^4$

Energy plots for the tape spring roll up and stowage time for the control tape springs with 1 hour stowage are shown in **Figures 5.22 and 5.23** below. The 1 day load case FEM simulation did not complete due to modeling convergence difficulties for its 24 hour (86,400 second) stowage period. Despite numerous attempts consuming several hundred hours to tune the model with mass scaling parameters for this load case, the analysis time increment eventually became unstable and aborted at 36,186 seconds.



**Figure 5.22 Energy Analysis for Steps 1 and 2 of Abaqus Simulation of Control Tape Springs with One Hour Stowage**

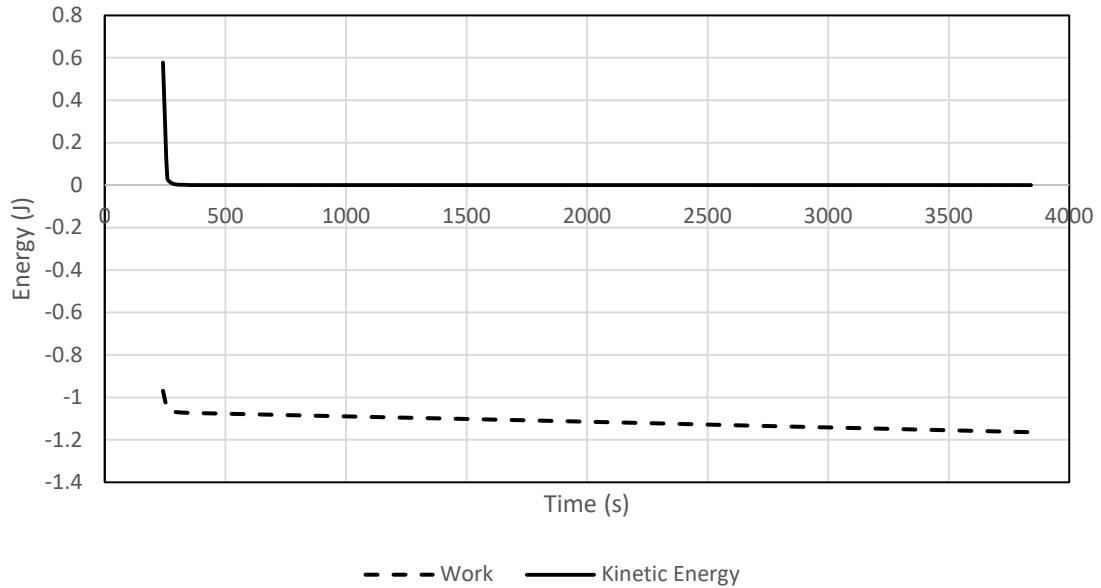


**Figure 5.23 Energy Analysis for Step 3 of Abaqus Simulation of Control Tape Springs with One Hour Stowage**

Note the work shown in **Figure 5.23** is negative because the torque applied to the tape spring to roll it up is the negative direction per the global coordinate system in Abaqus.

The remaining energy plots for the Abaqus simulated load cases are extraordinarily similar and provide no additional value or insight to include herein. However, a review of the energy plots revealed the energy values were found to be appropriate from a kinetic energy and work perspective but the degree of artificial strain energy with respect to internal energy may be too high for the dynamic rolling step (as seen in **Figure 5.23**). These results will be put into perspective after the tape springs' tip force results are compared and analyzed later in this chapter.

It was observed the strain plots for the stowed tape springs experienced negligible change in strain during the stowage periods. A plot of strain in the 1 hour control tape spring at the end of the end of the stowage period as predicted by Abaqus is shown in **Figure 5.24** below:

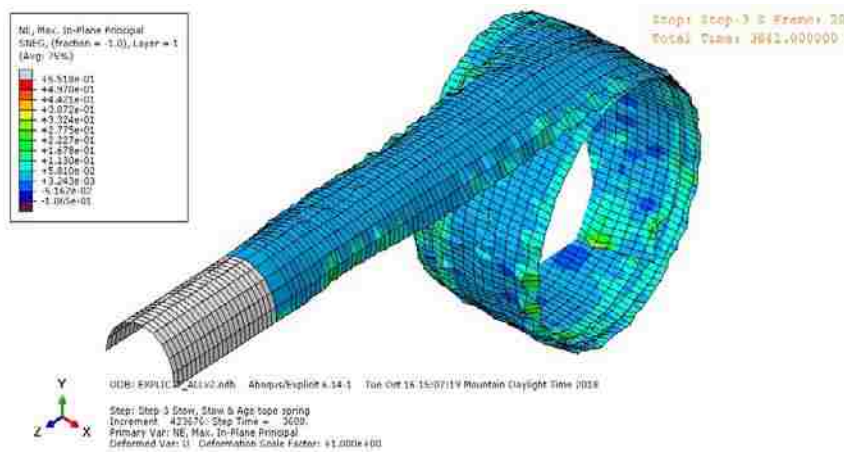


**Figure 5.24** Abaqus Predicted Strain in Control Tape Spring at End of 1 Hour Stow Period

The tape springs' deployment tip force as measured from the load cell during the experimental testing was compared to the predicted tape springs' deployment tip force from the FEM simulations. Five load cases were run with the only change being the five different stowage times: 1 hour at ambient temperature, 1 day at ambient temperature, 240 seconds at 200° F, 954 seconds at 200° F and 5,742 seconds at 200° F, the latter three load cases per the TTSP. The correlation of the experimental results with the FE predicted results for the load cases is provided below. Four of the five load cases are

presented with the exception being the 1 day load case per the note at the beginning of this section.

The comparative results for the control tape springs' 1 hour Abaqus FEM simulation-produced results and the 1 hour experimental structural test results (of the median control tape spring) are shown in **Figure 5.25** below.

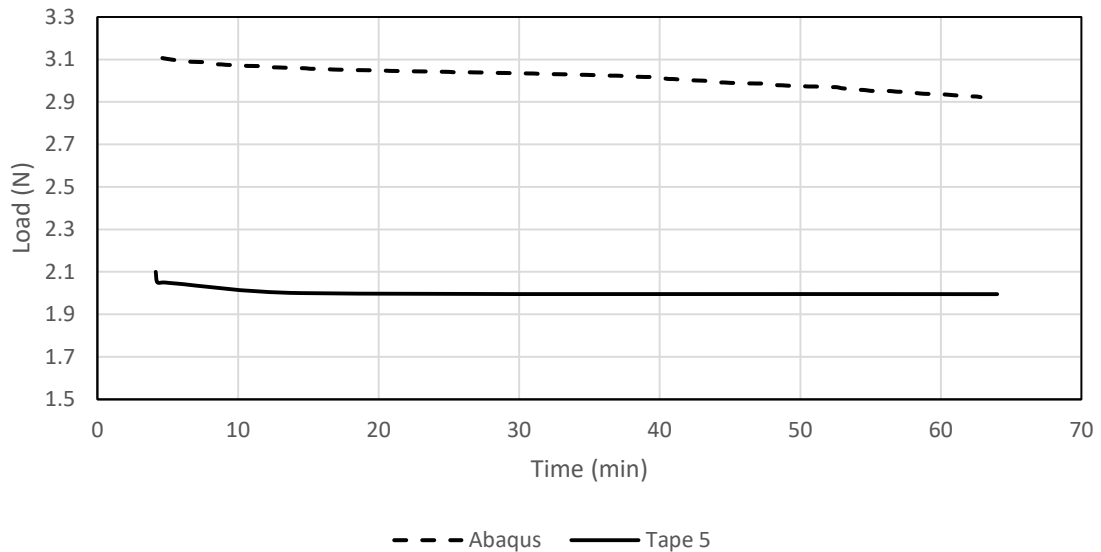


**Figure 5.25 Comparison of Abaqus Predicted Results and Experimental Structural Test Results for Median Control Tape Spring (Tape 5) for One Hour Stowage**

The Abaqus FEM simulation-produced results over predicted the tape spring tip deployment force by approximately 0.75 N. The FEM simulation-predicted results for the tape spring tip deployment force loss over 1 hour of stowage time was 0.27% compared to the experimental result from the median tape spring (tape spring 5) of 0.11%. The reasons for this over prediction can be numerous, including ideal assumptions in the modeling process annotated in Chapter 4 (e.g., CLT,

fiber/matrix/nanoparticle homogeneity), perfect/uniform tape spring geometry, frictionless test fixture and MTS Instron machine, composite layup idealizations, etc.

The Abaqus FEM simulation for the 1 day stowage did not complete its analysis run due to convergence problems with the long 24 hour quasi-static stow step. The stable time increment gradually became unstable and the simulation aborted at 36K seconds. It is left for future work to continue working the tuning of this load case model.

The comparative results for the control tape springs' 1 week Abaqus FEM simulation-produced results and the 1 week experimental structural test results (for the median control tape spring) are shown in **Figure 5.26** below.

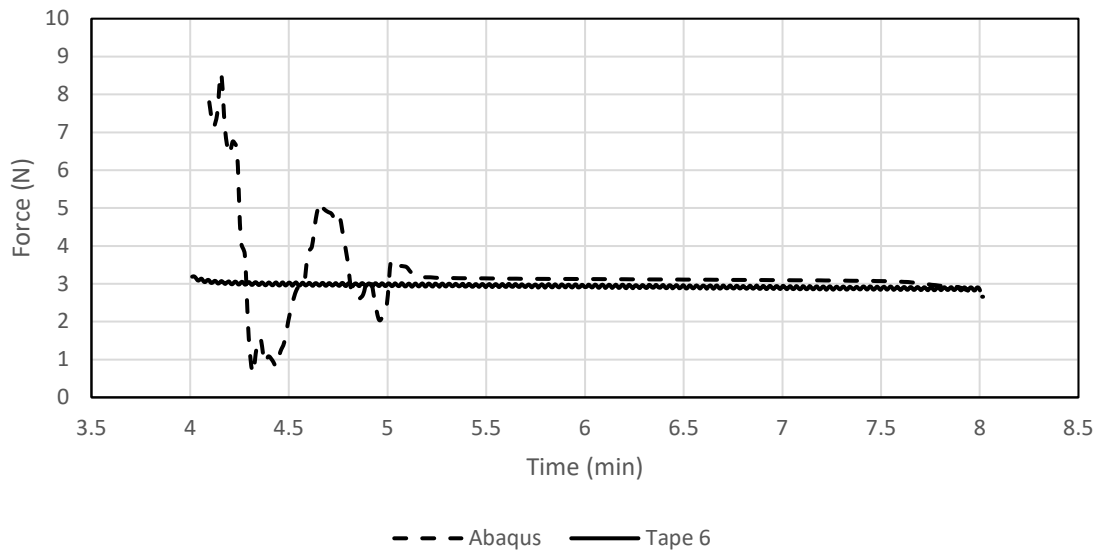


**Figure 5.26 Comparison of Abaqus Predicted Results and Experimental Structural Test Results for Median Control Tape Spring (Tape 6) for One Week Stowage**

The results in **Figure 5.26** show the Abaqus FEM simulation-produced results as approximately 3 N in a steady state quasi-static condition and the experimental results are also very close to 3 N. The Abaqus results show considerable noise in the prediction for the first minute of the stowage period, perhaps due to viscous pressure forces or an improper balance of material deformation speed to dilatational wave speed in Abaqus.

The decrease in tape spring tip deployment force as predicted by the Abaqus FEM simulation was 7.9% and the decrease in tape spring tip deployment force loss for the median tape spring (tape spring 6) during the experiment testing was 4.2%, an over prediction, due in some part to the noisy behavior the first approximately 90 seconds which was neglected in determining the overall deployment force loss percentage. The difference between the results may also be due to the idealized parameters in the FEM, CLT assumptions, frictional losses in the test fixture and/or MTS Instron machine, inexact Prony parameters and tape spring geometric or constituency irregularities. It may be a combination of those factors that caused the difference in results.

The comparative results for the control tape springs' 1 month Abaqus FEM simulation-produced results and the 1 month experimental structural test results (for the median control tape spring) are shown in **Figure 5.27** below.

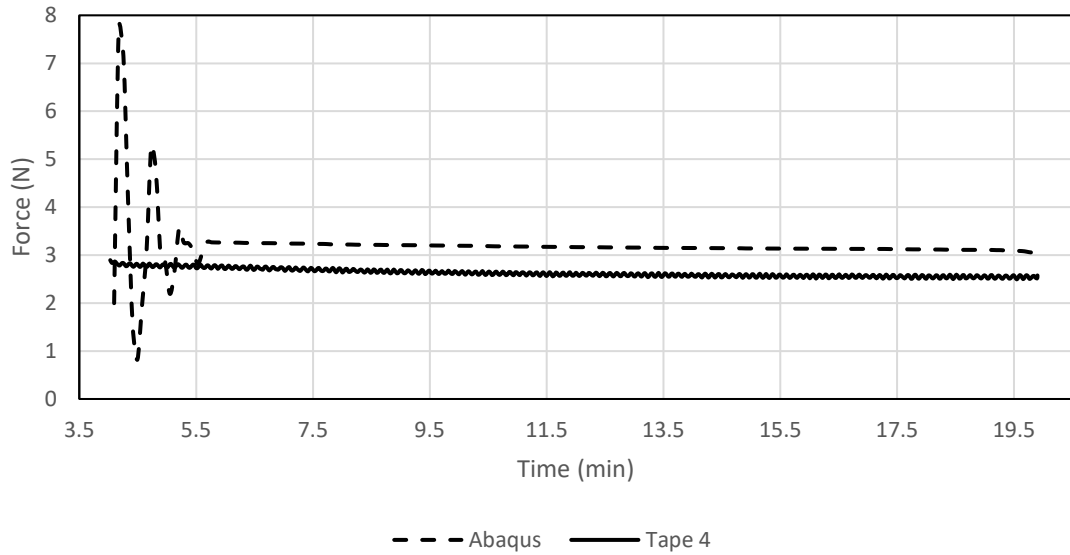


**Figure 5.27 Comparison of Abaqus Predicted Results and Experimental Structural Test Results for Median Control Tape Spring (Tape 4) for One Month Stowage**

The decrease in tape spring tip deployment force as predicted by the Abaqus FEM simulation was 1.76% and the decrease in the tape spring tip deployment force loss for the median tape spring (tape spring 4) during the experiment testing was 1.64%. These results compare quite closely and the small difference may be due to rounding in the data points.

The comparative results for the control tape springs’ 6 months Abaqus FEM simulation-produced results and the 6 months experimental structural test results (for the median control tape spring) are shown in **Figure 5.28**.

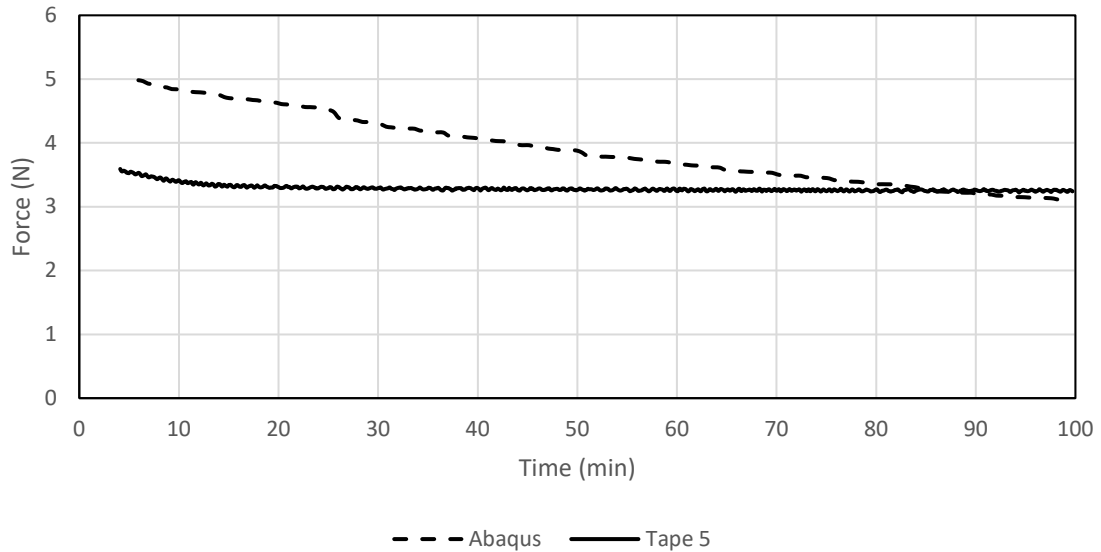


**Figure 5.28 Comparison of Abaqus Predicted Results and Experimental Structural Test Results for Median Control Tape Spring (Tape 5) for Six Months Stowage**

Review of the Abaqus FEM simulation-produced data compared to the experimental test results show a predicted tape spring deployment force loss over 6 months of stowage of 2.0% while the experimental tape spring deployment force loss for the median tape spring (tape spring 5) was 0.15%. The difference between the results may be due to the parameters in the FEM, CLT assumptions, frictional losses in the test fixture and/or MTS Instron machine, inexact Prony parameters and tape spring geometric or constituency irregularities. It may be a combination of those factors that caused the difference in results. Also, the nonlinear nature of viscoelastic behavior in the tape springs may not have been captured well in the modeling process as a significant amount of relaxation typically occurs during the first third to quarter of the structure’s service life.

## 5.6.2 Correlation of Abaqus FEM and ANP Tape Springs' Test Results

Energy plots of the stowage times for the ANP tape springs for the 1 hour stowage are shown in **Figures 5.29 and 5.30** below. The 1 day Abaqus FEM simulation did not complete due to modeling convergence difficulties for the 24 hour stowage period. Despite numerous attempts and hundreds of hours spent to tune the model for this load case, the analysis time increment eventually became unstable and aborted at 6,873 seconds.

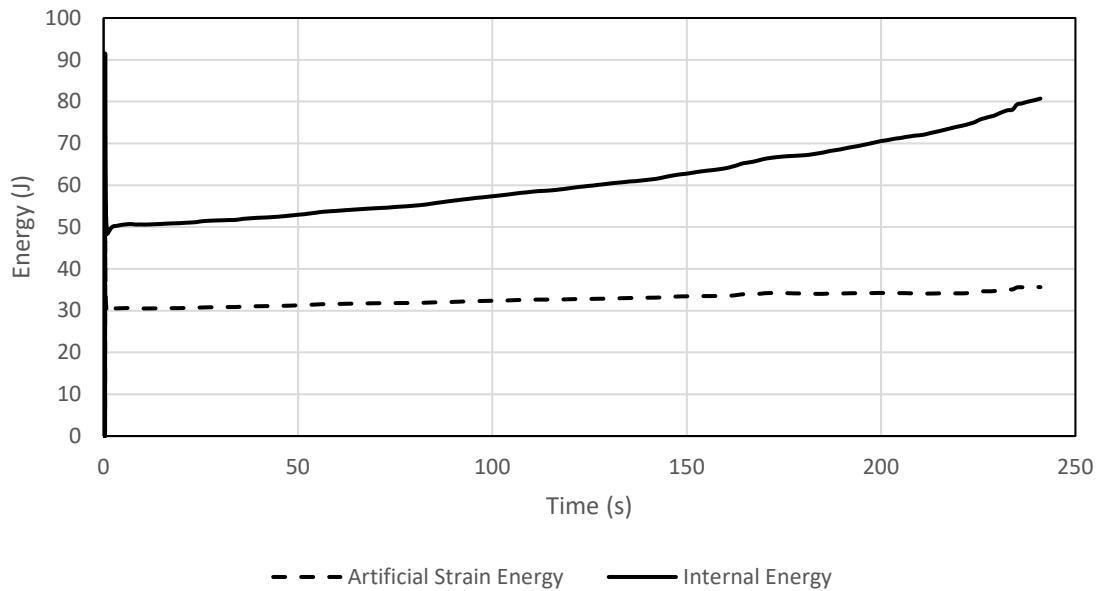


**Figure 5.29 Energy Analysis for Steps 1 and 2 of Abaqus Simulation of ANP Tape Springs with One Hour Stowage**

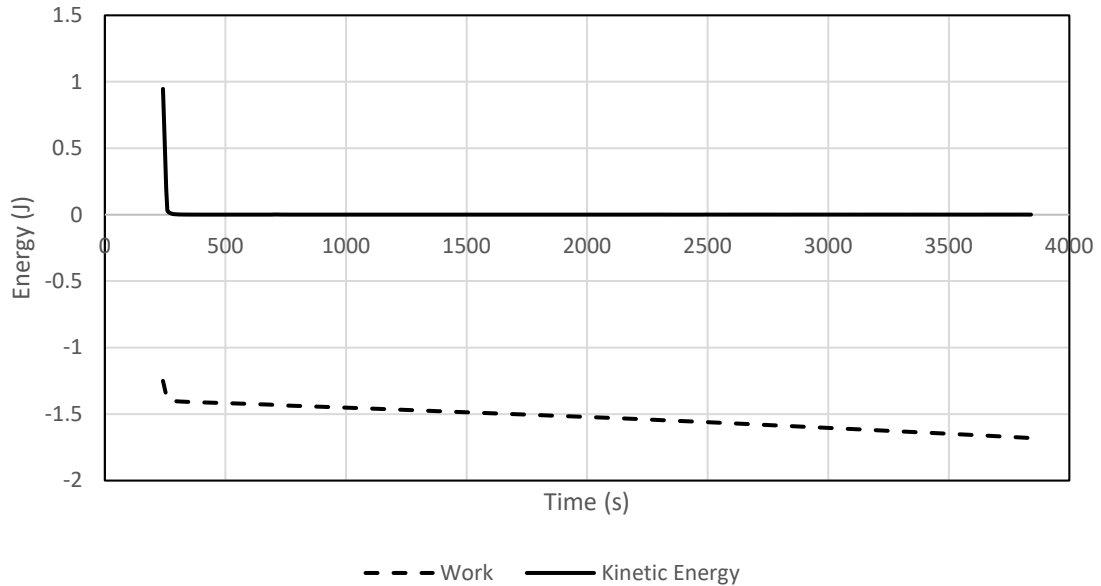


**Figure 5.30 Energy Analysis for Step 3 of Abaqus Simulation of ANP Tape Springs with One Hour Stowage**

The remaining energy plots for the Abaqus simulated load cases are extraordinarily similar and provide no additional value to include herein. However, a review of the energy plots revealed the energy values were found to be appropriate from a kinetic energy and work perspective but the degree of artificial strain energy with respect to internal energy may be too high for the dynamic rolling step (as seen in **Figure 5.29**). These results will be put into perspective after the tape springs' tip force results are compared and analyzed later in this chapter.

It was observed the strain plots for the stowed tape springs experienced negligible change in strain during the stowage periods. A plot of strain in the 1 hour ANP tape spring at the end of the end of the stowage period as predicted by Abaqus is shown in **Figure 5.31** below:

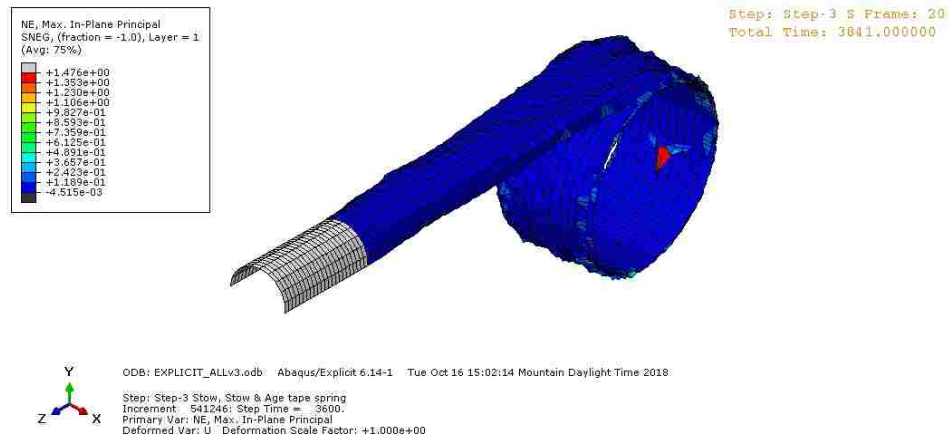


**Figure 5.31 Abaqus Predicted Strain in ANP Tape Spring at End of 1 Hour Stow Period**

The tape springs' tip force as measured from the load cell during the experimental testing was compared to the predicted tape springs' tip force from the Abaqus FEM simulations. Five load cases were run with the only change being the five different stowage times: 1 hour at ambient temperature, 1 day at ambient temperature, 348 seconds at 200° F, 1,386 seconds at 200° F and 8,334 seconds at 200° F, the latter three load cases via the TTSP. The correlation of the experimental results with the Abaqus FEM simulation-predicted results for the load cases (except the 1 day load case, as noted earlier in this section) is provided below.

The comparative results for the ANP tape springs 1 hour Abaqus FEM simulation-produced results and the one hour experimental structural test results (for the median ANP tape spring) are shown in **Figure 5.32**.

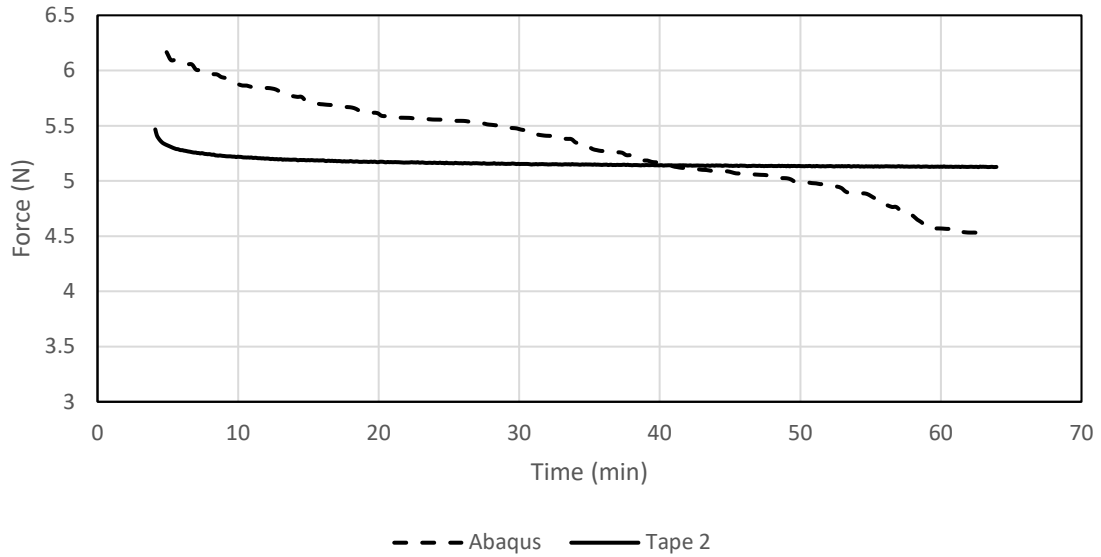


**Figure 5.32 Comparison of Abaqus Predicted Results and Experimental Structural Test Results for Median ANP Tape Spring (Tape 2) for One Hour Stowage**

The Abaqus FEM simulation results for the ANP tape spring predicted a tape spring deployment force loss of 2.45% over the course of 1 hour of stowage compared to the experimental result of the median tape spring (tape spring 2) of 0.21%. The Prony series parameters may not be correct or rounded or the difference in results may be attributed to complex nanocomposite interactions not captured well in the FEM such as the constituent interactions among the epoxy, ANPs and the silica fibers. Additionally, the interphase is also a potential source of mechanical enhancement to the tape spring's structural behavior and its effects on composite stiffness (among other properties) is not well understood.

The comparative results for the ANP tape springs 1 week Abaqus FEM simulation-produced results and the 1 week experimental structural test results (for the median ANP tape spring) are shown in **Figure 5.33** below.

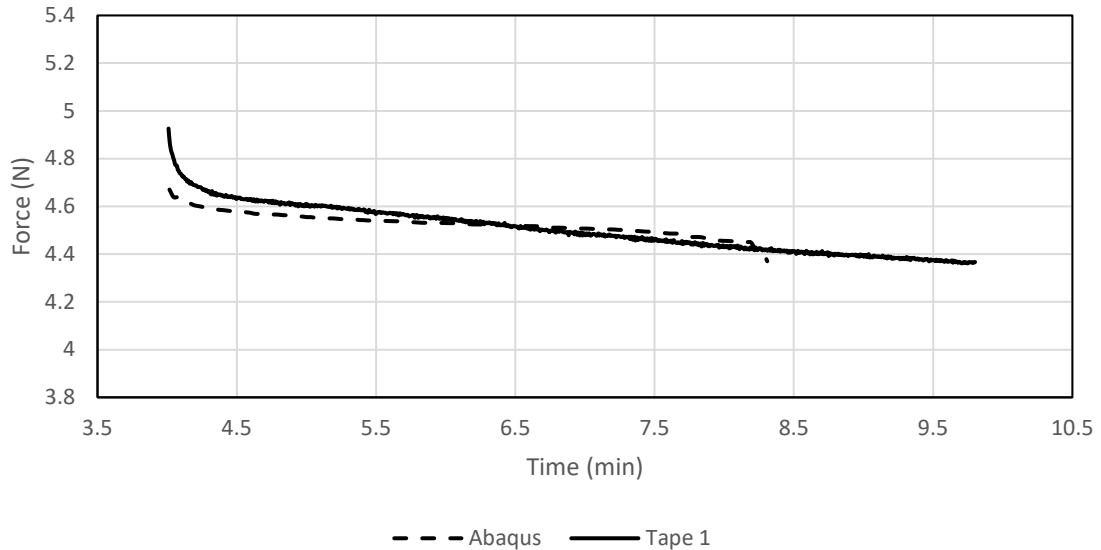


**Figure 5.33 Comparison of Abaqus Predicted Results and Experimental Structural Test Results for Median ANP Tape Spring (Tape 1) for One Week Stowage**

The Abaqus FEM simulation-predicted results produced a tape spring tip deployment force loss during the 1 week stowage period of 3.54%; the experimental results for the median tape spring (tape spring 1) had a deployment force loss of 5.74%, an under prediction in this case. The 2.2% difference in results may be explained from the complex behavior occurring during the first portion (~ 10%) of the structure's service life when the viscoelastic effects are most dramatic since the deployment force loss is nonlinear over the stowage time period. Moreover, modeling idealizations and

assumptions such as CLT may also be a contributing factor to the difference. Also, the Prony series parameters could be slightly off.

The comparative results for the ANP tape springs' 1 month Abaqus FEM simulation-produced results and the 1 month experimental structural test results (for the median ANP tape spring) are shown in **Figure 5.34** below.

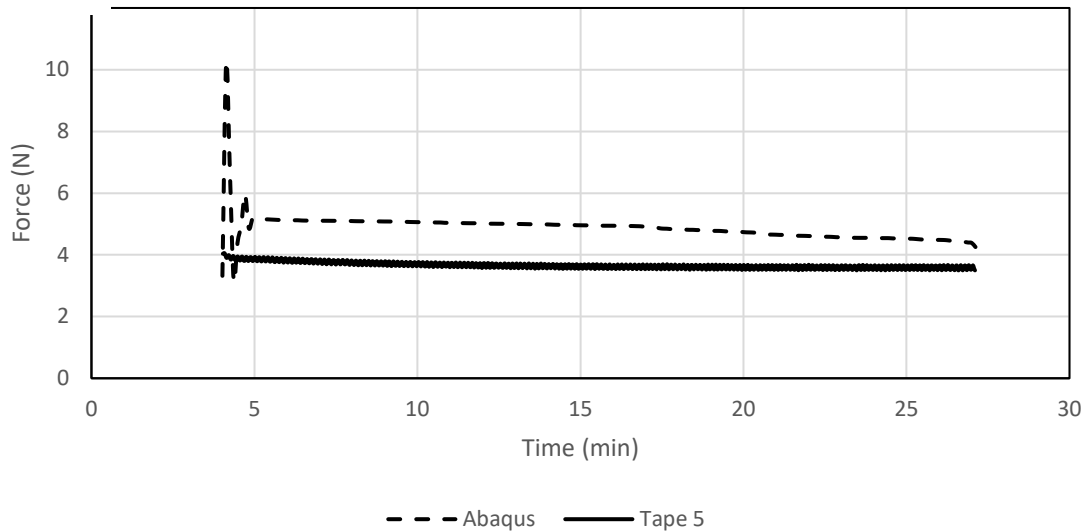


**Figure 5.34 Comparison of Abaqus Predicted Results and Experimental Structural Test Results for Median ANP Tape Spring (Tape 5) for One Month Stowage**

A review of the results for the Abaqus FEM simulation over 1 month stowage time show a predicted loss in tape spring tip deployment force of 3.66% during the storage period compared to the loss in the median tape spring (tape spring 5) deployment force of 1.19%, an over prediction. The 2.47% difference may be attributed to modeling assumptions and idealizations, incorrect Prony parameters, non-homogeneous composite tape springs, geometric imperfections, etc.

The comparative results for the ANP tape springs' 6 months Abaqus FEM simulation-produced results and the 6 months experimental structural test results (for the median ANP tape spring) are shown in **Figure 5.35** below.

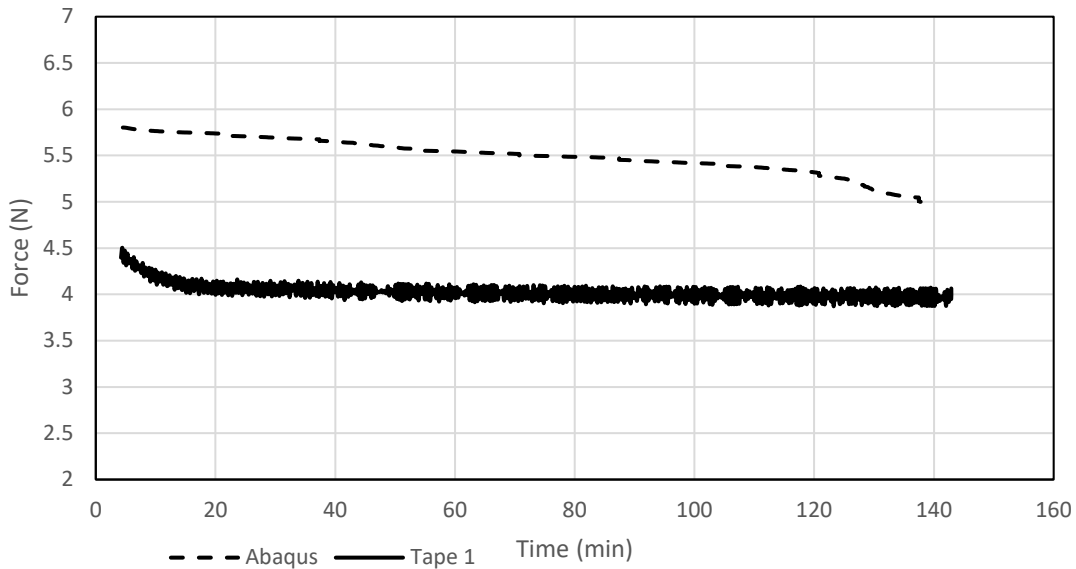


**Figure 5.35 Comparison of Abaqus Predicted Results and Experimental Structural Test Results for Median ANP Tape Spring (Tape 1) for Six Months Stowage**

A review of the results indicate the Abaqus FEM simulation predicted a tape spring tip deployment force loss of 0.49% for 6 months of stowage time while the experimental results for the median tape spring (tape spring 1) had a loss of 0.13%, an over prediction. While 0.36% separates the model predicted results versus the experimental results, several reasons could contribute to this difference such as model assumptions and idealizations, human error in the testing process, geometric imperfections of the tape springs, etc., though, it is a very small relative difference.

It is useful to compare all the results together to get a big picture of how the research turned out. **Table 5.6** shows how the tape spring tips' deployment force compared to the averaged experimental results for both the control and ANP test groups.

Table 5.6 Abaqus vs Experimental Tape Spring Tip Deployment Force Loss

Tape Springs' Stowage Time	Control Group Deployment Force Loss (%)	Abaqus FEM Simulation Predicted Deployment Force Loss (%)	ANP Group Deployment Force Loss (%)	Abaqus FEM Simulation Predicted Deployment Force Loss (%)
1 Hour	0.11	0.27	0.21	2.45
1 Day	0.004	--	--	--
1 Week	4.21	7.93	5.74	3.54
1 Month	1.64	1.76	1.19	3.66
6 Months	0.15	2.00	0.13	0.49

Alternatively, the results in **Table 5.6** can be plotted, as shown in **Figures 5.36 and 5.37**:

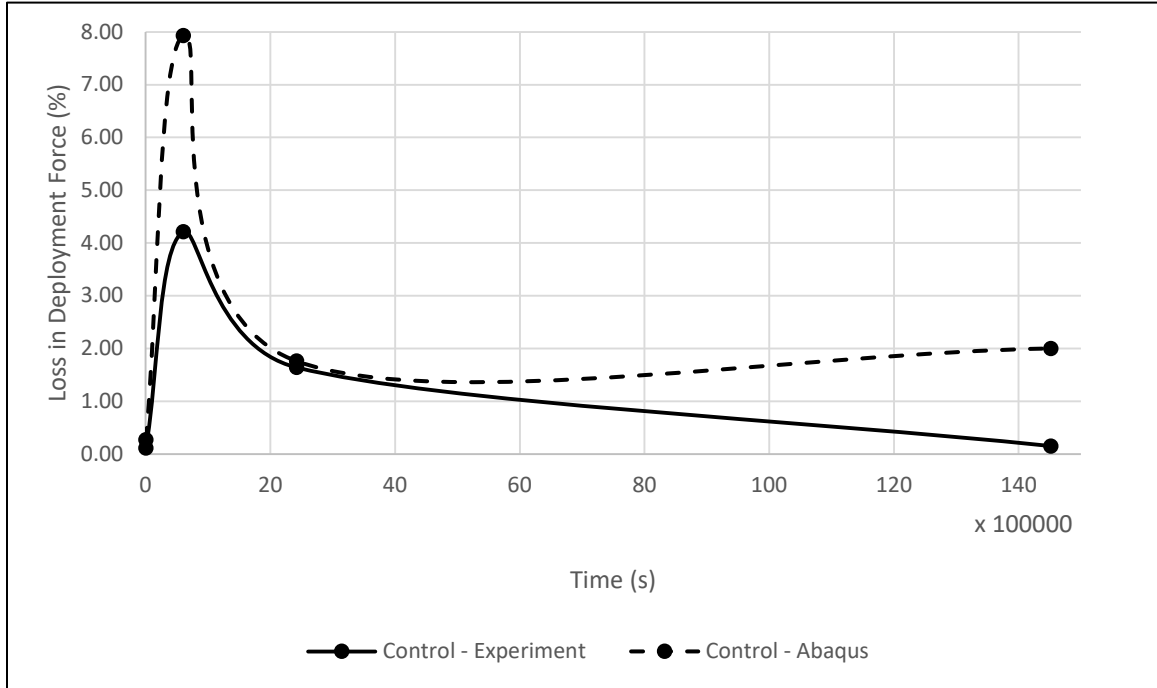


**Figure 5.36 Abaqus vs Experimental Tape Spring Tip Deployment Force Loss for Control Tape Springs**

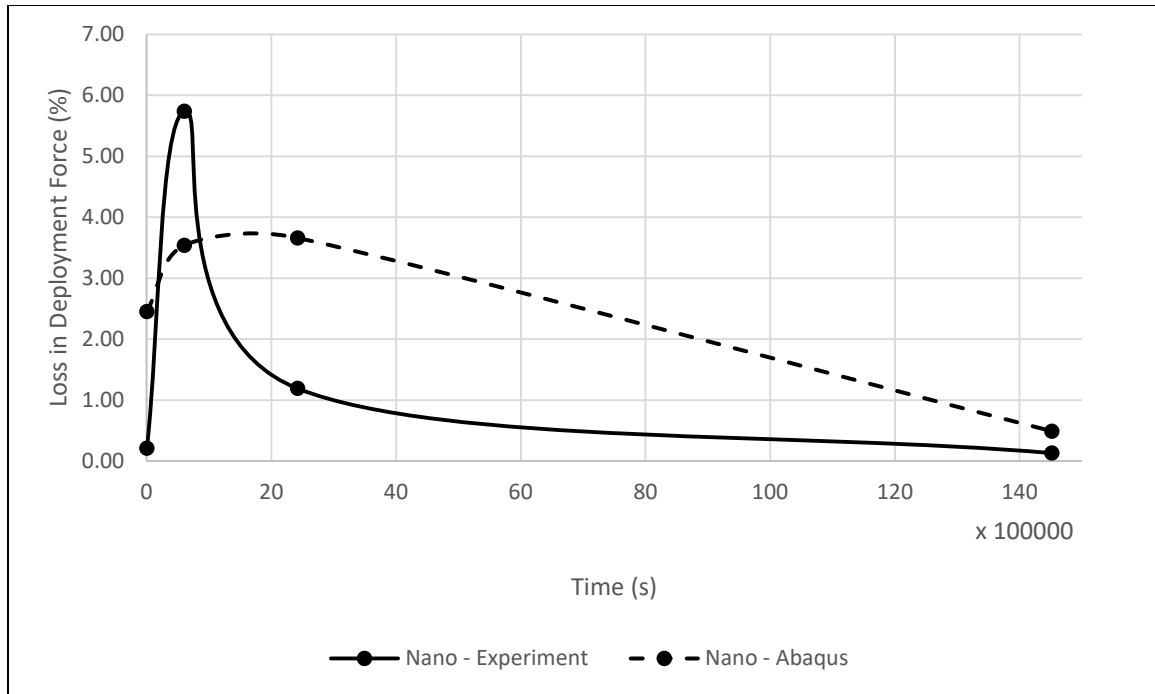


**Figure 5.37 Abaqus vs Experimental Tape Spring Tip Deployment Force Loss for ANP Tape Springs**

**Table 5.6** and **Figure 5.36** show the variation between the tape spring control experiments and Abaqus FEM simulation prediction results was a maximum over prediction of 3.72% for the 1 week stowage, and no under predictions. **Table 5.6** and **Figure 5.37** show the variation for the ANP tape spring experiments and Abaqus FEM simulation prediction results; the variance was between an under prediction of 2.20% for the 1 week stowage to an over prediction of 2.47% for the 1 month stowage. All FEM simulation predicted results and experimental test results were within 5% of each other for change in deployment force loss during the range of stowage times, both control and ANP tape springs.

## 5.7 Summary

This research investigated the structural behavior effects of incorporating ANP particles into the epoxy matrix of PW plies in composite laminate tape springs as deployable space structures. The tape springs are building blocks, or elements, of deployable space architectures with applications ranging from gravity gradient booms to solar array masts to antenna structures and more. These deployable space structures are often folded, bent, or rolled in a stowed configuration for many weeks, months, or even years, between assembly and deployment in space. Consequently, these structures are subject to prescribed loads or enforced displacements for very long periods of time and typically relax during storage and creep during deployment upon the sudden removal of the displacement constraints or load. The addition of ANPs to the matrix tailored the mechanical properties enabling more deployment force and less stress relaxation after stowage.

The focus of this research was experimental testing at the structural level for the tape springs' stowage time period which is often characterized by significant stress relaxation. (Kwok and Pellegrino, 2011) Also, of critical importance and a major challenge for all space missions is the material degradation over time in the harsh space environment. After a structure is deployed on orbit, the space environment batters it with ionizing particles, electromagnetic radiation and frequent cycling through extreme temperature ranges. Ionizing radiation (e.g., protons up to 200 MeV) is deposited and absorbed into the exposed materials and can raise the local temperature substantially.

Such a temperature increase may induce various phase transitions and can dramatically affect the structure's physical properties. (Chipara, 2002) Space structures can also experience detrimental mechanical shock during the dynamics of deployment. Thus, in addition to typical terrestrial design considerations such as strength, stiffness and structural efficiency, deployable space structures need to survive the space environmental conditions and their deployment needs to be damped and controlled while preserving the necessary deployment forces with creep and stress relaxation effects under consideration.

## CHAPTER 6 CONCLUSION AND RECOMMENDATIONS

### 6.1 Conclusions

The goal of this experimentally-focused research at the structural level was to develop a tape spring of a flexible thin composite laminate for a deployable space structure with high stiffness, dimensional stability and foldability to a very small diameter and then provide the structural testing and modeling tools necessary to evaluate the behavior of these types of structures. The incorporation of ANPs was hypothesized to tailor the viscoelastic properties of the composite and thus the tape springs' deployment profile and structural behavior could be engineered passively not requiring parasitical attendant systems for deployment on-orbit. The property of most importance for the tape spring structure is stiffness as strength usually does not drive the design of deployable space structures due to operation in a near zero gravity environment. High stiffness and low mass/density are paramount for deployable space structures.

This research looked at incorporation of ANPs into Patz PMT-F7 epoxy which was hypothesized to hinder stress relaxation effects, lower  $T_g$  and generally interrupt the chemical bonding of the epoxy in structural elements. In amorphous polymers (e.g., the PMT-F7 epoxy in this work), an attractive interface will decrease the mobility of the polymer chains, and conversely, a repulsive interface will increase the mobility. The change in polymer chain mobility is manifested via the changes in the composite's  $T_g$ . (Schadler et al., 2007) Previous research at the material level and with the FlexLam composite revealed the epoxy's  $T_g$  decreased a modest 3.8° C with the addition of 2%

weight ANPs. Moreover, the epoxy's crosslink density was reduced by 20.9% for the same ANP-epoxy also with 2% weight ANP. (Garner et al., 2017)

The expounded objective was to engineer passive strain energy-actuated deployments for space structures, i.e., at the structural level, by building upon prior research at the material level and coupon level. The tape springs' viscoelastic composite matrix was tailored to exploit the viscoelastic properties which determined the stress-strain behavior during the laminate's bending deformation upon rolling onto the hub for stowage. A unique, custom-designed test fixture was built and used to determine the tape springs' structural behavior resulting from ANPs incorporated into the epoxy matrix of the PW plies during the composite layup fabrication. To the author's knowledge, this is a one-of-a-kind test setup providing a way to evaluate viscoelastic effects on the structural behavior of deployable structural elements with nanoparticle additions.

Four samples of both neat epoxy and ANP epoxy were fabricated in-house at AFRL and with Adherent Technologies Inc. and Patz Materials and Technologies Inc., respectively. The samples were cut into coupons and DMA tested for viscoelastic properties of the epoxies. Master curves were produced for both epoxies (i.e., neat and ANP) and the WLF constants were determined through analysis of the DMA data. The DMA data and subsequent analysis permitted calculation of the shift factor with a user-selected test temperature of 200° F per the TTSP allowing reduced test times for 31 of the 51 tape springs.

Four tape springs (3 ANP and 1 control) were examined via SEM/EDS. The tape spring tips were dipped in liquid Argon, a small piece of the tip fractured off and

removed and then coated in gold for SEM examination. The SEM/EDS work revealed the ANP dispersion was dependent upon the particular coupon areas examined. Likewise, the elemental composition analysis depended heavily on what specific area of the coupon the SEM was focused upon. While not a focus of this research, ANP agglomerations or dispersion issues can have a detrimental effect on a composite's structural behavior such as inducing stress concentrations. Agglomerated nanoparticles can also reduce the nanoparticle-matrix adhesion and therefore weaken the composite's load transfer efficiency. To be an effective and economical approach for commercial aerospace applications, the techniques and processes for mass-producing nanocomposites must improve.

The structural testing involved 26 control tape springs and 25 ANP tape springs with stowage times ranging from 1 hour, 1 day, 1 week, 1 month to 6 months. The latter three test cases involved using the TTSP and a thermal chamber to substantially reduce the test times. The test fixture and setup had to be redesigned several times to evolve with the research strategy of obtaining stress relaxation data of stowed structural elements over long periods of time. Some variation in the test data was observed likely due to differences in tape springs' fabrication as thin elements are quite sensitive to even small deltas in geometry and/or layup. The most likely reasons for the increase in deployment force and reduction in stress relaxation were due to a decrease in the material's  $T_g$  (from 142.7° F for neat epoxy to 135.9° F for ANP epoxy at 2% weight) a lower density of crosslinks between the epoxy and ANPs and the ANPs inhibiting the resin from fully reacting with the hardener. (Garner et al., 2017)

Overall, the 25 ANP tape springs showed an average deployment force loss of 9.5% versus the 20.9% from the 26 control tape springs. The ANPs embedded in the tape springs' PW plies at 2% by weight demonstrated the ability to significantly control the deployment force loss of the tape springs by reducing it 55% compared to the control tape springs with neat epoxy. To be clear, the culmination of all experimental testing revealed the ANP tape springs retained 55% more tip force after stowage as compared to the control tape springs.

A comprehensive FEM of the composite laminate tape spring was built in Abaqus version 6.14-1 to simulate the tape spring's structural stowage and deployment process. This modeling involved writing a VUMAT in Fortran code to carefully define the unique composite material mechanical properties of the tape springs. Furthermore, the VUMAT incorporated the use of a 10-term Prony series to accurately reflect the viscoelastic behavior of the tape springs during the structural testing. Due to the features and capabilities of Abaqus, the structural testing simulation was divided into five analysis steps. All steps were done in Abaqus/Explicit with many iterations performed to determine the best mass scaling options to ensure the simulation would complete the job in a computationally efficient amount of time. For example, even with mass scaling the first two steps took over eight hours to complete with double precision. The Abaqus FEM-produced simulation results were correlated with the experimental structural test results.

The difference between the predictive Abaqus numerical results and the experimental structural test results for the ANP tape springs varied from under predicting

by 2.20% for the 1 week tape springs to an over prediction by 2.47% for the 1 month tape springs. The difference between the predictive Abaqus numerical results and the experimental structural results for the control tape springs was between a maximum over prediction of 3.72% for the 1 week tape springs to a minimum over prediction of 0.12% for the 1 month tape springs. Thus, in all test cases, the difference between the Abaqus FEM simulation predictions for the tape spring tips' force loss and that from the experimental structural testing of the tape springs was less than 5% providing good correlation of the stress relaxation and tip force loss for 51 tape springs during 5 different stowage periods varying from 1 hour to 6 months.

To summarize, 51 composite laminate tape springs were fabricated with 26 control tape springs and 25 ANP tape springs with 2% by weight of ANPs. The tape springs were all 20 inches long, 0.785 inches of flattened width and 0.0090 inches in thickness. The control and ANP tape springs were both split into 5 groups of 5 (with 1 extra control tape spring) for structurally testing the tape springs as they rolled up onto a storage hub with the assistance of an MTS Instron machine, remained stowed for periods of time ranging from 1 hour, 1 day, 1 week, 1 month and 6 months, and then deployed (unrolled) from the hub with assistance from the MTS Instron machine. The structural testing was performed with a custom-designed test fixture, a procedure specifically for this work and conducted on the MTS Instron machine. The three latter long stow times (i.e., 1 week, 1 month, 6 months) were tested in an efficient manner by utilizing the accepted TTSP in polymer physics. The TTSP allowed 30 structural tests to be performed within a much-reduced timeframe at a temperature of 200° F in an enclosed thermal chamber attached to the MTS Instron machine. In order to utilize the TTSP,

DMA testing was conducted on both control and ANP coupons to determine the required structural test parameters. To examine the composite laminate's microstructure and gain insight into the ANP dispersion and agglomeration, SEM with EDS was conducted on ANP and control tape spring specimens as well as the ANP-doped epoxy.

## **6.2 Limitations and Constraints**

As with most any research effort and testing campaign there are limitations and constraints on the work. While time and funding are practical constraints they don't hold much interest from a technical point of view. Some technical limitations and constraints for this research work included fabrication issues, measurements, modeling assumptions and FEM techniques and simulation approach.

Fabricating the 51 composite laminate tape springs introduced many potential sources of deviation from a perfect or ideal tape spring. Although the composite layup procedure is well detailed, different technicians may not perform the work in exactly the same fashion. Fortunately, the same lot of raw materials was used for the control and ANP tape springs. The dispersion of the ANPs was particularly difficult and the resin had to be returned to the vendor (Adherent Technologies, Inc.) to re-process it because Patz indicated the dispersed part A resin was lumpy and too viscous for the first batch. As mentioned in section 6.1, the dispersion process for achieving a well-dispersed, homogeneous matrix is critically important for both an effective load transfer and stress

transfer to occur in the structure itself. While several researchers have used functional agents to aid in the dispersion of nanofillers, the additional surfactant phase can be difficult to entirely remove from the composite, especially at the polymer chain to particle interface, resulting in undesirable (at the very least unknown) composite characteristics if residual surfactant remains in the composite. (Ash et al., 2001, West and Malhotra, 2006, Akinyede et al., 2009) Poor dispersion and agglomeration of nanoparticles can have a range of negative consequences.

Erroneous measurements can lead to gross miscalculations of thin laminate composites and the effect is magnified as the thickness is reduced. Accurate measurements, and thickness in particular, are critical to correlating the experimental test results with analytical and numerical results. Even very small deviations in ply thicknesses can cause the FEM to have drastically different results or not even converge at all. For example, increasing the laminate thickness by 6% in aggregate caused the FEM to abort the simulation job due to excessive distortion of elements and a ratio of deformation speed to elastic wave speed not allowable (i.e.,  $> 1.0$ ). Many variations of mass scaling factors were attempted but the simulation would not converge. There are numerous related factors affected by lamina and laminate thickness applied throughout the model, such as section properties, element control properties, element types, mesh size, etc.

Assumptions used in the modeling process must be understood and used with great care. This premise is valid for both analytical and numerical modeling but the focus here is on the assumptions made during the FEM build. The major assumptions

implemented in this research work included micromechanics/CLT and its associated assumptions, linear elasticity for the UD ply's carbon fibers, uniform and homogeneous dispersion of the ANPs, no friction or damping losses in the structural testing fixture or process, the Prony series curve fit as a perfect match for the experimental DMA data, and the very important material properties at the lamina level. Many, if not all, of these items contributed to the differences observed between the experimental structural test results and the predicted finite element results for deployment force loss manifested during stowage. While any of them in and of themselves might not contribute substantially to a delta in non-correlation, the synergistic effects of all or several of them combined may indeed prove quite detrimental for FEM correlation purposes and modeling accurately the structural behavior of the tape springs. It must be well understood what information and to what level is required for a reasonable model and how much is too much or adds too much complexity consuming valuable time and resources.

As far as FEM techniques, it is undoubtedly advantageous to utilize the user-defined materials (i.e., UMAT and VUMAT) in Abaqus to accurately define unique composite materials, though no options exist in the finite element package to explicitly address nanofillers in a composite material. An extensive UMAT/VUMAT could possibly capture these effects. Currently, one common way nanocomposite materials are handled from a modeling perspective is via a homogenization technique in conjunction with an RVE approach. Moreover, the application of boundary conditions, loads, interactions and constraints within Abaqus itself are naturally idealized and don't necessarily represent real material behavior in the actual environment. FEM techniques also permit options which help the model converge and quickly, but do not have physical

meaning. For example, a user can adjust the values of density, mass or damping to the whole model or just to specific parts or elements to bring the overall mass, stiffness or damping to expected levels of the real system. Even negative, nonphysical material values can be used for this purpose. The user must ensure the overall behavior of the structure is physical though if using non-real property values to adjust the FEM for correlation purposes.

### **6.3 Future Work**

An analytical, closed-form model of the stowage and subsequent deployment of the nanocomposite tape springs at the structural level would be highly beneficial. Such a model would permit systematic performance trades to evaluate meeting structural requirements dictated by the application and mission. For example, previous work by Gomez-Delrio and Kwok provided an analytical, closed-form solution for a composite tape spring for moment relaxation and recovery, but the tape spring was not rolled up (only folded) or stowed for lengthy amounts of time approaching typical deployable space structures' storage times (only 12 days). However, from this precedent, a nanocomposite tape spring analytical model could leverage that work, and possibly others, as a first step. (Gomez-Delrio and Kwok, 2018) A comprehensive parametric model capable of analyzing nanoparticle effects all the way up to the structural behavior would be extremely useful, but also very challenging to produce. The Dakota software

tool by Sandia National Laboratory may prove useful in evaluating the optimal constituent loading.

Future work also could entail design optimization of the composite laminate with respect to fibers, nanoparticles, plies, thickness and/or varying stiffnesses, etc. Because the design space for composite materials is so broad, a parameterized-model would be extremely beneficial as a means to assess trade studies and Monte Carlo analyses on the optimal design of the system. Case in point, Tsai and Pagano looked at the effect of lamina orientation on composite properties to derive them from angle relations instead of sine and cosine relations. They found invariant properties can be used as an effective measure of the performance of the composite. Their trace-based theory improves accuracy for multi-directional laminates. (Tsai and Pagano, 1968, Tsai and Melo, 2014) At the nanoscale and below, theoretical predictions on effective mechanical properties on nanocomposites are usually made under the assumption of high interfacial strength with perfect bonding. (Dastgerdi et al., 2014) It is clear a strong interfacial bond requires more energy (higher temperature) to break. Thus, the assumption of perfect bonding may not be viable for accurately modeling the composite behavior. It is preferred to utilize theory-based approaches as opposed to phenomenological approaches (e.g., failure criteria). Therefore, to properly describe the Young's modulus transition in a viscoelastic composite, the functionally graded variation interphase (FGVI) may be an option. With FGVI it is necessary to develop an analytical model considering both the van der Waals-based interface and the FGVI. Young's modulus variation in the form of a power law can be employed for the FGVI. The de-bonding process is simulated with the van der Waals interaction between FGVI and nanoparticles. As FGVI is a part of

polymer resin with its position dependent material properties, the rigid connection is assumed for the interaction between FGVI and polymer resin. (Zhang et al., 2013)

On the modeling and simulation front, materials with nanoparticles are “too small” for continuum-scale assumptions and “too large” for conventional atomistic computational techniques so for nanophenomena a mesoscale could possibly be used. When multi-continuum theory (MCT) is used for composites, it has typically produced reasonable results with the added benefit failure can be evaluated for each constituent. Failure of the tape springs was not addressed in this work, but it is important to evaluate for critical structural applications. MCT represents a mathematically tractable approach for incorporating micromechanical effects into a global analysis. (Hansen and Garnich, 1995) Moreover, MCT permits the awareness of constituent level behavior in the analysis unlike classical elastic and composite theories which report bulk properties and don't provide such insight. For example, whenever one or more fibers are broken in a woven fabric under stress, the load in the broken fiber(s) must be transferred through the matrix to the adjacent fibers in order to restore equilibrium. Thus, the tension-carrying fibers are connected by purely shear-carrying material, the matrix. MCT can provide details of mechanics and failure mechanisms to aid the engineer in the iterative design and modeling process. MCT could be an option for improving the design and modeling process as future work.

The brittleness and lack of matrix toughness in a neat aerospace-grade epoxy are two drawbacks reduced with the addition of nanofillers. While damage and failure were not addressed in this research, it is important to note high strain composites utilizing an

epoxy doped with nanoparticles can address two primary damage initiation modes in CFRPs, namely, matrix cracking and delamination. The nanoparticles can impede crack growth, promote crack front trapping and shield cracks. (Singh et al., 2002)

Nanoparticles also typically form an interphase in a composite but the nature of, properties and effects of the interphase on the bulk mechanical properties of the nanocomposite are not well known or researched. Future work could address both failure modes and analysis in these types of tape spring nanocomposite structural elements as well as aspects of the interphase.

The FEM simulation process was challenging. The import analysis / transfer results strategy between Abaqus/Explicit to Abaqus Standard and back to Abaqus/Explicit is left for future work. This modeling/simulation strategy may prove to be a more efficient simulation technique than performing the entire analysis in Abaqus/Explicit. In this work the FEM was used primarily to infer the mechanics of the composite tape springs as the research was experimentally focused. Additionally, analysis of the deployment step following the quasi-static stow step should deserve additional emphasis for evaluating the post-stowage deployment with more fidelity.

Bridging the technical and time gaps between modeling, testing and in-service use for composite structures is of great interest to the engineer and society. Bringing safer, better products to the government and commercial marketplace faster is a necessity in today's globally competitive environment. Only when we truly understand how nanoreinforcements affect materials from a performance and failure perspective can their efficacy be fully utilized. After all, advanced composites and nanotechnology have the

potential to greatly improve not only mechanical structures but also medicine, transportation and exploration.

## APPENDIX A: Control Tape Springs' Measurements

Table A.1 Control Tape Springs' Measurements

Specimen Number	Serial Number	Length (in)	Length (cm)	Flattened Width (cm)	Width (in)	Avg. Width (cm)	Thickness (mils)	Thickness (mm)	Avg. Thickness (mm)
1	2015129-003	19.7	50.038	1.99898	0.787	2.006854	8.5	0.215900432	0.220980442
				2.04343	0.8045		8.5	0.215900432	
				1.97485	0.7775		9.0	0.228600457	
				1.99898	0.787		9.0	0.228600457	
				2.01803	0.7945		8.5	0.215900432	
2	2015129-004	19.6	49.784	1.97231	0.7765	1.996651667	8.5	0.215900432	0.218440437
				2.00152	0.788		9.0	0.228600457	
				1.99517	0.7855		9.0	0.228600457	
				1.99136	0.784		8.5	0.215900432	
				2.00152	0.788		8.0	0.203200406	
3	2015129-005	19.7	50.038	1.99644	0.786	1.97231	9	0.228600457	0.220980442
				1.92278	0.757		8.5	0.215900432	
				1.94818	0.767		8.5	0.215900432	
				1.96215	0.7725		8.5	0.215900432	
				2.00279	0.7885		9	0.228600457	
4	2015129-006	19.6	49.784	1.99898	0.787	1.994746667	8.5	0.215900432	0.218440437
				1.98882	0.783		9	0.228600457	
				1.99517	0.7855		8.5	0.215900432	
				1.98882	0.783		8.5	0.215900432	
				1.9939	0.785		8.5	0.215900432	
5	20151229-001	19.6	49.784	1.99644	0.786	1.986915	8.5	0.215900432	0.218440437
				1.99517	0.7855		9	0.228600457	
				1.99898	0.787		8.5	0.215900432	
				1.97104	0.776		8.5	0.215900432	
				1.96596	0.774		8.5	0.215900432	
6	20151229-002	19.7	50.038	1.99644	0.786	1.985856667	9	0.228600457	0.226060452
				1.96977	0.7755		9	0.228600457	
				1.98882	0.783		8.5	0.215900432	
				1.98882	0.783		9	0.228600457	
				2.00533	0.7895		9	0.228600457	
7	20160505-001	19.7	50.038	2.00914	0.791	1.959652333	8.5	0.215900432	0.213360427
				1.971294	0.7761		8	0.203200406	
				1.97612	0.778		8.5	0.215900432	
				1.87452	0.738		8.5	0.215900432	
				1.92151	0.7565		8.5	0.215900432	
8	20160505-002	19.7	50.038	2.00025	0.7875	1.98374	8	0.203200406	0.208280417
				2.00025	0.7875		8.5	0.215900432	
				1.98247	0.7805		8	0.203200406	
				1.99771	0.7865		8.5	0.215900432	
				2.00025	0.7875		8	0.203200406	
9	20160505-003	19.7	50.038	2.07391	0.8165	2.011045	8	0.203200406	0.208280417
				2.02311	0.7965		8.5	0.215900432	
				2.00406	0.789		8	0.203200406	
				2.00025	0.7875		8	0.203200406	
				1.96469	0.7735		8.5	0.215900432	
10	20160505-004	19.7	50.038	1.98628	0.782	1.960668333	9	0.228600457	0.223520447
				1.91262	0.753		9	0.228600457	
				1.97612	0.778		8.5	0.215900432	
				1.93294	0.761		8.5	0.215900432	
				1.99136	0.784		9	0.228600457	
11	20160505-001	19.75	50.165	1.97993	0.7795	1.969135	9	0.228600457	0.220980442
				1.93294	0.761		8.5	0.215900432	
				1.9431	0.765		9	0.228600457	
				1.99517	0.7855		8.5	0.215900432	
				1.97231	0.7765		8.5	0.215900432	
12	20160505-001	19.7	50.038	1.97866	0.779	1.993688333	8	0.203200406	0.210820422
				1.9939	0.785		8.5	0.215900432	
				2.00787	0.7905		8.5	0.215900432	
				1.99644	0.786		8	0.203200406	
				2.01295	0.7925		8.5	0.215900432	
13	20160105-002	19.65	49.911	1.99771	0.7865	2.000038333	8	0.203200406	0.215900432
				2.00406	0.789		8.5	0.215900432	
				1.99644	0.786		8.5	0.215900432	
				1.99771	0.7865		9	0.228600457	
				1.99136	0.784		8.5	0.215900432	
14	20160105-003	19.75	50.165	2.04089	0.8035	2.014008333	9	0.228600457	0.215900432
				2.01549	0.7935		8.5	0.215900432	
				2.00152	0.788		8.5	0.215900432	
				2.01422	0.793		8.5	0.215900432	
				2.02057	0.7955		8	0.203200406	

Specimen Number	Serial Number	Length (in)	Length (cm)	Flattened Width (cm)	Width (in)	Avg. Width (cm)	Thickness (mils)	Thickness (mm)	Avg. Thickness (mm)
15	20160105-004	19.7	50.038	2.0066	0.79	1.995381667	8.5	0.215900432	0.220980442
				1.96977	0.7755		9	0.228600457	
				1.97231	0.7765		8.5	0.215900432	
				2.00025	0.7875		9	0.228600457	
				2.00279	0.7885		8.5	0.215900432	
16	20160105-005	19.65	49.911	2.03581	0.8015	2.045335	8.5	0.215900432	0.218440437
				1.97866	0.779		8.5	0.215900432	
				1.95707	0.7705		8.5	0.215900432	
				2.0828	0.82		9	0.228600457	
				2.21488	0.872		8.5	0.215900432	
17	20160105-006	19.75	50.165	2.00025	0.7875	2.02819	8.5	0.215900432	0.215900432
				1.98247	0.7805		8.5	0.215900432	
				1.98374	0.781		8.5	0.215900432	
				2.00787	0.7905		8.5	0.215900432	
				1.97993	0.7795		8.5	0.215900432	
18	20160526-001	19.7	50.038	1.97612	0.778	1.984375	8.5	0.215900432	0.213360427
				2.01041	0.7915		8	0.203200406	
				1.99898	0.787		8.5	0.215900432	
				1.96342	0.773		8.5	0.215900432	
				1.97739	0.7785		8.5	0.215900432	
19	20160526-002	19.7	50.038	2.21361	0.8715	2.170641667	8.5	0.215900432	0.220980442
				2.20726	0.869		8.5	0.215900432	
				2.2098	0.87		9	0.228600457	
				2.20345	0.8675		9	0.228600457	
				2.21234	0.871		8.5	0.215900432	
20	20160526-003	19.7	50.038	1.99136	0.784	2.029671667	8.5	0.215900432	0.218440437
				1.9812	0.78		8.5	0.215900432	
				2.0066	0.79		9	0.228600457	
				1.98628	0.782		8.5	0.215900432	
				2.00025	0.7875		8.5	0.215900432	
21	20160526-006	19.75	50.165	1.98755	0.7825	1.983316667	8	0.203200406	0.213360427
				2.0447	0.805		8.5	0.215900432	
				1.97612	0.778		8.5	0.215900432	
				1.91643	0.7545		8.5	0.215900432	
				1.97485	0.7775		8.5	0.215900432	
22	20160808-001	19.8	50.292	2.01422	0.793	1.994535	8	0.203200406	0.208280417
				1.99009	0.7835		8.5	0.215900432	
				1.9685	0.775		8	0.203200406	
				2.00533	0.7895		8	0.203200406	
				2.01422	0.793		8.5	0.215900432	
23	20160808-002	19.8	50.292	1.98882	0.783	1.981835	8.5	0.215900432	0.210820422
				1.93675	0.7625		8	0.203200406	
				1.91135	0.7525		8	0.203200406	
				2.03073	0.7995		8.5	0.215900432	
				2.00914	0.791		8.5	0.215900432	
24	20160808-004	19.8	50.292	1.99009	0.7835	1.997075	8	0.203200406	0.208280417
				1.99517	0.7855		8	0.203200406	
				2.00406	0.789		8.5	0.215900432	
				1.99136	0.784		8	0.203200406	
				1.99263	0.7845		8.5	0.215900432	
25	20160112-001	19.65	49.911	1.98374	0.781	1.998345	8.5	0.215900432	0.215900432
				2.00914	0.791		9	0.228600457	
				2.00279	0.7885		8.5	0.215900432	
				1.9939	0.785		8	0.203200406	
				2.00787	0.7905		8.5	0.215900432	
26	20160811-001	19.65	49.911	2.01803	0.7945	2.005753333	8.5	0.215900432	0.213360427
				2.00152	0.788		8.5	0.215900432	
				2.02438	0.797		8	0.203200406	
				1.98628	0.782		8.5	0.215900432	
				1.99644	0.786		8.5	0.215900432	
27	20160811-002	19.65	49.911	1.94564	0.766	1.973791667	8	0.203200406	0.208280417
				2.0193	0.795		8.5	0.215900432	
				1.9939	0.785		8	0.203200406	
				1.8923	0.745		8	0.203200406	
				1.99517	0.7855		8.5	0.215900432	
28	EXTRA	19.7	50.038	1.98882	0.783	1.970405	8.5	0.215900432	0.215900432
				2.00279	0.7885		9	0.228600457	
				1.94945	0.7675		8.5	0.215900432	
				1.9304	0.76		8.5	0.215900432	
				1.9558	0.77		8	0.203200406	

## APPENDIX B: ANP Tape Springs' Measurements

Table B.1 ANP Tape Springs' Measurements

Specimen Number	Serial Number	Length (in)	Length (cm)	Flattened Width (cm)	Width (in)	Avg. Width (cm)	Thickness (mils)	Thickness (mm)	Avg. Thickness (mm)
1	20180530-005	19.6	49.784	2.02057	0.7955	2.011172	10.0	0.254000508	0.264160528
				2.00025	0.7875		11.0	0.279400559	
				1.99771	0.7865		11.0	0.279400559	
				1.99136	0.784		10.0	0.254000508	
				2.04597	0.8055		10.0	0.254000508	
2	20180530-006	19.6	49.784	2.02057	0.7955	2.051261667	11.0	0.279400559	0.269240538
				1.99644	0.786		10.0	0.254000508	
				2.0574	0.81		11.0	0.279400559	
				2.12217	0.8355		11.0	0.279400559	
				2.06502	0.813		10.0	0.254000508	
3	20180524-012	19.6	49.784	2.04597	0.8055	2.016548333	10	0.254000508	0.264160528
				1.97739	0.7785		11	0.279400559	
				1.97866	0.779		10	0.254000508	
				1.99009	0.7835		11	0.279400559	
				2.04216	0.804		10	0.254000508	
4	20180524-009	19.7	50.038	1.9812	0.78	1.994535	10	0.254000508	0.25980518
				1.96215	0.7725		10	0.254000508	
				1.97612	0.778		11	0.279400559	
				1.98374	0.781		10	0.254000508	
				2.02184	0.796		10	0.254000508	
5	20180529-002	19.6	49.784	2.10312	0.828	2.03581	11	0.279400559	0.269240538
				2.07264	0.816		11	0.279400559	
				1.97866	0.779		10	0.254000508	
				1.98374	0.781		11	0.279400559	
				2.05486	0.809		10	0.254000508	
6	20180524-007	19.7	50.038	2.03581	0.8015	2.027343333	11	0.279400559	0.264160528
				1.99644	0.786		10	0.254000508	
				1.98755	0.7825		10	0.254000508	
				1.98247	0.7805		11	0.279400559	
				2.10693	0.8295		10	0.254000508	
7	20180531-002	19.6	49.784	2.04216	0.804	2.029883333	11	0.279400559	0.25980518
				1.9939	0.785		10	0.254000508	
				1.99263	0.7845		10	0.254000508	
				1.97993	0.7795		10	0.254000508	
				2.06375	0.8125		10	0.254000508	
8	20180524-006	19.7	50.038	2.03708	0.802	2.00025	10	0.254000508	0.248920498
				1.97612	0.778		10	0.254000508	
				1.97612	0.778		10	0.254000508	
				1.97231	0.7765		10	0.254000508	
				1.97612	0.778		9	0.228600457	
9	20180524-004	19.7	50.038	2.03073	0.7995	2.018241667	11	0.279400559	0.238760478
				2.00406	0.789		9	0.228600457	
				2.00025	0.7875		9	0.228600457	
				2.03073	0.7995		9	0.228600457	
				2.06756	0.814		9	0.228600457	
10	20180524-011	19.7	50.038	2.02057	0.7955	2.013796667	9	0.228600457	0.243840488
				2.00406	0.789		10	0.254000508	
				1.99009	0.7835		9	0.228600457	
				2.00533	0.7895		10	0.254000508	
				1.99517	0.7855		10	0.254000508	
11	20180531-001	19.7	50.038	1.94056	0.764	2.009986667	9	0.228600457	0.243840488
				1.99898	0.787		9	0.228600457	
				2.01676	0.794		10	0.254000508	
				2.02946	0.799		10	0.254000508	
				2.07899	0.8185		10	0.254000508	
12	20180529-005	19.6	49.784	1.92405	0.7575	1.986068333	11	0.279400559	0.264160528
				1.94945	0.7675		11	0.279400559	
				1.96215	0.7725		10	0.254000508	
				1.98501	0.7815		10	0.254000508	
				2.01676	0.794		10	0.254000508	
13	20180529-006	19.7	50.038	2.02438	0.797	1.995381667	11	0.279400559	0.254000508
				1.98501	0.7815		9	0.228600457	
				1.98247	0.7805		10	0.254000508	
				1.9812	0.78		10	0.254000508	
				1.98247	0.7805		10	0.254000508	
14	20180530-002	19.6	49.784	1.96596	0.774	1.995805	10	0.254000508	0.254000508
				1.99009	0.7835		10	0.254000508	
				2.00406	0.789		10	0.254000508	
				2.0066	0.79		10	0.254000508	
				2.02565	0.7975		10	0.254000508	

Specimen Number	Serial Number	Length (in)	Length (cm)	Flattened Width (cm)	Width (in)	Avg. Width (cm)	Thickness (mils)	Thickness (mm)	Avg. Thickness (mm)
15	20180524-001	19.6	49.784	2.03962	0.803	2.015701667	11	0.279400559	0.264160528
				2.02946	0.799		11	0.279400559	
				2.01422	0.793		10	0.254000508	
				1.9939	0.785		10	0.254000508	
				1.99136	0.784		10	0.254000508	
16	20180530-001	19.6	49.784	2.12852	0.838	2.062056667	10	0.254000508	0.248920498
				2.08661	0.8215		9	0.228600457	
				2.03708	0.802		10	0.254000508	
				2.02692	0.798		10	0.254000508	
				2.10185	0.8275		10	0.254000508	
17	20180524-008	19.7	50.038	2.11455	0.8325	2.052743333	10	0.254000508	0.259080518
				2.01803	0.7945		10	0.254000508	
				2.02565	0.7975		11	0.279400559	
				2.01041	0.7915		10	0.254000508	
				2.04597	0.8055		10	0.254000508	
18	20180530-003	19.7	50.038	2.01041	0.7915	2.01041	10	0.254000508	0.259080518
				1.96723	0.7745		11	0.279400559	
				1.95834	0.771		10	0.254000508	
				1.98501	0.7815		10	0.254000508	
				2.0955	0.825		10	0.254000508	
19	20180524-002	19.7	50.038	2.01803	0.7945	1.999826667	10	0.254000508	0.264160528
				1.97866	0.779		10	0.254000508	
				1.97739	0.7785		11	0.279400559	
				1.9685	0.775		11	0.279400559	
				1.96088	0.772		10	0.254000508	
20	20180529-003	19.7	50.038	2.032	0.8	1.987761667	9	0.228600457	0.248920498
				1.9812	0.78		10	0.254000508	
				1.95961	0.7715		10	0.254000508	
				1.97993	0.7795		10	0.254000508	
				2.01295	0.7925		10	0.254000508	
21	20180531-004	19.6	49.784	2.03708	0.802	2.001308333	9	0.228600457	0.248920498
				2.0066	0.79		10	0.254000508	
				1.99898	0.787		10	0.254000508	
				1.96977	0.7755		10	0.254000508	
				1.98247	0.7805		10	0.254000508	
22	20180529-004	19.7	50.038	2.02438	0.797	1.99009	10	0.254000508	0.254000508
				2.0066	0.79		10	0.254000508	
				1.99009	0.7835		10	0.254000508	
				1.97358	0.777		10	0.254000508	
				1.96342	0.773		10	0.254000508	
23	20180529-001	19.7	50.038	1.97612	0.778	2.009563333	11	0.279400559	0.264160528
				1.9939	0.785		11	0.279400559	
				2.01295	0.7925		10	0.254000508	
				2.032	0.8		11	0.279400559	
				2.07899	0.8185		9	0.228600457	
24	20180524-003	19.65	49.911	2.01041	0.7915	2.026708333	9	0.228600457	0.248920498
				1.99136	0.784		10	0.254000508	
				1.98755	0.7825		10	0.254000508	
				1.99263	0.7845		10	0.254000508	
				2.09931	0.8265		10	0.254000508	
25	20180524-010	19.65	49.911	2.02057	0.7955	2.008716667	10	0.254000508	0.248920498
				1.98755	0.7825		10	0.254000508	
				1.98628	0.782		9	0.228600457	
				1.98501	0.7815		10	0.254000508	
				1.97358	0.777		10	0.254000508	
26	20180531-003	19.7	50.038	2.02692	0.798	2.008293333	10	0.254000508	0.243840488
				1.98501	0.7815		10	0.254000508	
				2.01041	0.7915		10	0.254000508	
				1.98628	0.782		9	0.228600457	
				2.06756	0.814		9	0.228600457	
27	20180530-004	19.65	49.911	2.08915	0.8225	2.026285	10	0.254000508	0.254000508
				1.99263	0.7845		10	0.254000508	
				1.98374	0.781		10	0.254000508	
				1.98501	0.7815		10	0.254000508	
				2.03962	0.803		10	0.254000508	
28	20180524-005	19.7	50.038	2.03454	0.801	1.986491667	10	0.254000508	0.254000508
				1.97866	0.779		10	0.254000508	
				1.95834	0.771		10	0.254000508	
				1.95199	0.7685		10	0.254000508	
				1.9558	0.77		10	0.254000508	

## APPENDIX C: Abaqus VUMAT Fortran Code

The VUMAT for the control tape springs is as follows:

```
*****  
*USER SUBROUTINE  
    subroutine vumat(  
C Read only (unmodifiable) variables -  
    1 nblock, ndir, nshr, nstatev, nfieldv, nprops, lanneal,  
    2 stepTime, totalTime, dt, cmname, coordMP, charLength,  
    3 props, density, strainInc, relSpinInc,  
    4 tempOld, stretchOld, defgradOld, fieldOld,  
    5 stressOld, stateOld, enerInternOld, enerInelasOld,  
    6 tempNew, stretchNew, defgradNew, fieldNew,  
C write only (modifiable) variables -  
    7 stressNew, stateNew, enerInternNew, enerInelasNew)  
C  
    include 'vaba_param.inc'  
C  
    dimension props (nprops), density(nblock), coordMP(nblock,*),  
    1 charLength(nblock), strainInc(nblock, ndir+nshr),  
    2 relSpinInc (nblock, nshr), tempOld(nblock),  
    3 stretchOld(nblock, ndir+nshr), defgradOld(nblock,ndir+nshr+nshr),  
    4 fieldOld(nblock, nfieldv), stressOld(nblock, ndir+nshr),
```

```

5 stateOld(nblock, nstatev), enerInternOld(nblock),
6 enerInelasOld(nblock), tempNew(nblock),
7 stretchNew(nblock, ndir+nshr), defgradNew(nblock,ndir+nshr+nshr),
8 fieldNew(nblock, nfieldv), stressNew(nblock, ndir+nshr),
9 stateNew(nblock, nstatev), enerInternNew(nblock),
1 enerInelasNew(nblock)
C
character*80 cmname
C  INTEGER INTV(1)
C  REAL REALV(1)
C  CHARACTER*8 CHARV(1)
C  LOP = -3
C  CALL XPLB_ABQERR(LOP,'VUMAT initial',INTV,REALV,CHARV)
C  Line 35
dimension Qmat(3,3), Smat(3,3)
C  1 pstrain1(nblock), pstrain2(nblock), pstrain3(nblock),
C  2 sigma1(nblock), sigma2(nblock), sigma3(nblock),
C  3 epsilonE1(nblock), epsilonE2(nblock), epsilonE3(nblock),
C  4 sigmaX(nblock), sigmaY(nblock), sigmaXY(nblock),
C  5 epsilonX(nblock), epsilonY(nblock), epsilonXY(nblock), ENERGY(nblock)
C  DEFINE VARIABLES
C  Line 45
double precision:: t1,t2,t3,t4,t5,t6,t7,t8,t9,t10
double precision:: k1,k2,k3,k4,k5,k6,k7,k8,k9,k10
double precision:: b1,b2,b3,b4,b5,b6,b7,b8,b9,b10

```

```

double precision:: EMT, GMT, EX, EY, NUYYX
double precision:: E1, E2, G12, NU12, GF, NU21
double precision:: E1F, E2F, Em, NUm, NUf, VF
double precision:: TWOMU, SIXMU, ALAMDA
double precision:: pstrain1, pstrain2, pstrain3
double precision:: sigma1, sigma2, sigma3
double precision:: epsilonE1, epsilonE2, epsilonE3
double precision:: sigmaX, sigmaY, sigmaXY
double precision:: epsilonX, epsilonY, epsilonXY
double precision:: ENERGY

INTEGER INTV(1)

REAL REALV(1)

CHARACTER*8 CHARV(1)

LOP = -3

C   CALL XPLB_ABQERR(LOP,'VUMAT point 1',INTV,REALV,CHARV)

C   MATERIAL CONSTANTS DEFINED IN ABAQUS

E1F = PROPS(1)

E2F = PROPS(2)

Em = PROPS(3)

NUm = PROPS(4)

NUf = PROPS(5)

VF = PROPS(6)

C   CALL XPLB_ABQERR(LOP,'VUMAT point 2.',INTV,REALV,CHARV)

C   PRONY SERIES COEFFICIENTS

k1 = 0.401

```

$$k2 = 0.289$$

$$k3 = 0.302$$

$$k4 = 0.257$$

$$k5 = 0.214$$

$$k6 = 0.189$$

$$k7 = 0.163$$

$$k8 = 0.147$$

$$k9 = 0.153$$

$$k10 = 0.202$$

C Line 87

C CALL XPLB\_ABQERR(LOP,'VUMAT point 3.',INTV,REALV,CHARV)

$$t1 = 9.42E-14$$

$$t2 = 2.02E-11$$

$$t3 = 4.77E-09$$

$$t4 = 2.25E-06$$

$$t5 = 6.62E-04$$

$$t6 = 1.84E-01$$

$$t7 = 4.72E+01$$

$$t8 = 8.42E+03$$

$$t9 = 1.36E+06$$

$$t10 = 3.66E+08$$

C Line 98

C CALL XPLB\_ABQERR(LOP,'VUMAT point 4.',INTV,REALV,CHARV)

$$b1 = k1*(1-EXP(-stepTime/t1))$$

$$b2 = k2*(1-EXP(-stepTime/t2))$$

```

b3 = k3*(1-EXP(-stepTime/t3))
b4 = k4*(1-EXP(-stepTime/t4))
b5 = k5*(1-EXP(-stepTime/t5))
b6 = k6*(1-EXP(-stepTime/t6))
b7 = k7*(1-EXP(-stepTime/t7))
b8 = k8*(1-EXP(-stepTime/t8))
b9 = k9*(1-EXP(-stepTime/t8))
b10 = k10*(1-EXP(-stepTime/t10))
C  CALL XPLB_ABQERR(LOP,'VUMAT point 5.',INTV,REALV,CHARV)
C  TIME-DEPENDENT MATERIAL PROPERTIES CALCULATION
if (totalTime .eq. zero) then
    EMT = Em
    GMT = Em/(2*(1+NUm))
    GF = E1F/(2*(1+NUf))
    E1 = 0.5*VF*(E1F+E2F)+EMT*(1-VF)
    E2 = E1
    G12 = GMT/(1-sqrt(VF)*(1-GMT/GF))
    NU12 = (1-VF)*NUm+VF*NUf
    NU21 = NU12*(E2/E1)
    TWOMU = E1/(1 + NU12)
    SIXMU = 3*TWOMU
    ALAMDA = TWOMU*(E1-TWOMU)/(SIXMU-2*E1)
end if
if (totalTime .gt. zero) then
    EMT = Em-Em*(b1+b2+b3+b4+b5+b6+b7+b8+b9+b10)

```

$$\text{GMT} = \text{EMT}/(2*(1+\text{NUm}))$$

$$\text{GF} = \text{E1F}/(2*(1+\text{NUf}))$$

$$\text{E1} = 0.5*\text{VF}*(\text{E1F}+\text{E2F})+\text{EMT}*(1-\text{VF})$$

$$\text{E2} = \text{E1}$$

$$\text{G12} = \text{GMT}/(1-\text{sqrt}(\text{VF})*(1-\text{GMT}/\text{GF}))$$

$$\text{NU12} = (1-\text{VF})*\text{NUm}+\text{VF}*\text{NUf}$$

$$\text{NU21} = \text{NU12}*(\text{E2}/\text{E1})$$

$$\text{TWOMU} = \text{E1}/(1 + \text{NU12})$$

$$\text{SIXMU} = 3*\text{TWOMU}$$

$$\text{ALAMDA} = \text{TWOMU}*(\text{E1}-\text{TWOMU})/(\text{SIXMU}-2*\text{E1})$$

end if

C CALL XPLB\_ABQERR(LOP,'VUMAT point 6.',INTV,REALV,CHARV)

C CALCULATE COMPLIANCE MATRIX (S)

$$\text{Smat}(1,1) = 1/\text{E1}$$

$$\text{Smat}(1,2) = -\text{NU12}/\text{E1}$$

$$\text{Smat}(1,3) = 0\text{D}0$$

$$\text{Smat}(2,1) = \text{Smat}(1,2)$$

$$\text{Smat}(2,2) = 1/\text{E2}$$

$$\text{Smat}(2,3) = 0\text{D}0$$

$$\text{Smat}(3,1) = 0\text{D}0$$

$$\text{Smat}(3,2) = 0\text{D}0$$

$$\text{Smat}(3,3) = 1/\text{G12}$$

C CALCULATE REDUCED STIFFNESS Matrix (Q)

C Line 161

$$\text{Qmat}(1,1) = \text{E1}/(1-\text{NU12}*\text{NU21})$$

```

Qmat(1,2) = E2*NU12/(1-NU12*NU21)
Qmat(1,3) = 0D0
Qmat(2,1) = Qmat(1,2)
Qmat(2,2) = E2/(1-NU12*NU21)
Qmat(2,3) = 0D0
Qmat(3,1) = 0D0
Qmat(3,2) = 0D0
Qmat(3,3) = G12
C   CALL XPLB_ABQERR(LOP,'VUMAT point 7.',INTV,REALV,CHARV)
C   CALCULATE STRESSES
      do k = 1, nblock
      trace = strainInc(k,1) + strainInc(k,2) + strainInc(k,3)
C   Line 179
      stressNew(k,1) = stressOld(k,1) + TWOMU*strainInc(k,1) + ALAMDA*trace
      stressNew(k,2) = stressOld(k,2) + TWOMU*strainInc(k,2) + ALAMDA*trace
      stressNew(k,3) = stressOld(k,3) + TWOMU*strainInc(k,3) + ALAMDA*trace
      stressNew(k,4) = stressOld(k,4) + TWOMU*strainInc(k,4) + ALAMDA*trace
      if (nshr .gt. 1) then
C   Line 184
          do m = 1, nblock
          stressNew(m,5) = stressOld(k,5) + TWOMU*strainInc(m,5)
          stressNew(m,6) = stressOld(k,6) + TWOMU*strainInc(m,6)
          end do
      end if
      end do

```

```

C   CALL XPLB_ABQERR(LOP,'VUMAT point 8.',INTV,REALV,CHARV)
C   CALCULATE PRINCIPAL STRAINS ("pstrain")
C   Line 198
      do k = 1, nblock
      pstrain1 = Smat(1,1)*stressNew(k,1) + Smat(1,2)*stressNew(k,2)
      pstrain2 = Smat(2,1)*stressNew(k,1) + Smat(2,2)*stressNew(k,2)
      pstrain3 = Smat(3,3)*stressNew(k,3)
C   Line 197
C   UPDATE LOCAL STRESSES ("sigma") = Q MATRIX * STRAIN VECTOR (E)
      sigma1 = Qmat(1,1)*pstrain1 + Qmat(1,2)*pstrain2
      sigma2 = Qmat(2,1)*pstrain1 + Qmat(2,2)*pstrain2
      sigma3 = Qmat(3,3)*pstrain3
C   Line 210
C   GLOBAL (X,Y) COORDINATE STRESS ANALYSIS
C   WITH THETA = 45 degrees
      sigmaX = sigma1/2 + sigma2/2 - sigma3
      sigmaY = sigma1/2 + sigma2/2 + sigma3
      sigmaXY = sigma1/2 - sigma2/2
C   Line 217
C   UPDATE PRINCIPAL STRAINS ("epsilonE")
      epsilonE1 = pstrain1 + strainInc(k,1)
      epsilonE2 = pstrain2 + strainInc(k,2)
      epsilonE3 = pstrain3 + strainInc(k,3)
C   Line 223

```

C GLOBAL COORDINATE (X,Y) STRAIN ANALYSIS

C WITH THETA = 45 degrees

$$\text{epsilonX} = \text{epsilonE1}/2 + \text{epsilonE2}/2 - \text{epsilonE3}/2$$

$$\text{epsilonY} = \text{epsilonE1}/2 + \text{epsilonE2}/2 + \text{epsilonE3}/2$$

$$\text{epsilonXY} = \text{epsilonE1}/2 - \text{epsilonE2}/2$$

C Line 230

$$\text{ENERGY} = 0.5 * \text{sigmaX} * \text{epsilonX}$$

C STATE DEPENDENT VARIABLES

C CALL XPLB\_ABQERR(LOP,'VUMAT point 9.',INTV,REALV,CHARV)

$$\text{StateNew}(k,1) = \text{pstrain1}$$

$$\text{StateNew}(k,2) = \text{pstrain2}$$

$$\text{StateNew}(k,3) = \text{pstrain3}$$

$$\text{StateNew}(k,4) = \text{sigma1}$$

$$\text{StateNew}(k,5) = \text{sigma2}$$

$$\text{StateNew}(k,6) = \text{sigma3}$$

$$\text{StateNew}(k,7) = \text{epsilonE1}$$

$$\text{StateNew}(k,8) = \text{epsilonE2}$$

$$\text{StateNew}(k,9) = \text{epsilonE3}$$

$$\text{StateNew}(k,10) = \text{EMT}$$

$$\text{StateNew}(k,11) = \text{GMT}$$

$$\text{StateNew}(k,12) = \text{E1}$$

$$\text{StateNew}(k,13) = \text{E2}$$

$$\text{StateNew}(k,14) = \text{G12}$$

$$\text{StateNew}(k,15) = \text{NU12}$$

$$\text{StateNew}(k,16) = \text{sigmaX}$$

```
StateNew(k,17) = sigmaY
StateNew(k,18) = sigmaXY
StateNew(k,19) = epsilonX
StateNew(k,20) = epsilonY
StateNew(k,21) = epsilonXY
StateNew(k,22) = ENERGY

end do

return

end
```

The ANP group VUMAT is exactly the same as the control group VUMAT except for different Prony series terms as specified in **Table 5.2**.

## REFERENCES

Abaqus Version 6.14 Analysis Users Guide, Volumes I - IV

Adams, D. S., Mobrem, M. (2009). Lenticular Jointed Antenna Deployment Anomaly and Resolution Onboard the Mars Express Spacecraft. Journal of Spacecraft and Rockets, Vol. 46, Number 2, pp. 403 – 410

Ajayan, P. M., Stephan, O., Colliex, C., Trauth, D. (1994). Aligned Carbon Nanotube Arrays Formed by Cutting A Polymer Resin-Nanotube Composite. Science, Vol. 265, pp. 1212

Akinyede, O., Mohan, R., Kelkar, A., Sankar, J. (2009). Static and Fatigue Behavior of Epoxy/Fiberglass Composites Hybridized with Alumina Nanoparticles. Journal of Composite Materials, Vol. 43, Number 7, pp. 769 – 781

Aniskevich (2012). Long Term Deformability and Aging of Polymer Matrix Composites

Aniskevich, K., Starkova, O., Janson, J., Aniskevich, A. (2012). Long-Term Deformability and Aging of Polymer Matrix Composites. Nova Science Publishers, NY

Ash, B. J., Rogers, D. F., Wiegand, C. J., Schadler, L. S., Siegel, R. W., Benicewicz, B. C., Apple, T. (2002). Mechanical Properties of Al<sub>2</sub>O<sub>3</sub>/Polymethylmethacrylate Nanocomposites. Polymer Composites, Vol. 23, Number 6, pp. 1014 – 1025

Ash, B. J., Stone, J., Rogers, D. F., Schadler, L. S., Siegel, R. W., Benicewicz, B. C., Apple, T. (2001). Investigation into the Thermal and Mechanical Behavior of PMMA/Alumina Nanocomposites. Materials Research Society Symposium Proceedings, Vol. 661, KK2.10.1 - KK2.10.6

Baier, H., Datashvili, L., Rapp, S. (2012). Smart and Nano Materials for Performance Enhancement of Space Structures. Proc. of SPIE Vol. 8409

Banik, J. A., LaPointe, M., LaCorte, P. (2018). On-Orbit Validation of the Roll-Out Solar Array. 2018 AIAA Spacecraft Structures Conference

Ben, S., Zhao, J., Zhang, Y., Qin, Y., Rabczuk, T. (2015). The interface strength and debonding for composites structures: Review and recent developments. Composite Structures, Vol. 129, pp. 8 – 26

Benveniste, Y. (1987). A New Approach to the Application of Mori-Tanaka's Theory in Composite Materials. Mechanics of Materials, Vol. 6, pp. 147 – 157

- Berg, K. (1998). Appendix A, Typical Properties for Advanced Composites. Handbook of Composites. London. ISBN 0 412 54020 7, pp. 1053 - 1058
- Bishop, J. F. W., Hill, R. (1951). A Theoretical Derivation of the Plastic Properties of a Polycrystalline Face-Centered Metal. H. H. Wills Laboratory, University of Bristol, pp. 1298 – 1307
- Bishop, J. F. W., Hill, R. (1951). A Theory of the Plastic Distortion of a Polycrystalline Aggregate under Combined Stresses. H. H. Wills Physical Laboratory, University of Bristol, pp. 414 – 427
- Boul, P. J., Turner, K., Li, J., Pulikkathara, M. X., Dwivedi, R., C., Sosa, E. D., Lu, Y., Kuznetsov, O. V., Moloney, P., Wilkins, R., O'Rourke, M. J., Khabashesku, V. N., Arepalli, S., Yowell, L. (2009). Single Wall Carbon Nanotube Response to Proton Radiation. Journal of Physical Chemistry, Vol. 113, pp. 14467 – 14473
- Borowski, E., Soliman, E., Khan, A., Reda Taha, M. M. (2017). Stowage and Deployment of a Viscoelastic Orthotropic Carbon Fiber Composite Tape Spring, AIAA Journal of Spacecraft and Rockets
- Brinkmeyer, A., Pellegrino, S., Weaver, P. M., Santer, M. (2013). Effects of Viscoelasticity on the Deployment of Bistable Tape Springs. 19th International Conference on Composite Materials
- Bueche, A. M. (1957). Filler Reinforcement of Silicone Rubber. Journal of Polymer Science, Vol. XXV, pp. 139 – 149
- Canal, L. P., Gonzalez, C., Molina-Aldareguia, J. M., Segurado, J., Llorca, J. (2012). Application of digital image correlation at the microscale in fiber-reinforced composites. Composites: Part A 43, pp. 1630 – 1638
- Chamberlain, M. K., Kiefer, S. H., Banik, J. A. (2018). On-Orbit Structural Dynamics Performance of the Roll-Out Solar Array. AIAA Spacecraft Structures Conference, 2018
- Chen, T. (2000). Determining a prony series for a viscoelastic material from time varying strain data. NASA
- Cheng, L., Xia, X., Scriven, L. E., Gerberich, W. W. (2005). Spherical indentation of viscoelastic material. Mechanics of Materials, Vol. 37, pp. 213 – 226
- Cheng, R., Yang, H. (2005). Application of time-temperature superposition principle to polymer transition kinetics. Journal of Applied Polymer Science, Vol. 99, pp. 1767 – 1772
- Chipara, M. (2002). Nanomaterials in Space: Is the Future Granted?

- Chipara, M. (2005). Nanodosimetry: Present and perspectives. Material Res. Soc. Symp., Vol. 851, pp. 101 – 105
- Coleman, B. D., Noll, W. (1961). Foundations of Linear Viscoelasticity. Reviews of Modern Physics, Vol. 33, Number 2, April 1961
- Coleman, J. N., Khan, U., Blau, W. J., Gun'ko, Y. K. (2006). Small but strong: A review of the mechanical properties of carbon nanotube-polymer composites. Carbon, Vol. 44, pp. 1624 – 1652
- Cousin, P., Smith, P. (1994). Dynamic Mechanical Properties of Sulfonated Polystyrene/Alumina Composites. Journal of Polymer Science: Part B: Polymer Physics, Vol. 32, pp. 459 – 468
- da Veiga, L. B., Lovadina, C., Reali, A. (2012). Avoiding shear locking for the Timoshenko beam problem via isogeometric collocation methods. Computational Methods in Applied Mechanical Engineering 241 - 244, pp. 38 – 51
- Dastgerdi, J. N., Marquis, G., Salimi, M. (2014). Micromechanical modeling of nanocomposites considering debonding of reinforcements. Composites Science and Technology, Vol. 93, pp. 38 – 45
- Davis, S., Gutierrez, G. (2011). Structural, Elastic, Vibrational and Electronic Properties of Amorphous Al<sub>2</sub>O<sub>3</sub> from ab initio Calculations. Journal of Physics: Condensed Matter, Vol. 23, pp. 1 – 8
- Dorigato, A., Pegoretti, A., Kolarik, J. (2010). Nonlinear tensile creep of linear low density polyethylene/fumed silica nanocomposites: time strain superposition and creep prediction. Polymer Composites, Vol. 31, Number 11, pp. 1947 – 1955
- Dudkin, B. N., Zainullin, G. G., Krivoshapkin, P. V., Krivoshapkina, E. F., Ryazanov, M. A. (2007). Influence of Nanoparticles and Nanofibers of Aluminum Oxide on the Properties of Epoxy Composites. Journal of Glass Physics and Chemistry, Vol. 34, Number 2, pp. 187 – 191
- Dutta, P., Hui, D. (2000). Creep Rupture of a GFRP Composite at Elevated Temperatures. Computers and Structures, Vol. 76, pp. 153 – 161
- Eshelby, J. D. (1957). The Determination of the Elastic Field of an Ellipsoidal Inclusion, and Related Problems
- Ferry, J. D. (1980). Viscoelastic Properties of Polymers. John Wiley & Sons Inc., 3rd Ed., 1980

- Feynman, R. P. (1959). There's plenty of room at the bottom. Invited lecture, <http://www.zyvex.com/nanotech/feynman.html>
- Findley, Lai, Onaran (1976). Creep and Relaxation of Nonlinear Viscoelastic Materials.
- Francis, W. H., Hulse, M. (2015). High Strain Composite Slit Tubes for Roll-Out Structures. 2nd AIAA Spacecraft Structures Conference
- Fu, S.-Y., Feng, X.-Q., Lauke, B., Mai, Y.-W. (2008). Effects of Particle Size, Particle/Matrix Interface Adhesion and Particle Loading on Mechanical Properties of Particulate-Polymer Composites. Composites: Part B, Vol. 39, pp. 933-961
- Garner, A., Genedy, M., Kandil, U., Taha, M. R. (2017). Controlling Off-Axis Stiffness and Stress-Relaxation of Carbon Fiber Reinforced Polymer Using Alumina Nanoparticles. Journal of Composite Materials, Vol. 52, Number 18, pp. 2483 - 2491
- Gerngross, T., Pellegrino, S. (2007). Modelling of Anisotropic Viscoelastic Behaviour in Super-Pressure Balloons. AIAA 2007-1808
- Gerngross, T., Xu, Y., Pellegrino, S. (2008). Viscoelastic Behaviour of Pumpkin Balloons. Advances in Space Research, Vol. 42, pp. 1683 – 1690
- Glaskova, T., Aniskevich, K., Borisova, A. (2013). Modeling of creep for multiwall carbon nanotube/epoxy nanocomposite. Journal of Applied Polymer Science, 2013, pp. 3314 – 3324
- Goertzen, W. K., Kessler, M. R. (2006). Creep Behavior of Carbon Fiber/Epoxy Matrix Composites. Materials Science and Engineering A, Vol. 421, pp. 217 – 225
- Gomez-Delrio, A., Kwok, K. (2018). Viscoelastic Analysis of Stowage and Quasi-Static Deployment of Composite Tape Springs. AIAA SciTech Forum 2018
- Guest, S. D., Pellegrino, S. (1992). Inextensional Wrapping of Flat Membranes. Proceedings of the First International Seminar on Structural Morphology, Montpellier, 7 - 11 Sep, pp. 203 - 215
- Guest, S. D., Pellegrino, S. (1994). The Folding of Triangulated Cylinders, Part I: Geometric Considerations. Journal of Applied Mechanics, Vol. 61, pp. 773 – 777
- Guest, S. D., Pellegrino, S. (1994). The Folding of Triangulated Cylinders, Part II: The Folding Process. Journal of Applied Mechanics, Vol. 61, pp. 778 - 783
- Gupta, A., Raghaven, J. (2010). Creep of PW Polymer Matrix Composites Under On-Axis and Off-Axis Loading. Composites Part A, Vol. 41, pp. 1289 – 1300

- Halpin, J. C. (1969). Effects of Environmental Factors on Composite Materials. Technical Report AFML-TR-67-423
- Hansen, A., Garnich, M. (1995). A Multicontinuum Theory for Structural Analysis of Composite Material Systems. Composites Engineering, Vol. 5, Number 9, pp. 1091 – 1103
- Hashin, Z. (1962). Bounds for Viscosity Coefficients of Fluid Mixtures by Variational Methods. Office of Naval Research, NR 064-458
- Hashin, Z. (1965). On Elastic Behaviour of Fibre Reinforced Materials of Arbitrary Transverse Phase Geometry. Journal of the Mechanics of Physical Solids, Vol. 13, pp. 119 – 134
- Hashin, Z. (1966). Viscoelastic Fiber Reinforced Materials. AIAA Journal Vol. 4, Number 8, pp. 1411 - 1417
- Hashin, Z. (1970). Complex Moduli of Viscoelastic Composites I General Theory and Application to Particulate Composites. International Journal of Solids and Structures, Vol. 6, pp. 539 – 552
- Hashin, Z., Rosen, B. W. (1964). The Elastic Moduli of Fiber-Reinforced Materials. Journal of Applied Mechanics, June 1964, pp. 223 – 232
- Hashin, Z., Shtrikman, S. (1962). A Variational Approach to the Theory of the Elastic Behaviour of Multiphase Materials. Journal of Mechanics of Physical Solids, Vol. 11, pp. 127 – 140
- Hashin, Z., Shtrikman, S. (1962a). On Some Variational Principles in Anisotropic and Nonhomogeneous Elasticity. Journal of Mechanics of Physical Solids, Vol. 10, pp. 335 – 342
- Hashin, Z., Shtrikman, S. (1962b). A Variational Approach to the Theory of the Elastic Behaviour of Polycrystals. Journal of Mechanics of Physical Solids, Vol. 10, pp. 343 – 352
- Hedgepeth, J. M. (1961). Stress Concentrations in Filamentary Structures. NASA TN D-882
- Hernandez-Perez, A., Aviles, F., Mary-Pat, A., Valadez-Gonzalez, A., Herrera-Franco, P. J., Bartolo-Perez, P. (2008). Effective Properties of Multiwalled Carbon Nanotube/Epoxy Composites Using Two Different Tubes. Composites Science and Technology

- Hill, R. (1952). The Elastic Behaviour of a Crystalline Aggregate. Proceedings of the Physical Society A, Vol. 65, pp. 349 – 354
- Hill, R. (1963). Elastic Properties of Reinforced Solids: Some Theoretical Principles. J. Mech. Phys. Solids, Vol. 11, pp. 357 – 37
- Hill, R. (1964). Theory of Mechanical Properties of Fibre-Strengthened Materials: I. Elastic Behaviour. Journal of Mechanics of Physical Solids, Vol. 12, pp. 199 – 212
- Hill, R. (1965). A Self-Consistent Mechanics of Composite Materials. J. Mech. Phys. Solids, Vol. 13, pp. 213 – 222
- Hock, A. (2013). Results from VPM Dipole Antenna Creep Test. Internal AFRL Test Report.
- Hoskin, A. (2015). Blossoming of Coiled Deployable Booms. 56th AIAA/ASCE/AHS/ASC Structures, Structural Dynamics, and Materials Conference
- Hoskin, A., Viquerat, A. (2016). An Analysis of a Coiled Tape Spring during Compression and Extension. 3rd AIAA Spacecraft Structures Conference
- Hughes, T. V., Chambers, C. R. (1886). Manufacture of Carbon Filaments. United States Patent No. 405,480, dated June 18, 1889
- Iijima, S. (1991). Helical microtubules of graphitic carbon. Nature, Vol. 354, 7 November 1991
- Iqbal, K., Pellegrino, S. (2000). Bi-Stable Composite Shells. AIAA 2000-1385
- Iqbal, K., Pellegrino, S., Daton-Lovett, A. (1998). Bi-Stable Composite Slit Tubes.
- Jenkins, C. H. M. (2006). Recent Advances in Gossamer Spacecraft. AIAA
- Jeon, S. K., Murphey, T. W. (2011). Design and Analysis of a Meter-Class CubeSat Boom with a Motor-Less Deployment by Bi-Stable Tape Springs. 52nd AIAA/ASME/ASCE/AHS/ASC Structures, Structural Dynamics, and Materials Conference, AIAA Paper # 2011-1731
- Jia, Y., Peng, K., Gong, X.-L., Zhang, Z. (2011). Creep and Recovery of Polypropylene/Carbon Nanotube Composites. International Journal of Plasticity, Vol. 27, pp. 1239 – 1251
- Karakaya, S., Soykasap, O. (2012). Homogenized Tensile and Bending Properties of PW Single-Ply E-Glass/Epoxy. Polymer Composites, pp. 881 – 888

- Keil, T. J., Banik, J. A. (2011). Stowage and Deployment Strength of a Rollable Composite Shell Reflector. 52nd AIAA/ASME/ASCE/AHS/ASC Structures, Structural Dynamics and Materials Conference, AIAA 2011-2103
- Khan, A. I., Borowski, E. C., Soliman, E. M., Taha, M. M. R. (2017). Examining Energy Dissipation of Deployable Aerospace Composites Using Matrix Viscoelasticity. Journal of Aerospace Engineering, Vol. 30, 5, pp. 1 – 10
- Kolarik, J., Fambri, L., Pegoretti, A., Penati, A. (2002). Prediction of the Creep of Heterogeneous Polymer Blends: Rubber-Toughened Polypropylene/Poly(styrene-co-Acrylonitrile). Polymer Engineering and Science, Vol. 42, Number 1, pp. 161 – 169
- Kroto, H. W., Heath, J. R., O'Brien, S. C., Curl, R. F., Smalley, R. E. (1985). C60: Buckminsterfullerene. Nature, Vol. 318, Number 14, Nov 1985
- Kuo, M. C., Tsai, C. M., Huang, J. C., Chen, M. (2004). PEEK Composites Reinforced by Nano-sized SiO<sub>2</sub> and Al<sub>2</sub>O<sub>3</sub> Particulates. Materials Chemistry and Physics, Vol. 90, pp. 185 – 195
- Kuo, M. C., Tsai, C. M., Huang, J. C., Chen, M. (2005). PEEK Composites Reinforced by Nano-sized SiO<sub>2</sub> and Al<sub>2</sub>O<sub>3</sub> Particulates. Journal of Materials Chemistry and Physics, Vol. 90, pp. 185 – 195
- Kwok, K., Pellegrino, S. (2010). Shape Recovery of Viscoelastic Deployable Structures. AIAA Paper # 2010-2606
- Kwok, K., Pellegrino, S. (2011). Viscoelastic Effects in Tape-Springs. AIAA Paper # 2011-2022
- Kwok, K., Pellegrino, S. (2012). Micromechanical Modeling of Deployment and Shape Recovery of Thin-walled Viscoelastic Composite Space Structures, 53<sup>rd</sup> AIAA/ASME/ASCE/AHS/ASC Structures, Structural Dynamics, and Materials Conference, Honolulu, HI, April 2012
- Kwok, K., Pellegrino, S. (2013). Folding, Stowage and Deployment of Viscoelastic Tape Springs. AIAA Journal, Vol. 51, Number 8, pp. 1908 – 1918
- Kwok, K., Pellegrino, S. (2017). Micromechanics Models for Viscoelastic Plain-Weave Composite Tape Springs. AIAA Journal, Vol. 55, Number 1, pp. 309 – 321
- Lau, K-T., Nurse, A. D., Veprek, S., Cselle, T. (2005). Preface to Composites Science and Technology, Vol. 65, pp. 711-712
- Laws, N., McLaughlin, R. (1978). Self-Consistent Estimates for the Viscoelastic Creep Compliances of Composite Materials. Proc. R. Soc. Lond. A., Vol. 359, pp. 251 – 273

- Levesque, M., Gilchrist, M. D., Bouleau, N., Derrien, K., Baptiste, D. (2007). Numerical Inversion of the Laplace-Carson Transform Applied to Homogenization of Randomly Reinforced Linear Viscoelastic Media. Computational Mechanics, Vol. 40, pp. 771 – 789
- Li, K., Gao, X.-L., Roy, A. K. (2006). Micromechanical modeling of viscoelastic properties of carbon nanotube-reinforced polymer composites. Mechanics of Advanced Materials and Structures, Vol. 13, pp. 317 – 328
- Li, R. (2000). Time-temperature superposition method for glass transition temperature of plastic materials. Materials Science and Engineering, Vol. A278, pp. 36 – 45
- Liebich, R., Scholz, A., Wieschalla, M. (2012). Rotors Supported by Elastomer-Ring-Dampers - Experimental and Numerical Investigations. Proceedings on the 10th International Conference on Vibrations in Rotating Machinery, 11 - 13 Sep 2012, pp. 443 – 453
- Lionetto, F., Calo, E., Di Benedetto, F., Pisignano, D., Maffezzoli, A. (2014). A Methodology to Orient Carbon Nanotubes In a Thermosetting Matrix. Composites Science and Technology, Vol. 96, pp. 47 – 55
- Liu, B., Feng, X., Zhang, S.-M. (2009). The Effective Young's Modulus of Composites beyond the Voigt Estimation due to the Poisson Effect. Composites Science and Technology, Vol. 69, pp. 2198 – 2204
- Liu, C., Qin, H., Mather, P. T. (2007). Review of progress in shape-memory polymers. Journal of Materials Chemistry, Vol. 17, pp. 1543 – 1558
- Liu, Y., Du, H., Liu, L., Leng, J. (2014). Shape Memory Polymers and their Composites in Aerospace Applications: A Review. Smart Material Structures, Vol. 23, pp. 1 - 22
- Losi, G. U., Knauss, W. G., (1992). Free Volume Theory and Nonlinear Thermoviscoelasticity. Polymer Engineering and Science, Vol. 32, Number 8, pp. 542 – 557
- Lv, Y., Huang, Y., Kong, M., Yang, J., Yang, Q., Li, G. (2014). Creep Lifetime Prediction of Polypropylene/Clay Nanocomposites Based on a Critical Failure Strain Criterion. Composites Science and Technology, Vol. 96, pp. 71 – 79
- Lyle, K. H., Horta, L. G. (2012). Deployment Analysis of a Simple Tape-Spring Hinge Using Probabilistic Methods. AIAA
- Ma, P.-C., Siddiqui, N. A., Maron, G. Kim, J.-K. (2010). Dispersion and functionalization of carbon nanotubes for polymer-based nanocomposites: a review. Composites: Part A, Vol. 41, pp. 1345 – 1367

- Ma, W., Liu, L., Zhang, Z., Yang, R., Liu, G., Zhang, T., An, X., Yi, X., Ren, Y., Niu, Z., Li, J., Dong, H., Zhou, W., Ajayan, P. M., Xie, S. (2009). High-Strength Composite Fibers: Realizing True Potential of Carbon Nanotubes in Polymer Matrix through Continuous Reticulate Architecture and Molecular Level Couplings. Nano Letters, Vol. 9, Number 8, pp. 2855 – 2861
- Machado, M., Cakmak, U. D., Kallai, I., Major, Z. (2016). Thermomechanical Viscoelastic Analysis of Woven-Reinforced Thermoplastic-Matrix Composites. Composite Structures, Vol. 157, pp. 256 – 264
- MacNaughton, J. D. (1963). Unfurlable Metal Structures for Spacecraft. Astronautics Symposium of the Canadian Aeronautics and Space Institute, March 1, 1963
- Maddux, M. R., Murphey, T. W. (2005). The Effects of Folding On The Dimensional Stability of Rigidizable Composite Laminates. AIAA Paper # 2005-2365
- McNeil, B. (2015). Penta-graphene, a new structural variant of carbon, discovered. Virginia Commonwealth University Public Release.  
[http://eurekaalert.org/pub\\_releases/2015-02/vcu-pan020315.php](http://eurekaalert.org/pub_releases/2015-02/vcu-pan020315.php)
- Meyers, M., Chawla, K. (2010). Mechanical Behavior of Materials. Cambridge University Press, 2nd Edition
- Mikulas, Martin, M. (2000). Laminate Composite Notes, University of Colorado Boulder
- Mobrem, M., Peterson, L. D., Cormarkovic, V., Montazersadgh, F. (2017). An Evaluation of Structural Analysis Methodologies for Space Deployable Structures. 4th AIAA Spacecraft Structures Conference
- Monthioux, M., Kuznetsov, V. L. (2006). Who should be given the credit for the discovery of carbon nanotubes? Carbon, Vol. 44, pp. 1621 - 1623, Guest Editorial
- Moreira, D. C., Sphaier, L. A., Reis, J. M. L., Nunes, L. C. S. (2012). Determination of Young's Modulus in Polyester-Al<sub>2</sub>O<sub>3</sub> and Epoxy-Al<sub>2</sub>O<sub>3</sub> Nanocomposites using the Digital Image Correlation Method. Composites: Part A, Vol. 43, pp. 304 – 309
- Murphey, T. W., Francis, W. H., Davis, B. L., Mejia-Ariza, J., Santer, M., Footdale, J. N., Schmid, K., Soykasap, O., Guidanean, K., Warren, P. A. (2015). High Strain Composites. 2nd AIAA Spacecraft Structures Conference
- Murphey, T. W., Jeon, S., Biskner, A., Sanford, G. E. (2010). Deployable Booms and Antennas Using Bi-Stable Tape-Springs. 24th Annual AIAA/USU Conference on Small Satellites. Paper # SSC10-X-6

- Murphey, T. W., Sanford, G. E., Grigoriev, M. M. (2011). Nonlinear Elastic Constitutive Modeling of Large Strains in Carbon Fiber Composite Flexures. 16<sup>th</sup> International Conference on Composite Structures, A. J. M., Ferreira, ed., Porto, Portugal: FEUP
- Murphey, T. W., Peterson, M. E., Grigoriev, M. M. (2013). Four Point Bending of Thin Unidirectional Composite Laminas. 54<sup>th</sup> AIAA/ASME/ASCE/AHS/ASC Structures, Structural Dynamics, and Materials Conference, Boston, MA: AIAA
- Murphey, T. W., Meink, T., Mikulas, M. M. (2001). Some Micromechanics Considerations of the Folding of Rigidizable Composite Materials. AIAA-2001-1418, 42nd Annual AIAA/ASME/ASCE/AHS/ASC Structures, Structural Dynamics, and Materials Conference
- Murphey, T. W., Sanford, G. E. (2008). A Test Method to Assess the Foldability of Flexible Structural Materials. AIAA
- Murphey, T. W., Sanford, G. E., Grigoriev, M. M. (2011). Nonlinear Elastic Constitutive Modeling of Large Strains in Carbon Fiber Composite Flexures. 16th International Conference on Composite Structures, 2011
- Naous, W., U, X.-Y., Zhang, Q.-X., Naito, K., Kagawa, Y. (2006). Morphology, Tensile Properties, and Fracture Toughness of Epoxy/Al<sub>2</sub>O<sub>3</sub> Nanocomposites. Journal of Polymer Science: Part B: Polymer Physics, Vol. 44, pp. 1466 – 1473
- Ng, C. B., Schadler, L. S., Siegel, R. W. (1999). Synthesis and Mechanical Properties of TiO<sub>2</sub>-Epoxy Nanocomposites. Nanostructured Materials, Vol. 12, pp. 507 – 510
- Nguyen S.-N., Lee, J., Cho, M. (2015). Higher Order ZigZag Laminated Composite Shell Theory for Viscoelastic Behavior. 56th AIAA/ASCE/AHS/ASC Structures, Structural Dynamics, and Materials Conference.
- Novikov, L. S., Mileev, V. N., Voronina, E. N. (2009). Modeling and Testing Nanomaterials for Space Applications. Proceedings of the 9th International Conference: Protection of Materials and Structures from Space Environment, edited by Kleiman, J. I.
- Pathan, M. V., Tagarielli, V. L., Patsias, S. (2017). Effect of Fibre Shape and Interphase on the Anisotropic Viscoelastic Response of Fibre Composites. Composite Structures, Vol. 162, pp. 156 – 163
- Pellegrino, S. (1993). Structural Computations with the Singular Value Decomposition of the Equilibrium Matrix. International Journal of Solids and Structures, Vol. 30, No. 21, pp. 3025 – 3035
- Pellegrino, S. (1995). Large Retractable Appendages in Spacecraft. Journal of Spacecraft and Rockets Vol. 32, Number 6, pp. 1006 – 1014

- Peterson, M. E., Murphey, T. W. (2013). Large Deformation Bending of Thin Composite Tape Spring Laminates. AIAA Paper # 2013-1667
- Pollard, E., Murphey, T. (2006). Development of Deployable Elastic Composite Shape Memory Alloy Reinforced (DECSMAR) Structures. AIAA 2006-1681
- Pollard, E., Murphey, T. W., Sanford, G. E. (2007). Experimental and Numerical Analysis of a DECSMAR Structures' Deployment and Deployed Performance. AIAA 2007-2004
- Putz, K. W., Palmeri, M. J., Cohn, R. B., Andrews, R., Brinson, L. C. (2008). Effect of Cross-Link Density on Interphase Creation in Polymer Nanocomposites. Macromolecules, Vol. 41, pp. 6752 – 6756
- Radok, J. R. M. (1956). Viscoelastic Stress Analysis. Office of Naval Research Contract # Nonr-562(10)
- Rimrott, F. P. J. (1965). Storable Tubular Extendible Member: A Unique Machine Element. Machine Design, December 9, 1965, pp. 1 – 11
- Rimrott, F. P. J. (1966). Storable Tubular Extendible Members. Engineering Digest, September 1966, pp. 29 – 34
- Rimrott, F. P. J. (1966). Two Secondary Effects in Bending of Slit Thin-Walled Tubes. Journal of Applied Mechanics, Paper No. 65-APMW-20, pp. 75 – 78
- Rimrott, F. P. J. (1967). STEM Self-Extension Velocities. Canadian Aeronautics and Space Journal, Vol. 13, pp. 1-7
- Rimrott, F. P. J. (1980). Self-Extension of an Open Section Tube, Theory of Shells, North-Holland Publishing Company, pp. 495 - 508
- Roh, J.-H., Kim, H.-I., Lee, S.-Y. (2015). Viscoelastic effect on unfolding behaviors of shape memory composite booms. Composite Structures, Vol. 133, pp. 235 – 245
- Roscoe, R. (1969). Bounds for the Real and Imaginary Parts of the Dynamic Moduli of Composite Viscoelastic Systems. Journal of the Mechanics of Physical Solids, Vol. 17, pp. 17 – 22
- Rouzegar, J., Gholami, M. (2017). Creep and Recovery of Viscoelastic Laminated Composite Plates. Composite Structures, Vol. 181, pp. 256 - 272
- Salviato, M., Zappalorto, M., Quaresimin, M. (2013). Nanoparticle debonding strength: A comprehensive study on interfacial strength. International Journal of Solids and Structures, Vol. 50, pp. 3225 – 3232

- Sanford, G., Biskner, A., Murphey, T. W. (2010). Large Strain Behavior of Thin UD Composite Flexures. AIAA
- Schadler, L. S., Brinson, L. C., Sawyer, W. G. (2007). Polymer Nanocomposites: A Small Part of the Story. Journal of the Minerals, Metals and Materials Society, Vol. 59, No. 3, pp. 53 – 60
- Schapery, R. A. (1966). A Theory of Nonlinear Thermoviscoelasticity Based on Irreversible Thermodynamics. Work supported by Air Force Rocket Propulsion Laboratory, contract # AF 04(611)-11371
- Scott, D. W., Lai, J. S., Zureick, A.-H. (1995). Creep Behavior of Fiber-Reinforced Polymeric Composites: A Review of the Technical Literature. Journal of Reinforced Plastics and Composites, Vol. 14, pp. 588 – 617
- Seffen, K. A., Pellegrino, S. (1997). Deployment Dynamics of Tape Springs. Proceedings of the Royal Society of London A, Vol. 455, pp. 1003 – 1048
- Seitz, J. T., Balazs, C. F. (1968). Application of time-temperature superposition principle to long term engineering properties of plastic materials. Polymer Engineering and Science, April 1968, pp. 151 – 160
- Simoës, R., Cunha, A. M., Brostow, W. (2006). Molecular dynamics simulations of polymer viscoelasticity: effect of the loading conditions and creep behaviour. Modelling Simul. Mater. Sci. Eng., Vol. 14, pp. 157 – 178
- Singh, R. P., Zhang, M., Chan, D. (2002). Toughening of a Brittle Thermosetting Polymer: Effects of Reinforcement Particle Size and Volume Fraction. Journal of Materials Science, Vol. 37, pp. 781 – 788
- Soliman, E., Kandil, U. F., Taha, M. R. (2012). Limiting Shear Creep of Epoxy Adhesive at the FRP-Concrete Interface Using Multiwalled Carbon Nanotubes. International Journal of Adhesion and Adhesives, Vol. 33, pp. 36 – 44
- Soykasap, O. (2006). Micromechanical Models for Bending Behavior of Woven Composites. Journal of Spacecraft and Rockets, Vol. 43, Number 5, pp. 1093 – 1100
- Soykasap, O. (2011). Analysis of Plain-Weave Composites. Mechanics of Composite Materials, Vol. 47, Number 2, pp. 161 – 176
- Spitalsky, Z., Tsoukleri G., Tasis, D., Krontiras, C., Georga, S. N., Galiotis, C. (2009). High Volume Fraction Carbon Nanotube-Epoxy Composites. Nanotechnology, Vol. 20

- Sprenger, S. (2014). Fiber-reinforced composites based on epoxy resins modified with elastomers and surface-modified silica nanoparticles. Journal of Materials Science, Vol. 49, pp. 2391 – 2402
- Stolarski, H., Telytschko, T. (1983). Shear and membrane locking in curved  $C^0$  elements. Computer Methods in Applied Mechanics and Engineering, Vol. 41, pp. 279 – 296
- Straubel, M., Block, J., Sinapius, M., Huhne, C. (2011). Deployable Composite Booms for Various Gossamer Space Structures. AIAA Paper # 2011-2023
- Sun, E. Q. (2010). Shear Locking and Hourglassing in MSC Nastran, ABAQUS, and ANSYS
- Taha, M. R., Masia, M. J., Choi, K.-K., Shrive, P. L., Shrive, N. G. (2010). Creep Effects in Plain and Fiber-Reinforced Polymer Strengthened Reinforced Concrete Beams. ACI Structural Journal, Vol. 107, Number 6
- Talreja, R. (2014). Assessment of the fundamentals of failure theories for composite materials. Composites Science and Technology, Vol. 105, pp. 190 – 201
- Tavakoli, A. H., Maram, P. S., Widgeon, S. J., Rufner, J., Benthem, K. V., Ushakov, S., Sen, S., Navrotsky, A. (2013). Amorphous Alumina Nanoparticles: Structure, Surface Energy, and Thermodynamic Phase Stability. The Journal of Physical Chemistry C, Vol. 117, Number 17, pp. 123 - 130
- Thostenson, E. T., Chou, T-W. (2003). On the elastic properties of carbon nanotube-based composites: modelling and characterization. Journal of Physics D: Applied Physics, Vol. 36, pp. 573 – 582
- Thostenson, E. T., Ren, Z., Chou, T-W. (2001). Advances in the science and technology of carbon nanotubes and their composites: a review. Composites Science and Technology, Vol. 61, pp. 1899 – 1912
- Thostenson, E., Ren, Z., Chou, T-W. (2001). Advances in the Science and Technology of Carbon Nanotubes and Their Composites: A Review. Composites Science and Technology, Vol. 61, pp. 1899 – 1912
- Tian, Y., Zhang, H., Zhang, Z. (2017). Influence of Nanoparticles on the Interfacial Properties of Fiber-Reinforced-Epoxy Composites. Composites: Part A, Vol. 98, pp. 1 – 8
- Tian, Y., Zhang, H., Zhao, J., Li, T., Bie, B.-X., Luo, S.-N., Zhang, Z. (2016). High Strain Rate Compression of Epoxy Based Nanocomposites. Composites: Part A, Vol. 90, pp. 62 – 70

- Tomlins, P. E. (1996). Comparison of different functions for modelling the creep and physical ageing effects in plastics. Polymer, Vol. 37, Number 17, pp. 3907 – 3913
- Tsai, S. W., Pagano, N. J. (1968). Invariant Properties of Composite Materials.
- Tsai, S., Melo, J. (2014). An Invariant-Based Theory of Composites. Composites Science and Technology, Vol. 100, pp. 237 – 243
- Van den Oord, G. A. H. (2005). Introduction to Locking in Finite Element Methods. Bachelor Final Report. Eindhoven, June 29, 2005
- Vermeulen, A. H., Heppler, G. R. (1998). Predicting and Avoiding Shear Locking in Beam Vibration Problems using the B-Spline Field Approximation Method. Computer Methods in Applied Mechanics and Engineering, Vol. 158, pp. 311 – 327
- Voevodin, A. A., Zabinski, J. S. (2005). Nanocomposite and Nanostructured Tribological Materials for Space Applications. Composites Science and Technology, Vol. 65, pp. 741 – 748
- Walpole, L. J. (1966). On Bounds for the Overall Elastic Moduli of Inhomogeneous Systems-I. Journal of the Mechanics of Physical Solids, Vol. 14, pp. 151 – 162
- Wang, J. F., Liew, K. M. (2015). On the study of elastic properties of CNT-reinforced composites based on element-free MLS method with nanoscale cylindrical representative volume element. Composite Structures, Vol. 124, pp. 1 – 9
- Weidt, D., Figiel, L. (2015). Effect of CNT waviness and van der Waals interaction on the nonlinear compressive behaviour of epoxy/CNT nanocomposites. Composites Science and Technology, Vol. 115, pp. 52 – 59
- Weidt, D., Figiel, L. (2015). Effect of CNT waviness and van der Waals interaction on the nonlinear compressive behaviour of epoxy/CNT nanocomposites. Composites Science and Technology, Vol. 115, pp. 52 – 59
- West, R. D., Malhotra, V. M. (2006). Rupture of Nanoparticle Agglomerates and Formulation of Al<sub>2</sub>O<sub>3</sub>-Epoxy Nanocomposites Using Ultrasonic Cavitation Approach: Effects on the Structural and Mechanical Properties. Polymer Engineering and Science, pp. 426 – 430
- Wetzel, B., Hauptert, F., Zhang, M. Q. (2003). Epoxy Nanocomposites with high Mechanical and Tribological Performance. Composites Science and Technology, Vol 63, pp. 2055 – 2067

- Wilkins, R., Armendariz, L. (2002). Radiation Exposure Effects and Shielding Analysis of Carbon Nanotube Materials. Center for Applied Radiation Research (CARR) Prairie View A&M University, Grant No. NAG 9-1370
- Yee, J. C. H., Pellegrino, S. (2003). Foldable Composite Structures.
- Yee, J. C. H., Pellegrino, S. (2005). Folding of Woven Composite Structures. Composites Part A, Vol. 36, pp. 273 – 278
- Yee, J. C. H., Soykasap, O., Pellegrino, S. (2004). Carbon Fibre Reinforced Plastic Tape Springs. AIAA 2004-1819
- Yee, J. C. H., Soykasap, O., Pellegrino, S. (2004). Carbon Fibre Reinforced Plastic Tape Springs. AIAA Paper # 2004-1819
- You, Z., Pellegrino, S. (1994). Study of the Folding and Deployment Aspects of a Collapsible Rib Tensioned Surface (CRTS) Antenna Reflector. European Space Agency document # CUED/D-STRUCT/TR 144, 15 March 1994
- Yu, J., Huo, R., Wu, X., Wang, G., Jiang, P. (2012). Influence of Interface Structure on Dielectric Properties of Epoxy/Alumina Nanocomposites. Macromolecular Research, Vol. 20, Number 8, pp. 816 – 826
- Zare, Y. (2016). The Roles of Nanoparticles Accumulation and Interphase Properties in Properties of Polymer Particulate Nanocomposites by a Multi-Step Methodology. Composites: Part A, Vol. 91, pp. 127 – 132
- Zhang, M. Q., Rong, M. Z., Yu, S. L., Wetzel, B., Friedrich, K. (2002). Effect of Particle Surface Treatment on the Tribological Performance of Epoxy Based Nanocomposites. Journal of Wear, Vol. 253, pp. 1086 – 1093
- Zhang, M., Singh, R. P. (2004). Mechanical Reinforcement of Unsaturated Polyester by Al<sub>2</sub>O<sub>3</sub> Nanoparticles. Materials Letters, Vol. 58, pp. 408 – 412
- Zhang, Y., Matthews, F. L. (1983). Initial Buckling of Curved Panels of Generally Layered Composite Materials. Composite Structures, Vol. 1, pp. 3 – 30
- Zhang, Y., Zhao, J., Jia, Y., Mabrouki, T., Gong, Y., Wei, N., Rabczuk, T. (2013). An analytical solution on interface debonding for large diameter carbon nanotube-reinforced composite with functionally graded variation interphase. Composite Structures, Vol. 104, pp. 261 – 269
- Zhao, J., Li, H., Cheng, G., Cai, Y. (2016). On predicting the effective elastic properties of polymer nanocomposites by novel numerical implementation of asymptotic homogenization method. Composite Structures, Vol. 135, pp. 297 – 305

Zhu, B., Yu, T. X., Tao, X. M. (2007). An Experimental Study of In-Plane Large Shear Deformation of Woven Fabric Composite. Composites Science and Technology, Vol. 67, pp. 252 – 261

Zhu, H., Fan, T., Xu, C., Zhang, D. (2016). Nano-Structured Interpenetrating Composites with Enhanced Young's Modulus and desired Poisson's Ratio. Composites: Part A, Vol. 91, pp. 195 - 202

Zolesi, V. S., Ganga, P. L., Scolamiero, L., Micheletti, A., Podio-Guidugli, P., Tibert, G., Donati, A., Ghiozzi, M. (2012). On an innovative deployment concept for large space structures. AIAA Paper # 2012-3601